


Dieter Scholz, Egbert Torenbeek (Editors)

Continuous Open Access Special Issue "Aircraft Design"



Number 2 / 2020

in the Journal "Aerospace"

Basel, Switzerland: MDPI, 2020



an Open Access Journal by MDPI



Aircraft Design (SI - 2 / 2020)

Guest Editors
Prof. Dr. Dieter Scholz, Prof. em. Egbert Torenbeek

Deadline
31 December 2020

Special Issue

mdpi.com/si/25829 Invitation to submit

Affiliated to the CEAS Technical Committee Aircraft Design (TCAD)

Homepage: Special Issue "Aircraft Design" at MDPI:

https://www.mdpi.com/journal/aerospace/special_issues/aircraft_design

Homepage: Special Issue "Aircraft Design" at the CEAS Technical Committee Aircraft Design:

<http://journal.AircraftDesign.org>

Homepage: Special Issue "Aircraft Design" 2 / 2020, long URL:

https://www.mdpi.com/journal/aerospace/special_issues/aircraft_design_2_2020

Homepage: Special Issue "Aircraft Design" 2 / 2020, short URL:

<https://www.mdpi.com/si/25829>

DOI:

<https://doi.org/10.5281/zenodo.4624993>

URN:

<https://nbn-resolving.org/urn:nbn:de:gbv:18302-aero2020-12-31.011>

Associated URLs:

<https://nbn-resolving.org/html/urn:nbn:de:gbv:18302-aero2020-12-31.011>

© by authors

The work is licensed under a Creative Commons Attribution 4.0 International License: CC BY

<https://creativecommons.org/licenses/by/4.0>



This document combines the papers of the Special Issue "Aircraft Design" 2 / 2020 in one

PDF for further dissemination and archiving. It is published by

Aircraft Design and Systems Group (AERO)

Department of Automotive and Aeronautical Engineering

Hamburg University of Applied Science

This report is deposited and archived:

- Deutsche Nationalbibliothek (<https://www.dnb.de>)
 - Repositorium der Leibniz Universität Hannover (<https://www.repo.uni-hannover.de>)
 - Internet Archive (<https://archive.org>)
- Item: <https://archive.org/details/AircraftDesign2-2020.pdf>

Special Issue "Aircraft Design (SI-2/2020)"

Special Issue Editors

Prof. Dr. Dieter Scholz, MSME

Guest Editor

E-Mail: info@ProfScholz.de

Website: <http://english.ProfScholz.de>

Aircraft Design and Systems Group (AERO),

Department of Automotive and Aeronautical Engineering,

Hamburg University of Applied Sciences, Berliner Tor 9, 20099 Hamburg, Germany

Interests: aircraft design; flight mechanics; aircraft systems; open access publishing

Prof. em. Egbert Torenbeek

Honorary Guest Editor

Website: https://en.wikipedia.org/wiki/Egbert_Torenbeek

Flight Performance and Propulsion, Delft University of Technology, Kluyverweg 1,

2629 HS Delft, The Netherlands

Interests: aircraft design

Special Issue Information

Dear Colleagues,

Aircraft design is, as we know, the first fascinating step in the life of an aircraft, where visions are converted into reality.

In a practical sense, aircraft design supplies the geometrical description of the aircraft. Traditionally, the output is a three-view drawing and a list of aircraft parameters. Today, the output may also be an electronic 3D model. In the case of civil aircraft, a fuselage cross-section and a cabin layout are provided in addition.

In an abstract sense, aircraft design determines the design parameters to ensure that the requirements and constraints are met and design objectives are optimized. The fundamental requirements for civil aviation are payload and range. Many constraints come from certification rules demanding safety. The objectives are often of a financial nature, like lowest operating costs. Aircraft design always strives for the best compromise among conflicting issues.

The design synthesis of an aircraft goes from the conceptual design to the detailed design. Frequently, expert knowledge is needed more than computing power. Typical work involves statistics, the application of inverse methods, and use of optimization algorithms. Proposed designs are analyzed with respect to aerodynamics (drag), structure (mass), performance, stability and control, and aeroelasticity, to name just a few. A modern aircraft is a complex, computer-controlled combination of its structure, engines, and systems. Passengers demand high comfort at low fares, society demands environmentally friendly aircraft, and investors demand a profitable asset.

Overall aircraft design (OAD) comprises all aircraft types in civil and military use, considers all major aircraft components (wing, fuselage, tail, undercarriage) as well as the integration of engines and systems. The aircraft is seen as part of the air transport system and beyond contributing to multimodal transport. Aircraft design applies the different aerospace sciences and considers the aircraft during its whole life cycle. Authors from all economic sectors (private, public, civic, and general public) can submit to this Special Issue (SI). Education and training in aircraft design is considered as important as research in the field.

The SI can be a home for those active in the European Workshop on Aircraft Design Education (EWADE) or the Symposium on Collaboration in Aircraft Design (SCAD), both independent activities under the CEAS Technical Committee Aircraft Design (TCAD). Please see <http://AircraftDesign.org> for details.

Following the successful initial Special Issue on “Aircraft Design (SI-1/2017)”, this is already the second SI “Aircraft Design (SI-2/2020)”. Depending on the need, further special issues may follow. Activities in the past showed that aircraft design may be a field too small to justify its own (subscription-based) journal. A continuous open access special issue may fill the gap. As such, the Special Issue “Aircraft Design” can be a home for all those working in the field who regret the absence of an aircraft design journal.

The Special Issue "Aircraft Design" is open to the full range of article types. It is a place to discuss the "hot topics" (zero-emission airplanes, electric flight, urban air mobility—you name it). The classic topics in aircraft design remain:

- Innovative aircraft concepts
- Methodologies and tools for aircraft design and optimization
- Reference aircraft designs and case studies with data sets

It is up to us as authors to shape the Special Issue “Aircraft Design” according to our interests through the manuscripts we submit.

Prof. Dr. Dieter Scholz and Prof. em. Egbert Torenbeek, Guest Editors

Table of Contents

Dieter Scholz:

Publishing in “Aircraft Design” with a Continuous Open Access Special Issue

<https://doi.org/10.3390/aerospace7010005>

Arjit Seth, Rhea P. Liem:

Amphibious Aircraft Developments: Computational Studies of Hydrofoil Design for Improvements in Water-Takeoffs

<https://doi.org/10.3390/aerospace8010010>

Jakob R. Müller, Massimo Panarotto, Ola Isaksson:

Design Space Exploration of a Jet Engine Component Using a Combined Object Model for Function and Geometry

<https://doi.org/10.3390/aerospace7120173>

Marco Berci, Francesco Torrigiani:

Multifidelity Sensitivity Study of Subsonic Wing Flutter for Hybrid Approaches in Aircraft Multidisciplinary Design and Optimisation

<https://doi.org/10.3390/aerospace7110161>

Stanislav Karpuk, Yaolong Liu, Ali Elham:

Multi-Fidelity Design Optimization of a Long-Range Blended Wing Body Aircraft with New Airframe Technologies

<https://doi.org/10.3390/aerospace7070087>

Francesco Nicassio, Gennaro Scarselli:

Simulation and Test of Discrete Mobile Surfaces for a RC-Aircraft

<https://doi.org/10.3390/aerospace6110122>

Xingliang Jiang, Yangyang Wang:

Studies on the Electro-Impulse De-Icing System of Aircraft

<https://doi.org/10.3390/aerospace6060067>

Editorial

Publishing in “Aircraft Design” with a Continuous Open Access Special Issue

Dieter Scholz 

Aircraft Design and Systems Group (AERO), Hamburg University of Applied Science (HAW Hamburg), Berliner Tor 9, 20099 Hamburg, Germany; info@ProfScholz.de

Received: 29 December 2019; Accepted: 31 December 2019; Published: 14 January 2020



Abstract: The article looks at publishing options in the field of aircraft design to find that no dedicated journal on aircraft design exists. For this reason, a Continuous Special Issue Aircraft Design of the well established journal “Aerospace” at the Open Access publisher MDPI is started. Often special issues of a journal are introduced for “hot topics”. Here, the subset “special issue” is used for a scientific domain—in this case “aircraft design”. Recurring single special issues are numbered in sequence and are identified by the year of the deadline for manuscript submissions. This allows for the delivery of several single special issues over time in a row without the need to define a publishing schedule up front. Together these single issues form the Continuous Special Issue Aircraft Design and offer a new publishing home for the aircraft design community.

Keywords: aerospace; aviation; aeronautics; airplanes; aircraft; design; publishing; open access; special issue; MDPI; permalink; archive

1. Introduction

Aerospace consists of *aeronautics* (atmospheric flight) and *astronautics* (space flight) [1]. The scientific foundation of aeronautics is called *aeronautical science*, which includes *aeronautical engineering*. One of the many disciplines in aeronautical engineering is *aircraft design*. Aircraft design is the very first step in aeronautical engineering, where requirements are converted into a geometrical description of the aircraft.

A list of **scientific journals in the area of “aerospace”** is available from Google Scholar [2], CWTS Journal Indicators [3], and the University of Illinois [4]. A ranking of the top 40 aerospace journals was done by the German Society for Aeronautics and Astronautics (DGLR) in 2015 [5]. Among all of these listed journals, only two carry “aircraft” in their name. These two are the *Journal of Aircraft* by AIAA (ISSN 0021-8669) and *Aircraft Engineering and Aerospace Technology* by Emerald (ISSN 1748-8842). None of them specifically deals with aircraft design.

In 1998 the situation was much the same as today. For this reason, Prof. Egbert Torenbeek [6] started the **journal “Aircraft Design”** (ISSN 1369-8869) together with Prof. Dr. Jan Roskam [7] at Elsevier [8]. Both of them served as Editor. Torenbeek took care of authors in Europe and Roskam likewise took care of authors in the USA [9]. The journal started successfully and published 58 articles in the four years until 2001 [10]. The subscription-based publishing model, however, proved inadequate to serve the rather small aircraft design community. As a consequence, Elsevier’s title had to be discontinued in 2002, when it was decided that the number of subscriptions was too low.

Today, this pitfall can be avoided with the **Open Access** (OA) publishing model [11,12] because the papers finance themselves with article processing charges (APC), which is referred to as “gold OA”. In turn, the papers can be read free of charge on the Internet (“gratis OA”) and are in addition free of most copyright and licensing restrictions (“libre OA”). Often, the Creative Commons Attribution

(CC BY) license is used, for example, this article makes use of CC BY. Please refer to the bottom of this article for the CC BY logo and the link leading to further details.

Furthermore, the motivation back in 1998 for establishing a journal was much the same as today. The European Workshop on Aircraft Design Education (EWADE) had been started in 1994 and was held every two years [13]. No workshop passed without expressing regret about the absence of a dedicated aircraft design journal [13–15]. In the same way as in the past, today people working in the domain of aircraft design also see each other as a close-knit and affectionate **community**. The European Workshop on Aircraft Design Education (EWADE) [16] was continued along with the Symposium on Collaboration in Aircraft Design (SCAD) [17], both became independent activities under the CEAS Technical Committee Aircraft Design (TCAD) [18]. CEAS is the Council of European Aerospace Societies [19]. Presently, CEAS has twelve European national aerospace societies as members. In eastern or central Europe engineers come together in a workshop called Research and Education in Aircraft Design (READ) [20]. Similarly, in the USA the AIAA Aircraft Design Technical Committee is very active [21]. AIAA is the American Institute of Aeronautics and Astronautics. For these and other aircraft design related communities a Special Issue Aircraft Design can serve as a publishing home in the absence of a dedicated journal for the discipline.

2. Set Up of the Special Issue “Aircraft Design”

MDPI (Multidisciplinary Digital Publishing Institute) uses the Open Access publishing model for all of its journals including its special issues. “Aerospace” (ISSN 2226-4310) is one such journal at MDPI, which was started in 2014, and its aims include the “design . . . of aircraft” [22]. The first **Special Issue Aircraft Design** (SI-1/2017) [23] at “Aerospace” was managed by Guest Editor Dr. Mohammad Sadraey and includes five papers. The second Special Issue Aircraft Design (SI-2/2020) [24] is managed by Prof. Dr. Dieter Scholz, MSME [25] as Guest Editor. In addition, Prof. em. Egbert Torenbeek contributes with his experience as Honorary Guest Editor.

As can be seen above, the special issues are consecutively **numbered**. The year given after the issue number is the year in which the Special Issue closed or is scheduled to close. This allows for the delivery of a continuous sequence of special issues over time without the need to define a certain publishing sequence from the start. It enables the *Continuous Special Issue Aircraft Design*, which stands for the sum of all individual Special Issues Aircraft Design and the mechanism to make this an ongoing activity.

Each special issue has its own **home page** at MDPI. These separate home pages allow for changes to be expressed in the aims and scope or among the Guest Editors. In addition, the special issue home page can be seen as the front matter of a particular special issue. The banner of the special issue (Figures 1 and 2) can be shown on the home page as the graphical abstract of an Editorial located at the start of the list of papers.

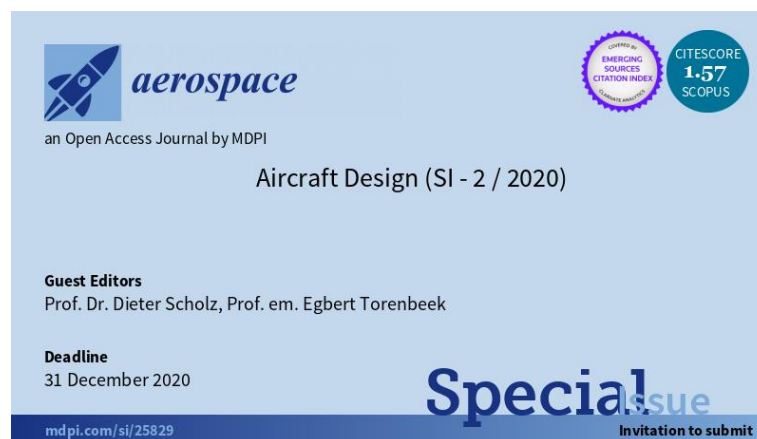


Figure 1. Banner of the Special Issue Aircraft Design (SI-2/2020).



Figure 2. Banner of the Special Issue Aircraft Design (SI-1/2017).

The URL of the currently open Special Issue Aircraft Design is always: https://www.mdpi.com/journal/aerospace/special_issues/aircraft_design. Linking to this URL also means linking to the central anchor point of the Continuous Special Issue Aircraft Design as a whole now and in the future. This page shows links to direct readers to all past special issues. Linking directly to a single past issue is also possible: a long user-friendly URL is available as well as a short URL based on MDPI's internal number of that special issue. Table 1 shows the systematic of these URLs.

Table 1. Systematic of URLs of the Continuous Special Issues Aircraft Design.

	Special Issue Aircraft Design (SI-1/2017)
Closed SIs:	
long URL	https://www.mdpi.com/journal/aerospace/special_issues/aircraft_design_1_2017
short URL	https://www.mdpi.com/si/6497 ²
Open SI:	Special Issue Aircraft Design (SI-2/2020)
long URL	https://www.mdpi.com/journal/aerospace/special_issues/aircraft_design ¹
short URL	https://www.mdpi.com/si/25829 ²

¹ The currently open Special Issue Aircraft Design has always this URL. ² The internal special issue number can be obtained from the editorial office.

Presently, the special issue is also advertised on a **CEAS web page**. The URL of the page is particularly easy to remember: <http://journal.AircraftDesign.org>. The page provides further details about the Continuous Special Issues Aircraft Design, e.g., related to possible reductions of the standard article processing charges (APC) [26] and links to all relevant web pages.

The **Digital Object Identifier (DOI)** is always used when linking to an individual paper. The DOI for a recent "Aerospace" paper at MDPI is structured as follows: <https://doi.org/10.3390/aerospaceVMMxxxx>. Here, 10.3390 stands for MDPI, V is the Volume (related to the year, starting with 1 in 2014), MM is the month, and xxxx is the number of the paper. Allocation starts with 0001 in the beginning of each year, counting up. The setup is shown in Figure 3.

When writing for the Special Issue Aircraft Design, authors should make sure to use **persistent links to archived resources**. Often we refer to journal articles that are usually long term archived by the publisher and have a persistent identifier (a DOI) to connect to the online resource. But in all other cases, it is the author's responsibility to archive the web pages, PDFs, or other data files. Please refer to Appendix A to see how references can be archived with available tools on the Internet.

A Continuous Special Issue as described above is not much different from what is otherwise known at MDPI as a "**Topical Collection**". A topical collection is a variant of a special issue. Topical collections run continuously (without any numbering) under the same home page. Topical Collections are just another form to structure journal content.

Aerospace

(ISSN 2226-4310)

<https://www.mdpi.com/journal/aerospace>

DOI structure:

<https://doi.org/10.3390/aerospaceVMMxxxx>

Continuous Special Issue Aircraft Design

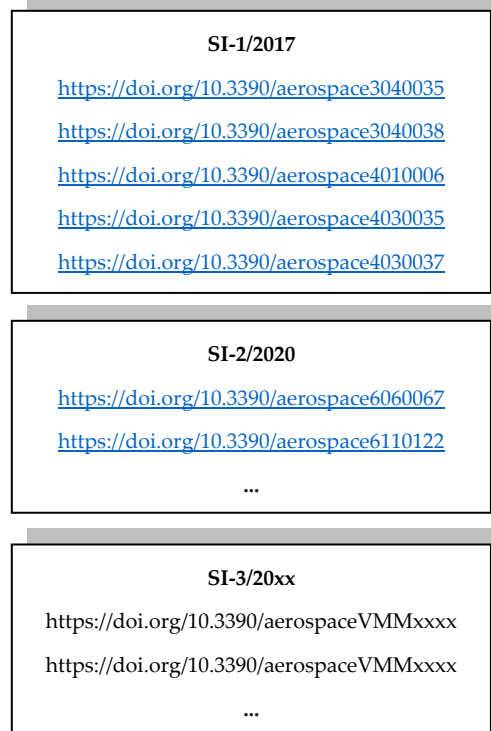


Figure 3. Identification of articles in the Continuous Special Issue Aircraft Design of the journal Aerospace by means of their DOI.

3. Aims and Scope

The Special Issue “Aircraft Design” is open to the full range of **article types**. In addition to original **research** articles, review papers, letters or communications, technical reports, and the extended version of conference papers are also accepted. Furthermore, an interest exists in aircraft design **education**. Certainly, the special issue is also the place to discuss topics like zero-emission airplanes, electric flight, urban air mobility—you name what is currently debated. Nevertheless, the **classic topics** in aircraft design remain:

- Innovative aircraft concepts (Figure 4);
- Methodologies and tools for aircraft design and optimization;
- Reference aircraft designs and case studies with datasets; and
- Aircraft design education.



Figure 4. Examples of innovative aircraft concepts [27].

The **keywords** are: aircraft, design, overall aircraft design (OAD), configuration, requirements, payload, range, certification, safety, constraints, objectives, synthesis, optimization, aerodynamics, drag, high-lift, structure, mass, performance, stability, control, aeroelasticity, engine, systems, operating costs, direct operating costs (DOC), passenger, cabin, ticket, price, environment, profit, asset, wing, fuselage, tail, undercarriage, landing gear, engine, systems.

Authors from all **economic sectors** (private, public, civic, and general public) can submit to this Special Issue. Education and training in aircraft design is considered as important as research in the field.

4. The Journal “Aerospace” at MDPI

“Aerospace” (ISSN 2226-4310) is a **well reputed journal** as can be seen from the authors publishing with “Aerospace”. Its latest journal metrics CiteScore (CS), SRJ and SNIP (from Scopus, Elsevier) is given on the journal’s home page. Articles have a high visibility; papers are visible Open Access at the journal “Aerospace” and also alongside the Special Issue Aircraft Design as soon as they are ready. The journal “Aerospace” is covered by many databases [28] including Web of Science (Clarivate Analytics) and Scopus (Elsevier). Papers from “Aerospace” are archived for centuries to come at CLOCKSS and in the Swiss National Library Digital Archive [28]. “Aerospace” adheres to best practice in Open Access publishing (accessibility, openness, discoverability, reuse author rights, and many other criteria). This is expressed at the Directory of Open Access Journals (DOAJ) with the “DOAJ Seal” given to “Aerospace” [29,30]. MDPI is a member of many relevant publishing organizations (OASPA, COPE, STM, . . .) [31]. Membership to most organizations is only granted after a thorough check of the publisher and its journals.

The journal “Aerospace” is known for **rapid publication** [32]. Manuscripts are peer-reviewed and a first decision is provided to authors approximately three weeks after submission; the length of the peer review itself can vary considerably, but reviewers are reminded by the editorial office to make the review a priority; acceptance to publication is undertaken in one week. Once accepted, the manuscripts undergo professional copy-editing, proofreading by the authors, final corrections, and publication on the journal website. This means that papers will be visible alongside with the “Special Issue Aircraft Design” and the journal “Aerospace” as soon as they are ready.

5. Aircraft Design

Aircraft design is the **first fascinating step** in the life of an aircraft, where visions are converted into reality.

In a **practical sense**, aircraft design supplies the geometrical description of the aircraft. Traditionally, the output is a three-view drawing and a list of aircraft parameters. Today, the output may also be an electronic 3D model. In the case of civil aircraft, a fuselage cross-section and a cabin layout are provided in addition.

In an **abstract sense**, aircraft design determines the design parameters to ensure that the requirements and constraints are met and design objectives are optimized. The fundamental requirements for civil aviation are payload and range. Many constraints come from certification rules demanding safety. The objectives are often of a financial nature, like the lowest operating costs. Aircraft design always strives for the best compromise among conflicting issues.

The **design synthesis** of an aircraft goes from conceptual design to detailed design. Frequently, expert knowledge is needed more than computing power. Typical work involves statistics, the application of inverse methods, and use of optimization algorithms. Proposed designs are analyzed with respect to aerodynamics (drag), structure (mass), performance, stability and control, and aeroelasticity, to name just a few. A modern aircraft is a complex, computer-controlled combination of its structure, engines, and systems. Passengers demand high comfort at low fares, society demands environmentally friendly aircraft, and investors demand a profitable asset.

Overall aircraft design (OAD) comprises all aircraft types in civil and military use, considers all major aircraft components (wing, fuselage, tail, undercarriage) as well as the integration of engines and systems. The aircraft is seen as part of the air transport system and beyond contributing to multimodal transport. Aircraft design applies the different aerospace sciences and considers the aircraft during its whole life cycle [33].

6. Summary

A journal titled “Aircraft Design” was published successfully from 1998 to 2001 by Elsevier, but had to be discontinued due to the low number of subscriptions. The demise was caused by a publishing model not adequate for the small aircraft design community. No other attempt to start an Aircraft Design journal has been made since then. The Open Access publishing model is a viable and better alternative for small communities. In a new endeavor toward creating something like an Aircraft Design journal, the subset of an Open Access journal within the wider topic “Aerospace” was used. The form of a Continuous Special Issue was chosen as the journal subset. The established journal “Aerospace” helps to overcome the problem of achieving “critical mass” for the new venture. Furthermore, MDPI provides a proven publishing infrastructure and support.

Funding: This article received no external funding.

Conflicts of Interest: The author declares no conflicts of interest.

Abbreviations

AIAA	American Institute of Aeronautics and Astronautics (www.aiaa.org)
CC	Creative Commons (www.creativecommons.org)
CEAS	Council of European Aerospace Societies (www.ceas.org)
CLOCKSS	Controlled LOCKSS (www.clockss.org)
COPE	Committee on Publication Ethics (www.publicationethics.org)
CS	CiteScore [34]
CWTS	Centre for Science and Technology Studies (www.cwts.nl)
DGLR	Deutsche Gesellschaft für Luft- und Raumfahrt Lilienthal-Oberth e.V. (www.dglr.de)
DOC	Direct Operating Costs
DOI	Digital Object Identifier (www.doi.org)
EWADE	European Workshop on Aircraft Design Education (www.ewade.aircraftdesign.org)
ISSN	International Standard Serial Number (www.issn.org)
LOCKSS	Lots of Copies Keep Stuff Safe (www.lockss.org)
MDPI	Multidisciplinary Digital Publishing Institute (www.mdpi.com)
OAD	Overall Aircraft Design
OASPA	Open Access Scholarly Publishers Association (www.oaspa.org)
READ	Research and Education in Aircraft Design (www.read.aircraftdesign.org)

SCAD	Symposium on Collaboration in Aircraft Design (www.scad.aircraftdesign.org)
SI	Special Issue
SNIP	Source Normalized Impact per Paper [34]
SRJ	SCImago Journal Rank [34]
STM	Here: The worldwide association of STM publishers (www.stm-assoc.org);
STM	Science, Technology and Medicine
TCAD	CEAS Technical Committee Aircraft Design (www.aircraftdesign.org)
URL	Uniform Resource Locator

Appendix A

The Appendix explains the use of **persistent links to archived resources** as applied in this Editorial. Authors writing for the Special Issue Aircraft Design are encouraged to follow this practice!

Journal articles (like those from MDPI) are usually archived and have a persistent identifier in the form of a DOI to connect to the online resource. But often, we make use of web pages, PDFs, or other data files taken from places on the Internet, where the resource is not archived and provided with a persistent identifier. We know from experience, “websites change, go away, and get taken down. When linked citations lead to broken, blank, altered, or even malicious pages, that’s called link rot.” [35]. Today, with tools at hand, **it is the author’s responsibility to create a permanent, reliable, unbreakable link to an unalterable, archived record of the web page or the web resource** cited in the work if this is otherwise not available. A comfortable way to do this is with Perma.cc (www.perma.cc). Perma.cc requires an account, which can be obtained free of charge e.g., from a participating university library. Alternatively, the Internet Archive with its Wayback Machine (www.web.archive.org) and the function “Save Page Now” can capture a web page or another online resource as it appears now for use as a trusted citation in the future. Links to the Internet Archive tend to be very long and would need to be shortened. This can be done e.g., with Bitly (www.bit.ly). The resulting short links fit well into the List of References.

Following best practice, the List of References should have two links for each entry to a self-archived web resource; the original link and the link to its archived version. **At MDPI typesetting rules only allow specifying one link.** It is helpful that Perma.cc as well as the Internet Archive show also the link to the original resource in their archived documents. Therefore, specifying only the permanent link is not the best solution, but sufficient. If required, the reader would need to go via the archived version to find the original link. Please consult the References below to see how it works.

References

1. Wikipedia: Aerospace. 2019. Available online: <https://en.wikipedia.org/wiki/Aerospace> (accessed on 28 December 2019).
2. Google Scholar: Top-Publications, Aviation & Aerospace Engineering. 2019. Available online: <https://perma.cc/ZX9X-5FUZ> (accessed on 28 December 2019).
3. CWTS Journal Indicators—Aerospace Engineering. 2018. Available online: <https://perma.cc/GT6Q-KHDQ> (accessed on 28 December 2019).
4. University of Illinois: Top Aerospace Engineering Journals. 2019. Available online: <https://perma.cc/R53E-7Z3X> (accessed on 28 December 2019).
5. Scholz, D. DGLR-Top 40—Aerospace Journal Ranking. 2015. Available online: <https://perma.cc/953C-PQJE> (accessed on 28 December 2019).
6. Wikipedia: Egbert Torenbeek. 2019. Available online: https://en.wikipedia.org/wiki/Egbert_Torenbeek (accessed on 28 December 2019).
7. Wikipedia: Jan Roskam. 2019. Available online: https://en.wikipedia.org/wiki/Jan_Roskam (accessed on 28 December 2019).
8. ScienceDirect: Aircraft Design—All Journal Issues. 2019. Available online: <https://perma.cc/BM3C-UVKR> (accessed on 28 December 2019).
9. DARcorporation: About Us—Dr. Jan Roskam. 2019. Available online: <https://perma.cc/4CA3-57N5> (accessed on 28 December 2019).
10. Scopus: Source Details—Aircraft Design, ISSN_1369-8869, All Documents. 2019. Available online: <https://perma.cc/N9FU-3WE6> (accessed on 28 December 2019).
11. Informationsplattform Open Access: What is Open Access? 2019. Available online: <https://perma.cc/292A-MY3F> (accessed on 28 December 2019).
12. Informationsplattform Open Access: Open Access Journals. 2019. Available online: <https://perma.cc/NGV7-AXKF> (accessed on 28 December 2019).

13. Torenbeek, E. Aircraft design education in Europe. *Aircr. Des.* **2000**, *3*, 205–206. Available online: <https://perma.cc/J2UK-RWVV> (accessed on 28 December 2019). [CrossRef]
14. Scholz, D. Open Access Publishing in Aerospace—Opportunities and Pitfalls. In Proceedings of the 4th CEAS Conference in Linköping, Linköping, Sweden, 19 September 2013; pp. 503–515. Available online: <http://doi.org/10.5281/zenodo.546649> (accessed on 28 December 2019).
15. Scholz, D. Publication Options Suitable for Aircraft Design—Open Access Journals Edited by Members of European Aerospace Organizations. In Proceedings of the 4th Symposium on Collaboration in Aircraft Design, Toulouse, France, 25–27 November 2014. Available online: <http://doi.org/10.5281/zenodo.3594626> (accessed on 28 December 2019).
16. Scholz, D. European Workshop on Aircraft Design Education (EWADE). 2019. Available online: <http://EWADE.AircraftDesign.org> (accessed on 28 December 2019).
17. Scholz, D. CEAS Technical Committee Aircraft Design (TCAD)—Research Activity (SCAD). 2019. Available online: <http://SCAD.AircraftDesign.org> (accessed on 28 December 2019).
18. Scholz, D. CEAS Technical Committee Aircraft Design (TCAD). 2019. Available online: <http://www.AircraftDesign.org> (accessed on 28 December 2019).
19. Council of European Aerospace Societies (CEAS): About CEAS. 2019. Available online: <https://ceas.org/about-ceas> (accessed on 28 December 2019).
20. Scholz, D. The History of READ/RRDPAE. 2019. Available online: <http://READ.AircraftDesign.org> (accessed on 28 December 2019).
21. American Institute of Aeronautics and Astronautics (AIAA): Technical Committees. 2019. Available online: <https://perma.cc/QN9L-QH4V> (accessed on 28 December 2019).
22. MDPI: About Aerospace. 2019. Available online: <https://www.mdpi.com/journal/aerospace/about> (accessed on 28 December 2019).
23. MDPI: Special Issue Aircraft Design (SI-1/2017). 2019. Available online: <https://www.mdpi.com/si/6497> (accessed on 28 December 2019).
24. MDPI: Special Issue Aircraft Design (SI-2/2020). 2019. Available online: https://www.mdpi.com/journal/aerospace/special_issues/Aircraft_Design (accessed on 28 December 2019).
25. Scholz, D. Prof. Dr.-Ing. Dieter Scholz, MSME. 2019. Available online: <http://english.ProfScholz.de> (accessed on 28 December 2019).
26. MDPI: Open Access and Article Processing Charge (APC). 2019. Available online: <https://www.mdpi.com/journal/aerospace/apc> (accessed on 28 December 2019).
27. Scholz, D. Evolutionary Aircraft Configurations—Possible A320 Successor. 2019. Available online: <http://airport2030.ProfScholz.de> (accessed on 28 December 2019).
28. MDPI: Aerospace—Indexing & Archiving. 2019. Available online: <https://www.mdpi.com/journal/aerospace/indexing> (accessed on 28 December 2019).
29. Directory of Open Access Journals (DOAJ): Aerospace. 2019. Available online: <https://perma.cc/F6VX-89JB> (accessed on 28 December 2019).
30. Directory of Open Access Journals (DOAJ): Journal Application Form—The qualifiers for the DOAJ Seal. 2019. Available online: <https://perma.cc/2RQV-Q3ZY> (accessed on 28 December 2019).
31. MDPI: About—Memberships. 2019. Available online: <https://www.mdpi.com/about#Memberships> (accessed on 28 December 2019).
32. MDPI: Aerospace—Open Access Journal. 2019. Available online: <https://www.mdpi.com/journal/aerospace> (accessed on 28 December 2019).
33. Scholz, D. *Aircraft Design*; Hamburg University of Applied Sciences: Hamburg, Germany, 2015. Available online: <http://HOOU.ProfScholz.de> (accessed on 28 December 2019).
34. Elsevier: Measuring a Journal’s Impact. 2019. Available online: <https://perma.cc/Q2YP-DL2X> (accessed on 28 December 2019).
35. Perma.cc: Websites change. Perma Links don’t. 2019. Available online: <https://perma.cc> (accessed on 28 December 2019).



Article

Amphibious Aircraft Developments: Computational Studies of Hydrofoil Design for Improvements in Water-Takeoffs [†]

Arjit Seth [‡]  and Rhea P. Liem ^{*‡} 

Department of Mechanical and Aerospace Engineering, Hong Kong University of Science and Technology, Hong Kong 999077, China; aseth@connect.ust.hk

* Correspondence: rpliem@ust.hk

[†] This paper is an extended version of our paper published in Proceedings of the AIAA Aviation 2019 Forum, Dallas, TX, USA, 17–21 June 2019; p. 3552.

[‡] These authors contributed equally to this work.

Abstract: Amphibious aircraft designers face challenges to improve takeoffs and landings on both water and land, with water-takeoffs being relatively more complex for analyses. Reducing the water-takeoff distance via the use of hydrofoils was a subject of interest in the 1970s, but the computational power to assess their designs was limited. A preliminary computational design framework is developed to assess the performance and effectiveness of hydrofoils for amphibious aircraft applications, focusing on the water-takeoff performance. The design framework includes configuration selections and sizing methods for hydrofoils to fit within constraints from a flying-boat amphibious aircraft conceptual design for general aviation. The position, span, and incidence angle of the hydrofoil are optimized for minimum water-takeoff distance with consideration for the longitudinal stability of the aircraft. The analyses and optimizations are performed using water-takeoff simulations, which incorporate lift and drag forces with cavitation effects on the hydrofoil. Surrogate models are derived based on 2D computational fluid dynamics simulation results to approximate the force coefficients within the design space. The design procedure is evaluated in a case study involving a 10-seater amphibious aircraft, with results indicating that the addition of the hydrofoil achieves the purpose of reducing water-takeoff distance by reducing the hull resistance.

Keywords: amphibious aircraft; hydrofoils; takeoff performance; computational fluid dynamics; optimization



Citation: Seth, A.; Liem, R.P. Amphibious Aircraft Developments: Computational Studies of Hydrofoil Design for Improvements in Water-Takeoffs. *Aerospace* **2021**, *8*, 10. <https://doi.org/10.3390/aerospace8010010>

Received: 4 November 2020

Accepted: 24 December 2020

Published: 30 December 2020

Publisher's Note: MDPI stays neutral with regard to jurisdictional claims in published maps and institutional affiliations.



Copyright: © 2020 by the authors. Licensee MDPI, Basel, Switzerland. This article is an open access article distributed under the terms and conditions of the Creative Commons Attribution (CC BY) license (<https://creativecommons.org/licenses/by/4.0/>).

1. Introduction

Amphibious aircraft have the potential to play an important role in passenger transport as part of general aviation, particularly in short-range flights [1]. Aircraft designed for takeoff and landings solely on runways are limited by the number of airports present in regions. The use of water bodies and ports as additional takeoff and landing points pose larger versatility and scope for missions with the use of amphibious aircraft. Mission profiles, weight estimation, fuel efficiency, range, payload, and stability are key considerations in the preliminary design and development of any aircraft. However, the takeoff and landing flight segments for amphibious aircraft present greater complications than ones in general aviation aircraft design because of the increased complexities involving water analyses. These aircraft suffer from several restrictions in analyses, due to the complexities of characteristic aerodynamic and hydrodynamic parameters, that make it difficult to non-dimensionalize and test models with respect to a length scale; these complexities are described in Section 2.1.

Amphibious aircraft are mostly used as utility vehicles for search and rescue operations, payload delivery in remote and undeveloped areas, and firefighting efforts, among others. Sikorsky Aircraft developed numerous amphibious aircraft from the mid-1920s till 1940 for varied customers (Popular Aviation, October 1931: <https://books.google.com/books?id=>

[qZhdXqWu4gC&pg=PA89](#)). The Piaggio P. 136 was an amphibious aircraft used by the Italian Air Force in the 1950s (<http://www.aeroflight.co.uk/waf/italy/af/ital-af2-all-time.htm>). More recently, the ShinMaywa US-2 has been in production, with a history of amphibious aircraft development since the 1950s (https://www.shinmaywa.co.jp/aircraft/english/us2/us2_history.html). The Dornier Seastar is an amphibious aircraft from the 1970s with a new generation currently under development (<https://www.flightglobal.com/business-aviation/dorniers-new-generation-seastar-makes-maiden-sortie/137601.article>). The AVIC AG-600 “Kunlong”, currently under development in China, is claimed to be the largest amphibious aircraft developed for aerial firefighting, maritime patrol, and search and rescue operations (http://www.xinhuanet.com/english/2018-05/13/c_137176292.htm). The research on amphibious aircraft development is lacking partly due to its focus on specific missions for utility purposes [2], as well as the increased complexities of hull and float analyses. The early developments of amphibious aircraft relied mainly on experimental water tank tests and empirical methods. As such, a thorough design exploration and optimization was not possible due to computational limitations [3,4]. A common strategy is to take conventional aircraft and convert them into amphibious configurations by the addition of a hull or float, which results in suboptimal designs. The aim for truly optimal amphibious aircraft design would require a systematic design procedure that considers preliminary sizing, stability and control, and shape optimization. A conceptual design and sizing framework for amphibious aircraft was developed by Cary [5]. While numerical optimization has been commonly used in aircraft design since the late 1970s [6,7], its application in amphibious aircraft is still limited. Qiu and Song recently performed a response-surface-based multiobjective optimization to find the optimum hull step configuration, achieving an 18% improvement in takeoff distance without sacrificing cruise performance substantially [8]. Puorger et al. performed an aerostructural optimization for a fire-extinguisher amphibious aircraft [9], focusing mainly on the ground effect during low-altitude cruise, without any water-takeoff considerations. A water-takeoff performance calculation method using low-cost empirical models has also been recently developed by Wang et al. [10]; this method was derived based on digital virtual flight, and included a pilot model to study the impact of a lack of visual references during water-takeoff. The model was validated against some experimental data with less than 10% error.

A particular technology for the potential improvement of amphibious aircraft water-takeoff performance is the hydrofoil. In this paper, a hydrofoil is defined as a lifting surface that travels through water. The implementation of the technology allows a ship’s hull to reach a planing stage more quickly, and effectively unport the hull from water. This reduces motor effort by reducing hull resistance, which allows it to travel at higher speeds. They have been researched and implemented in water-based craft since the late 1800s, with extensive research projects performed between the 1930s and the 1960s to improve performance of marine vehicles [11]. Experiments showing the effectiveness of hydrofoils dated as early as 1861 by Thomas Moy [12], in 1907 and 1914 by the Wright brothers [3], and in 1937–1940 by Sottorf [13], among many others. Most modern studies of hydrofoils relate to marine and naval technologies, including unmanned surface vehicles (USV) [14–16], aquatic unmanned aerial vehicle (AquaUAV) [17], turbomachinery [18], naval propellers [19], the propulsion of marine vehicles [20,21], or axial-flow pumps [22]. Hydrofoil boats, such as the “Raketa” developed in Russia in 1957, were manufactured and used for commercial transportation [23]. Studies of hydro-aerodynamic characteristics of hydrofoil systems in vessels were performed by Plisov and Rozhdestvenski [24]. A hydrofoil, as opposed to an airfoil, can suffer from cavitation and ventilation [25], further described in Section 2.2. Shen and Eppler researched various hydrofoil profiles using inverse design methods for U.S. hydrofoil craft [26]. Studies of two-phase boundary layer control in cavitating and supercavitating conditions were performed by La Roche and Trevisani in relation to the Supramar company [27]. Garg et al. performed multipoint hydrodynamic shape and hydrostructural optimizations of 3D hydrofoils in partially cavitating conditions to improve fuel efficiency of ships [28]. This analysis, however, did not consider multiphase flows

and enforced a cavitation constraint based on the pressure coefficient to obtain a shape that did not undergo cavitation, which might not be suitable for high-speed conditions. Vernengo et al. performed shape optimizations of 2D supercavitating hydrofoils with multiphase flows for the development of high-speed planing craft [29].

Amphibious aircraft with hulls can also benefit from hydrofoils similarly by reaching their takeoff speeds more quickly, reducing the distance and time in the water-takeoff stage. The research on hydrofoils for amphibious aircraft design is sparse; the number of designed hydrofoil profiles is far lesser compared to that of airfoils, and the number of investigations into hydrofoil shape optimization with the relevant constraints is much lesser, as well. The Thurston Aircraft Corporation published a report which extensively considered hydrofoils for seaplane design [3] based on experimental results, but not for amphibious aircraft with the relevant constraints. David Thurston also investigated general amphibious aircraft design with minor focus on the implementation of a hydrofoil in a working concept called the HRV-1 flown in 1974, but the rigor of analysis for the takeoff condition was limited to a basic sizing and did not consider multiple configurations [2]. Cary applied Thurston's procedure into the amphibious aircraft design framework with hydrofoil considerations, but the scope of foil profile selection, viability of design, and stability were not investigated [5]. The hydrodynamic lift for flying boats and seaplanes via the use of hydrofoils for a particular retractable configuration was invented by Zimmer and patented under Dornier Luftfahrt [30]. The LISA Akoya (LISA Airplanes: <http://lisa-airplanes.com/en/light-amphibious-aircraft-akoya/>), which is a two-seater aircraft designed for leisure flight, is an amphibious aircraft known to implement this technology in its design.

A rigorous computational framework that can systematically evaluate and assess the impact of hydrofoil performance in amphibious aircraft is still lacking. The numerical studies on amphibious aircraft performance mentioned above [8–10] did not consider hydrofoils and thus would not be directly applicable to amphibious aircraft with hydrofoils. Such a framework will enable tradeoff studies and optimization, which can help bring revolutionary technological improvement to amphibious aircraft design, e.g., by optimizing the shape of the hull and hydrofoils. The current investigation aims to formulate a computational design framework for preliminary hydrofoil design in the context of amphibious aircraft application. This will include procedures for hydrofoil sizing and placement, with longitudinal stability considerations. One goal of the implementation is to provide a "riding" surface for amphibious aircraft while in the planing stage to reduce hull drag by minimizing its water contact. In particular, we will investigate and compare the performance of amphibious aircraft hull with and without hydrofoils in different speed regimes during the water-takeoff procedure. The results will give us physical insights into the design problem.

The paper is structured as follows. Section 2 discusses the framework of fluid dynamics important in amphibious aircraft design, including hydrofoils. Section 3 outlines the research methodology, including the sizing procedure of the hydrofoil, the explanation of the water-takeoff model for amphibious aircraft, the considerations of the effects of the hydrofoil on the stability of the aircraft, and the design framework for the analysis and optimization of the hydrofoil. Section 4 discusses the application of the hydrofoil design framework to a 10-seater amphibious aircraft design with its results. The summary of key findings and conclusion of this work are then presented in Section 5.

2. Theory and Hydrofoil Design Challenges

2.1. Hydrodynamic Analyses

Three key non-dimensional parameters in water analysis are the Reynolds (Re), Froude (Fr), and Weber (We) numbers:

$$Re \equiv \frac{\rho u L}{\mu}, \quad Fr \equiv \frac{u}{\sqrt{gL}}, \quad We \equiv \frac{\rho u^2 L}{\kappa}, \quad (1)$$

where ρ is the density of the fluid, u is the freestream speed, L is the reference length of the body of analysis, μ is the dynamic viscosity, g is the gravitational acceleration, and κ is the surface tension between the two fluids under consideration. Fluid parameters corresponding to air will be denoted by a subscripted A , e.g., μ_A , and similarly W for water. The Weber number does not scale accordingly with Reynolds and Froude numbers because it goes as the square of the velocity, so the benefits of non-dimensional analysis are lost when attempting to size a water-based component of a transport vehicle based on a scale model with experimental results. The case worsens with the Froude number going as the reciprocal of the square root of the length against the Reynolds numbers' proportional relationship to length. The mitigating strategy is to use the same Froude number in the model tests and to adjust for different Reynolds numbers when scaling. Some errors exist in water spray, wave pattern and foaming predictions due to the difference in Weber numbers, but these are negligible in resistance prediction of scaled-up hulls [31].

A preliminary calculation under assumptions of constant viscosity and density shows that the Reynolds number in fresh water is approximately 16 times greater than the Reynolds number in air for the same speed and reference length. Lift and drag forces in fresh water are approximately 815 times ($\rho_W/\rho_A \approx 840$ at International Standard Atmosphere sea level conditions with salinity considerations) greater for foils of the same profile and dimensions traveling at a given speed with completely attached flow in both cases. Turbulence, cavitation, and ventilation effects correspondingly result in non-trivially determined differences between the two mediums.

Hydrodynamic forces important in hull design, such as resistance and buoyant force, are non-dimensionalized by division with $\rho_W g B^3$, where B is the hull width, as opposed to the product of the dynamic pressure and wing area in aerodynamics; this is usually because the hull lengths are fixed and the widths are varied for design analyses. Archimedes' principle also justifies the inclusion of gravitational acceleration as a term to account for buoyancy forces.

The following hydrodynamic coefficients, called the load, resistance, and velocity coefficients (C_Δ , C_R , and C_V , respectively), play an important role in the water-takeoff analysis of an amphibious aircraft with a hull as non-dimensional measures of buoyancy Δ , resistance R , and speed u :

$$C_\Delta \equiv \frac{\Delta}{\rho_W g B^3}, \quad C_R \equiv \frac{R}{\rho_W g B^3}, \quad C_V \equiv \frac{u}{\sqrt{gB}}. \quad (2)$$

The trim angle α_{trim} of a hull is defined as the angle at which a boat must be longitudinally inclined for a given speed with respect to its orientation at rest such that it maintains optimal performance via minimization of resistance generated. The resistance and trim angle of a hull are experimentally determined with variations against speed via tank tests of models, which are then scaled using methods, such as one from the International Towing Tank Conference in 1978 (ITTC-78) [31].

The non-dimensional lift C_L , drag C_D , and moment C_M coefficients that characterize airfoil performance are also used for hydrofoils with the freestream density and dynamic viscosity of water as reference. However, phase changes can occur over lifting bodies traveling in water at speeds within the takeoff speed regime of aircraft, leading to additional complications not seen in airfoils. Here, we use the generic non-dimensionalization for the lift L , drag D , and moment M :

$$C_L \equiv \frac{L}{\frac{1}{2}\rho u^2 S}, \quad C_D \equiv \frac{D}{\frac{1}{2}\rho u^2 S}, \quad C_M \equiv \frac{M}{\frac{1}{2}\rho u^2 S c} \quad (3)$$

where ρ , u , S , c refer to density, velocity, area, and chord of the lifting component, respectively. The subscripts hf , h , and w will denote the parameters corresponding to hydrofoil, horizontal tail, and wing, respectively.

2.2. Cavitation and Ventilation

Cavitation and ventilation can notably reduce hydrodynamic efficiency of hydrofoils. Cavitation occurs when the local pressure approaches the saturated vapor pressure [28], which can cause flow-induced noise and vibration, decreased lift and thrust, and increased drag [32]. Ventilation refers to the phenomenon where air bubbles are found in the submerged part of the body [15], and this can result in a loss of lift [3,16]. The measure of ventilation effects is considered to be the depth of submergence of the lifting surface from the free surface. In the case of a ventilation analysis for a hydrofoil, the depth of submergence in water from sea level is the appropriate measure. Early work to optimize the hydrodynamics of hydrofoils did not consider cavitation [33], though most subsequent works considered it [18,20,34–36]. These works mainly used potential flow as their bases. In recent decades, some studies have used high-fidelity models, in particular the Unsteady Reynolds-averaged Navier–Stokes (URANS) approach with a physical model of cavitation [19,37]. While the cavitation effects of hydrofoils have been well-investigated, studies of ventilation are still scarce [14,38]. As ventilation is a highly complex phenomenon for which systematic data are very difficult to obtain either experimentally or numerically, it is not explicitly considered in the preliminary design phase discussed in this paper.

Cavitation is an unsteady phenomenon that takes place in water when the local pressure on a surface is below the saturated vapor pressure of water, with bubble and vapor formation taking place along the lifting surface. This is known to cause “cavitation damage” in the form of corrosion of rotor blades of boat motors. In the case of aircraft, a disadvantageous effect is the increase in drag of the aircraft during takeoff and possibly some form of cavitation damage along the hull for certain configurations. Cavitation performance is usually compared via the non-dimensional cavitation number, defined as:

$$Ca \equiv \frac{p_\infty - p_V}{\frac{1}{2}\rho_W u_\infty^2}, \quad p_\infty = p_{\text{atm}} + \rho_W g h, \quad (4)$$

where p_∞ is the freestream pressure, u_∞ is the freestream speed, p_{atm} is the atmospheric pressure, p_V is the vapor pressure, and h is the reference height corresponding to the hydrostatic pressure head.

The condition for cavitation inception over hydrofoils is given as $-C_{p_{\min}} \geq Ca$, where $C_{p_{\min}}$ is the minimum pressure coefficient over the hydrofoil. As a result, cavitation inception usually occurs on the upper surface of foils as the local pressure is lower than the freestream pressure for foils under lifting conditions. Numerical studies in hydrodynamic analysis and optimization for foil shapes usually consider variations of lift and drag forces against cavitation numbers.

Another issue involving cavitation inception is that the Reynolds, Mach, and cavitation numbers now play roles in the similarity analysis of flows over hydrofoils due to the flow’s additional dependence on the vapor pressure of the fluid in liquid state. If a particular Reynolds number is set for analysis, its cavitation and Mach numbers are determined for a fixed reference length. As the cavitation number is independent of a length scale, adjusting the reference length to obtain a freestream speed for a fixed Reynolds number adjusts the cavitation number accordingly. This changes the characteristics of cavitation formation over the hydrofoil, as the pressure coefficient conditions for cavitation inception change, viz. the location of incipient cavitation over the hydrofoil surface will change.

The major issue with existing studies of hydrofoils is that they have originally been designed for cruising speeds of ships, which correspond to certain cavitation numbers as their design points. In the water-takeoff regime for an amphibious aircraft, such a fixed design point does not apply as the flow is accelerating.

3. Research Methodology

The work presented in this paper focuses on the hydrofoil design and analysis. The general preliminary design, weight estimation, and sizing procedures for the aircraft are therefore outside the scope of this work. For the discussion presented below, we

assume that the aforementioned procedures have been completed and the maximum takeoff weight, the required wing area, aircraft stall speed, and the powerplant selection have been determined. A hull selection and design are also already determined based on hull resistance and trim angle variations with speed. The Douglas Sea Scale [39] is used to measure the height and swell of a sea on a 0–10 degree scale. In this paper, a level 0 (no wave) condition in calm water is assumed in all considerations for the initial design. The high-fidelity computational analyses are performed in 2D with a fixed reference length based on the sizing procedure. The 2D analyses are deemed suitable for the preliminary design stage [29]. Performing high-fidelity 3D analyses that involve multiphase flows could be computationally prohibitive and would be more appropriate at detailed design stages.

The drag force caused by the empennage is considered as negligible in all equations of motion compared to the forces generated by the wing and hydrofoil. All aerodynamic forces are assumed to be concentrated as point loads from the aerodynamic center of the respective lifting surface, assumed to be located at 25% of the chord length from the leading edge. No control surfaces for the hydrofoils will be considered in the current investigation as the design framework considers the stability without the need of these devices.

Based on these assumptions for the design scope, the hydrofoil conceptual design and preliminary sizing, water-takeoff analysis, and stability analysis are discussed in this section.

3.1. Hydrofoil Conceptual Design Framework and Preliminary Sizing

The following design procedure considers hull-based amphibious aircraft instead of float-based, as the primary goal is to minimize large hull contact with water. This section provides guidelines to determine the suitable hydrofoil configuration, geometry, and location for preliminary design purposes.

3.1.1. Configuration and Profile Selection

There are many possible hydrofoil configurations for amphibious aircraft including, but not limited to, surface-piercing hydrofoils, foldable-protruding hydrofoils, and strut-based hydrofoils [3,24]. As the name suggests, a surface-piercing hydrofoil has a hydrofoil protruding directly from the hull of the aircraft that pierces the water surface, such as the ones in LISA Akoya. When such a hydrofoil is foldable, it is considered as a foldable-protruding hydrofoil. The last category refers to a hydrofoil with a strut-based structure extending from the body of the aircraft. The surface-piercing and strut-based hydrofoil configurations are depicted in Figure 1. For the water-takeoff consideration in our design and analysis discussion, the hydrofoils are assumed to be fully deployed. The major dimensional constraints that will be discussed are relevant to this state, as well.

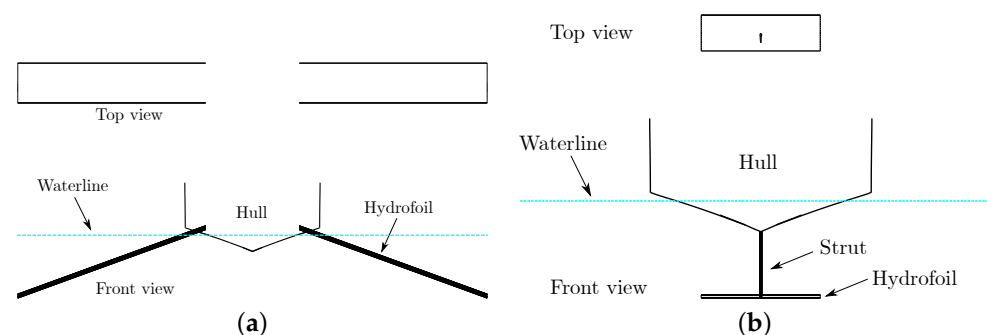


Figure 1. Hydrofoil configurations. (a) Surface-piercing Hydrofoil; (b) Strut-based Hydrofoil.

The number of hydrofoils on the aircraft is an important consideration in the weight and stability estimation of the initial design. The LISA Akoya implements two hydrofoils, one set near its wing and one set below the empennage; this configuration seems to eliminate the complex hull design considerations, such as stepped and planing configura-

tions, and enables the design of more aerodynamic fuselages as the hydrofoils provide lift throughout the water-takeoff run and reduce the wetted hull area.

To select an appropriate hydrofoil profile, we identify several criteria to ensure efficient performance. These criteria include: low hydrofoil drag coefficient within the entire takeoff speed range, and high lift-to-drag ratios within the speed range in which hull resistance is dominant. To ensure stability, the rate of change of the hydrofoil moment coefficient with respect to angle of attack should be negative within the range of hull trim angle. A higher hydrofoil lift coefficient is desirable as it will reduce the required hydrofoil area, to be further discussed in Section 3.1.2.

There are three main classifications for cavitation of hydrofoils, namely (1) subcavitating, where flow is fully attached over the hydrofoil; (2) partially cavitating, where flow separation of water takes place at some transition point with vapor cavities partially forming over the upper surface of the hydrofoil; and (3) supercavitating, where the hydrofoil undergoes separated flow from water with the formation of a large vapor cavity over the entire upper surface [3]. Past literature has shown hydrofoils have been designed to be efficient in either subcavitating or supercavitating regimes. Note that the assumption of the “aerodynamic center” of the hydrofoil located at approximately 25% of the chord length does not apply for these foils under cavitating conditions. The available databases of hydrofoils (e.g., University of Illinois at Urbana-Champaign (UIUC) Airfoil Database: https://m-selig.ae.illinois.edu/ads/coord_database.html) pale in comparison to their aerodynamic counterparts and a designer must resort to sifting through historical literature to find shapes. Moreover, the cavitation phenomenon will change the flow performance characteristics in hydrofoils compared to those of airfoils, as will be seen in the lift and drag coefficient profiles presented in Section 4.

The estimated range for the minimum pressure coefficient to ensure a subcavitating regime for an amphibious aircraft can be determined by its design water-takeoff speed. Consider, for instance, the LISA Akoya, a small two-seater aircraft, which has a stall speed of $u_s = 23$ m/s and an estimated average hydrofoil height of 1 m from the free surface (<http://lisa-airplanes.com/en/light-amphibious-aircraft-akoya/equipment-performance/>). Estimating its takeoff speed at sea level by $u_{TO} = 1.2$, $u_s = 27.6$ m/s, its cavitation number constraint is the following:

$$-C_{p_{\min}} < \frac{101,325 + 998.2 \times 9.81 \times 1 - 3640}{\frac{1}{2} \times 998.2 \times 27.6^2} \approx 0.2827. \quad (5)$$

This means that the lowest pressure coefficient over the hydrofoil must be $C_{p_{\min}} \geq -0.2827$ to prevent incipient cavitation; it is unlikely for subcavitating foils to satisfy this pressure coefficient constraint with beneficial (L/D) ratios. Thus, at the required speeds for water-takeoff, which are bound to be higher for larger aircraft, cavitation is almost an inevitable phenomenon as the cavitation number reduces with increase in dynamic pressure underwater, indicating that supercavitating hydrofoils are the only viable solution. Thurston and Vagianos showed that hydrofoils designed for supercavitating regimes far outperformed their subcavitating counterparts in terms of (L/D) ratios as a result of negligible effects of ventilation in supercavitating conditions, and should be primary considerations for amphibious aircraft [3]. A study on the performance of hydrofoils designed for subcavitating and partially cavitating regimes for use in amphibians supports this conclusion [1]. It is thus imperative to use supercavitating hydrofoils in amphibious aircraft applications.

Experimental data exist for some supercavitating profiles [40], which can be used as a reference when sizing the hydrofoil. The attainable maximum lift coefficient for supercavitating hydrofoils appears to be $C_{L_{hf_{\max}}} \approx 0.27$ including ventilation effects in the supercavitating regime according to Thurston’s review in the 1970s [2]. However, some supercavitating profiles, such as the SCSB profiles developed by Brizzolara [14], have shown improved performance in subcavitating and partially cavitating conditions in terms of (L/D)_{hf} ratios compared to previous designs.

3.1.2. Preliminary Sizing

The design considerations and criteria to determine hydrofoil geometry parameters including area, sweep angle, taper, dihedral, and aspect ratio are summarized and presented here. The selection is mainly based on the physical properties and hydrofoil performance. The span and incidence angle selection process, which relies on a water-takeoff minimization procedure, will be described separately in Section 3.1.3.

3.1.2.1. Hydrofoil Area

The hydrofoil needs to generate lift to unport the hull from the water while it is submerged. The stall speed of the hydrofoil (u_{hfs}) is defined as the lift required by the hydrofoil to counter the weight of the aircraft minus the lift of the wing at the same speed. The required area for this condition can be derived from the results of the preliminary wing and horizontal tail sizing procedures by equating this stall speed to the speed at which the horizontal tail's elevator (u_{he}) is able to provide effective corrections as an initial design point.

$$u_{hfs} = u_{he}. \quad (6)$$

The required area $S_{hf_{req}}$ is then determined by equating the lift generated by the hydrofoil at its stall speed to the difference between the weight of the aircraft W and the lift generated by the wing in the same condition:

$$\frac{1}{2}\rho W u_{hfs}^2 S_{hf_{req}} C_{L_{hf_{max}}} = W - \frac{1}{2}\rho A u_{he}^2 S_w C_{L_w} \quad (7)$$

$$\implies S_{hf_{req}} = \frac{2W - \rho A u_{he}^2 S_w C_{L_w}}{\rho W u_{hfs}^2 C_{L_{hf_{max}}}}, \quad (8)$$

where W is the aircraft weight. A high $C_{L_{hf_{max}}}$ will therefore reduce the effective hydrofoil area, which reduces the drag generated by the hydrofoil. Note that this is the required area for a hydrofoil with no dihedral to generate sufficient lift for the aircraft weight, which can be slightly generalized as will be discussed in the dihedral sizing description below.

The determination of C_{L_w} depends on the Reynolds number, set by u_{he} , and α_w , determined by the wing incidence angle α_{wi} and hull trim angle at the corresponding point during the water-takeoff. As a first estimation in the design stage, C_{L_w} can be determined via quick, low-fidelity analysis tools, such as XFOIL [41]. The value of $C_{L_{hf_{max}}}$ depends on the hydrofoil profile selection, as mentioned in Section 3.1.1. This method implicitly accounts for the losses of lift due to ventilation effects as a heuristic, assuming that the hydrofoil will not yield the ideal maximum lift coefficient at this design point due to ventilation.

3.1.2.2. Sweep Angle and Taper

King and Land [42] observed that the implementation of sweep in subcavitating conditions delayed the onset of cavitation inception to higher speeds for angles between 0–45° at the cost of decreased (L/D) ratios, so its implementation might be beneficial for aircraft designed for water-takeoffs in only subcavitating conditions for hydrofoils. It is, however, not efficient for supercavitating hydrofoils as they are designed for optimal performance in supercavitating conditions. They also observed that the implementation of taper has little effect on the characteristics of the flow and the performance.

3.1.2.3. Dihedral Angle

For surface-piercing hydrofoils, anhedral would be required to maintain lifting performance while the hull is unported from the water. The effective area of the hydrofoil with

a dihedral angle δ_{hf} is then given by $S_{hf} = S_{hf_{req}} / \cos^2 \delta_{hf}$, which is then substituted into Equation (8) to give:

$$S_{hf} = \frac{2W - \rho_A u_{he}^2 S_w C_{Lw}}{\rho_W u_{hf_s}^2 C_{L_{hf_{max}}} \cos^2 \delta_{hf}}. \tag{9}$$

For a hull-protruding hydrofoil with a generic foil profile to be a beneficial lifting surface while reducing hull contact area, δ_{hf} should be between -45° and 0° to enable unporting the hull while still being submerged, as the hydrofoil should protrude below the base of the hull and not above.

3.1.2.4. Aspect Ratio

The aspect ratio (AR) must be set, for a hull-protruding hydrofoil with positive δ_{hf} , such that the height of the deployed hydrofoil is not greater than the distance of the landing gear’s wheels from the aircraft’s center of gravity (CG, z_{lg}).

$$AR_{hf} \leq \frac{az_{lg}^2}{S_{hf_{req}} \tan^2 \delta_{hf}}, \quad 0 < a < 1, \tag{10}$$

where a is a factor of safety that can be set by the designer to account for ground strikes during takeoffs on land in case of mechanical failures.

The aspect ratio selected should ideally be high (i.e., greater than 5) according to Thurston [3]. For aircraft with strut-based hydrofoils, this may result in the effective span of the hydrofoil being larger than the fuselage width. In these cases, retractable/folding mechanisms should be considered in the design of the strut to fold the hydrofoil and retract it into the fuselage/hull. The determination of the aspect ratio is further investigated by optimization of the span length of the hydrofoil, discussed in Section 3.1.3.

3.1.3. Span and Incidence Angle Optimization

In this work, the hydrofoil’s span and incidence angle are determined via the minimization of the water-takeoff distance, in which they are treated as design variables. The water-takeoff distance calculation, as the objective function, will be elaborated in Section 3.2. A lift constraint is considered, to model that the total lift provided by the lifting surfaces (wing, hydrofoil and horizontal tail) does not exceed the aircraft weight during the water-takeoff procedure, to satisfy the inequality constraint in residual form $\mathcal{R}(L_{hf}) = L_{hf} + L_w + L_h - W \leq 0$. The variable bounds for the speed and angle of attack, which are used in the water-takeoff calculation, also need to be specified. The design limit of aspect ratio, which is related to the span as $b_{hf} = \sqrt{AR_{hf} \times S_{hf}}$, is also imposed following the discussion in Section 3.1.2. The optimization procedure is summarized in Table 1.

Table 1. Optimization problem formulation for the optimal hydrofoil span and incidence angle.

Optimization	Function Variables	Description
Minimize	x_W	Water-takeoff distance.
Design variables	b_{hf} α_{hf_i}	Span length of the hydrofoil. Incidence angle of the hydrofoil.
Constraints	$L_{hf} + L_w + L_h \leq W$	The total lift provided by the lifting surfaces must not exceed the aircraft weight.
Bounds	$0 < u \leq u_{TO}$ $\alpha_{min} \leq \alpha_{hf} \leq \alpha_{max}$ $AR_{hf_{min}} \leq AR_{hf} \leq AR_{hf_{max}}$	Speed range within takeoff regime. Angle of attack within operational bounds. Aspect ratio within design bounds.

The corresponding extended design structure matrix (XDSM) (<https://github.com/mdolab/pyXDSM>) representation [43] is shown in Figure 2. In this representation, mathematical functions with well-defined inputs and outputs are colored in green, implicit components that solve residual equations are colored in red, optimizations and design of experiments are colored in blue, solvers pertaining to physics are colored in orange, and metamodels are colored in yellow. Data links between components are presented as thick, gray lines with slanted boxes denoting the communicated variables; inputs into components are fed “right-down” and outputs from components are returned “left-up”, depending on the order of execution. Inputs and outputs that are not connected to any other systems, such as initial guesses (denoted with $-_0$ subscripts) and optimization results (denoted with $-^*$ superscripts) of some optimizations, are shown as parameters inside white boxes. Processes are indicated with black lines representing arrows.

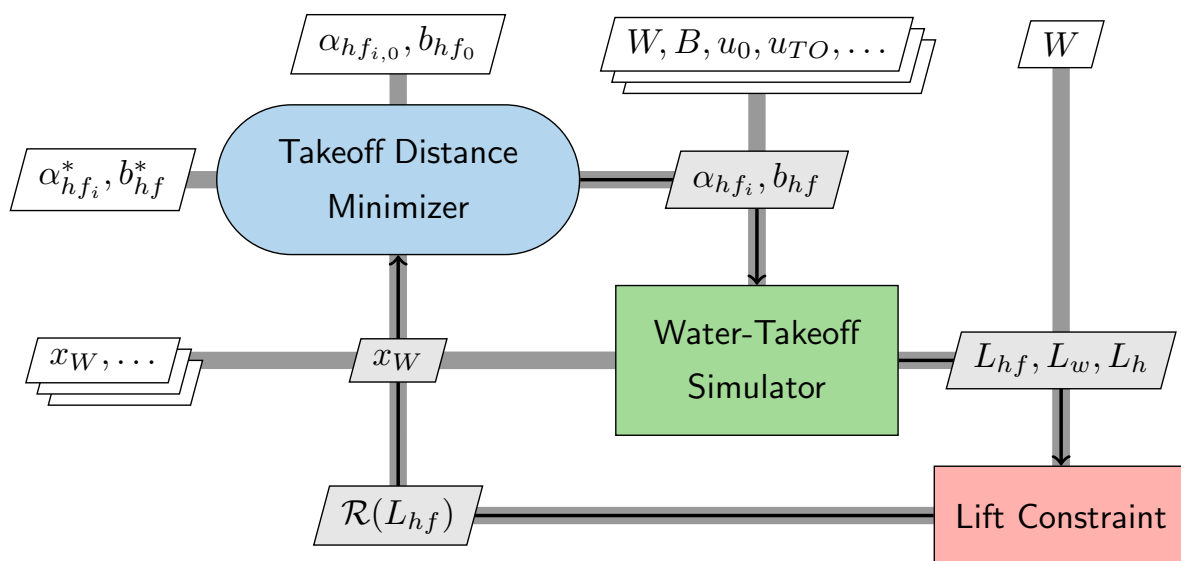


Figure 2. XDSM diagram for the hydrofoil span and incidence angle optimization.

In this study, we only consider hydrofoils with rectangular planforms, as sweep and taper have no appreciable effects on the hydrofoil performance from the discussion in Section 3.1.2.2. To start the optimization procedure, an initial span length is selected based on the initial guess of the aspect ratio. This span length is then used to determine the chord length \bar{c}_{hf} of the hydrofoil that is used in computational fluid dynamics (CFD) analyses, elaborated in Section 3.4.2.

The hydrofoil must be able to operate at the optimum angle for efficient performance in the takeoff regime. The angle of attack of the aircraft is subject to changes during water-takeoff due to hull designs and wave formations, which results in changes of the angle of attack of the hydrofoil. Hence, the incidence angle should be determined by accounting for the hull trim angle while considering the required angle of attack for the chosen hydrofoil profile:

$$\alpha_{hf_i} = \alpha_{\text{trim}} - \alpha_{hf}. \quad (11)$$

The angle of attack varies with time as a result of the hull’s dynamic trim angle. The consideration of an actuated system for adjusting the angle of attack, while possible, is too complex for an initial design consideration and is deemed beyond the scope of the present study. Note that such an implementation would add structural weight, which needs to be considered in the design process. The lift constraint is considered for the reason that if the aircraft and the hydrofoil are unported from water, the loss of lift from the hydrofoil

is extremely large due to the change in density of the fluid from water to air. This would result in the weight exceeding the total lift in this condition, and the aircraft would crash onto the water, resulting in unstable effects on the resistance and trim.

3.1.4. Location Optimization

The hydrofoil location in the amphibious aircraft is determined primarily based on the stability and trim requirements. The hydrofoil must generate minimal moments about the aircraft center of gravity (CG) until the speed at which the elevator is effective enough to provide corrections is reached, while simultaneously providing optimal lift to minimize hull resistance. This objective is attained by considering minimization of the maximum stabilizer force required during a simulated water-takeoff run. The reasoning for the consideration of this objective function will be presented in Section 3.3, and the water-takeoff simulation model will be described in Section 3.2. The optimization problem formulation to determine the hydrofoil location is summarized in Table 2. The hydrofoil location is indicated by the coordinates of its reference point, (x_{hf}, z_{hf}) with respect to the CG as origin. The optimum span and incidence angle from the takeoff distance optimization problem in Section 3.1.3 are provided to the stabilizer force minimization problem, which determines the optimal hydrofoil position. The XDSM diagram is presented in Figure 3.

Table 2. Optimization problem formulation to determine the hydrofoil’s location.

Optimization	Function Variables	Description
Minimize	$\max L_h $	Maximum horizontal stabilizer force required during takeoff.
Design variables	(x_{hf}, z_{hf})	Coordinates of hydrofoil’s reference point.
Bounds	$x_{nose} \leq x_{hf} \leq 0$ $z_{lg} \leq z_{hf} \leq z_{base}$	Horizontal position between aircraft nose and CG. Vertical position between landing gear and aircraft base.

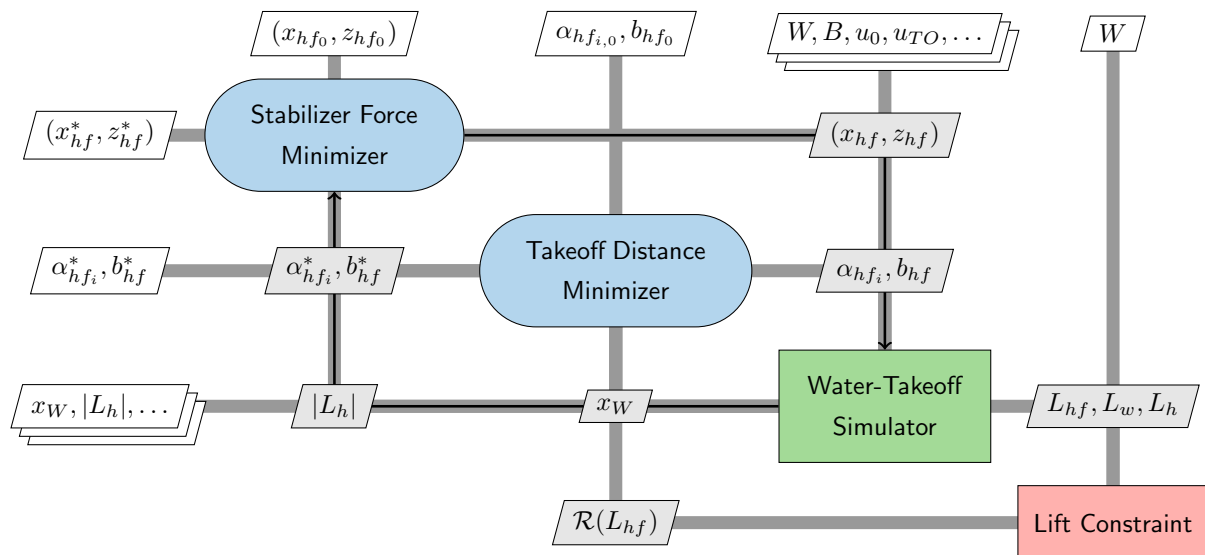


Figure 3. XDSM diagram for the hydrofoil location optimization.

3.2. Water-Takeoff Analysis

In this analysis, the water-takeoff distance is defined as the horizontal distance traveled by the aircraft during acceleration in water, to reach a pre-determined speed at which the

aircraft generates sufficient lift to achieve takeoff at a particular angle of attack. The water-takeoff analysis is performed based on Newton's second law, as follows:

$$m\dot{u} = \underbrace{T \cos \phi_t}_{\text{Thrust}}, \quad (12a)$$

$$- \underbrace{\rho_W g B^3 \frac{C_\Delta}{C_{\Delta_0}} C_R}_{\text{Wave resistance}}, \quad \text{where} \quad \frac{C_\Delta}{C_{\Delta_0}} = 1 - \frac{\rho_W g B C_V^2 C_{L_w}}{2(W/S_w)} - \frac{C_{L_{\text{hull}}}}{C_{\Delta_0}}, \quad (12b)$$

$$- \underbrace{\frac{1}{2} \rho_W S_{\text{wet}} u^2 \frac{C_\Delta}{C_{\Delta_0}} C_F}_{\text{Viscous resistance}}, \quad (12c)$$

$$- \underbrace{\frac{u^2}{2} \left[\rho_A (C_{D_w} \cos \alpha_w + C_{L_w} \sin \alpha_w) + \rho_W (C_{D_{hf}} \cos \alpha_{hf} + C_{L_{hf}} \sin \alpha_{hf}) \right]}_{\text{Contributions from wing and hydrofoil lift and drag}}, \quad (12d)$$

where m and \dot{u} denote mass and acceleration, respectively. Equation (12d) consists of the contributions towards lift and drag from the wing and hydrofoil at their respective angles of attack, and Equation (12a) is the thrust force T at some thrust inclination angle ϕ_t . The remaining force terms on the right-hand side, such as the hull resistance and viscous resistance, are described in detail below.

Equation (12b) represents the wave resistance (unrelated to wave drag) of the hull with respect to variations in its trim angle based on towing tank tests. This term is scaled by the submerged volume ratio C_Δ/C_{Δ_0} at a given instant during takeoff with respect to the submerged volume at rest. At each point of the water-takeoff calculation, the 'effective weight' of the aircraft (its weight minus the total lift) is considered to be balanced by the buoyant forces, hence $\Delta = W - \sum_i L_i$, $i \in \{hf, h, w\}$, which is non-dimensionalized to give C_Δ . During the planing stage, the hull contact with water is minimal, i.e., $C_\Delta/C_{\Delta_0} \approx 0$, where C_{Δ_0} is the maximum load coefficient in the absence of lift, but it may generate viscous skin-friction resistance proportional to a small wetted area S_{wet} in contact with the water, hence an additional viscous resistance term is added for the planing stage given by Equation (12c). Determining this wetted area is complex without knowledge of the exact waterline height and the spray pattern, so an initial value is set based on a geometric estimation and then scaled by the submerged volume ratio C_Δ/C_{Δ_0} . The skin-frictional resistance coefficient C_F is obtained via the ITTC-57 formula, based on data from empirical towing tank tests [31]:

$$C_F = \frac{0.075}{(\log_{10} Re - 2)^2}. \quad (13)$$

During a water-takeoff run for an amphibious aircraft without a hydrofoil, this viscous resistance term dominates the drag in water during the planing stage. In the model considered, when the hull is unported from the water with the help of the hydrofoil, viz. the buoyant force is zero, this term is also zero.

The kinematic equations are modeled via a time-stepping approach, in which the speed u , time t , and displacement x variables are discretized, with subscripts $0 \leq i \leq N_t$ for N_t timesteps. The dot notation is used to denote time derivatives. This approach is similar to the water-takeoff model for amphibious aircraft used in the work of Qiu and Song [8]; they did not, however, consider the implementation of a hydrofoil in their study. The following equations are solved for the speed and displacement by integration of the equations of motion for some initial condition $(t_0, x_0, u_0, \dot{u}_0)$. The output consists of

variables including the water-takeoff distance x_W , the time taken t_W , and the other relevant parameters for analysis and optimization.

$$u_i = u_{i-1} + \dot{u}_i(t_i - t_{i-1}), \quad (14a)$$

$$x_i = x_{i-1} + \frac{1}{2}(u_i + u_{i-1})(t_i - t_{i-1}). \quad (14b)$$

In the water-takeoff regime, the wetted area of the hydrofoil underwater with dihedral angle δ_{hf} (negative, hence anhedral) reduces as the waterline height of the aircraft decreases due to the lift generated by the hydrofoil. The lift generated by the submerged area of the hydrofoil with cavitation effects as an initial approximation can be modeled as:

$$L_{hf} = \frac{1}{2}\rho_W u^2 C_{L_{hf}} S_{hf_{wet}}(h), \quad (15)$$

where the submerged area $S_{hf_{wet}}(h)$, now a function of the height h , is assumed to be fully wetted underwater, and the lift coefficient of the hydrofoil takes the losses due to cavitation effects into account. For an initial approximation assuming the waterline interface as a flat surface, this underwater wetted area can be determined geometrically as:

$$S_{hf_{wet}}(h) \approx \frac{S_{hf_{req}}}{b_{hf}^2} \left(b_{hf} + \frac{h}{\sin \delta_{hf}} \right)^2, \quad -90^\circ \leq \delta_{hf} < 0^\circ. \quad (16)$$

To obtain the lift and drag forces over the hydrofoil, either experiments or simulations including at least cavitation modeling need to be performed to obtain a reasonable estimate at this stage of the design process. It is computationally very expensive to determine the hydrodynamic forces via high-fidelity CFD at every time-discretized point in a takeoff analysis as observed by Seth and Liem [44], so a surrogate model, or an approximation model, is generated for use in the water-takeoff analysis for the optimization problems to reduce the computational burden. The surrogate models will compute the non-dimensional coefficients of the hydrofoil as functions of speed and angle of attack.

In this work, sample-based surrogate models are selected for their simplicity and non-intrusive nature. To construct the surrogate models, we first need to generate samples by running the high-fidelity analyses. A design of experiments is performed to generate the design space by selecting N in the speed range $u_0 \leq u \leq u_{TO}$, with initial speed u_0 , to generate a set $\{u\}$ and N_α samples in the angle of attack range $\alpha_{\min} \leq \alpha \leq \alpha_{\max}$ to generate a set $\{\alpha\}$. The Cartesian product of these sets defines the design space to generate CFD training and testing data for the surrogate, as will be discussed in Section 4.2.2. Similar arguments can be applied to airfoils, so surrogate models are also considered for them in the framework, although they may not be necessary with the use of low-fidelity solvers, which is to be further discussed in Section 3.4.2. The water-takeoff analysis with surrogate models is presented as an XDSM in Figure 4.

Note that this takeoff procedure alone does not guarantee the aircraft will satisfy the required stability and trim characteristics, which are considered in the following section to further elaborate the considerations for the optimization problem presented in Table 2.

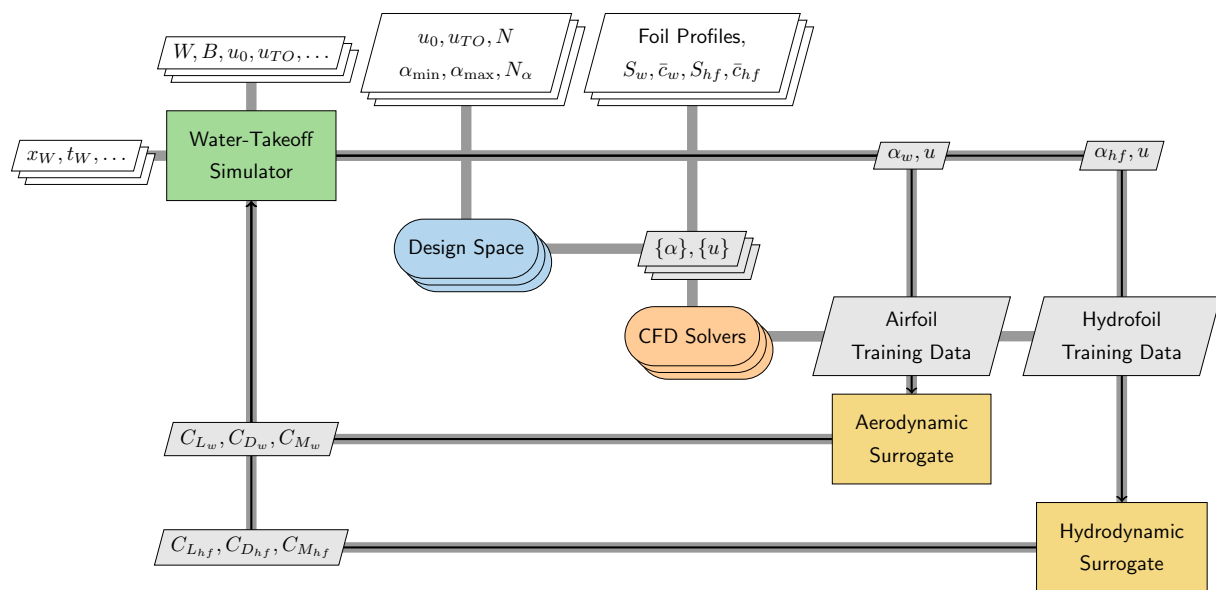


Figure 4. XDSM diagram for the water-takeoff simulator with surrogate models.

3.3. Stability Considerations and Analysis

In this section, we first discuss the physical considerations in evaluating the longitudinal stability requirements of amphibious aircraft, followed by the details of trim analysis. As we assume a no-wave condition, the lateral stability conditions caused by irregular wave patterns and effects of sponsons during water-takeoff are not considered at this preliminary design stage.

3.3.1. Physical Considerations

Consider Cartesian coordinates indicating the position of the aerodynamic center of the hydrofoil (x_{hf}, z_{hf}) where the origin is set at the aircraft CG, assumed to be located at 33% MAC of the wing aft of the leading edge for the following analysis. The large lift and drag forces produced by the hydrofoil will generate significant moments. Looking at an amphibious aircraft with its nose facing left, the hydrofoil will be located below the CG (thus, $z_{hf} < 0$), and its drag will resultantly contribute a nose-down pitching moment, which must be corrected by the elevator to maintain the required hull trim angle. To minimize elevator effort, it is best to counter this anti-clockwise moment by placing the hydrofoil ahead of the CG (thus, $x_{hf} < 0$), so the hydrofoil is able to provide lift that also provides an opposing pitch-up moment to compensate for the moment caused by its drag. This motivates a positioning procedure, such that the minimum takeoff distance is achieved during the water-takeoff run while maximizing moments generated by lift and minimizing moments generated by drag. A complication of this procedure is that the lift and drag of the hydrofoil suffer from variations in speed and angles of attack dissimilar to their airfoil counterparts due to cavitation and ventilation effects and are, thus, not predictable via tools meant for airfoil analysis; hence, the considerations using high-fidelity CFD and surrogate models introduced in Section 3.2. The effects of ventilation, however, are not explicitly modeled in this work, for reasons described in Section 2.2.

3.3.2. Trim Analysis

The non-dimensionalized moment equation is derived in the body-axis system of the aircraft following the process of Raymer [45] with modifications for the hydrofoil. The drag of the hydrofoil is not considered as negligible in this derivation unlike as usually considered for the tail, as the density of water is approximately three orders of magnitude

greater than that of air. The following expression is solved for the trim condition of the moment coefficient about the center of gravity $C_{M_{cg}} = 0$, to determine the required C_{L_h} to correct the moments generated by the hydrofoil and the wing.

$$C_{M_{cg}} = C_{M_w} + C_{M_{eng}} + C_{L_w}(\bar{x}_{cg} - \bar{x}_{ac_w}) - \eta_h V_h C_{L_h} + \eta_{hf} [V_{hf} C_{L_{hf}} - Z_{hf} C_{D_{hf}}], \quad (17)$$

where $C_{M_{eng}}$ is the moment coefficient corresponding to the engine, $\bar{x}_{cg} = x_{cg}/\bar{c}_w$ is the non-dimensionalized location of the center of gravity and $\bar{x}_{ac_w} = x_{ac_w}/\bar{c}_w$ is the location of the aerodynamic center of the wing with respect to the nose of the aircraft as the origin. The dynamic pressure ratios η_h and η_{hf} are defined as:

$$\eta_h \equiv \frac{\frac{1}{2}\rho_A u_h^2}{\frac{1}{2}\rho_A u_w^2}, \quad \eta_{hf} \equiv \frac{\frac{1}{2}\rho_W u_{hf}^2}{\frac{1}{2}\rho_A u_w^2}. \quad (18)$$

The longitudinal stability coefficients for a component c corresponding to a lifting surface are defined as:

$$V_c \equiv \frac{S_c l_c}{S_w \bar{c}_w}, \quad Z_c \equiv \frac{S_c z_c}{S_w \bar{c}_w}, \quad (19)$$

with moment arms $l_{hf} \equiv x_{cg} - x_{hf}$, $z_{hf} \equiv z_{cg} - z_{hf}$, which will be determined via the optimization procedure for the hydrofoil location presented in Section 3.1.4.

3.4. Design Framework and Solvers

In this section, we summarize the entire framework of the hydrofoil design process described in the previous sections, and present the relevant computational solvers for analyses.

3.4.1. Overall Design Process

The entire design process is depicted in the XDSM presented in Figure 5, with the descriptions of diagram components are as described in Section 3.1.3. The water-takeoff simulator is first executed without any hydrofoil to obtain the initial aircraft design's water-takeoff performance. The hydrofoil design parameters, determined from the preliminary sizing, are then used for the generation of its surrogate model using high-fidelity CFD, and similarly for the wing if required, for the design space of takeoff speeds and operational angles of attack. These surrogate models are used in the minimization of the water-takeoff distance to determine the optimal span and incidence angle of the hydrofoil. These optimal values are then provided to the optimization loop to minimize the required stabilizer force to achieve trim during the water-takeoff run by adjusting the position of the hydrofoil for the optimum. The relevant data, such as the optimized takeoff distance, span length, incidence angle, minimum stabilizer force, hydrofoil location, and the data obtained from the water-takeoff procedure, are provided to the designer to assess the performance and feasibility of the design.

3.4.2. Computational Fluid Dynamics Solvers

The choice of the computational method of CFD for the determination of the coefficients of the airfoil and hydrofoil is extremely important, depending on the appropriate compromise between accuracy and speed at the required stage of the design process. Reasonably accurate low-fidelity solvers with good computational efficiency are openly available for airfoil analyses, but the same are not openly available for hydrofoil analyses with cavitation models, so open-source high-fidelity solvers are considered instead. In this work, low-fidelity solvers are deemed sufficient to evaluate the aerodynamic performance of aircraft wing within the operational regime considered in this study, while high-fidelity solvers are required to evaluate the hydrodynamic performance of hydrofoils, as described briefly below.

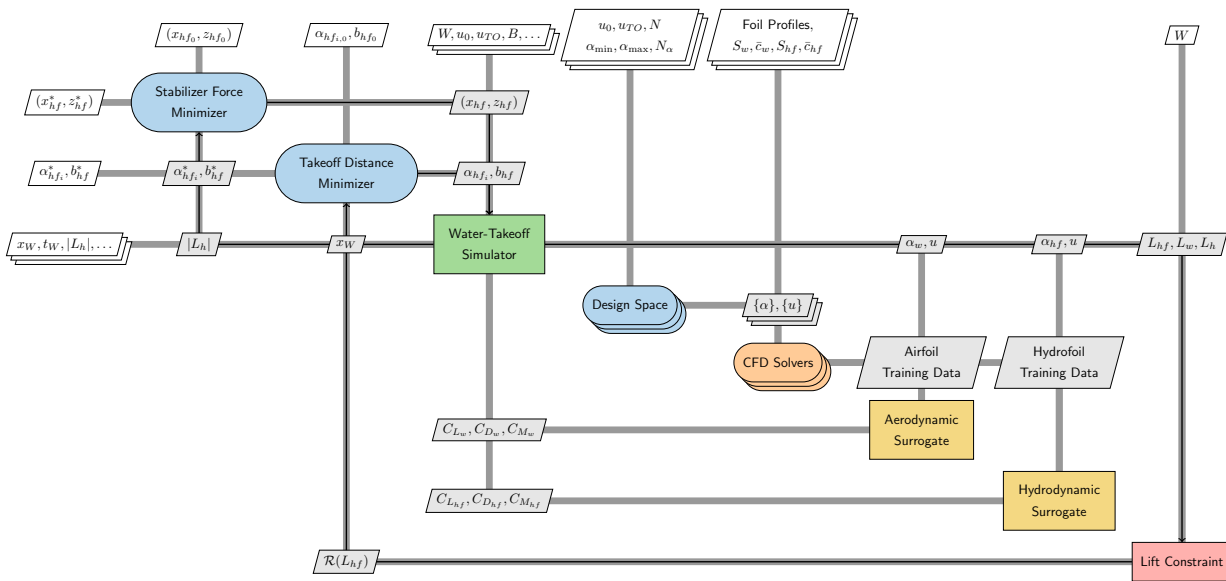


Figure 5. XDSM diagram for the hydrofoil design process.

3.4.2.1. Low-Fidelity Solvers

To reduce computational burden, XFOIL [41], a well-established viscous-inviscid design and analysis tool for airfoils at low Reynolds numbers, can be used to compute the aerodynamic coefficients for the wing by computing the lift coefficients of the airfoil C_{L_a} with flap ΔC_{L_f} and ground effect ΔC_{L_g} corrections in the takeoff simulation itself:

$$C_{L_w} = C_{L_a} + \Delta C_{L_f} + \Delta C_{L_g}. \tag{20}$$

Note that XFOIL may not be able to predict the coefficients for flows that occur at high angles of attack beyond the stall angle, in which case high-fidelity CFD must be used; however, angles greater than the stall angle are not usually reached until the aircraft rotates after reaching the takeoff speed. A surrogate model via high-fidelity CFD can also be generated for the airfoil to account for ground effects more accurately during takeoff.

3.4.2.2. High-Fidelity Solvers

The unsteady analyses with cavitation modeling over the hydrofoil are performed by solving the URANS equations via the interPhaseChangeFoam module of the OpenFOAM framework [46], following the approach of Vernengo et al. [29]. One difference from this analysis is that the Reynolds numbers for these cases are in the turbulent regime; hence, the Spalart-Allmaras turbulence model is used based on the approach of Garg et al. [28]. The cavitation model used in this analysis is the Schnerr-Sauer model [47], and the equations are solved using the segregated PIMPLE approach.

4. Case Study Description and Results—10-Seater Amphibious Aircraft

A preliminary design of a 10-seater aircraft based on a DHC-6 Twin Otter is considered for the case study. A planing hull from the National Advisory Committee for Aeronautics (NACA) Technical Note TN-2481 report [49] is adopted for this design, where we derive a curve-fit from the available experimental data for the water-takeoff simulation purpose, as shown in Figure 6. The aircraft weight is approximately $W = 5620 \times 9.81$ N, its wing area is approximately $S_w = 39.2$ m² with an incidence angle of $\alpha_w = 0^\circ$. The takeoff speed is selected to be 44 m/s, similar to the Twin Otter’s. The selection of the airfoil for the wing is the NACA 63(4)–12 profile. A surrogate model for this airfoil using RANS without ground effects has been generated by Seth and Liem [1], which is used here.

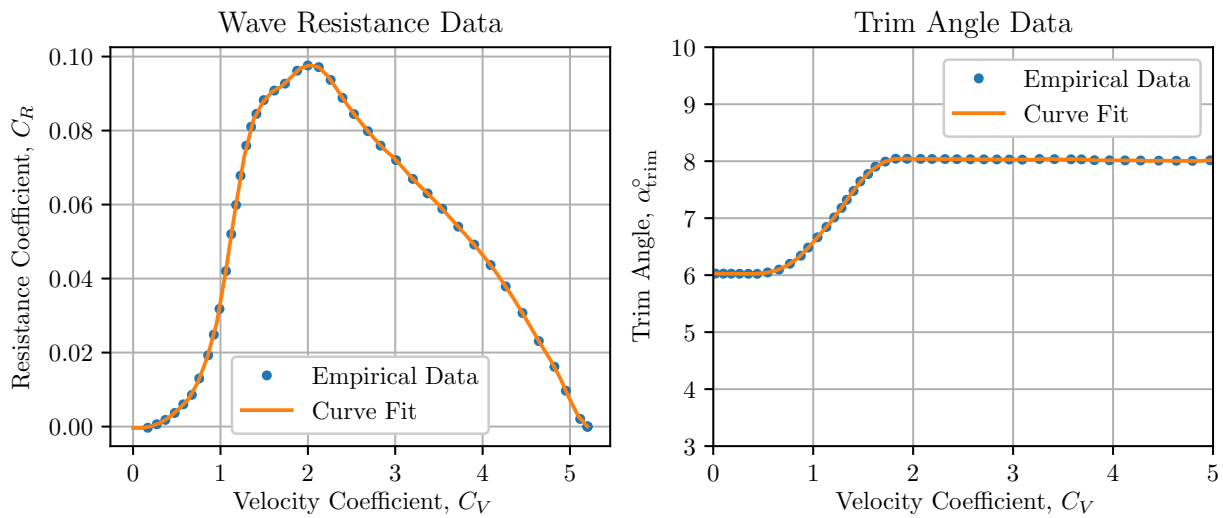


Figure 6. NACA TN-2481 planing hull data.

A quadratic thrust model presented by Gudmundsson [50] is used based on the specifications of a Pratt and Whitney Canada PT6A-34 turboprop engine via the following expression with T as the thrust of the engine as a function of speed u , as shown in Equation (21). Figure 7 shows the thrust model only within the takeoff speed range of interest; note that the bounds of the domain make it look more linear than quadratic. The engine thrust is scaled for the first 10 s of the takeoff according to the expression in Equation (22) as a heuristic pilot model for the increase in thrust, similar to the case considered in Gudmundsson [50].

$$T(u) = \left(\frac{T_{static} - 2T_{u_{max}}}{u_{max}^2} \right) u^2 + \left(\frac{3T_{u_{max}} - 2T_{static}}{u_{max}} \right) u + T_{static}, \tag{21}$$

$$r(t) = \begin{cases} 0.25 + 0.75(t/10) & t \leq 10, \\ 0 & t > 10. \end{cases} \tag{22}$$

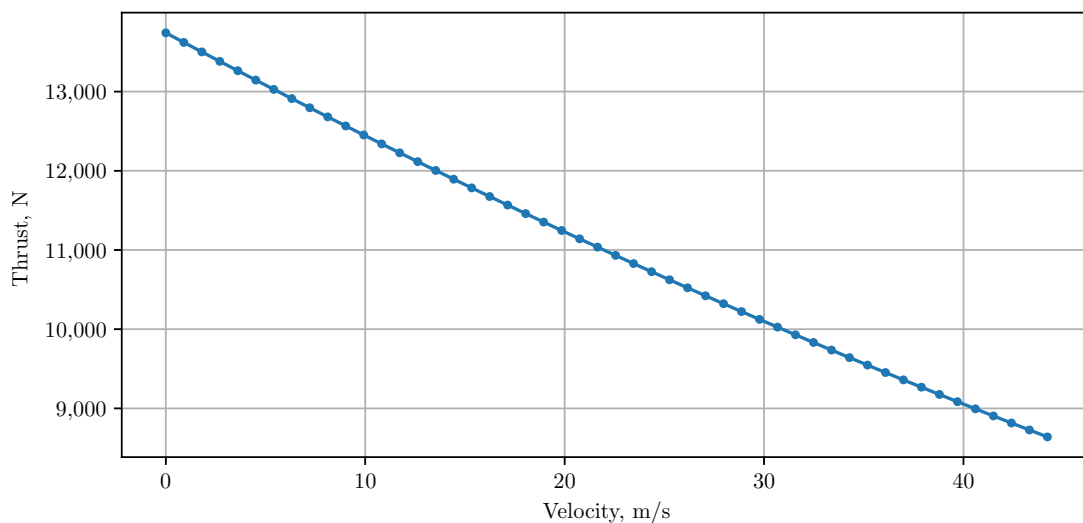


Figure 7. Thrust model as a function of speed, based on the specifications of a Pratt and Whitney Canada PT6A-34 turboprop engine.

4.1. Sizing and Profile Selection

The elevator effectiveness speed is considered to be $u_{he} \approx 15$ m/s. The wing lift at this speed with the corresponding trim angle at $\alpha_{trim} = 6^\circ$ is estimated to be $C_{L_w} = 1.5$ using XFOIL and assuming $\Delta C_{L_f} + \Delta C_{L_g} = 0.3$. This does not account for interference effects between the wing and the fuselage. The hydrofoil profile selected for this case is the Waid-Lindberg hydrofoil profile [40] in a strut-based configuration. The cavitation number at this speed is $Ca \approx 0.87$, which is in the cavitating regime for the hydrofoil. The $C_{L_{hfmax}}$ in this regime according to the experimental data is approximately 0.9, and the hydrofoil size can, hence, be determined by Equation (8), giving $S_{hf,req} \approx 0.455$ m². Considering a retractable, non-foldable hydrofoil system, an aspect ratio of 6 is selected initially, giving a chord length $\bar{c}_{hf} \approx 0.275$ m and initial span value $b_{hf_0} \approx 1.65$ m. The relevant parameters for the study are tabulated in Table 3.

Table 3. Aircraft and hydrofoil parameters.

Parameter	Value
Wing Area, m ²	39.2
Wing Aspect Ratio	10.0
Wing Span, m	19.8
Wing Chord, m	1.98
Wing Stall Speed, m/s	36.8
Wing Incidence Angle, °	0.0
Wing Dihedral Angle, °	3.0
Hull Beam Width, m	1.71
Takeoff Speed, m/s	44.0
Hydrofoil Area, m ²	0.454
Hydrofoil Aspect Ratio	6.0
Hydrofoil Span, m	1.65
Hydrofoil Chord, m	0.275
Hydrofoil Mass, kg	60.0

4.2. CFD and Surrogate Model Generation

This section discusses the use of CFD and surrogate models in the case study. The grid generation, CFD analyses, and surrogate model validations are described.

4.2.1. Grid Generation, Convergence Study, and Validation

The meshes are generated using a hyperbolic grid generator via the Python module pyHyp (<https://github.com/mdolab/pyhyp>) developed by the Multidisciplinary Design Optimization Lab (MDOLab) at University of Michigan based on the theory from Luke et al. [51]. This generates structured hexahedral meshes which keep a low cell count with high quality, which are then converted into the unstructured OpenFOAM format for this study. The domain extends to approximately 30 chord lengths from the hydrofoil. The sharp leading edge of the hydrofoil is modified to create a small, blunt leading edge to ensure high quality grid generation, and a large number of elements is concentrated near the blunt trailing edge to resolve unsteady behaviour more accurately. At this preliminary design stage, we consider non-accelerating flows using a constant speed boundary condition.

The meshes and solver are validated using the experimental results from Waid and Lindberg [40] at $Re = 7.8 \times 10^5$, $Ca = 0.293$, $u = 9.144$ m/s, $\alpha_{hf} = 6^\circ$, and three grids ($L_{0,1,2}$) are analyzed via Richardson extrapolation of the time-averaged drag coefficient $\bar{C}_{D_{hf}}$, using a grid refinement ratio of $\sqrt{N_{i-1}/N_i} = 2$, where N_i is the number of cells of the coarsened grid with respect to the finer grid N_{i-1} . A wall distance of 2×10^{-4} m is selected to match $y^+ > 30$ with the use of wall functions using the Spalart-Allmaras turbulence model to

avoid extremely small timesteps, which would drastically increase the computation time. The appropriate chord length c_{hf} and non-dimensional time τ are selected such that the cavitating flow is developed over the entire chord length of the hydrofoil to determine the required simulation time t , given by Equation (23):

$$\tau = \frac{tu_{hf}}{\bar{c}_{hf}} \geq 4. \quad (23)$$

The L_1 grid and the leading edge modification mentioned previously are shown in Figure 8. The extrapolation is shown in Figure 9. The results are provided in Table 4, with a depiction of the cavity over the hydrofoil shown in Figure 10. Computing the relevant ratio of the grid convergence indices (GCI) for $\bar{C}_{D_{hf}}$ as the quantity of interest gives approximately $0.944 \approx 1$ within the asymptotic range and approximate solver convergence $p = 1.34$. The error from the L_1 grid is considered as acceptable for a preliminary design study with lower computational costs of analyses. The analyses at this Reynolds number are within the laminar regime, and the use of turbulence models may have contributed to the error. Further analyses on this grid are performed at higher Reynolds numbers in the water-takeoff regime for amphibious aircraft, for which experimental data are not available; hence, this design point was used to validate the convergence study with available experimental data.

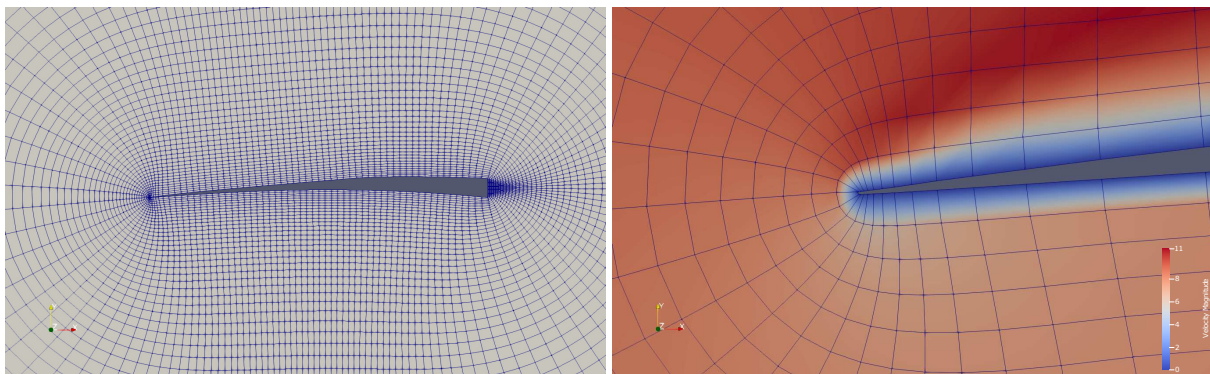


Figure 8. L_1 grid resolution and blunt leading edge with velocity contours (in m/s).

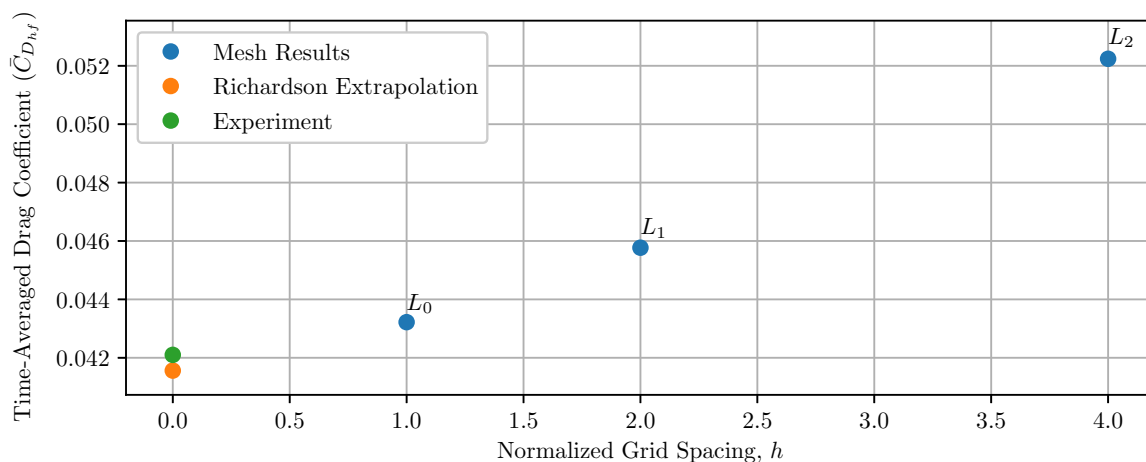


Figure 9. Grid convergence study via Richardson extrapolation.

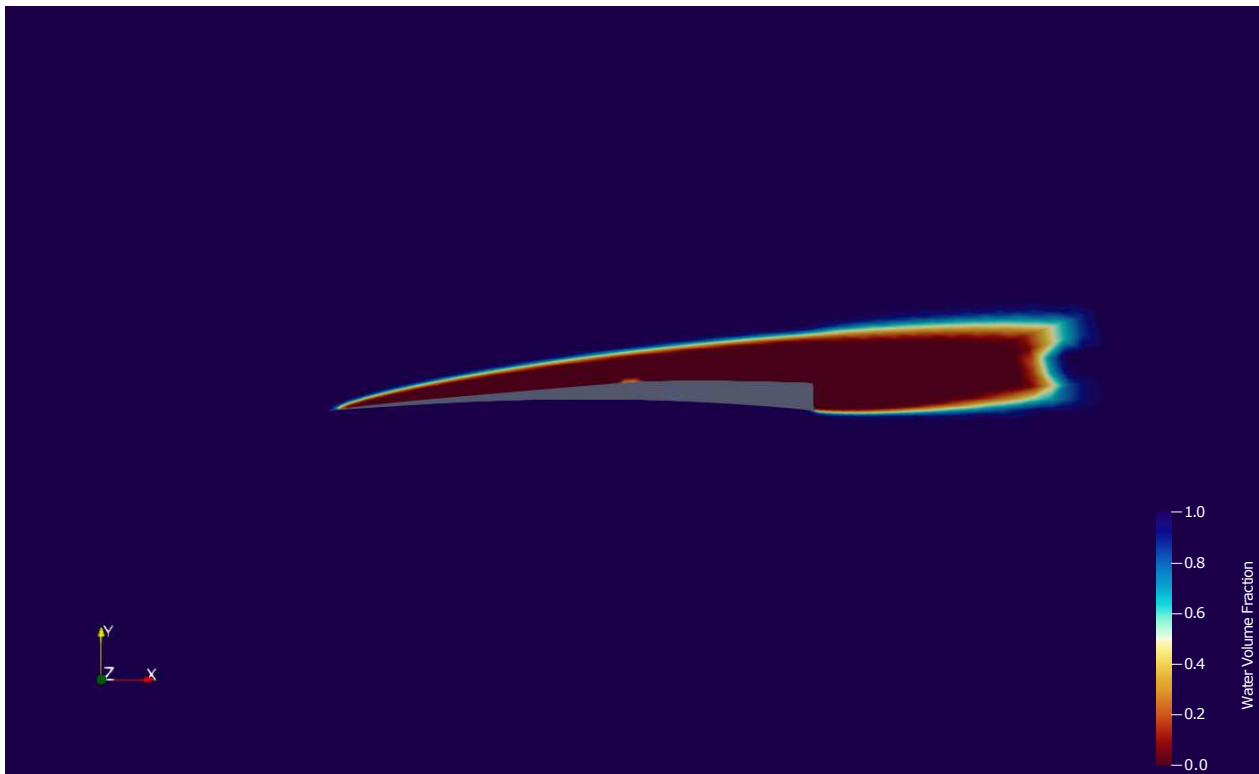


Figure 10. Supercavity over Waid-Lindberg profile.

Table 4. Grid convergence study and validation.

Grid	Grid Size	$\bar{C}_{D_{hf}}$	Error	$\bar{C}_{L_{hf}}$	Error
Experiment	–	0.0421	0%	0.4199	0%
L_2	3950	0.0522	23.99%	0.4667	11.14%
L_1	15,958	0.0458	8.79%	0.4556	8.5%
L_0	63,832	0.0432	2.61%	0.4480	6.69%

4.2.2. Surrogate Models

The surrogate models for time-averaged C_L , C_D , and C_M of the supercavitating hydrofoil are presented in Figure 11. Note that the profiles shown here significantly differ from ones generated by airfoils, as the cavitation effects are accounted for [1]. The surrogate models are generated using Kriging models via the SMT: Surrogate Modeling Toolbox [52] for the Waid-Lindberg hydrofoil profile using 25 sample points over $0 \leq \alpha_{hf} \leq 15$ and $2 \leq u \leq 45$. The 25 samples are selected from a data-set of uniformly distributed 100 points generated via the high-fidelity computational model mentioned in Section 3.4.2.2, i.e., the unsteady analyses with cavitation modeling. The timestep set for the CFD analyses was 2×10^{-5} s, and the iterations indicated a maximum Courant-Friedrich-Lewys (CFL) number of 2 per timestep. The remaining 75 samples, denoted by x_{s_i} , are used for validation purposes, in which we compute the normalized root-mean square deviation (NRMSD), as shown in Equation (24). The errors are normalized by the ranges of the corresponding non-dimensional coefficients. The computed NRMSD values for C_L , C_D , and C_M are tabulated in Table 5. These errors are deemed acceptable in approximating the coefficients.

$$\text{NRMSD} = \frac{1}{R} \sqrt{\frac{1}{N_s} \sum_{i=0}^{N_s} e_i^2}, \quad R = x_{\max} - x_{\min}, \quad e_i = x_i - x_{s_i}, \quad x \in \{C_D, C_L, C_M\}. \quad (24)$$

The $(L/D)_{hf} = (C_L/C_D)_{hf}$ ratios, computed pointwise over the design space, are presented as a surface in Figure 12. The drastic reduction of $(L/D)_{hf}$ at higher speeds, which is caused by cavitation, is clearly visible in this profile.

Table 5. Error analysis of surrogate model for Waid-Lindberg supercavitating hydrofoil.

	C_D	C_L	C_M
NRMSD, %	2.8212	3.0168	3.8037

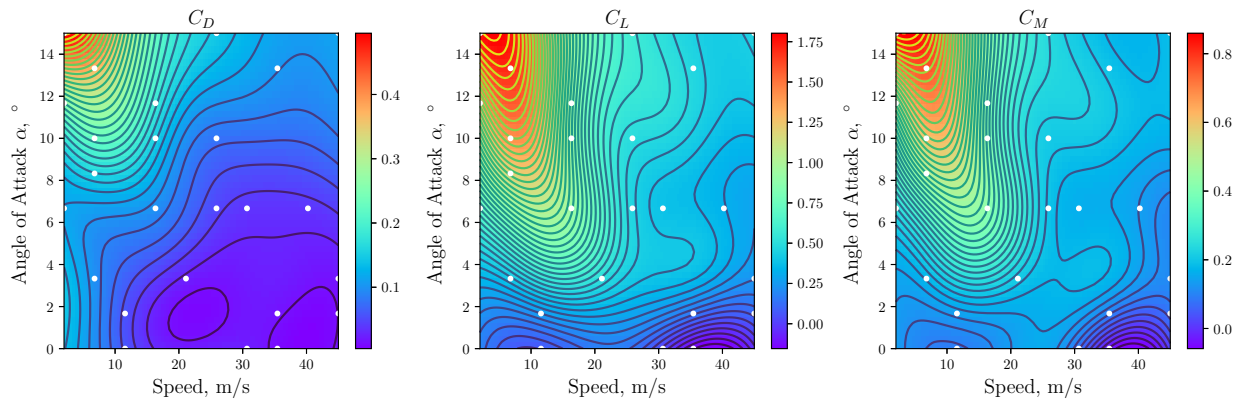


Figure 11. Surrogate contour plots for the coefficients of the Waid-Lindberg supercavitating hydrofoil. These profiles include the cavitation effects.

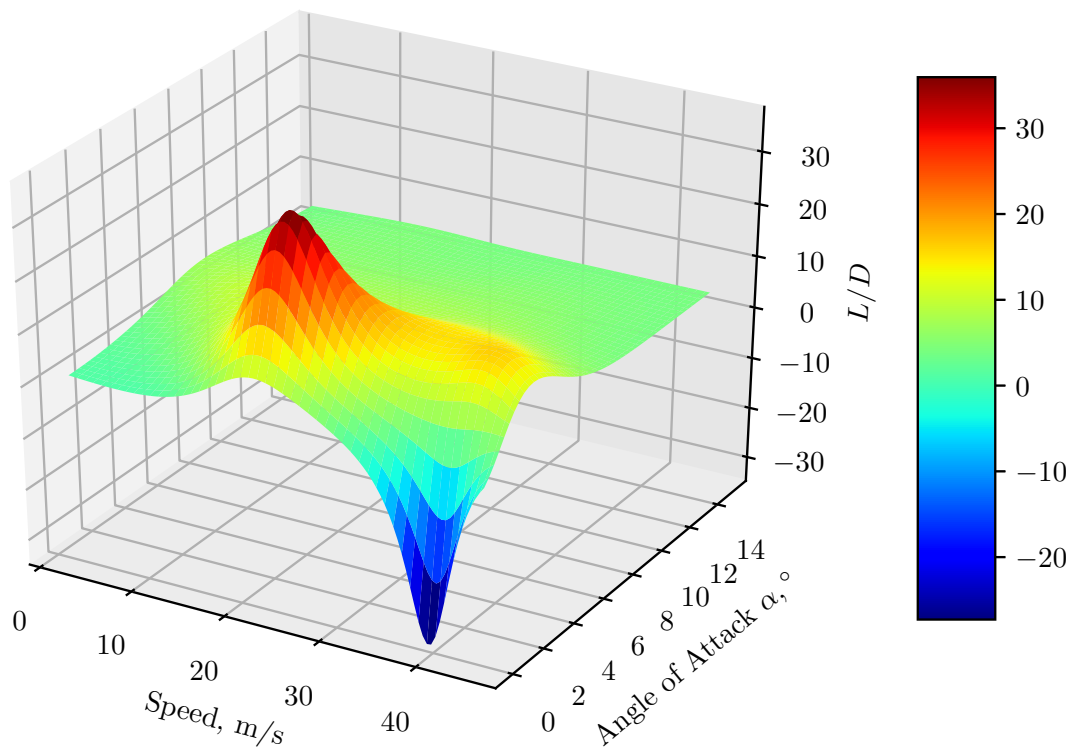


Figure 12. Response surface for the Waid-Lindberg supercavitating hydrofoil's $(L/D)_{hf}$ surrogate.

4.3. Optimization Studies

The optimizer used for the following studies is the Sequential Least-Squares Quadratic Programming algorithm provided via the SciPy package in Python [48]. This optimizer is suitable for optimization problems with bounds and constraints. The optimizers are set to converge at a tolerance of 10^{-12} .

4.3.1. Water-Takeoff Distance Minimization

A water-takeoff distance minimization study is performed to find the optimum span and incidence angle of the hydrofoil, following the procedure described in Section 3.1.3. As a retractable, non-foldable configuration is considered, the span is bounded from above by the hull beam width for the hydrofoil system to fit into the hull upon retraction.

The constrained design space with the baseline and optimum points are shown in Figure 13, in which dark dots with larger radii indicate design points in the feasible region at which the lift constraint is satisfied, and the colors corresponding to the colorbar depict the takeoff values for all points. This diagram also depicts the sensitivities of the objective function to the design variables. The number of iterations required to obtain convergence was 16, with 181 function evaluations and 16 gradient evaluations. The water-takeoff distance exhibits nonlinear behavior with respect to both variables, and the minimization problem appears to be multimodal and sensitive to initial guesses. Observing slices of fixed span lengths with varying incidence angles indicates that the takeoff distance sharply increases at specific incidence angle values. As the span length increases, the corresponding incidence angle decreases, and eventually extends to multiple incidence angles as can be seen in the region $2.2 \text{ m} \leq b_{hf} \leq 4.0 \text{ m}$, $0^\circ \leq \alpha_{hf} \leq 4.0^\circ$. This physically corresponds to the regions in which the hydrofoil generates large drag and insufficient lift to reduce the hull resistance effectively. At larger angles, such as the region between $6\text{--}14^\circ$ for span lengths between $1 \text{ m} \leq b_{hf} \leq 6 \text{ m}$, the hydrofoil generates larger lift, hence reducing the takeoff distance values; however, this region violates the lift constraint and the optimizer chooses the lower takeoff distance values satisfying the constraint at the optimum shown in the diagram.

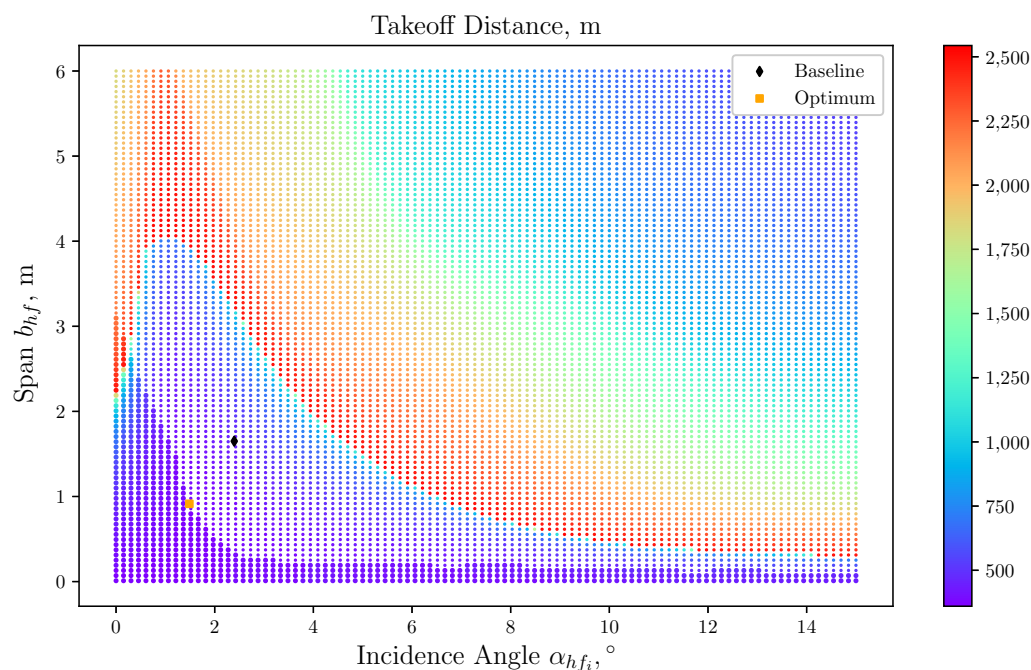


Figure 13. The design space for water-takeoff distance minimization to find the span and incidence angle of the hydrofoil. The darker region with larger radii depicts the area satisfying the lift constraint.

If an incidence angle of $\alpha_{hf_i} \geq 5^\circ$ is selected as an initial guess with the initial span value, then the optimizer tends to miss the minimum at lower angles, as it tends towards higher angles. By choosing the right starting point, on the other hand, the global optimum within the bounds can be found more effectively. In particular, the initial guess is selected through an initialization process that aims to maximize the average $(L/D)_{hf}$. The maximum average $(L/D)_{hf}$ ratio over the takeoff speed range of the hydrofoil is evaluated as an initial guess to feed to the water-takeoff distance minimizer. This is done by evaluating the averages of the $(L/D)_{hf}$ diagram in Figure 12 over the speed range, providing the average $(L/D)_{hf}$ ratio as a function of the angle of attack of the hydrofoil. This procedure results in the graph shown in Figure 14. The maximum point obtained in this initialization procedure is then used to determine the incidence angle's initial value in the water-takeoff distance minimization procedure. A similar profile was obtained from a study on the YS-920 hydrofoil, designed for subcavitating conditions [1]. However, it suffered from lower $(L/D)_{hf}$ ratios and higher water-takeoff distances, indicating profiles designed for subcavitating regimes were not suitable for amphibious aircraft and further emphasized the need for using supercavitating hydrofoils in this particular application.

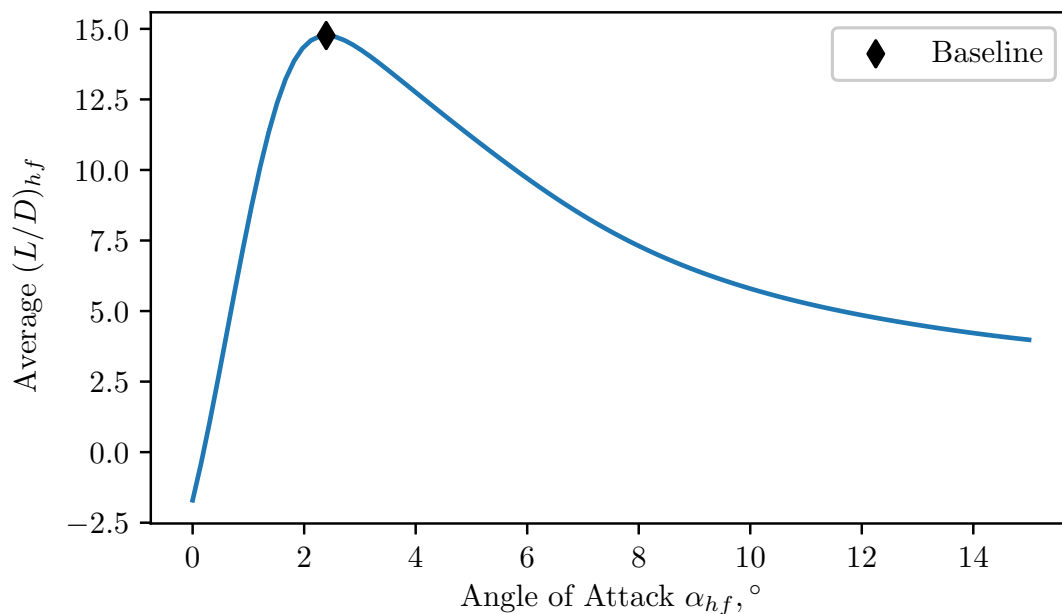


Figure 14. Average $(L/D)_{hf}$ Ratios for the Waid-Lindberg supercavitating hydrofoil.

4.3.2. Stabilizer Force Minimization

The optimum span and incidence angle are then provided to the stabilizer force minimization problem, to find the optimal hydrofoil position. The optimization procedure follows the description presented in Section 3.1.4. The initial values selected for the hydrofoil location are based on the criteria presented in [3] that the longitudinal position of the hydrofoil be located at approximately $0.5\bar{c}_w$ forward of the aircraft's CG. Its design space is depicted in Figure 15, which also depicts the sensitivities of the objective function to the design variables. It indicates that the stabilizer force is more sensitive to the horizontal location of the hydrofoil than its vertical location. It also indicates that the upper bound for z_{hf} , shown as the horizontal red line in the figure, will be the solution, and will calculate the appropriate x_{hf} to minimize the stabilizer force, which is physically consistent with the considerations presented in Section 3.3.1. The number of iterations required to obtain convergence was 18, with 98 function evaluations and 18 gradient evaluations.

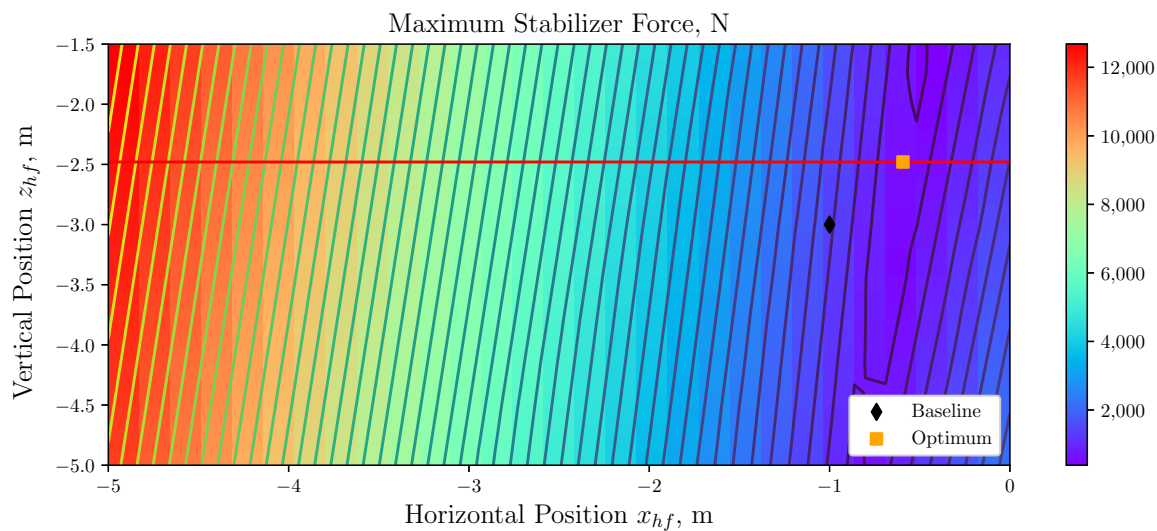


Figure 15. Hydrofoil position design space for the stabilizer force minimization. The red line indicates the upper bound of the hydrofoil's vertical position.

The results of both optimization procedures are summarized in Table 6. Detailed discussions on the performance comparison between the baseline and optimized designs are presented in the next section.

Table 6. Span length, incidence angle, and position optimization results.

Optimization Problem	Parameter	Optimal Value
Water-Takeoff Distance	Distance, x_W	359 m
	Incidence angle, α_{hf_i}	1.486°
	Span, b_{hf}	0.914 m
Maximum Stabilizer Force	Force, $ L_h _{\max}$ Hydrofoil location, (x_{hf}, z_{hf})	435 N (−0.5959 m, −2.48 m)

4.4. Performance Evaluations, Comparisons, and Discussion

In this section, we evaluate the performance of hydrofoils in the context of amphibious aircraft application. The water-takeoff analysis procedure described in Section 3.2, yields detailed information of force and load variations during takeoff, which provides insights into the effectiveness of adding hydrofoils.

First, we compare the water-takeoff performance of the aircraft with and without hydrofoils; note that the optimized hydrofoil configuration is considered in this comparison. The comparison of its effects on the hull resistance is shown in Figure 16. It indicates minor reductions in the wave resistance of the hull, and substantial reductions in the viscous resistance. These observations physically correspond to the hydrofoil reducing the submerged volume and wetted area during the water-takeoff by the hull being unported from water, as can be seen in the water-takeoff results shown in Figure 17, satisfying the purposes of the design. The viscous resistance of the configuration without hydrofoils indicates the hull is still submerged to some extent as it reaches the takeoff speed, whereas hydrofoils can help completely unport the hull before this speed. The optimization procedure of the incidence angle and span ensures that the lift constraint in Table 1 is satisfied; the hydrofoil's lift reduces as the wing's lift increases while the aircraft's speed is below the required takeoff speed, as observed in Figure 18.

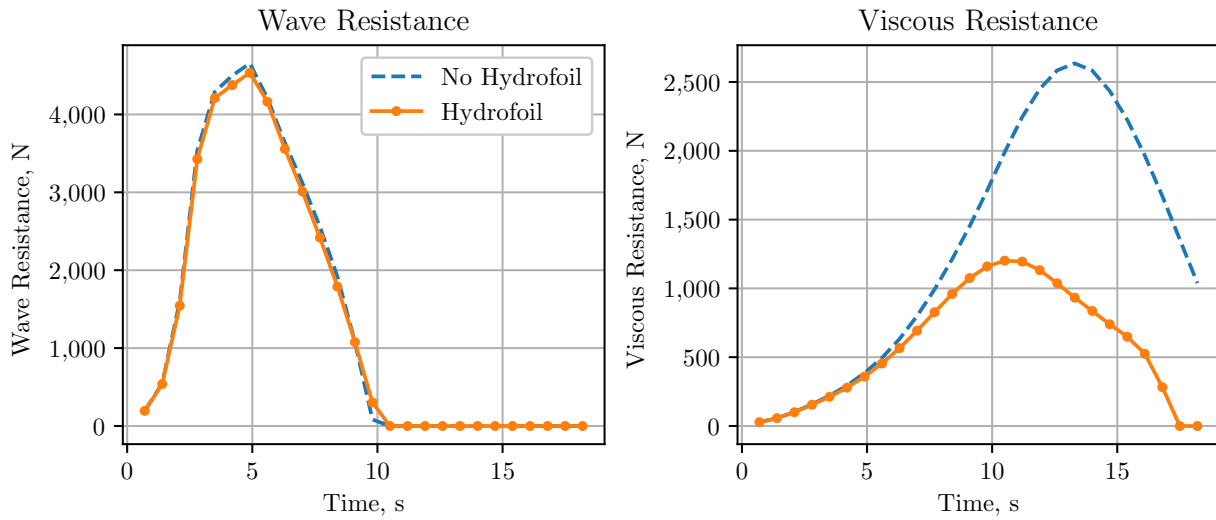


Figure 16. Hull resistance comparisons with and without the hydrofoil.

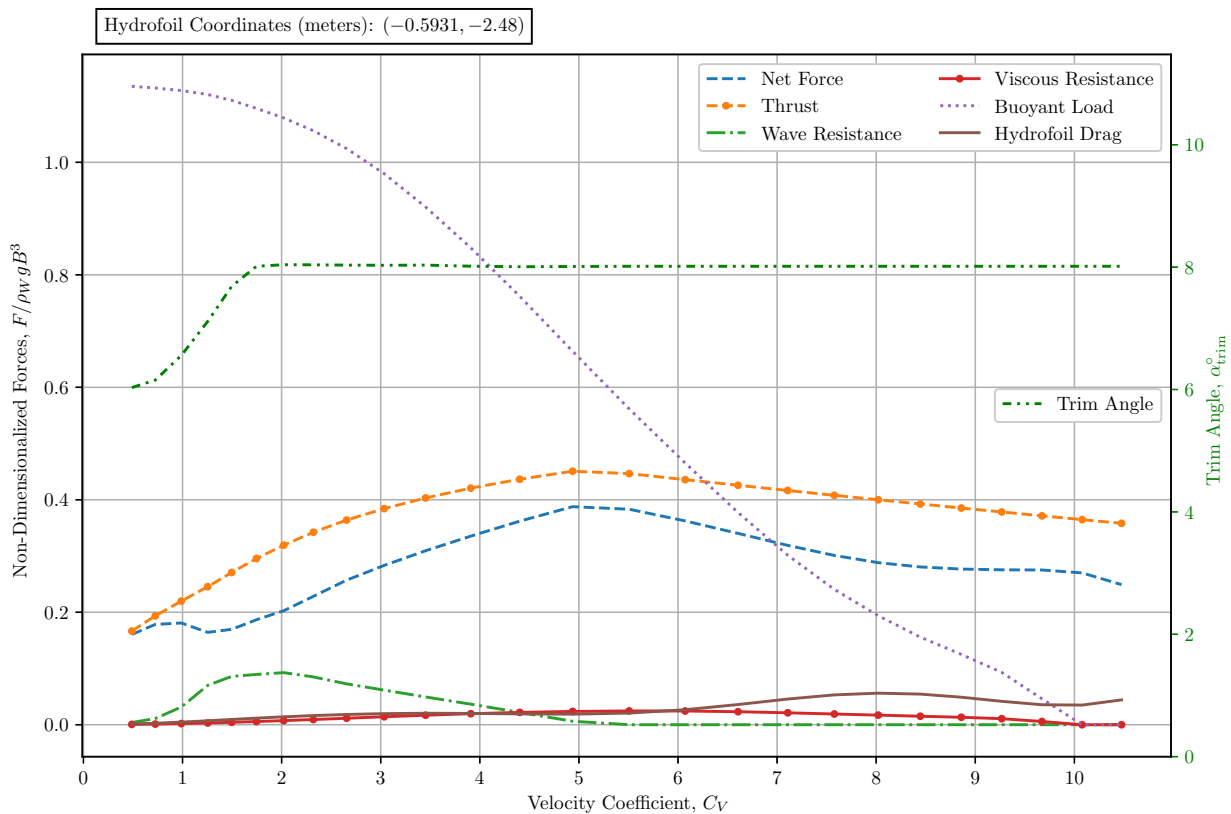


Figure 17. Variations of hydrodynamic and propulsive forces during water-takeoff process.

The results of the aircraft configuration with the baseline hydrofoil design (i.e., when using the initial values of the optimization design variables) are compared to those without and with the optimized hydrofoil design in Figure 19 to determine the performance differences and the relevant physics. A drawing depicting the differences between the baseline and optimized designs is presented in Figure 20. The comparisons between the three configurations in terms of water-takeoff distance and maximum stabilizer force are tabulated in Table 7. The notable reductions of both objective functions in the optimized design, compared to the baseline design, are evident in these results, which confirm the

effectiveness of the optimization procedure. More importantly, the results show that the optimized hydrofoils help reduce the water-takeoff distance by approximately 3.5% and the maximum stabilizer force by almost half as compared to those of the no-hydrofoil configuration, demonstrating the benefits of adding hydrofoils to amphibious aircraft. These results also emphasize the importance of performing optimizations, as adding hydrofoils based on physical reasoning alone does not guarantee performance improvement. The water-takeoff distance achieved by the aircraft configuration with the baseline hydrofoil, for instance, is longer than that of the no-hydrofoil configuration, which would defeat the purpose of adding hydrofoils.

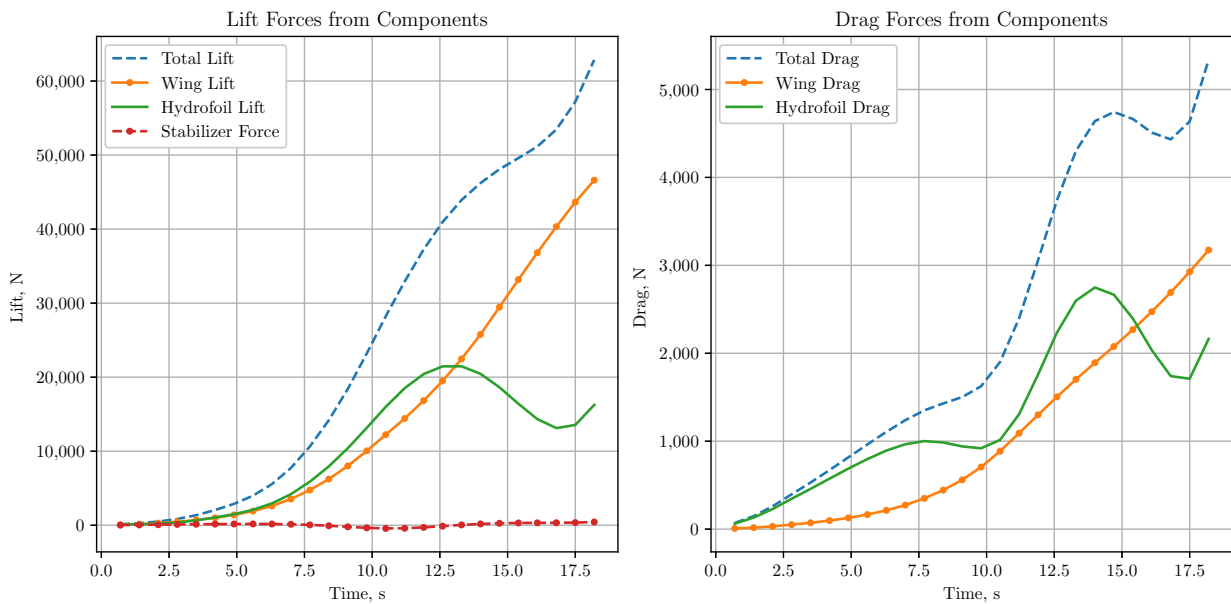


Figure 18. Lift and drag forces of components during water-takeoff process.

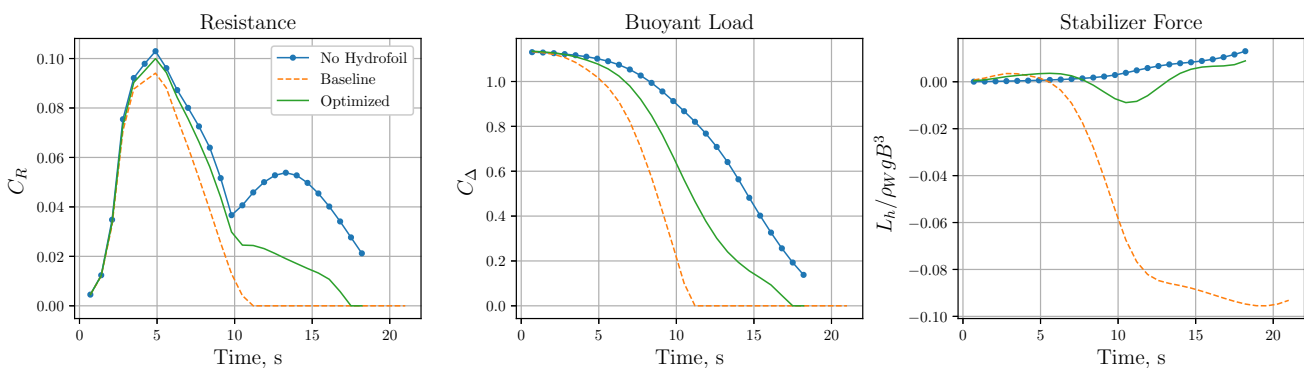


Figure 19. Force comparisons of the amphibious aircraft with and without the hydrofoil, considering both the baseline and optimized hydrofoil configurations.

The baseline design achieves the aim of reducing the buoyant load, shown in Figure 19, before the no-hydrofoil configuration, but it generates excessive moments that may not be corrected by the elevator, based on the required stabilizer force also seen in Figure 19. The relatively lower absolute values of the stabilizer force required for the optimized design as compared to the baseline design indicate the optimization procedure for the hydrofoil location is appropriate. Physically, the optimized design exhibits growing sinusoidal oscillations of the required stabilizer force, indicating a porpoising tendency for the aircraft during the water-takeoff if the trim corrections are not performed.

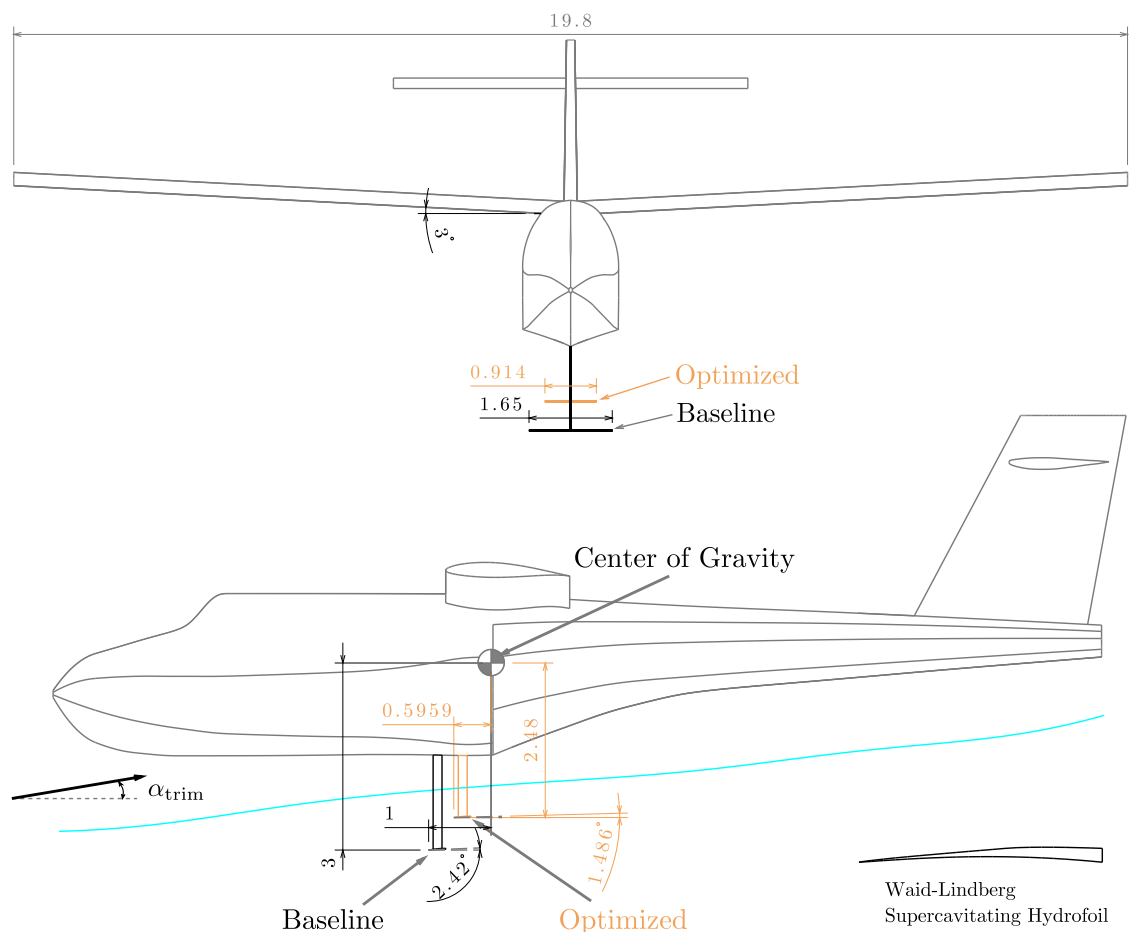


Figure 20. Aircraft drawing with baseline and optimized hydrofoil configurations (in meters).

Table 7. Water-takeoff performance results and comparisons between the different configurations.

	No Hydrofoil	Baseline	Optimized
Water-Takeoff Distance, m	372	461	359
Maximum Stabilizer Force, N	604	4743	435

5. Conclusions

In the present study, the key considerations for the preliminary design of a hydrofoil for amphibious aircraft were investigated. A sizing procedure was formulated with recommendations for profile selection and different configurations. In particular, we observed that a supercavitating hydrofoil profile was required for amphibious aircraft application. An optimization framework was formulated to minimize the water-takeoff distance of the aircraft by finding the optimal span length and incidence angle. Its detrimental effects on the longitudinal stability of the aircraft with respect to the required horizontal stabilizer force to maintain the trim angle were also minimized, by finding the optimal position of the hydrofoil with respect to the aircraft's center of gravity. The effectiveness of the design was analyzed by a water-takeoff physics simulator using surrogate models of the hydrofoil. These models were generated via CFD sample data to determine the performance of a selected hydrofoil over a range of speeds and angles of attack within the water-takeoff regime below the takeoff speed.

To evaluate and assess the performance and effectiveness of adding hydrofoils to amphibious aircraft, the developed preliminary design framework was applied in a 10-seater aircraft as a case study. Results from the water-takeoff simulator showed the variations of forces and loads during the water-takeoff run, providing insights into the physics and

behavior of the aircraft during the process. The aircraft's porpoising tendency, for instance, was evident by observing the stabilizer variations, which highlighted the importance of trim corrections. These results were unique to amphibious aircraft, i.e., the hydrofoil performance was different from that of marine applications, and the takeoff performance was different from that of conventional ground-based aircraft.

The results of the water-takeoff procedure indicated that the hydrofoil performed the required purposes of reducing hull resistance and buoyant load. These reductions demonstrated the hydrofoil's effectiveness in improving the water-takeoff performance and efficiency of amphibious aircraft, as evident in the reduction of the water-takeoff distance observed in the case study. Our results showed, however, that adding hydrofoils alone, without being properly optimized, could not guarantee a performance improvement. This observation further emphasized the need to develop a comprehensive design framework for amphibious aircraft and highlighted the benefits of performing optimization in design studies. The optimization results indicated that the water-takeoff distance minimization with respect to the span and incidence angle as design variables was non-differentiable and multimodal with the required constraints, depending on the hydrofoil's profile. The problem of minimizing the stabilizer force was relatively less complex, but still an important part of the design procedure.

To the best of our knowledge, ours is the first study that systematically evaluates hydrofoil performance in the context of amphibious aircraft operation, particularly during the water-takeoff process. The modular design of the framework gives flexibility to replace the current models, be it aerodynamic, hydrodynamic, or propulsive, with higher-fidelity models in future development. The computation with the surrogate models allows for rapid analysis with variations of parameters, taking less than two minutes to complete for a case, which offers a desirable computational efficiency. This computational framework will reduce reliance on expensive experiments which have limited the technological advancement and progress in amphibious aircraft development. More importantly, the developed framework will enable performing detailed amphibious aircraft design optimization and tradeoff studies with more computational rigor. We will be able to perform multidisciplinary design optimization that simultaneously considers the aerodynamic and hydrodynamic performance (e.g., to optimize hull and hydrofoil shapes) to obtain a truly optimal design, thereby advancing the amphibious aircraft development.

Author Contributions: Conceptualization, A.S. and R.P.L.; methodology, A.S.; software, A.S.; validation, A.S.; formal analysis, A.S.; investigation, A.S.; resources, R.P.L.; data curation, A.S.; writing—original draft preparation, A.S.; writing—review and editing, R.P.L.; visualization, A.S.; supervision, R.P.L.; project administration, R.P.L.; funding acquisition, R.P.L. All authors have read and agreed to the published version of the manuscript.

Funding: This research was funded by the HKUST Initiation Grant (Grant No. R9354).

Institutional Review Board Statement: Not applicable.

Informed Consent Statement: Not applicable.

Data Availability Statement: The data presented in this study are available on request from the corresponding author. The data are not publicly available due to ongoing research with further refinements for future studies.

Acknowledgments: The authors would like to thank the HKUST Post-Graduate International Student Fellowship Scheme for partially funding the first author.

Conflicts of Interest: The authors declare no conflict of interest.

Abbreviations

The following symbols used in the manuscript are provided here for reference:

(x, z)	2D coordinates with respect to center of gravity as origin
t	Time
τ	Non-dimensional time
$\overline{(\)}$	Time-averaged quantity
$\Delta(\)$	Change in quantity
$\dot{(\)}$	Time derivative of quantity
g	Acceleration due to gravity on Earth
h	Reference height for hydrostatic pressure head
u	Speed in horizontal direction
$p_\infty, p_{\text{atm}}, p_V$	Freestream, atmospheric and vapor pressure
ρ	Density of fluid
η	Dynamic pressure ratio
μ	Dynamic viscosity of fluid
Re, We, Fr, Ca	Reynolds, Weber, Froude, and cavitation number
$(\)_w, (\)_h, (\)_{hf}$	Quantity corresponding to wing, horizontal tail, and hydrofoil
L, D, M	Lift, drag and moment
C_L, C_D, C_M	Lift, drag, and moment coefficients
C_p, C_F	Pressure and skin-friction resistance coefficients
C_Δ, C_R, C_V	Load, resistance and speed coefficients
$\alpha, \alpha_i, \alpha_{\text{trim}}$	Angle of attack, incidence, and trim angle
L/D	Lift-to-drag ratio
V_c, Z_c	Longitudinal stability coefficients of component c
l_h, l_v	Horizontal and vertical moment arms
b, c	Span and chord lengths
S	Reference area
L	Reference length
AR	Aspect ratio
W	Aircraft weight
B	Hull beam width
δ	Dihedral angle
\bar{c}	Mean aerodynamic chord length
(\bar{x}, \bar{z})	Coordinates non-dimensionalized with respect to mean aerodynamic chord
T	Thrust
ϕ_T	Thrust angle

References

- Seth, A.; Liem, R.P. Hydrofoil Conceptual Design and Optimization Framework for Amphibious Aircraft. In Proceedings of the AIAA Aviation 2019 Forum, Dallas, TX, USA, 17–21 June 2019; p. 3552.
- Thurston, D.B. *Amphibian Aircraft Design*; SAE Technical Paper: New York, NY, USA, 1974.
- Thurston, D.B.; Vagianos, N.J. *Hydrofoil Seaplane Design*; Unclassified Final Report No. 6912 for Naval Air Systems Command under Contract N00019-69-0475. 1970. Available online: <https://apps.dtic.mil/dtic/tr/fulltext/u2/873851.pdf> (accessed on 18 September 2018).
- Thurston, D.B. *Design for Flying*, 2nd ed.; McGraw-Hill: New York, NY, USA, 1994.
- Cary, J.; Crouse, G. Preliminary Design Optimization of an Amphibious Aircraft. In Proceedings of the 50th AIAA Aerospace Sciences Meeting Including the New Horizons Forum and Aerospace Exposition, Nashville, TN, USA, 9–12 January 2012; p. 250.
- Jameson, A. Aerodynamic Design via Control Theory. *J. Sci. Comput.* **1988**, *3*, 233–260. [[CrossRef](#)]
- Jameson, A. Automatic Design of Transonic Airfoils to Reduce the Shock Induced Pressure Drag. In Proceedings of the 31st Israel Annual Conference on Aviation and Aeronautics, Tel Aviv, Israel, 21–22 February 1990; pp. 5–17.
- Qiu, L.; Song, W. Efficient Multiobjective Optimization of Amphibious Aircraft Fuselage Steps with Decoupled Hydrodynamic and Aerodynamic Analysis Models. *J. Aerosp. Eng.* **2016**, *29*, 04015071. [[CrossRef](#)]
- Puorger, P.C.; Dessi, D.; Mastroddi, F. Preliminary Design of an Amphibious Aircraft by the Multidisciplinary Design Optimization Approach. In Proceedings of the 48th AIAA/ASME/ASCE/AHS/ASC Structures, Structural Dynamics, and Materials Conference, Honolulu, HI, USA, 23–26 April 2007.
- Wang, L.; Yin, H.; Yang, K.; Liu, H.; Zhu, J. Water takeoff performance calculation method for amphibious aircraft based on digital virtual flight. *Chin. J. Aeronaut.* **2020**. [[CrossRef](#)]

11. Michel, W.; Hoerner, S.; Ward, L.; Buermann, T. *Hydrofoil Handbook. Volume 2: Hydrodynamic Characteristics of Components*; Technical Report; Gibbs and Cox Inc.: New York, NY, USA, 1954.
12. King, H.F. *Aeromarine Origins: The Beginnings of Marine Aircraft, Winged Hulls, Air-Cushion and Air-Lubricated Craft, Planing Boats and Hydrofoils*, 1st ed.; Aero Publishers Inc.: Fallbrook, CA, USA, 1966.
13. Rothblum, R.S. *Experimental Investigations of Hydrofoils, ZWB Document FB 1319*; Technical Report; Die Messeinrichtungen Des Schlepversuchswagens Im Institut Fur Seeflugwesen: Hamburg, Germany, 1940.
14. Brizzolara, S.; Young, Y.L. Physical and Theoretical Modeling of Surface-Piercing Hydrofoils for a High-Speed Unmanned Surface Vessel. In Proceedings of the ASME 2012 31st International Conference on Ocean, Offshore and Arctic Engineering, Volume 4: Offshore Geotechnics; Ronald W. Yeung Honoring Symposium on Offshore and Ship Hydrodynamics, Rio de Janeiro, Brazil, 1–6 July 2012; Volume 44915, pp. 831–837. [[CrossRef](#)]
15. Young, Y.L.; Brizzolara, S. Numerical and Physical Investigation of a Surface-Piercing Hydrofoil. In Proceedings of the Third International Symposium on Marine Propulsors, Launceston, Australia, 5–8 May 2013.
16. Andrun, M.; Šarić, B.; Bašić, J.; Blagojević, B. CFD analysis of surface-piercing hydrofoil ventilation inception. In Proceedings of the XXII Theory and Practice of Shipbuilding, Trogir, Croatia, 6–8 October 2016.
17. Yang, X.; Wang, T.; Liang, J.; Yao, G.; Liu, M. Survey on the novel hybrid aquatic-aerial amphibious aircraft: Aquatic unmanned aerial vehicle (AquaUAV). *Prog. Aerosp. Sci.* **2015**, *74*. [[CrossRef](#)]
18. Papoutsis-Kiachagias, E.M.; Kyriacou, S.A.; Giannakoglou, K.C. The continuous adjoint method for the design of hydraulic turbomachines. *Comput. Methods Appl. Mech. Eng.* **2014**, *278*, 621–639. [[CrossRef](#)]
19. Leroux, J.B.; Coutier-Delgosha, O.; Astolfi, J.A. A joint experimental and numerical study of mechanisms associated to instability of partial cavitation on two-dimensional hydrofoil. *Phys. Fluids* **2005**, *17*, 052101. [[CrossRef](#)]
20. Eppler, R.; Shen, Y.T. Wing Sections for Hydrofoils—Part 1: Symmetric Profiles. *J. Ship Res.* **1979**, *23*, 209–217.
21. Shen, Y.T. Wing Sections for Hydrofoils—Part 3: Experimental Verifications. *J. Ship Res.* **1985**, *29*, 39–50.
22. Wei, Q.; Chen, H.X.; Zhang, R. Numerical research on the performance of slot hydrofoil. *J. Hydrodyn.* **2015**, *27*, 105–111. [[CrossRef](#)]
23. Kolyshkin, N. *Some Data on the Hydrofoil Motorvessel 'Raketa' and Results in Operation*; Technical Report; Directorate of Scientific Information Services: Ottawa, ON, Canada, 1960.
24. Plisov, N.B.; Rozhdestvinski, K.V.; Treshkov, V.K. *Aerohydrodynamics of Ships with Maintenance Dynamic Principles*; Technical Report; Sudostroenie: Leningrad, Russia, 1991.
25. Conesa, F.R.; Liem, R.P. Slotted hydrofoil design optimization to minimize cavitation in amphibious aircraft application: A numerical simulation approach. *Adv. Aircr. Spacecr. Sci.* **2020**, *7*, 309–333. [[CrossRef](#)]
26. Shen, Y.T.; Eppler, R. Wing Sections for Hydrofoils—Part 2: Nonsymmetrical Profiles. *J. Ship Res.* **1981**, *255*, 191–200.
27. La Roche, U.; Trevisani, H. Supramar cavitation suppression at hydrofoil thick sections reference paper: Replacing cavitation and supercavitation bubbles on profiles for high speed propellers and foil by two-phase boundary layers on profiles at high speed and low sigma. In Proceedings of the Second High-Performance Marine Vehicles Conference, Hamburg, Germany 2–5 May 2001.
28. Garg, N.; Kenway, G.K.; Martins, J.R.; Young, Y.L. High-fidelity Multipoint Hydrostructural Optimization of a 3-D Hydrofoil. *J. Fluids Struct.* **2017**, *71*, 15–39. [[CrossRef](#)]
29. Vernengo, G.; Bonfiglio, L.; Gaggero, S.; Brizzolara, S. Physics-based design by optimization of unconventional supercavitating hydrofoils. *J. Ship Res.* **2016**, *60*, 187–202. [[CrossRef](#)]
30. Zimmer, H. Hydrodynamic Lift for Flying Boats or Sea Planes. U.S. Patent 5,018,686A, 28 May 1991.
31. Larsson, L.; Raven, H. *Ship Resistance and Flow*; The Society of Naval Architects and Marine Engineers, SNAME, The Principles of Naval Architecture Series: Jersey City, NJ, USA, 2010.
32. Amromin, E.L. Design approach for cavitation tolerant hydrofoil and blades. *J. Fluids Struct.* **2014**, *45*, 96–106. [[CrossRef](#)]
33. Hsin, C.Y. Application of the panel method to the design of two-dimensional foil sections. *J. Chin. Soc. Nav. Archit. Mar. Eng.* **1994**, *13*, 1–11.
34. Bocket, T. *Minimum Pressure Envelopes for Modified NACA-66 Sections with NACA a = 0.8 Camber and Buships Type 1 and Type 2 Sections*; DTIC: Fort Belvoir, VA, USA, 1996. Available online: <https://apps.dtic.mil/dtic/tr/fulltext/u2/629379.pdf> (accessed on 27 February 2019).
35. Kinnas, S.; Mishima, S.; Brewer, W. Nonlinear analysis of viscous flow around cavitating hydrofoils. In Proceedings of the 20th Symposium on Naval Hydrodynamics, Santa Barbara, CA, USA, 21–26 August 1996; pp. 21–26.
36. Mishima, S.; Kinnas, S.A. A numerical optimization technique applied to the design of two-dimensional cavitating hydrofoil sections. *J. Ship Res.* **1996**, *40*, 28–38.
37. Coutier-Delgosha, O.; Reboud, J.L.; Delannoy, Y. Numerical simulation of the unsteady behaviour of cavitating flows. *Int. J. Numer. Methods Fluids* **2003**, *42*, 527–548. [[CrossRef](#)]
38. Barden, T.A.; Binns, J.R. On the Road to Establishing Ventilation Probability for Moth Sailing Dinghies. In Proceedings of the 18th Australasian Fluid Mechanics Conference, Launceston, Australia, 3–7 December 2012.
39. Encyclopedia.com. Douglas Sea Scale. 2018. Available online: <https://www.encyclopedia.com/science/encyclopedias-almanacs-transcripts-and-maps/douglas-sea-scale> (accessed on 18 October 2018).
40. Waid, R.L.; Lindberg, Z. *Experimental and Theoretical Investigations of a Supercavitating Hydrofoil*; Technical Report; California Institute of Technology, Pasadena, CA, USA, 1957. Available online: https://authors.library.caltech.edu/6035/1/Report_No_47-8.pdf (accessed on 21 September 2019).

41. Drela, M. XFOIL: An analysis and design system for low Reynolds number airfoils. In *Low Reynolds Number Aerodynamics*; Mueller T.J., Ed.; Lecture Notes in Engineering; Springer: Berlin/Heidelberg, Germany, 1989; Volume 54, pp. 1–12. [CrossRef]
42. King, D.A.; Land, N.S. *Effects of Sweepback and Taper on the Force and Cavitation Characteristics of Aspect-Ratio-4 Hydrofoils*; Technical Report; NACA Research Memorandum: 1952; p. L52J10. Available online: <https://digital.library.unt.edu/ark:/67531/metadc59494/> (accessed on 28 July 2019).
43. Lambe, A.B.; Martins, J.R.R.A. Extensions to the Design Structure Matrix for the Description of Multidisciplinary Design, Analysis, and Optimization Processes. *Struct. Multidiscip. Optim.* **2012**, *46*, 273–284. [CrossRef]
44. Seth, A.; Liem, R.P. Takeoff Analysis of Amphibious Aircraft with Implementation of a Hydrofoil. In Proceedings of the Structures18—The 2018 Structures Congress, Incheon, Korea, August 27–31 2018.
45. Raymer, D. *Aircraft Design: A Conceptual Approach*, 4th ed.; American Institute of Aeronautics and Astronautics: Washington, DC, USA, 2012.
46. The OpenFOAM Foundation. 2018. Available online: <http://openfoam.org/> (accessed on 27 August 2019).
47. Schnerr, G.H.; Sauer, J. Physical and numerical modeling of unsteady cavitation dynamics. In Proceedings of the Fourth International Conference on Multiphase Flow, New Orleans, LA, USA, 27 May–1 June 2001; Volume 1.
48. Jones, E.; Oliphant, T.; Peterson, P. SciPy: Open Source Scientific Tools for Python. 2001. Available online: <https://www.scipy.org> (accessed on 20 March 2018).
49. Suydam, H.B. *Hydrodynamic Characteristics of a Low-Drag, Planing-Tail Flying-Boat Hull: NACA Technical Note 2481*; NACA: Washington, DC, USA, 1948.
50. Gudmundsson, S. *General Aviation Aircraft Design: Applied Methods and Procedures*; Butterworth-Heinemann: Oxford, UK, 2013.
51. Luke, E.; Collins, E.; Blades, E. A fast mesh deformation method using explicit interpolation. *J. Comput. Phys.* **2012**, *231*, 586–601. [CrossRef]
52. Bouhlel, M.A.; Hwang, J.T.; Bartoli, N.; Lafage, R.; Morlier, J.; Martins, J.R. A Python surrogate modeling framework with derivatives. *Adv. Eng. Softw.* **2019**, *135*, 102662. [CrossRef]

Article

Design Space Exploration of a Jet Engine Component Using a Combined Object Model for Function and Geometry

Jakob R. Müller , Massimo Panarotto  and Ola Isaksson 

Department of Industrial and Materials Science, Chalmers University of Technology, Chalmersplatsen 4, 412 96 Gothenburg, Sweden; massimo.panarotto@chalmers.se (M.P.); ola.isaksson@chalmers.se (O.I.)

* Correspondence: jakob.muller@chalmers.se

Received: 23 October 2020; Accepted: 3 December 2020; Published: 8 December 2020



Abstract: The design of aircraft and engine components hinges on the use of computer aided design (CAD) models and the subsequent geometry-based analyses for evaluation of the quality of a concept. However, the generation (and variation) of CAD models to include radical or novel design solutions is a resource intense modelling effort. While approaches to automate the generation and variation of CAD models exist, they neglect the capture and representation of the product’s design rationale—what the product is supposed to do. The design space exploration approach Function and Geometry Exploration (FGE) aims to support the exploration of more functionally and geometrically different product concepts under consideration of not only geometrical, but also teleological aspects. The FGE approach has been presented and verified in a previous presentation. However, in order to contribute to engineering design practice, a design method needs to be validated through application in industrial practice. Hence, this publication reports from a study where the FGE approach has been applied by a design team of a Swedish aerospace manufacturers in a conceptual product development project. Conceptually different alternatives were identified in order to meet the expected functionality of a guide vane (GV). The FGE was introduced and applied in a series of workshops. Data was collected through participatory observation in the design teams by the researchers, as well as interviews and questionnaires. The results reveal the potential of the FGE approach as a design support to: (1) Represent and capture the design rationale and the design space; (2) capture, integrate and model novel solutions; and (3) provide support for the embodiment of novel concepts that would otherwise remain unexplored. In conclusion, the FGE method supports designers to articulate and link the design rationale, including functional requirements and alternative solutions, to geometrical features of the product concepts. The method supports the exploration of alternative solutions as well as functions. However, scalability and robustness of the generated CAD models remain subject to further research.

Keywords: product development process; design space exploration; function modelling; CAD; aerospace

1. Introduction

The development of new components for aircraft engines often relies on improvement and refinement of an existing “legacy design”. To be able to meet the targets set by Flightpath 2050 [1], as well as contemporary developments in air travel [2], manufacturers need to explore and develop conceptually new designs. Such novel concepts are required on an aircraft and engine system level, but equally on a component level [3,4].

Examples for such novel product concepts are the open rotor design [5] or electrical and hybrid propulsion designs [6]. Such concepts bring new arrangements of parts, and require new functions to be met by the engine components.

Such radically new concepts—as well as the components they are composed of—need to be developed, designed and evaluated first. In the case of developing physical products, such as aeroengine components, this requires their embodiment in a sufficient level of detail for engineering analysis. In most cases, this means that a geometry model in the form of computer aided design (CAD) of each concept needs to be created. To be able to assess all relevant product properties, analyses on solid geometry models may be required [7]. As a result, this publication is focused on the management and generation of solid CAD models.

To be able to develop novel products outside the already known design space, developers need reliable methods and tools that support them in the generation of concepts and models as well as their analysis and evaluation [8–10]. Currently available—and applied—methods such as parameterisation [11] or knowledge-based engineering (KBE) [12] cover only a dimensional variation of existing concepts or require an expensive setup of a master model. Therefore, these geometry based approaches only allow for the exploration of a subset of the available design space [8,13]. To enable conceptual design, which explores alternative functions and solutions, a design space exploration (DSE) method needs to take into account a representation of the product's function [14,15].

The DSE method function and geometry exploration (FGE) has been developed to fulfil this premise: through a connection of the functional and geometrical domain, a wider and more efficient exploration is to be enabled [16]. However, while the FGE approach itself has been presented and verified in [16], its effect on improving DSE in practice has not been validated. This publication reports from a study to validate the approach through application in an industrial setting. Validation refers in this case to test whether it is useful, that means it has a positive impact on the product development process in an applied context [17,18].

The validation is performed through a qualitative study about the application of the FGE approach in a development project for a static turbine structure, a fan frame guide vane (GV). The study has been conducted in tight collaboration with an aerospace manufacturer. The study investigates into whether FGE does improve DSE in that it enables the capture, representation and embodiment of novel design concepts.

An over view over the underlying theories is given in Section 2, and the FGE approach itself is shortly explained in Section 2.1. How the study has been setup and how the approach has been evaluated is explained in Section 3. The application of FGE in the industrial setting is presented in Section 4. The practitioners' evaluation and reflections on the application of the approach are presented in Section 4.2. Section 5 discusses these results in relation to the problematic described above as well as compared to similar approaches from literature. Lastly, Section 6 summarises the contribution of this paper and proposes directions for further development of the approach.

2. Frame of Reference

In the conceptual phases of product development, multiple alternative concepts need to be evaluated. The sum of all possible concepts which fulfil the respective requirements is called the design space [19]. The more, and more different, concepts can be investigated—corresponding to a larger area of the design space being covered—the higher the probability that a good, or even the best possible, concept has been selected [8].

To achieve this, the design space needs to be defined and the concepts residing in it need to be devised and evaluated against each other [9]. For the evaluation against each other, that is assessing whether, and how well, they fulfil requirements and functions, the concepts' need to be simulated in terms of different behaviour. For most of such simulations, a geometrical product representation in the form of a CAD model is needed [10].

CAD models are a representation of a product's geometry and topology. Geometry refers to the shape of the product, whereas topology refers to the relations of the individual shapes towards each other [20]. Most commercial CAD software operate as feature-based parametric CAD, where geometric and topological information is contained in features, which are set into relation in a procedurally operated feature-tree. If set-up and maintained correctly, the alteration and exchange of such features should allow for easy adjustment of the CAD model [21]. Furthermore does parameterisation allow for a variation of geometry model's dimensions [22].

While parameterised, feature-based CAD models are theoretically easily altered, in practice the alteration of is difficult. A lack of consistent modelling practices, the complexity of relations in a master model and ambiguous feature definitions make CAD models difficult to edit and lead to failures in their regeneration [20,21,23]. Furthermore is parameterisation considered "a big challenge", and even in the best case "offers little flexibility", since the parameterisation of the master model already defines all possible concepts and does not allow for the introduction of novel solutions [24].

To avoid such failures, CAD models are build following design guidelines. While the composition of a CAD model's structure represents the model's design intent, this does rarely coincide with the product's design rationale (DR). Hence are changes to the product, which are based on the introduction of new functions or new solutions for identified functions, difficult, since the CAD model does not contain any of this teleological information [14,15].

Function models on the other hand can represent a product's DR, together with architectural or systemic product properties. As such, they provide a good basis for teleologically motivated DSE: through the representation of functions and solutions, developers can precisely target their design effort [25]. Furthermore can function models be used for systemic analysis [26], automated DSE and concept generation [27,28] or product platforms [25,29]. However, while in some cases enabling "physics-based reasoning" [30], function models do not provide a basis for most engineering analysis, where product geometry models are needed. Connecting the two modelling domains of function and geometry has been a long standing challenge in engineering design research (EDR) [14,15,31].

enhanced function-means (EF-M) modelling is a function modelling approach which represents the design space through alternating functional requirement (FR) and design solution (DS) objects [32]. A DS can be subject to individual constraints, which place limits on design parameters or behaviour. The basic modelling elements of EF-M are presented in Figure 1. They create a hierarchical product architecture representation, which enables the introduction of novel solutions and sub-functions on arbitrary levels of granularity into an existing product structure [33].

Since EF-M follows the axiom of independence of Suh's axiomatic design [34], each FR is—in one concept—solved by only one DS. If there are more DS per FR modelled, these represent alternatives. This is illustrated in Figure 1 in the form of "Solution A" and "Solution B".

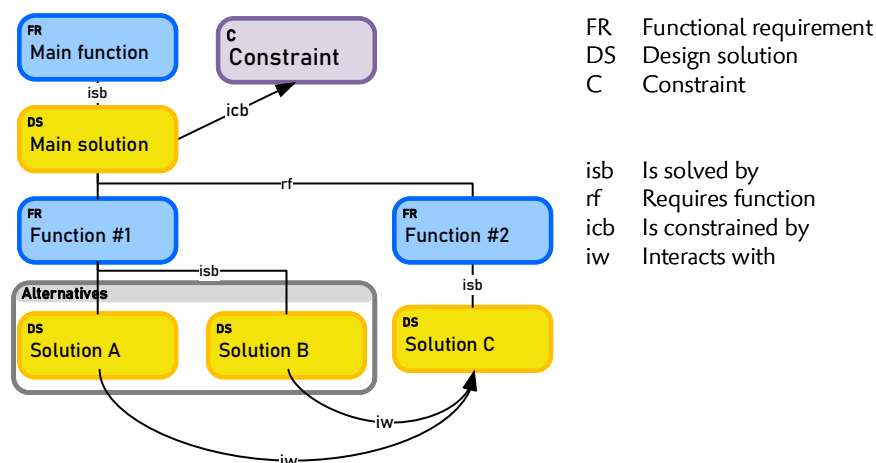


Figure 1. Enhanced Function-Means (EF-M) modelling elements after [32].

Since new DS are captured for different functions on individual branches of the EF-M tree, they can be combined into a multitude of different concepts. In the presented example in Figure 1, only two concepts can be instantiated, one with each alternative DS. In Figure 2 two times two alternatives become four concepts.

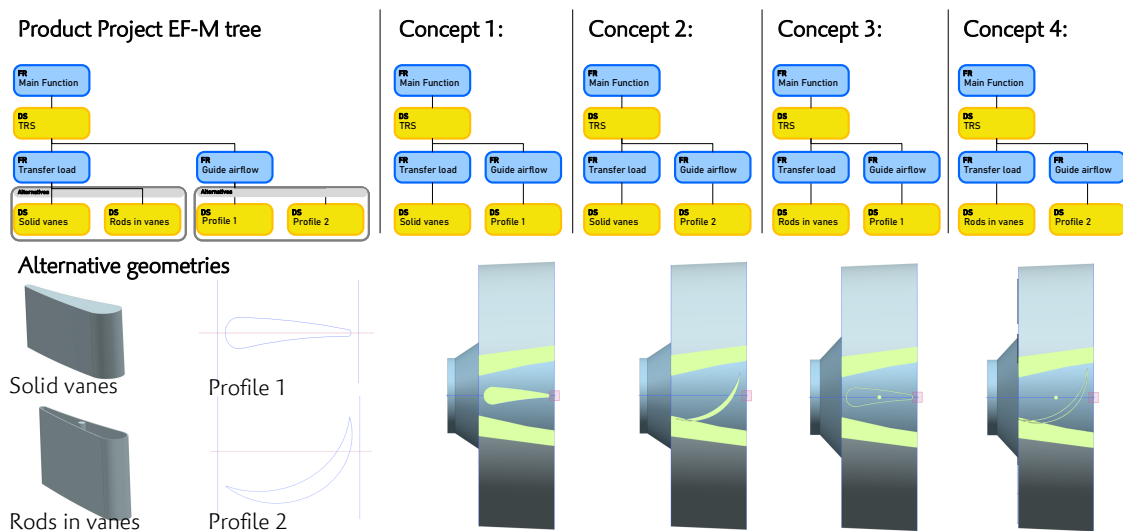


Figure 2. Instantiation in EF-M and the associated computer aided design (CAD) model. Left hand side shows the EF-M model with alternative design solutions (DS), and below the respectively associated user defined feature (UDF). To the right are the four resulting concept instances, on top in EF-M and their respective embodiment below. All models have been created using a proof-of-concept tool of Function and Geometry Exploration (FGE) [16].

2.1. The FGE Approach

The function and geometry exploration (FGE) approach combines the representation of product architecture and DR, and the flexibility to introduce novel solutions into an existing legacy design with a feature based CAD approach. The approach builds on the function modelling method EF-M and combines it with a design automation (DA) approach based on user defined features (UDFs). One main assumption behind the approach is that every geometrical element in a product has a specific function [35]. This function can be identified, and the related geometry can be isolated. As a result, these two information sets can be coupled. The other main assumption for the approach is that if the function of a geometry element is identified, alternative solutions for that function can be identified and integrated into the product architecture [25,36].

The FGE method is based on three main phases: decomposition of the legacy CAD model, an innovation stage in the functional domain and an embodiment phase to generate CAD models of the concepts. Figure 3 presents the steps inside these three main stages: the decomposition takes part in both the function- as well as geometry-model, whereas the geometrical modularisation is based on the structure of the EF-M model and the resulting UDF are directly linked to their respective DS. The innovation stage includes redesign, where novel functions and solutions are captured in the function model, embodiment of said solutions into UDF and the matching of their interfaces towards the existing product structure. Lastly, the different concepts are instantiated first from the function model and then embodied through the included assembly algorithm.

To represent the relations between function modelling objects and design features, the FGE approach relies on the object model for function and geometry (OMFG). This object model has been presented and verified in [16].

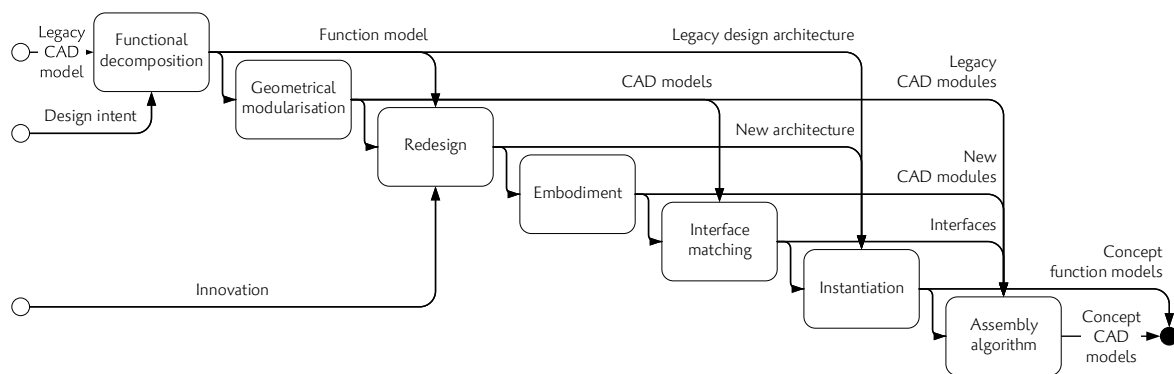


Figure 3. IDEF0 process model of the applied FGE approach.

The FGE approach assumes the existence of a legacy design in the form of a CAD model. In the first step the model is decomposed into an EF-M model, in a bottom-up approach where the functions of individual geometric elements are identified. Once the geometrical elements are captured as DS, they are linked to their function in the form of FR. Potential constraints are also captured in the EF-M model in relation to the respective DS. The decomposition of a legacy design into an EF-M model and the constraining of the design space in both the functional and geometrical domain is described in detail in [37]. Once they are associated to a DS, the geometrical features are captured in a UDF with clearly defined interfaces and design parameters. Both of these are captured in the OMFG and provide the basis for the DA of FGE.

Since UDF are available in most commercial CAD systems, these geometry modules can be generated and edited by CAD engineers with minimal additional training. Through the flexibility of UDF and the possibility to parameterise them, this enables a fine granular control of the geometry via the EF-M model [38]. The interfaces between the UDF—and therefor DS—are captured in the OMFG and represented in the EF-M model as interacts with (*iw*) connections.

Alternative concepts are instantiated from the alternative solutions captured in the EF-M model. The instantiation algorithm produces concepts as a combinatorial of all alternative DS, as is illustrated in Figure 2. The assembly algorithm based on architectural and geometrical data captured in the OMFG automatically generates the CAD models of all technically feasible concepts captured in the EF-M model.

This assembly algorithm, presented in as a UML diagram in Appendix A, Figure A1, iterates through all DS of a concept and tries to place the UDF into a part file. While the current implementation of the OMFG into a DA tool generates part files, the generation of assemblies is theoretically feasible using the same technologies and approaches. The individual UDF are attempted to be placed in an arbitrary order, and placed at the back of the queue if the requirements for placement (availability of interfaces and parameters) are not given. Only if all UDF have been placed, or all remaining UDF have failed to be placed, is the model returned. While this approach is computationally expensive, since it may require multiple placement attempts for even larger UDF, it provides a high flexibility and theoretical robustness against interface mismatches.

Following this approach, presented and verified in [16], the geometry not for each new concept has to be remodelled, but only for each new DS, which reduces the cost of introducing new product concepts based on a legacy design. This modularisation, including a precise interface capture and management through the FGE object model, allows for automated generation of the CAD models of all feasible concepts.

3. Materials and Methods

This study is conducted in tight collaboration with a Swedish aerospace manufacturer, and is centred around the design of a new part for turbofan engines, a guide vane (GV). The part is located in the bypass of the turbofan engine, positioned just behind the fan, as shown in Figure 4. The set of all

GV has the main function to deswirl the airflow from the main rotor, thereby reducing aerodynamic losses. Furthermore, the vane has a structural function in that it connects the shroud of the bypass to the engine core, thereby creating a load path for the turbine mass to the pylon. Furthermore, the part has to withstand axial loads from the engine thrust.

For the GV being a relatively large component, it is necessary to find low weight designs. As a result, low-weight designs are given high priorities by the design team. This can be achieved by the introduction of new manufacturing and material options. The common manufacturing and material choice is a metallic core structure [39]. Alternative options are composites or combined solutions.

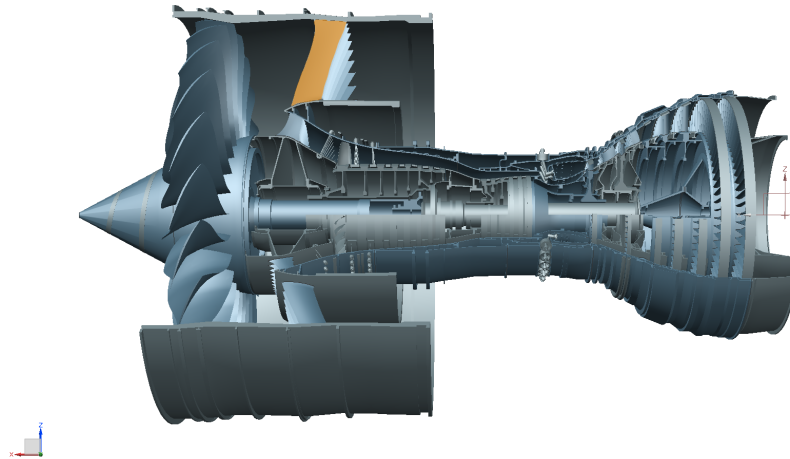


Figure 4. A Rolls Royce Trent 900 engine rendered in CAD with one GV highlighted in orange (CAD model by Chris Shakal on grabcad.com).

A GV commonly consists of a vane structure, a predominantly aerodynamically defined structure, and two end attachments which fasten the vane to the engine core on the inside, and the outer fan case on the outside, as can be seen in Figures 4 and 5. Both parts provide interfaces the GV assembly has to comply to.

The development team is composed of both design and analysis engineers with experience in aerospace engineering ranging from five to thirty years. These engineers partake in the development in defined percentage of their work-time, between 10% and 70%.

It is important to mention that the company is using and developing KBE techniques with a high degree of DA for design space exploration. This means that the engineers possess a benchmark system for comparison with the FGE. The benchmark system can be compared in make-up and extend to the parameterisation-based multi-disciplinary analysis (MDA) framework presented in [40].

Study Setup

The research has been performed as a participatory action research study, where the researchers accompany the development process investigating into new opportunities for a fan frame GV [41]. The researchers participated in regular team meetings together with the design team, and had the ability to observe the engineers during their work. Notes from these meetings and observations are part of the data supporting the presented results.

Beyond the observation throughout the product development project, a set of studies has been conducted to investigate the perception of the presented method. For the specific purpose of validating the FGE method and tool, two consecutive workshops were organised together with the design team.

In a first workshop together with the GV development team (eight participants), a functional decomposition of the part was performed and captured. Hence, this workshop is referred to as the “decomposition workshop”. The actual workshop was predated with a one hour long test-workshop in one of the regular team meetings to evaluate the motivation of the practitioners and the requirements

for the actual workshop. The results of this “test-workshop” are included in the results of the decomposition workshop. The decomposition was performed using large-scale print-outs of drawings a GV which were annotated in a group exercise. The annotated drawings were collected, digitised and used for the creation of function-geometry model in FGE for the legacy design.

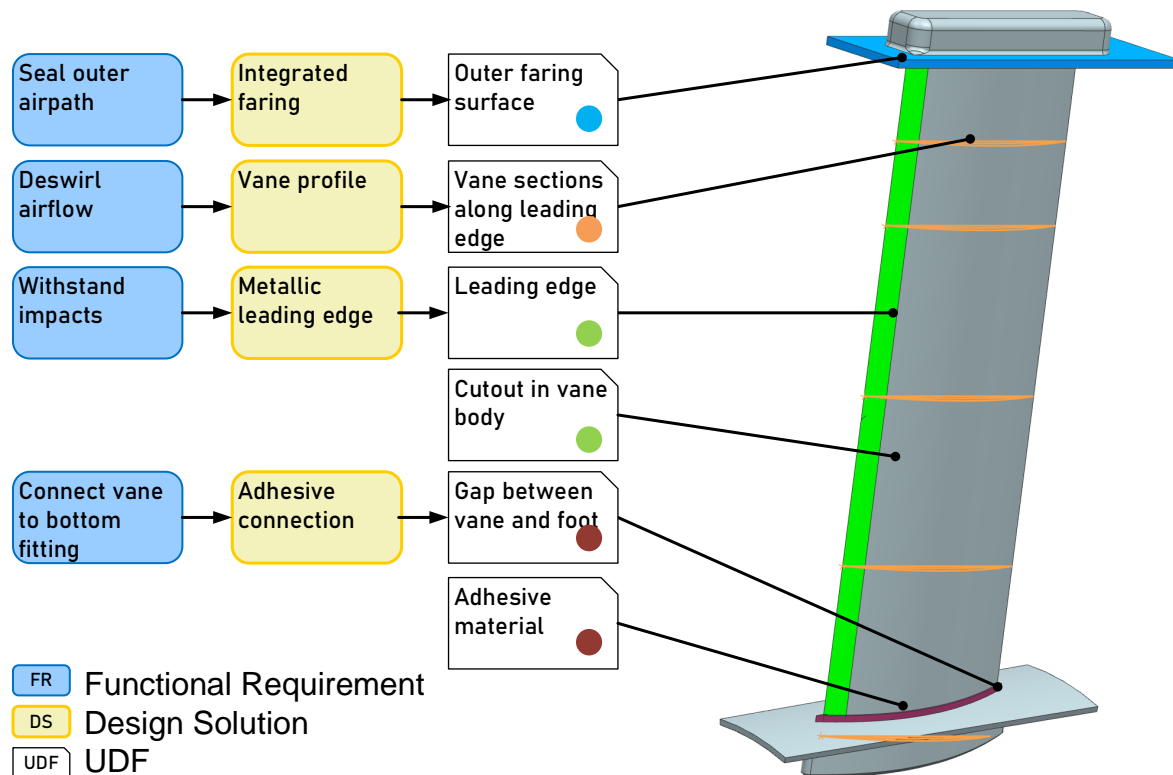


Figure 5. Example of function and design solutions of a guide vane (GV), connected to geometry elements as UDF. The different geometry elements are colour coded to show the extend of the UDF.

A second workshop (eight participants) covered the innovation stage of the FGE approach. The workshop was held with the same development team, using the same product. The workshop was held online due to the social distancing regulations in response to the COVID-19 pandemic.

For the second workshop, a proof-of-concept tool of the FGE approach was created. The tool works server-based with a web interface (illustrated in Figure 6), allowing users with different skill levels and operating systems to connect to the same database. The tool incorporates a fully functional implementation of an EF-M modeller with additional functionality to capture geometric information for each DS. As such, it is able to capture alternative design solutions and instantiate them into different concepts. Furthermore, the tool includes a geometrical modelling algorithm to automatically generate CAD models of each concept, based on previous geometrical modularisation in Siemens NX. The structure and mechanics of the tool are illustrated in [16].

After each workshop, the practitioners were asked for their experiences through questionnaires and open feedback discussions. The results of the first workshop were recorded through adhesive notes and remarks on the drawings, as well as protocol notes. The results of the online workshop were captured through audio and video recording and through a change protocol in the database of the FGE tool.

For this publication, a generic design of a GV was created, which differs from the design used in the workshops. However, the generic design has a sufficient degree of realism to enable dialogue, but with company specific features left out.

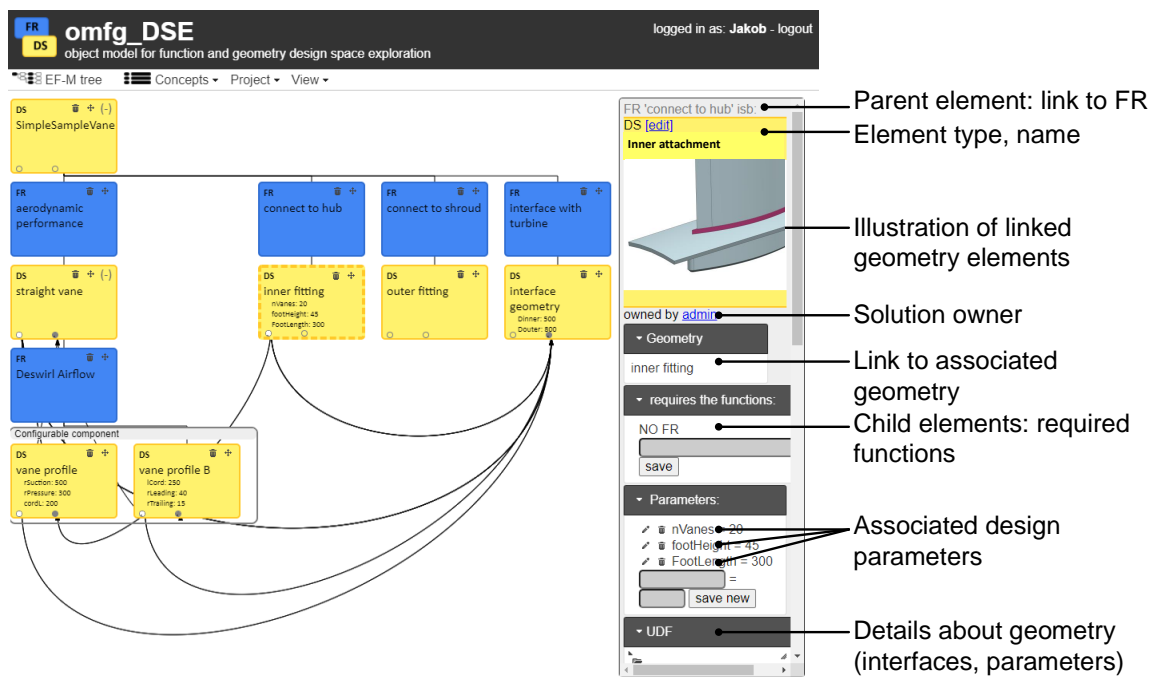


Figure 6. Web-based interface of the FGE tool “omfgDSE” (object model for function and geometry based design space exploration), showing a simplified EF-M model of a GV. The right-hand pane illustrates the design rationale of the selected DS, such as associated function, geometry and parameters.

4. Results

This section presents the results of the application of FGE in the industrial context as well as the practitioners feedback and observations.

4.1. Design Space Exploration Using FGE

The DSE approach is separated into three phases decomposition, innovation and embodiment, following [36]. The presented workshop focuses on the interactions with practitioners in the phases decomposition and innovation.

In the first workshop (decomposition), the legacy design of the GV was captured in an EF-M model based on the available geometry. The model contains three main functions, and 18 different design solutions on the concrete (lowest) level. Since the model was created through decomposition, all DSs are directly linked to one or several geometry elements. A modularised CAD model was created based on the original geometry, modularised according to the decomposition.

Figure 5 exemplary shows this modularisation and connection for four individual DSs and the related UDFs. For example, the leading edge of the decomposed GV is covered by a metallic edge. This metallic edge, as a geometrical element, has been associated with the function “Withstand impacts” through the solution “Metallic edge”. The respective geometry, of both the edge insert and the cutout in the vane to place it in, are captured as two UDFs which are then associated with the DSs.

This decomposition served as input for the following workshop, focused on innovation.

In the second workshop (innovation) the prototype tool was used to capture novel design solutions. As a result, the product model was extended by five new sub-functions with their respective solutions and 10 new alternative DSs. As an example for new FR, sub-functions related to acoustic performance were added to the model. The nature of the DSs ranged from material alternatives over different interface approaches to variations in shape and dimensions of the existing solutions. The entire EF-M tree, with all new FR and DS highlighted with red borders, is shown in Figure 7a. Based on the new alternative DSs, 52 different concepts could be instantiated.

The majority of the novel solutions shows a conceptual difference from the legacy design. As an example, the FR “Join vane to attachment” is in the legacy design solved by the DS “Adhesive connection”, meaning that the vane is glued to the attachment using resin. This DS, and the respective UDF, are illustrated in Figure 5. The two alternative DSs, as results from the workshop, were “Bolted joint” and “Fully integrated solution”. The respective DS are shown in Figure 7b, whereas the geometry related to these DSs is shown in the context of the GV in Figure 8.

The embodiment phase of the FGE approach has not been performed in its entirety, since the DA section of the proof-of-concept tool has not sufficiently matured to handle the complex geometries of the solutions devised in the innovation workshop. For a verification of the proof-of-concept tool on another turbine structure, see [16].

Figure 8 shows an exemplary embodiment of three concepts with alternative DSs for the FR “Join vane to attachment” shown in Figure 7b. While otherwise using the same configuration, each of the geometries is adapted to accommodate the respective geometric changes in the concept. The instantiation and assembly algorithms embedded in the FGE model allow for automated generation of the CAD models of all feasible concepts.

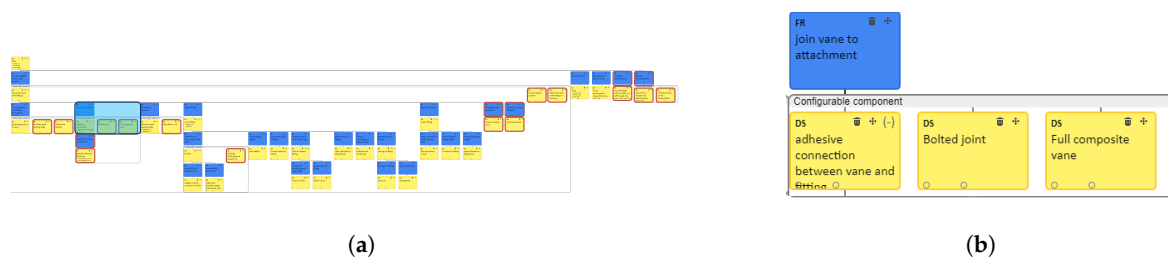


Figure 7. EF-M model after the innovation workshop. (a) Full EF-M tree, with all new DS and functional requirement (FR) highlighted with a red border. Readability has been dismissed on purpose to protect company intellectual property (IP). (b) Detail: alternative solutions for DS “Join vane to attachment”, highlighted in blue in (a).

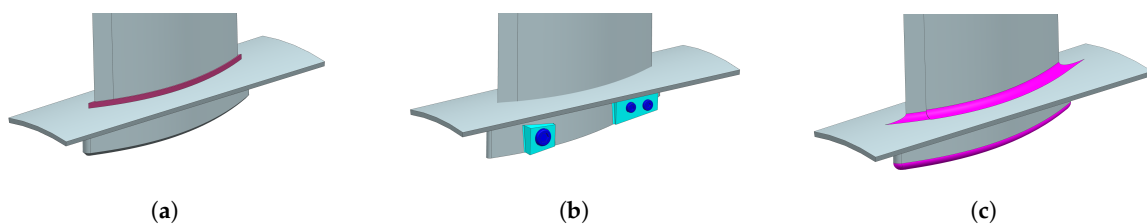


Figure 8. Embodiment of three concepts, differentiating in the solutions for the FR “Join vane to attachment”, from left: (a) “Adhesive connection”, (b) “Bolted joint” and (c) “Fully integrated solution”. Respective alternative geometric elements relating to the respective user defined feature (UDF) are highlighted in colour.

The following section reports on the practitioners’ feedback and reflections after the application of the method on their industrial use case.

4.2. Reflections From Industrial Practitioners Regarding the Application of the Method

The practitioners have stated that the workshops—as activities in addition to their regular design activities—contribute to the development project. Furthermore, all workshop participants would like to repeat the workshop concept, both in the same, but even more so in other projects. The following sections will go through the main mechanisms that have been highlighted by the industrial practitioners, in particular the ability of the approach to:

1. Represent and capture design rationale and the design space
2. Capture, integrate and model novel solutions
3. Provide support for the embodiment of novel concepts that would otherwise remain unexplored

4.2.1. Capture and Representation of Design Rationale and Design Space

“I learned a lot of things about the GV just by reading the graph.”

—aerodynamics analysis engineer

This quote illustrates a common problem during the design of aerospace products. As components are designed and conceptualised over long times, and by heterogeneous teams, it is difficult to retain the design rationale (DR) of a product (that is, why a product has been designed in this form) [42]. This DR is especially hard to read in highly integrated and complex products such as aerospace engine components, where a single geometrical artefact may fulfil multiple functions in different domains [43]. For practitioners, the FGE approach supports the ability to visualise the rationale in both the geometrical domain, visualising “what is”, and the functional domain, “why it is”.

In terms of the use of FGE, it appears to be a major benefit of FGE for the practitioners that they improved their knowledge about the product and participated in a forum that permitted exchange about the product’s functions and solutions. The questionnaire accompanying the workshop revealed that no team member had full confidence about the GV, but most rated their understanding of the GV higher after the workshop than before. The workshop also fostered the awareness of meta-product-knowledge, since many engineers were not even aware who knew the rationale behind a specific element. Only through discussions and participation of engineers of multiple disciplines could the entire DR be captured in the EF-M model.

An example for how FGE enables access to DR is the interface of the tool used in the study, which collects all information of a solution in a single place. Figure 6 shows on the right hand side how the geometry, parameterisation and other information about a solution is collected in a single window pane. The top of the pane shows which function is solved, and the highlighting of the solution shows its position in the product architecture.

Furthermore, the approach can illustrate the geometrical interfaces between solutions through iw connectors in the EF-M model. This are seen as black arcs in the interface of Figure 6, left hand side. This approach of information representation was referred to as “comprehensive” by the workshop participants.

Beyond the information about individual solutions, the FGE interface provides an overview over the possible alternatives through EF-M. This was perceived to be an efficient way to represent the design space, providing “good possibilities to look at different solutions”. However, it was also noted by one participant in the workshop that the function models can quickly grow to be too complex. The function model created in this study (see Figure 7a) was considered “almost too large”.

4.2.2. Ability to Capture, Integrate and Model Novel Solutions

“Parametric solutions exist but limited to parameters that we easily can change, dimensions, angles or thicknesses for example. When it comes to exploring different design solutions in early phases we foresee larger challenges.”

—development team leader

This quote stands exemplary for the practitioners’ reflections over the in-house KBE system for DSE adopted by the company, which is built around state of the art KBE approaches. However, the practitioners are well aware about the limitations of highly automated CAD approaches in representing conceptually different design solutions. While the exploration of dimensional variety is possible and appreciated by the practitioners, the need to realise topologically and geometrically different options has been stated explicitly. This matches with observations from literature, where it is stated that “a parametric model offers little flexibility” [44].

According to the practitioners, FGE has the potential to deliver this through the modularisation of the geometry, and the connection to the DR of the product.

It was perceived by the participants of the workshop that the use of the FGE approach supports the introduction of new solutions (4 on a scale of 1 “no support for new solutions” to 5 “totally supports”). It was furthermore stated that part of the identified DS would probably not have been found—or considered—in a regular modelling approach, with a majority (71%) stating “maybe some, but not all”. The other participants stated either “none of them” or “most of them” would have been identified without FGE.

Beyond only exploring new solutions for existing functions, FGE also enables the capture of newly identified functions or sub-functions. The workshop results showed that through five new functions being identified during the innovation workshop. Practitioners feedback further supported this, although the ability to integrate new solutions is perceived to be more important than that of new functions.

To summarise this, the practitioners perceive FGE as a viable method to capture novel solutions and functions. Having a formal, and even computer supported, modelling approach at hand when generating conceptual alternatives directly in creative design meetings was found very applicable.

4.2.3. Support for the Embodiment of Novel Concepts

“There are still gaps within early concept phase—this is one possibility to generate, and evaluate, lots of concepts, get trend curves and so on.”

—design engineer

As has been stated in the section above, there is a substantial need for a DSE modelling approach to capture geometrically and topologically different DS. The practitioners agree that FGE is an approach which can support such exploration.

However, the sole representation of alternative concepts in function models would be insufficient. To enable the necessary analyses, geometry models in the form of CAD are required.

The practitioners stated that the CAD models needed for effective DSE need to be of sufficient quality to be meshed automatically. This requires certain quality criteria such as surface continuity. Furthermore would the CAD models require automated “tagging” of relevant geometry elements for analyses, for example where forces attack or constraints apply.

After a demonstration of the assembly algorithm of FGE and the geometry modularisation, the practitioners agreed that such an approach can deliver the required models. Therefore, the ability to generate topologically different variant concepts was seen as a benefit of the presented method:

“Generation of CAD models based on different configurations is a key functionality.”

—development team leader

4.2.4. Implementation Challenges

Despite the interest in the approach, the practitioners pointed out certain implementation challenges.

As a feedback to the modelling process, using EF-M to capture and represent alternative solutions, a practitioner mentioned that the re-use of existing solution's geometry for another function is hardly possible to model using EF-M. Although there exist horizontal relations in EF-M modelling, they increase the modelling complexity and reduce readability. Therefore, such complex relationship modelling has not been implemented yet in the prototype tool, and does not contribute to alleviate the challenges of complexity in function modelling stated by [31,33].

The ratio of complexity between the functional domain and geometrical domain was point for critique. It was stated that a large function model (such as the one in the workshop became through the innovation) reduces the overview over the model. It was suggested to use less FR/DR elements and more, but potentially more complex, geometric modules. However, the experience with function modelling and/or web-based applications may play a role in how difficult the tool use was perceived.

While FGE supports the exploration of technically, functionally and topologically different solutions, the in-house KBE solution is optimised for parametric variation. Being used to the already existing MDA method at the company, the practitioners rather viewed an implementation of FGE as a complement, preferably integrated with the existing system.

5. Discussion

The FGE approach aims to support DSE in the conceptual product development phases through a three-phase approach, namely decomposition, innovation and embodiment. The approach relies on the OMFG, which provides a connection between the previously divided modelling domains of function and geometry. As a result, novel solutions can be integrated into an existing legacy design, and be embodied based on information stored in the function model. This information, the DR of the product, is the driving force behind the implemented DA approach. The coupling of the function and geometric modelling domain, and the resulting opportunities for DSE, distinguish the approach from other DA approaches and CAD model parameterisation. The approach has been evaluated in a case study with a product development team of an aerospace manufacturer.

The practitioners gave an overall positive feedback about the approach, stating that FGE—or a similar approach—can provide what is needed to improve current product development practice. The need was stated to be about capturing and presenting alternative solutions in a systematic way, as well as an automated generation of CAD models ready for analysis. The use of a non-geometrical modelling approach representing teleological product knowledge, “how it all connects”, has been received positively by the practitioners. This is in line with authors such as [8,14,15] who call for models for DSE to carry information beyond the geometrical domain.

While the results of this study can be interpreted as generally positive for the presented FGE method in terms of user acceptance and improved DSE, it is only a single case study, and hence difficult to generalise from [45]. While the engineering design research community is aware of the challenge to properly validate a new method or methodology [46,47], this study can only be an initial step into validating FGE. Similar studies with other development teams, and in other engineering domains, are required before a conclusive image of the contribution of FGE to DSE can be presented.

Practitioner feedback has shown challenges of understanding the instantiation, EF-M and CAD integration of the approach. In general, from the observations throughout the workshops, did the time to understand and learn the new approach take up a large part of the workshops' time. Hence, the studies results and conclusions are influenced by the novelty of the tool and method for the practitioners. This can be a factor in the enthusiasm and positive feedback for the method, in a variant of the “Hawthorne-effect” [48]. However, it could also be argued that the method can only show its full contribution once the practitioners have grown familiar with it. Which of these two factors predominates cannot be said at this moment.

Many participants highlighted the contribution of the method for knowledge capture and exchange inside the group. Although this is not among the primary objectives of the FGE method, the capture, representation and retrieval of design rationale is beneficial to the product development process [49]. However, it can be argued that not the use of this specific method, but the general interaction of engineers of different disciplines focused on a shared product could provide this [50].

The registered numbers for captured novel design solutions, concepts and functions have been identified by the participants in the study as subjectively higher than without the method. However, to be able to judge a significant impact of the use of method on the quantity—or quality—of the generated design concepts, further and especially more longitudinal studies are required [45]. The presented FGE approach for DSE relies heavily on a DA implementation for the assembly of individual concepts' CAD models. This approach has been presented in detail in [16]. The practitioners in the study have already voiced concerns about the robustness of the DA approach and the quality of the resulting CAD models for meshing and FEM. Similar to other DA approaches and parameterisation, FGE is sensitive to modelling errors, ambiguously defined datums or over-constrained models [20,21,23]. The definite sensitivity to modelling errors has to be evaluated in further studies.

However, the actual contribution of the FGE approach lies not in the DA implementation, which in similar fashion can be found in existing feature-based design approaches [51]. More than providing a feature-based geometry approach does FGE provide a function-based approach to geometry modelling. A change in product function—or change of a solution—directly impacts the CAD model. The underlying OMFG provides a direct link between the two domains, and therefore enables a DSE approach which is guided by “the most important concept in determining a product's basic characteristics”: function [14].

6. Conclusions

FGE is a novel DSE approach which has been presented in [16]. While this previous presentation has presented the technical workings of the approach and verified the DA algorithm, the approach as a method in EDR has to be validated through application in an industrial context.

This paper presented the application of a DSE approach combining function modelling and automated geometry model generation for the conceptual product development phases of turbofan engines. The modelling approach tackles the challenges of representing alternative concepts in the design space, design rationale capture and storage as well as support for the generation of CAD models. Through the application of the FGE approach in an engineering case, the method has been validated to target a real problem in the conceptual development of aerospace engine components and to provide a feasible solution for it.

Through the use of a prototype tool implementing the FGE method, engineers in a aerospace supplier were able to share product knowledge and explore novel design solutions. This has led to both, a perceived increased knowledge about the developed product inside the development team, as well as the opportunity to explore previously unconsidered design solutions. According to the statements of the product developers participating in this study, this leads to more and more novel functions and solutions being explored.

The FGE approach uses function modelling as a tool to represent the design space and perform its population. While this has shown to be feasible, domain specific challenges similar to as reported for example in [31] have shown. This points towards further development for EF-M modelling in order to increase applicability and reduce abstraction. Furthermore did practitioners point out the problems of modelling a “make use of” relationship for a DS, as described in Section 4.2. Similar challenges have already been identified in [33] and pointed towards further development of the EF-M approach.

The presented prototype tool has shown to efficiently provide an interface for collaborative DSE. To a degree it has reduced the abstraction of function modelling by providing a connection to tangible geometry. However, further studies with increased practitioner training are seen as a goal for future

work. While the embodiment process has been illustrated in [16], further studies have to show the scalability of it. In particular, the quality of the generated CAD models—with a focus on meshing—has to be in the focus of development, since in the presented study it has been highlighted that it is crucial for analysis of the concepts.

In summary, while there have been identified areas for improvement, the FGE approach was perceived to be “one possibility to generate, and evaluate, lots of concepts”—which is what it aims for.

Author Contributions: Conceptualisation: J.R.M., M.P. and O.I.; formal analysis, writing—original draft preparation, visualisation: J.R.M. and M.P.; methodology, software, validation, investigation: J.R.M.; writing—review and editing, supervision: M.P. and O.I.; project administration, funding acquisition: O.I. All authors have read and agreed to the published version of the manuscript.

Funding: This work was funded by the Swedish Research Agency VINNOVA through the Swedish National Aeronautics Research Programme (NFFP) in the project MEPHISTO, grant number 2017-04858, and executed in collaboration with GKN Aerospace.

Acknowledgments: The study presented in this publication has been performed in collaboration with GKN Aerospace Engine Systems Sweden.

Conflicts of Interest: The authors declare no conflict of interest.

Abbreviations

The following abbreviations are used in this manuscript:

CAD	computer aided design
DA	design automation
DR	design rationale
DS	design solution
DSE	design space exploration
EDR	engineering design research
EF-M	enhanced function-means
FGE	function and geometry exploration
FR	functional requirement
GV	guide vane
iw	interacts with
KBE	knowledge-based engineering
MDA	multi-disciplinary analysis
OMFG	object model for function and geometry
UDF	user defined feature

Appendix A. UML Process Model of FGE Assembly Algorithm

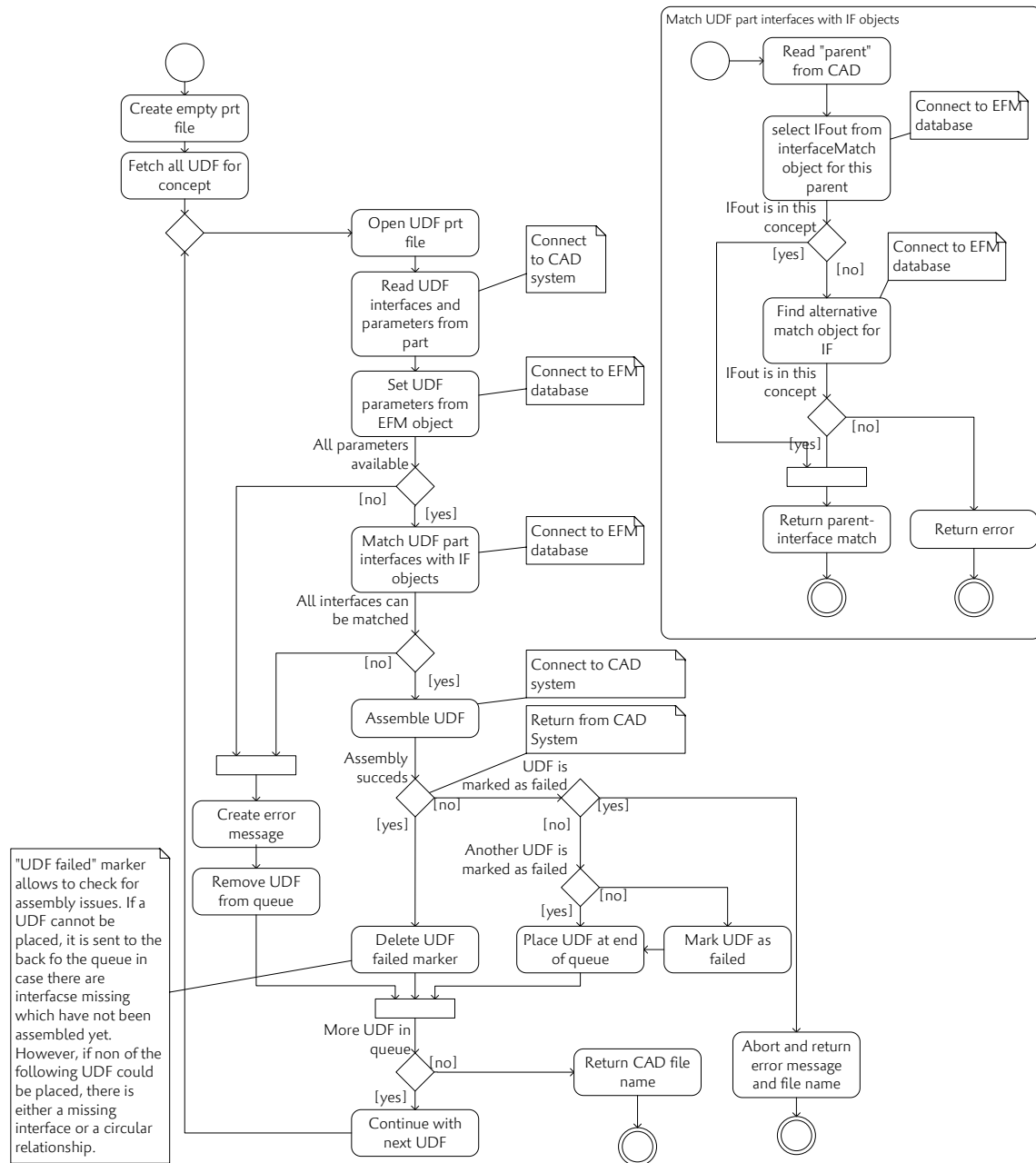


Figure A1. UML process model of the assembly algorithm as implemented in the FGE proof of concept tool.

References

1. Advisory Council for Aviation Research and Innovation in Europe (ACARE). *Strategic Research and Innovation Agenda*; Technical Report; Advisory Council for Aviation Research and Innovation in Europe; European Union: Brussels, Belgium, 2017. Available online: <https://www.acare4europe.org/sites/acare4europe.org/files/document/ACARE-Strategic-Research-Innovation-Volume-1.pdf> (accessed on 31 October 2020).
2. Schmidt, J.; Gelle, M. Commercial Aerospace Insight Report 2020. accenture. 2020. Available online: <https://www.accenture.com/us-en/insights/aerospace-defense/commercial-aerospace-report-lead-in-the-new> (accessed on 31 October 2020).

3. Filipenko, M.; Biser, S.; Boll, M.; Corduan, M.; Noe, M.; Rostek, P. Comparative analysis and optimization of technical and weight parameters of turbo-electric propulsion systems. *Aerospace* **2020**, *7*, 107. [[CrossRef](#)]
4. Parker, R.; Lathoud, M. Green aero-engines: Technology to mitigate aviation impact on environment. *Proc. Inst. Mech. Eng. Part C J. Mech. Eng. Sci.* **2010**, *224*, 529–538. [[CrossRef](#)]
5. Larsson, B.; Sundqvist, J.; Emmitt, S. Component manufacturers' perceptions of managing innovation. *Build. Res. Inf.* **2006**, *34*, 552–564. [[CrossRef](#)]
6. Dale, E.; Jorns, B.; Gallimore, A. Future Directions for Electric Propulsion Research. *Aerospace* **2020**, *7*, 120. [[CrossRef](#)]
7. Hirz, M.; Dietrich, A.W.; Gfrerrer, A.; Lang, J. *Integrated Computer-Aided Design in Automotive Development: Development Processes, Geometric Fundamentals, Methods of CAD, Knowledge-Based Engineering Data Management*; Springer: Berlin, Germany, 2013. [[CrossRef](#)]
8. Woodbury, R.F.; Burrow, A.L. Whither design space? *Artif. Intell. Eng. Des. Anal. Manuf. AIEDAM* **2006**, *20*, 63–82. [[CrossRef](#)]
9. Kang, E.; Jackson, E.K.; Schulte, W. An Approach for Effective Design Space Exploration. In *Foundations of Computer Software: Modeling, Development, and Verification of Adaptive Systems, Proceedings of the 16th Monterey Workshop 2010, Redmond, WA, USA, 31 March–2 April 2010*; Revised Selected Papers; Springer: Berlin, Germany, 2011; pp. 33–54. [[CrossRef](#)]
10. Isaksson, O. A Collaborative Engineering Design Research Model—An Aerospace Manufacturers View. In *Impact of Design Research on Industrial Practice*; Springer International Publishing: Cham, Switzerland, 2016; pp. 363–381. [[CrossRef](#)]
11. Van Der Laan, A.H.; Van Tooren, M.J. Parametric Modeling of Movables for Structural Analysis. *J. Aircr.* **2005**, *42*, 1605–1613. [[CrossRef](#)]
12. Sandberg, M.; Tyapin, I.; Kokkolaras, M.; Isaksson, O.; Aidanpää, J.O.; Larsson, T. A Knowledge-based master-model approach with application to rotating machinery design. *Concurr. Eng. Res. Appl.* **2011**, *19*, 295–305. [[CrossRef](#)]
13. Müller, J.R.; Panarotto, M.; Isaksson, O. Connecting functional and geometrical representations to support the evaluation of design alternatives for aerospace components. In Proceedings of the 22nd International Conference on Engineering Design (ICED19), Delft, The Netherlands, 5–8 August 2019; pp. 1423–1432. [[CrossRef](#)]
14. Umeda, Y.Y.; Tomiyama, T. Functional reasoning in design. *IEEE Expert Intell. Syst. Their Appl.* **1997**, *12*, 42–48. [[CrossRef](#)]
15. Cohrs, M.; Klimke, S.; Zachmann, G. Streamlining Function-oriented Development by Consistent Integration of Automotive Function Architectures with CAD Models. *Comput. Aided Des. Appl.* **2014**, *11*, 399–410. [[CrossRef](#)]
16. Müller, J.R.; Panarotto, M.; Isaksson, O. Function Model Based Generation of CAD Model Variants. *Comput. Aided Des. Appl.* **2020**, forthcoming.
17. Pedersen, K.; Bailey, R.; Allen, J.K.; Mistree, F. Validating Design Methods & Research: The Validation Square. In Proceedings of the ASME Design Engineering Technical Conferences, Baltimore, MD, USA, 10–14 September 2000; pp. 1–12. [[CrossRef](#)]
18. Eckert, C.M.; Clarkon, P.J.; Stacey, M.K. The Spiral of Applied Research: A Methodological View on Integrated Design Research. In Proceedings of the ICED03: 14th International Conference on Engineering Design, Stockholm, Sweden, 19–21 August 2003.
19. Saxena, T.; Karsai, G. Towards a generic design space exploration framework. In Proceedings of the 10th IEEE International Conference on Computer and Information Technology (CIT-2010), Bradford, UK, 29 June–1 July 2010; pp. 1940–1947. [[CrossRef](#)]
20. González-Lluch, C.; Company, P.; Contero, M.; Camba, J.D.; Plumed, R. A survey on 3D CAD model quality assurance and testing tools. *CAD Comput. Aided Des.* **2017**, *83*, 64–79. [[CrossRef](#)]
21. Camba, J.D.; Contero, M.; Company, P.; Hartman, N. The cost of change in parametric modeling: A roadmap. *Comput. Aided Des. Appl.* **2021**, *18*, 634–643. [[CrossRef](#)]
22. Camba, J.D.; Contero, M.; Company, P. Parametric CAD modeling: An analysis of strategies for design reusability. *Comput. Aided Des.* **2016**, *74*, 18–31. [[CrossRef](#)]
23. Kasik, D.J.; Buxton, W.; Ferguson, D.R. Ten cad challenges. *IEEE Comput. Graph. Appl.* **2005**, *25*, 81–92. [[CrossRef](#)]

24. Li, H.; Brockmöller, T.; Gembariski, P.C.; Lachmayer, R. An Investigation of a Generative Parametric Design Approach for a Robust Solution Development. In *Proceedings of the Design Society: DESIGN Conference*; Cambridge University Press: Cambridge, MA, USA, 2020; Volume 1, pp. 315–324. [[CrossRef](#)]
25. Levandowski, C.E.; Raudberget, D.; Johannesson, H. Set-Based Concurrent Engineering for early phases in platform development. In *Proceedings of the 21st International Conference on Concurrent Engineering (CE 2014)*, Beijing, China, 8–11 September 2014; Cha, J., Chou, S.Y., Stjepandić, J., Curran, R., Xu, W., Eds.; pp. 564–576. [[CrossRef](#)]
26. Albers, A.; Sadowski, E. The Contact and Channel Approach (C&C2-A): Relating a system's physical structure to its functionality. In *An Anthology of Theories and Models of Design*; Chakrabarti, A., Blessing, L.T.M., Eds.; Springer: London, UK, 2014. [[CrossRef](#)]
27. Helms, B.; Shea, K. Computational Synthesis of Product Architectures Based on Object-Oriented Graph Grammars. *J. Mech. Des.* **2012**, *134*, 021008. [[CrossRef](#)]
28. Jin, Y.; Li, W. Design Concept Generation: A Hierarchical Coevolutionary Approach. *J. Mech. Des.* **2007**, *129*, 1012. [[CrossRef](#)]
29. Landahl, J.; Johannesson, H. Product Variety and Variety in Production. In *Proceedings of the International Design Conference (Design 2018)*, Dubrovnik, Croatia, 21–24 May 2018; pp. 817–828.
30. Mokhtarian, H.; Coatanéa, E.; Paris, H. Function modeling combined with physics-based reasoning for assessing design options and supporting innovative ideation. *Artif. Intell. Eng. Des. Anal. Manuf. AIEDAM* **2017**, *31*. [[CrossRef](#)]
31. Tomiyama, T.; Van Beek, T.J.; Cabrera, A.A.A.; Komoto, H.; D'Amelio, V. Making function modeling practically usable. *Artif. Intell. Eng. Des. Anal. Manuf. AIEDAM* **2013**, *27*, 301–309. [[CrossRef](#)]
32. Schachinger, P.; Johannesson, H. Computer modelling of design specifications. *J. Eng. Des.* **2000**, *11*, 317–329. [[CrossRef](#)]
33. Müller, J.R.; Siiskonen, M.; Malmqvist, J. Lessons Learned from the Application of a Function-Means Modelling Method. In *Proceedings of the Design Society: DESIGN Conference*; Cambridge University Press: Cambridge, MA, USA, 2020; pp. 1325–1334. [[CrossRef](#)]
34. Suh, N.P. *The Principles of Design*; Oxford University Press: New York, NY, USA, 1990.
35. Gero, J.S.; Kannengiesser, U. The situated function-behaviour-structure framework. *Des. Stud.* **2004**, *25*, 373–391. [[CrossRef](#)]
36. Müller, J.R.; Isaksson, O.; Landahl, J.; Raja, V.; Panarotto, M.; Levandowski, C.E.; Raudberget, D.S. Enhanced function-means modeling supporting design space exploration. *Artif. Intell. Eng. Des. Manuf.* **2019**, *1*, 502–516. [[CrossRef](#)]
37. Müller, J.R.; Borgue, O.; Panarotto, M.; Isaksson, O. Mapping the design space in function and geometry models supporting re-design for additive manufacturing. *J. Des. Res.* **2020**, forthcoming.
38. King, L. *Benefits of Using User-Defined Features to Generate Preliminary Geometry*; Technical Report; Rolls Royce plc: London, UK, 2017.
39. Sjunnesson, A.; Rikemanson, D.; Reimers, R.; Concepts, A. Feasibility of Light Weight Composite Fan Outlet Guide Vanes for Large Turbofan Engines. In *Proceedings of the International Society for Air Breathing Engines (ISABE 2019)*, Canberra, Australia, 22–27 September 2019; pp. 1–12.
40. Sandberg, M.; Tyapin, I.; Kokkolaras, M.; Lundbladh, A.; Isaksson, O. A knowledge-based master model approach exemplified with jet engine structural design. *Comput. Ind.* **2017**, *85*, 31–38. [[CrossRef](#)]
41. Yin, R.K. Case Study Reserach - Design and Methods. *Clin. Res.* **2006**, *2*, 8–13. [[CrossRef](#)]
42. Bracewell, R.; Wallace, K.; Moss, M.; Knott, D. Capturing design rationale. *CAD Comput. Aided Des.* **2009**, *41*, 173–186. [[CrossRef](#)]
43. Raja, V.; Kokkolaras, M.; Isaksson, O. A simulation-assisted complexity metric for design optimization of integrated architecture aero-engine structures. *Struct. Multidiscip. Optim.* **2019**, *60*, 287–300. [[CrossRef](#)]
44. Li, T.; Lockett, H.; Lawson, C. Using requirement-functional-logical-physical models to support early assembly process planning for complex aircraft systems integration. *J. Manuf. Syst.* **2020**, *54*, 242–257. [[CrossRef](#)]
45. Blessing, L.T.M.; Chakrabarti, A. *DRM, a Design Research Methodology*; Springer: Berlin, Germany, 2009.
46. Barth, A.; Caillaud, E.; Rose, B. How To Validate Research in Engineering Design? In *Proceedings of the International Conference on Engineering Design ICED11*, Lyngby/Copenhagen, Denmark, 15–18 August 2011; pp. 41–50.

47. Almefelt, L.; Berglund, F.; Nilsson, P.; Malmqvist, J. Requirements management in practice: Findings from an empirical study in the automotive industry. *Res. Eng. Des.* **2006**, *17*, 113–134. [[CrossRef](#)]
48. MacCarney, R.; Warner, J.; Iliffe, S.; van Haselen, R.; Griffin, M.; Fisher, P. The Hawthorne Effect: A randomised, controlled trial. *BMC Med. Res. Methodol.* **2007**, *7*, 30. [[CrossRef](#)]
49. Stokes, M. *Managing Engineering Knowledge—MOKA: Methodology for Knowledge Based Engineering Applications*; Professional Engineering Publ.: London, UK, 2001.
50. Tayal, S. Concurrent Engineering. In Proceedings of the National Conference on Trends and Advances in Mechanical Engineering, Faridabad, Haryana, 19–20 October 2012; pp. 676–680.
51. Shahin, T.M. Feature-based design—An overview. *Comput. Aided Des. Appl.* **2008**, *5*, 639–653. [[CrossRef](#)]

Publisher’s Note: MDPI stays neutral with regard to jurisdictional claims in published maps and institutional affiliations.



© 2020 by the authors. Licensee MDPI, Basel, Switzerland. This article is an open access article distributed under the terms and conditions of the Creative Commons Attribution (CC BY) license (<http://creativecommons.org/licenses/by/4.0/>).

Article

Multifidelity Sensitivity Study of Subsonic Wing Flutter for Hybrid Approaches in Aircraft Multidisciplinary Design and Optimisation

Marco Berci ¹ and Francesco Torigiani ^{2,*},[†]

¹ Pilatus Aircraft Ltd, 6371 Stans, Switzerland; m.berci07@members.leeds.ac.uk

² Deutsches Zentrum für Luft- und Raumfahrt, 21129 Hamburg, Germany

* Correspondence: Francesco.Torigiani@dlr.de

[†] Current address: DLR, Institute of System Architectures in Aeronautics, Hein-Saß-Weg 22, 21129 Hamburg, Germany.

Received: 31 August 2020; Accepted: 3 November 2020; Published: 12 November 2020



Abstract: A comparative sensitivity study for the flutter instability of aircraft wings in subsonic flow is presented, using analytical models and numerical tools with different multidisciplinary approaches. The analyses build on previous elegant works and encompass parametric variations of aero-structural properties, quantifying their effect on the aeroelastic stability boundary. Differences in the multifidelity results are critically assessed from both theoretical and computational perspectives, in view of possible practical applications within airplane preliminary design and optimisation. A robust hybrid strategy is then recommended, wherein the flutter boundary is obtained using a higher-fidelity approach while the flutter sensitivity is computed adopting a lower-fidelity approach.

Keywords: aircraft design; aeroelastic stability; sensitivity analysis; flexible wing; subsonic flow

1. Introduction

Within aircraft multidisciplinary design and optimisation (MDO) [1,2], efficient methods and robust tools are highly sought after as effective reduced-order models (ROMs) [3–5] for fast parametric aeroelastic analyses [6–8], especially for sensitivity and uncertainty evaluation purposes at the preliminary design stage [9–11]. Simplified semi-analytical formulations for the bending–torsion instabilities of flexible wings have been available for a long time but have inherent limitations [12–14], whereas complex fluid–structure interaction (FSI) [15] procedures based on the finite element method (FEM) [16] and computational fluid dynamics (CFD) [17] have recently been used to improve accuracy and generality, but remain computationally expensive and require special care [18,19] with significant effort to pre- and post-process the numerical simulations.

Continuing previous studies on multilevel techniques for practical aeronautical applications [20,21], this conceptual work investigates a robust hybrid strategy where the flutter boundary is accurately obtained using a higher-fidelity approach while the flutter sensitivity is efficiently computed by adopting a (tuned) lower-fidelity approach as an effective ROM. A comparative sensitivity study is hence presented for the aeroelastic stability boundary of a uniform cantilever wing in subsonic flow as the standard benchmark [22]. The Typical Section idealisation [23,24] is employed as the analytical lower-fidelity model, whereas the numerical higher-fidelity model couples a beam-based FEM with panel-based CFD. Considering Loring’s wing [25] with a NACA0002 airfoil [26], the flutter analyses build on earlier publications [27,28] and encompass parametric variations of wing properties, such as its structural inertia, stiffness and aspect ratio. The effects of the latter on the aeroelastic instability are quantified and differences between lower-fidelity and higher-fidelity results are critically assessed from

both theoretical and computational perspectives, in order to study the necessary trade-off between complexity and costs of model fidelity for intensive industrial MDO activities [29].

2. Problem Formulation

Uniform cantilever wings have long been used as the standard benchmark for fundamental studies on aeroelastic analyses and parametric sensitivities for the bending–torsion instabilities of flexible wings, both numerically and experimentally [12,22]. They feature constant material properties (i.e., structural density ρ_m , Young’s elastic modulus E and shear modulus G), chord c , mass m and moment of inertia μ per unit length at the inertial axis x_{CG} (i.e., the line of sectional centres of gravity); bending stiffness EI and torsion stiffness GJ at the elastic axis $x_{EA} \equiv 0$ (i.e., the line of sectional shear centers) along the semi-span l ; structural damping is typically small and conservatively neglected [30].

With $\theta(y, t)$ and $h(y, t)$ the pitch and plunge motion of the flexural axis at the time t , respectively, the wing vertical displacement $w(x, y, t)$ is given as $w = h + x\theta$ directly, x and y being the chordwise and spanwise directions. Assuming an Euler–Bernoulli beam model [31], the linear system of coupled partial differential equations (PDEs) for the dynamic aeroelastic response of wing bending and torsion undergoing small deformations reads:

$$m(\ddot{h} - x_{CG}\ddot{\theta}) + EIh'''' = \Delta L, \quad \mu\ddot{\theta} - mx_{CG}(\ddot{h} - x_{CG}\ddot{\theta}) - GJh'' = \Delta M, \quad (1)$$

with $\Delta L(y, t)$ and $\Delta M(y, t)$ being the sectional lift and pitching moment, respectively; the governing equations are then completed by both geometrical and natural boundary conditions, namely:

$$\theta(0, t) = GJ\theta'(l, t) = 0, \quad h(0, t) = h'(0, t) = EIh''(l, t) = EIh'''(l, t) = 0. \quad (2)$$

As for the case of Loring’s wing, the problem formulation assumes an isotropic material without loss of generality; an anisotropic material (e.g., for the case of composite wings [32]) would feature elastic coupling between bending and torsion (due to different mechanical characteristics in respective directions [12]) but would not introduce conceptual changes to the overall methodology and main conclusion of this work.

2.1. Uncoupled Natural Vibration Modes

Assuming $h \approx \phi_h\chi_h$ and $\theta \approx \phi_\theta\chi_\theta$, where $\chi(\omega, t)$ are the generalised coordinates of the uncoupled vibration mode shapes $\phi(y)$ with natural frequencies ω , the latter for the cantilever wing’s bending and torsion dynamics can independently be obtained by solving the relative homogeneous PDEs via separation of variables with the respective boundary conditions, namely [12]:

$$\omega_h = \left(\frac{\gamma}{l}\right)^2 \sqrt{\frac{EI}{m}}, \quad \omega_\theta = \frac{\nu}{l} \sqrt{\frac{GJ}{\mu}}, \quad \cosh \gamma \cos \gamma + 1 = 0, \quad \cos \nu = 0, \quad (3)$$

$$\phi_h = \cosh\left(\gamma\frac{y}{l}\right) - \cos\left(\gamma\frac{y}{l}\right) - \left(\frac{\cosh \gamma + \cos \gamma}{\sinh \gamma + \sin \gamma}\right) \left[\sinh\left(\gamma\frac{y}{l}\right) - \sin\left(\gamma\frac{y}{l}\right)\right], \quad \phi_\theta = \sin\left(\nu\frac{y}{l}\right), \quad (4)$$

which form a complete set of modal bases for the generalised solution of the aeroelastic equations; yet, note that these uncoupled bending and torsion modes are inherently orthogonal within their own bases but not to one another.

2.2. Unsteady Aerodynamic Model

According to thin aerofoil theory for incompressible potential flow, the sectional unsteady aerodynamic loads due to the wing motion may be written as [22]:

$$\Delta L = \frac{c}{2}\rho \left[\frac{\pi}{2}c(U\dot{\theta} - \dot{h} + x_{MC}\ddot{\theta}) + \kappa UC_{l/\alpha}(C_T V) \right], \quad V = U\theta - \dot{h} + x_{MC}\dot{\theta}, \quad (5)$$

$$\Delta M = -\frac{c}{2}\rho \left\{ \frac{\pi}{2}c \left[\frac{c^2}{32}\ddot{\theta} + x_{CP}U\dot{\theta} - x_{MC}(\ddot{h} - x_{MC}\ddot{\theta}) \right] + \kappa U x_{AC} C_{l/\alpha} (C_T V) \right\}, \quad (6)$$

where ρ and U are the reference air density and horizontal flow speed; the aerodynamic centre x_{AC} (where the circulatory load acts) and the control point x_{CP} (where the non-penetration boundary condition for the vertical flow speed $V(y, t)$ is imposed) lay at the first- and third-quarter chords, respectively; x_{MC} refers to the mid-chord (where the non-circulatory load acts); $C_{l/\alpha}$ is the derivative of the sectional lift coefficient C_l with respect to the nominal angle of attack α .

Within tuned strip theory [21], the scaling factor κ introduces steady three-dimensional downwash effects due to the tip vortices [33] and takes part in the derivative of the wing lift coefficient $C_{L/\alpha} = \kappa C_{l/\alpha}$ [34], while the complex lift-deficiency function $C_T(k)$ is defined in the reduced-frequency k domain and embeds the lag due to two-dimensional inflow effects from the travelling flat wake [35], namely:

$$C_{l/\alpha} = 2\pi \left(1 + \frac{4\epsilon}{3\sqrt{3}} \right), \quad \kappa = \frac{\pi\eta}{\pi\eta e + C_{l/\alpha}}, \quad C_T = \frac{H_1^2}{H_1^2 + iH_0^2}, \quad k = \frac{c\omega}{2U}, \quad (7)$$

with ϵ being the aerofoil thickness ratio, η the wing aspect ratio, $e(\eta)$ Jones' edge-velocity factor (i.e., the ratio between wing semi-perimeter and span [36]) and $H_n^2(k)$ Hankel's functions of the second type and n -th order. Note that the proposed approximate correction for the wing lift coefficient is analogous to applying Oswald's efficiency factor [37], whereas $\kappa \equiv 1$ for standard strip theory.

In summary, unsteady aerodynamics account for both circulatory lag and non-circulatory inertia effects [38], whereas quasi-unsteady aerodynamics neglect circulatory lag terms [39] within a quasi-static approach (i.e., $C_T \approx 1$ with $k \ll 1$). Quasi-steady and steady aerodynamics then disregard non-circulatory inertia terms too, within a static approach (i.e., $C_T = 1$ and $k \approx 0$) where the control point coincides with the elastic axis in the former case (in order to avoid unrealistic aerodynamic damping [23]) and all time derivatives are eventually discarded in the latter case. Note that the structural motion represents a time-dependent boundary condition for the incompressible airflow in all cases, but a synchronous proportional variation of the circulatory airload occurs within quasi-static approaches only [40].

2.3. Modal Approach and Stability Analysis

Given the natural vibration modes of the wing, the relative equations of motion can be transformed into ordinary differential equations (ODEs) by employing Ritz's method [41], where generalised coordinates $\{\chi(t)\}$ multiply the natural vibration mode shapes ϕ . Recasting the whole aero-structural model in vector-matrix form, the governing modal equations then read:

$$[M] \{\ddot{\chi}\} + [C] \{\dot{\chi}\} + [K] \{\chi\} = \{0\}, \quad \{F_A\} = [M_A] \{\ddot{\chi}\} + [C_A] \{\dot{\chi}\} + [K_A] \{\chi\}, \quad (8)$$

where the aeroelastic mass $[M]$, damping $[C]$ and stiffness $[K]$ matrices are given by:

$$[M] = [M_S] - [M_A], \quad [C] = [C_S] - [C_A], \quad [K] = [K_S] - [K_A], \quad (9)$$

and enforce a monolithic FSI, with $\{F_A(t)\}$ the aerodynamic load; as anticipated, $[C_S] = [0]$ is hereby assumed for convenience without loss of generality.

Due to linearity, the parametric aeroelastic stability of the wing is then monitored from the root locus of the characteristic equation for the flutter determinant as the reference airspeed increases; in particular, the system becomes metastable when the real part of at least one eigenvalue λ vanishes and leaves the response undamped, namely:

$$\{\chi\} \approx \{u\} e^{\lambda t}, \quad (\lambda^2 [M] + \lambda [C] + [K]) \{u\} = \{0\}, \quad (10)$$

with $\lambda = i\omega$ in the case of dynamic flutter where a coupled resonant harmonic motion excites the eigenmode $\{u\}$ (Hopf’s bifurcation occurring when a couple of complex conjugate eigenvalues cross the imaginary axis), whereas $\lambda = 0$ in the case of static divergence (occurring when the aeroelastic stiffness matrix becomes singular). Note that the eigenvalues and eigenvectors are suitably assumed to form a complete distinct set, as per most of the practical cases [42]; of course, a sufficient number of natural vibration modes shall be employed in order to grant proper convergence of the modal analysis [43].

2.4. Sensitivity Analysis

The aeroelastic stability boundary acts as a typical constraint in aircraft MDO problems, where parametric sensitivities of both flutter and divergence speeds with respect to variations in the design variables are required for gradient-based optimisation algorithms [44,45]. In general, such derivatives may numerically be obtained by performing many simulations with small alterations of each and every design variable; nevertheless, the aircraft’s conceptual and preliminary design stages would require extensive robust computations for the trends of both objective function and constraints while changing the design parameters [46,47]. Effective analytical solutions (with explicit expressions in a few special cases) have hence been derived by differentiating the governing equations, taking advantage of the self-adjoint nature of complex eigenproblems and then separating real and imaginary parts [48,49].

Especially when the sensitivity of the critical mode shape is also required, the continuation method may efficiently be employed to calculate the critical point and obtain all desired derivatives at the same time [50]. The eigenproblem arising in flutter and divergence analysis may indeed be considered as a system of nonlinear equations with a normalisation condition for the eigenvectors; the solution is then numerically sought by the Newton–Raphson method, where the aeroelastic equations are differentiated with respect to a design parameter of interest p and the system is linearised at each iteration [51]. Within a single unified procedure, the eigenvalues’ and (right) eigenvectors’ derivatives may then automatically be determined along with the eigensolution itself at once, with no information about the transposed (left) problem being required; higher-order derivatives may be obtained by further differentiation. In particular, with $U = U_c(p)$, $\omega = \omega_c(p)$ and $\{u\} = \{u_c(p)\}$ in the critical flight condition, the nonlinear eigenproblem for the flutter mode reads [9]:

$$[S] \{u_c\} = 0, \quad \{u_c\}^T \{u_c\} = 1, \quad [S] = -\omega_c^2 [M] + i\omega_c [C] + [K], \quad (11)$$

and is differentiated to give the eigensolution sensitivity with respect to the design parameter as:

$$\begin{bmatrix} Re [S] & -Im [S] & Re \{v\} & Re \{\zeta\} \\ Im [S] & Re [S] & Im \{v\} & Im \{\zeta\} \\ Re \{u_c\}^T & -Im \{u_c\}^T & 0 & 0 \\ Im \{u_c\}^T & Re \{u_c\}^T & 0 & 0 \end{bmatrix} \frac{\partial}{\partial p} \begin{bmatrix} Re \{u_c\} \\ Im \{u_c\} \\ U_c \\ \omega_c \end{bmatrix} = \begin{bmatrix} Re \{\iota\} \\ Im \{\iota\} \\ 0 \\ 0 \end{bmatrix}, \quad (12)$$

where the submatrices and subvectors involve the derivatives of the aeroelastic model, namely:

$$\{\zeta\} = \frac{\partial [S]}{\partial \omega_c} \{u_c\}, \quad \frac{\partial [S]}{\partial \omega_c} = -\omega_c^2 \frac{\partial [M]}{\partial \omega_c} + i\omega_c \frac{\partial [C]}{\partial \omega_c} + \frac{\partial [K]}{\partial \omega_c} - 2\omega_c [M] + i [C], \quad (13)$$

$$\{v\} = \frac{\partial [S]}{\partial U_c} \{u_c\}, \quad \frac{\partial [S]}{\partial U_c} = -\omega_c^2 \frac{\partial [M]}{\partial U_c} + i\omega_c \frac{\partial [C]}{\partial U_c} + \frac{\partial [K]}{\partial U_c}, \quad (14)$$

$$\{\iota\} = -\frac{\partial [S]}{\partial p} \{u_c\}, \quad \frac{\partial [S]}{\partial p} = -\omega_c^2 \frac{\partial [M]}{\partial p} + i\omega_c \frac{\partial [C]}{\partial p} + \frac{\partial [K]}{\partial p}; \quad (15)$$

in the degenerate case of static divergence with $Im \{u_c\} = 0$ and $\omega_c = 0$, all quantities are inherently real and the matrix of algebraic equations above specialises without the second and fourth rows and columns, respectively. Following previous studies [27], the derivatives may finally be normalised with

respect to the reference values of the involved quantities, thereby comparing all sensitivities within a coherent representation.

3. Lower-Fidelity Model

The Typical Section abstraction [52] is hereby employed as the analytical lower-fidelity model, as it is conceptually illuminating, inherently robust and computationally efficient within its limitations. It resembles the section of the uniform wing and its fundamental aeroelastic behaviour for the bending–torsion coupling mechanism; matching the wing inertia and natural frequencies, such an abstraction, may be regarded as a condensed ROM. The structural arrangement is a classic mass-spring system for the wing section, where the coupled pitch and plunge motion is restrained by vertical and angular linear springs with equivalent stiffnesses $k_h = m\omega_h^2$ and $k_\theta = \mu\omega_\theta^2$ (see Appendix A), respectively; it is representative of the inertial and elastic properties per unit length of the wing at about 75% of its span, where the structural arrangement becomes progressively flexible and the aerodynamic load is still high. The model is hereby extended to include all bending modes having natural frequency below that of the first torsion mode, as the instability may involve any combination of them in general.

Considering the first two uncoupled bending modes and the first uncoupled torsion mode of Euler–Bernoulli’s beam model (with $\gamma_1 \approx 1.875$, $\gamma_2 \approx 4.694$ and $\nu_1 \approx 1.571$) [12], the aeroelastic equations of motion for the wing’s Typical Section in (time-varying) steady incompressible flow are:

$$[M_S] = \begin{bmatrix} m & 0 & -mx_{CG}f \\ 0 & m & -mx_{CG}g \\ -mx_{CG}f & -mx_{CG}g & \mu + mx_{CG}^2 \end{bmatrix}, \quad [K_S] = \begin{bmatrix} k_h & 0 & 0 \\ 0 & k_h r & 0 \\ 0 & 0 & k_\theta \end{bmatrix}, \quad (16)$$

$$[M_A] = [0], \quad [C_A] = [0], \quad [K_A] = \frac{\rho}{2} U^2 c C_{L/\alpha} \begin{bmatrix} 0 & 0 & f \\ 0 & 0 & g \\ 0 & 0 & -x_{AC} \end{bmatrix}, \quad (17)$$

where the cross-projections of the non-orthogonal modes scale the off-diagonal coupling terms:

$$f = \frac{1}{l} \int_0^l \phi_h(y, \gamma_1) \phi_\theta(y, \nu_1) dy, \quad g = \frac{1}{l} \int_0^l \phi_h(y, \gamma_2) \phi_\theta(y, \nu_1) dy, \quad r = \frac{\gamma_2^4}{\gamma_1^4}; \quad (18)$$

in particular, all the latter are constant and read $f \approx 0.959$, $g \approx 0.274$ and $r \approx 39.275$ for homogeneous aero-structural properties. Note that assuming a static aerodynamic approach is consistent with the rigorous application of the scaling factor κ , which is hereby based on steady lifting-line theory; no damping is hence provided to the aeroelastic response. It is also worth stressing that the equations for the first and second bending/plunge modes are not coupled directly, but the equation for the torsion/pitch mode couples them indirectly.

Aero-Structural Parametric Derivatives

The sensitivity of the aeroelastic matrices with respect to aero-structural parameters can readily be obtained in explicit analytical form, where the chain rule applies [28]. In particular, the derivatives with respect to the material density ρ_m and elastic modulus E are given by:

$$\frac{\partial [M]}{\partial \rho_m} = \frac{1}{\rho_m} [M_S], \quad \frac{\partial [K]}{\partial \rho_m} = [0], \quad \frac{\partial [M]}{\partial E} = [0], \quad \frac{\partial [K]}{\partial E} = \frac{1}{E} [K_S], \quad (19)$$

whereas those with respect to reference flow speed U and perturbation frequency ω read:

$$\frac{\partial [M]}{\partial U} = [0], \quad \frac{\partial [K]}{\partial U} = \frac{2}{U} [K_A], \quad \frac{\partial [M]}{\partial \omega} = [0], \quad \frac{\partial [K]}{\partial \omega} = [0], \quad (20)$$

and with respect to the wing semispan l it is:

$$\frac{\partial [M]}{\partial l} = [0], \quad \frac{\partial [K]}{\partial l} = -\frac{2}{l} [D] [K_S] + \frac{1}{C_{L/\alpha}} [K_A] \frac{\partial C_{L/\alpha}}{\partial l}, \quad [D] = \begin{bmatrix} 2 & 0 & 0 \\ 0 & 2 & 0 \\ 0 & 0 & 1 \end{bmatrix}, \quad (21)$$

$$\frac{\partial C_{L/\alpha}}{\partial l} = \frac{2}{c} \frac{\partial C_{L/\alpha}}{\partial \eta}, \quad \frac{\partial C_{L/\alpha}}{\partial \eta} = C_{L/\alpha} \left(\frac{1 - \kappa}{\eta} \right). \quad (22)$$

4. Higher-Fidelity Model

The high-fidelity model is based on a FEM of a slender beam solved with the commercial code Nastran [53] for the structural analysis; the latter is coupled with either the doublet lattice method (DLM) available in the same software [54] or an in-house panel code based on Morino's boundary element method (BEM) for the steady and unsteady aerodynamic analysis [55,56], thereby enforcing a numerical FSI. Both Nastran-based structural FEM and in-house aerodynamic BEM are generated with automatised routines, in order to ease parametric studies; this capability is exploited to perform numerical convergence studies (see Appendix B) and compare the analytical flutter derivatives with their numerical counterparts obtained via finite difference.

4.1. Structural Model

Following previous works [21], the wing structure is modelled with CBEAM elements and accounts for the distance between inertial and elastic axes; the node lying at the wing root is then clamped (see Figure 1). Further FEM nodes are placed at the leading and trailing edges of the wing and connected to the beam nodes with the rigid elements RBE2, in order to support mapping with the aerodynamic grid (in terms of both structural deformation and aerodynamic load: the latter modifies the former, which changes the airflow boundary condition in turn) according to the closely-spaced rigid diaphragm (CSRD) assumption [57]. For the natural vibration analysis, shear deformation is neglected in order to obtain the Euler–Bernoulli beam model, with PBEAM defining the properties (i.e., inertia and stiffness) of the beam element and SPC1 defining the single-point constraint for the clamped root. Using Nastran's SOL103 to obtain the structural eigenvalues and eigenvectors, the vibration analysis is performed while selecting Lanczos' method [58] as available in EIGRL and normalising the modes to unit values of the generalised mass.

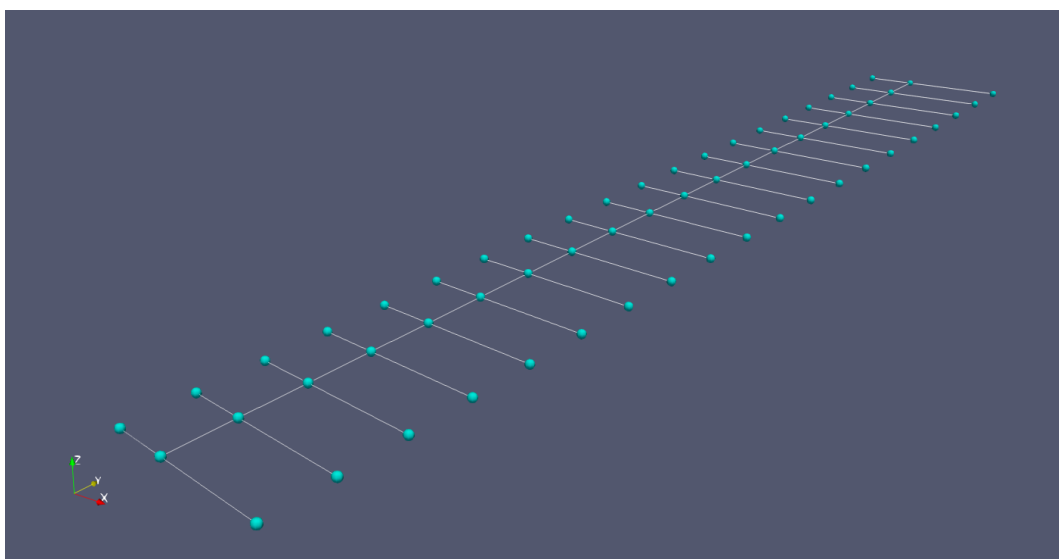


Figure 1. Structural FEM of Loring's wing.

4.2. Aerodynamic Model

Standard flutter prediction methods in the industrial environment are based on aerodynamic panel codes (mostly DLM [59,60]) that idealise wing and empennage as lifting surfaces; if considered, the aircraft fuselage is treated with dedicated elements for non-lifting bodies. The lower computational cost compensates for the lower fidelity of the model; however, the reliability may be increased by correcting the aerodynamic influence coefficients with higher-fidelity data (which are generally not available at the preliminary stage of an MDO process though). Considering small perturbations of an unsteady irrotational flow, the BEM proposed by Morino [55,56] is hereby adopted and consists of an integral representation of the velocity potential at any point of the computational domain in terms of the values on the surface surrounding the aircraft body and wake; the principle of superposition applies. The linear equation of acoustic waves propagation governs the unsteady flow for the case of isentropic compressible fluid and accounts for the finite speed of sound [61], whereas Laplace's equation is resumed for the case of steady flow by taking advantage of Prandtl–Glauert's transformation [62]. Green's function representing a unit-impulsive point source, the theoretical formulation of the boundary value problem for the perturbation potential is then based on Green's formula [33], with (Neumann-type, generally instationary) non-penetration boundary conditions on the aircraft surface and wake as well as (Dirichlet-type, generally stationary) unperturbed asymptotic conditions far from the latter. Bernoulli's theorem is linearised to calculate the pressure coefficient and Kutta's condition is imposed at the trailing edge of lifting surfaces, where the wake detaches and is shed back with the reference airspeed, trailing circulation variations without sustaining any pressure load [37]; its trajectory then represents a streamline at any time and may generally become part of a nonlinear iterative solution where roll-up occurs due to downwash effects, if it is not prescribed a priori (as is in fact typical for most practical applications [53,63], especially when characterised by moderately unsteady flow). Thus, Morino's BEM is able to deal with arbitrary 3D geometries in a unified manner, reducing the effort of the abstraction process and easing the integration with complex structural models. Although the original theory is valid for arbitrary motion in time or frequency domain, only harmonic oscillations in the frequency domain are here considered as suitable for flutter analysis.

The current implementation of Morino's BEM is described in previous works [64] and is equivalent to an appropriate combination of doublets (for lifting bodies and wake) and point sources/sinks (for thickness effects and non-lifting bodies). The 3D geometry is approximated with flat quadrilateral panels that follow the local wing surface and the aerodynamic potential is assumed constant over them, with an analytic expression for their mutual induction. Note that similar flow conditions can be modelled by either vortex or doublet distributions and a quadrilateral doublet element is equivalent to a vortex ring placed at the panel edges [65]; higher-order methods have also been formulated in order to improve accuracy and computational efficiency for complex geometries and configurations, but they are more prone to becoming ill-posed and typically not necessary as long as enough quadrilateral panels refine the aerodynamic grid for lower-order methods to capture high pressure gradients while still staying away from ill-conditioning [66]. Through the wake being assumed as flat, rigid and parallel to the free-stream velocity in order to perform rigorous comparisons with Nastran's DLM and Theodorsen's theory without loss of generality (in the absence of aircraft fuselage and empennages [67]), a linear system is obtained:

$$T_{\sigma}\sigma^k = T_{\vartheta}\vartheta^k, \quad (23)$$

where frequency-dependent T_{σ} and T_{ϑ} are the matrices of aerodynamic influence coefficients (AIC), whereas σ^k and ϑ^k are the aerodynamic potential and normal wash associated with the k -th mode shape of the structural displacement [68], having mapped the latter onto the aerodynamic grid with an effective implementation of the infinite plate spline (IPS) method [69]. The elements Q_{hk} of the generalised aerodynamic forces (GAF) matrix $Q(s)$ are then calculated from the work done by the

aerodynamic pressure C_p due to the k -th mode on the displacement defined by the h -th mode ϕ^h for a prescribed range of reduced frequencies [40], namely:

$$Q_{hk} = \sum_{i=1}^N \phi_i^h \cdot n_i A_i C_p^i(\sigma^k), \quad (24)$$

where n_i and A_i are the normal vector and area of the i -th aerodynamic panel, respectively.

The NACA0002 aerofoil [26] is suitably adopted to obtain a baseline 3D representation of Loring's wing surface (see Figure 2); this particular choice of thin symmetric aerofoil is consistent with the original work with no loss of generality, as the parametric sensitivity of the aeroelastic stability boundary with respect to aerofoil thickness was already found to be poor for small perturbations of subsonic potential flow (i.e., in the absence of strong shock waves and/or significant flow separation) [70].

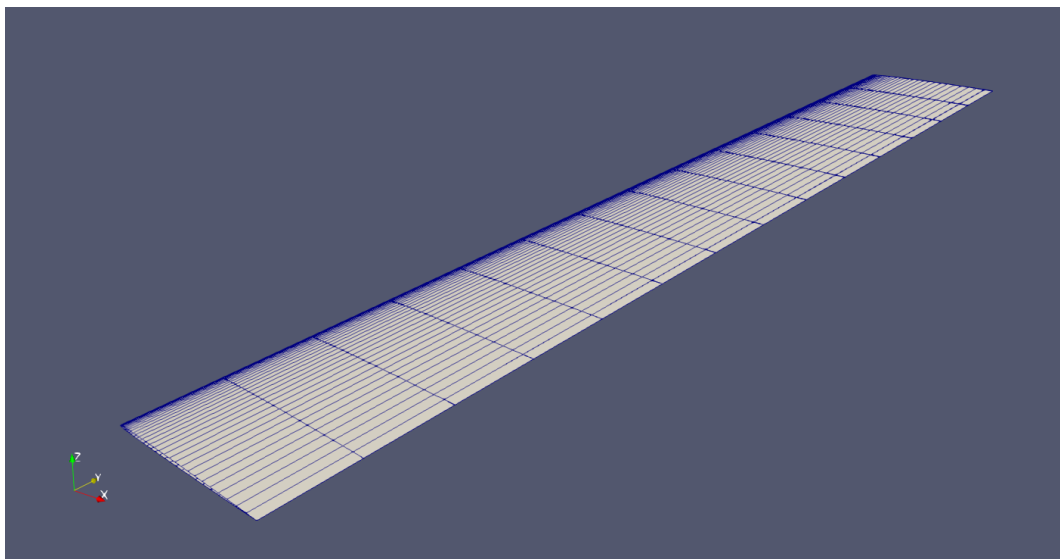


Figure 2. Aerodynamic panels model of Loring's wing.

4.3. Aeroelastic Model

After obtaining the natural vibration modes, the GAF are computed with Morino's BEM, and the continuation method [50] is used to solve the aeroelastic stability eigenproblem and trace the root locus. In order to avoid its costly re-computation during the stability analysis, the GAF matrix is approximated by a rational expression in which the non-linear dependency on the complex reduced frequency s appears explicitly. Here the matrix fraction approach (MFA) [71] is used and preferred to the rational function approximation (RFA) [72], since the former exhibits higher accuracy than the latter for the same number of poles [73]; yet, both methods provide the analytical continuation of the GAF for complex reduced frequency, increasing the accuracy of damped solutions with respect to the $p - k$ method. According to MFA, the GAF matrix is expressed as fraction of matrix polynomials:

$$Q \approx \left(\sum_{i=0}^{M+2} N_i s^i \right) \left(\sum_{i=0}^M D_i s^i \right)^{-1}, \quad (25)$$

and the accuracy of the approximation increases with increasing the number of poles M , which is equal to the size of the state-space system [74]; in particular, three poles have been used in this proof-of-concept work. The approximation matrices D_i and N_i are both obtained by solving a least-square problem in which the distance from the GAF samples $Q(ik)$ is minimised.

The continuation method hereby adopted provides a straightforward and efficient tracking technique without using any correlation function, such as the modal assurance criterion (MAC) [75]. For this reason, the method is rather insensitive to the number of poles used for the aerodynamic finite-state approximation and is able to distinguish between actual and artificial aerodynamic states by construction. In the continuation method, the aeroelastic equations are differentiated with respect to the free-stream airspeed, thereby resulting in a system of ODEs which are solved with a predictor–corrector integration schema starting from an initial airspeed value for which a true solution is known (e.g., the natural vibration frequencies for $U = 0$).

For validation purposes, flutter analysis is also carried out with Nastran’s DLM directly: a flat plate aligned with the free-stream is used as lifting surface and the aerodynamic panels are defined with CAERO1 and PAERO1 cards; the distribution and number of such panels follow established guidelines and convergence studies (see Appendix B). The mode shapes are mapped onto the aerodynamic grid with the IPS method [76] using the SPLINE1 card and the GAF matrix is then generated for sixteen reduced frequencies specified in the MKAERO1 card, suitably ranging from $k = 0$ to $k = 1$ (with logarithmic-like spacing) as per literature studies and common practice [53,63]; a cubic spline is then exploited to interpolate the GAF therein. For the dynamic aeroelastic stability analysis, the $p - k$ method as available in the FLUTTER card is used: the aerodynamic damping is approximated as the imaginary part of the GAF matrix computed for (undamped) harmonic motion, limiting results’ accuracy to the case of lightly damped aeroelastic solutions [12]. The $p - k$ approximation of the aeroelastic eigenproblem [77] is then solved for all the free-stream speed values defined in the FLFACT card, according to the reference length and air density specified in the AERO card. After damping ratios are obtained in the given speed range for all modes, the (undamped) flutter point is determined by linear interpolation.

4.4. Aero-Structural Parametric Derivatives

To calculate the sensitivity of the flutter boundary with respect to any aero-structural parameter, the derivatives of the aeroelastic matrices are also necessary in the first place. In particular, the derivatives of structural eigenvalues and eigenvectors with respect to structural parameters, such as wing material properties (e.g., density or elastic modulus) and element properties (e.g., moments of inertia or distance between elastic and inertia axis), are obtained with Nastran SOL200. The design variable label and initial value are defined with the DESVAR card, which is connected to the relative bulk data entry by DVMREL1 or DVPREL1 cards for material or element properties, respectively; derivatives are hence computed for the structural responses defined by DRESP1 cards, which are the first n structural eigenvalues and eigenvectors.

The GAF matrix is differentiated with respect to both reduced frequency and design variables: according to MFA, the finite-state approximation allows the analytic differentiation with respect to the complex reduced frequency s , whereas the method presented in previous works [73] was used for the derivatives with respect to the design variables p . In particular, by defining the functions $P(\sigma^k, p)$ and $R(\sigma^k, p)$ as:

$$P = Q_{hk}(\sigma^k, p), \quad R = T_\sigma \sigma^k - T_\theta \theta^k, \quad (26)$$

a sub-differentiation process is set up, and depending on the number of design variables and mode shapes to be considered [11], the derivatives may be obtained by either a direct approach:

$$\frac{dP}{dp} = \frac{\partial P}{\partial p} + \frac{\partial P}{\partial \sigma} \frac{d\sigma}{dp}, \quad \frac{\partial R}{\partial \sigma} \frac{d\sigma}{dp} = -\frac{\partial R}{\partial p}, \quad (27)$$

or an adjoint approach:

$$\frac{dP}{dp} = \frac{\partial P}{\partial p} + \Lambda \frac{\partial R}{\partial p}, \quad \left(\frac{\partial R}{\partial \sigma}\right)^T \Lambda = -\left(\frac{\partial P}{\partial \sigma}\right)^T. \quad (28)$$

In computing the partial derivatives, it is important to note that the imaginary component is introduced only by the normal wash ϑ and the wake's influence coefficients inside matrix T_σ ; therefore, the partial derivatives of the steady (real) contribution to the GAF are computed via complex step [78] and the partial derivatives of the unsteady (complex) contribution are then analytically assembled.

5. Results and Discussion

Loring's uniform slender thin wing [25] is hereby considered, as both experimental wind-tunnel data and numerical results assuming two-dimensional incompressible potential flow are available and all results can hence be explained from both physical and mathematical standpoints; moreover, this fundamental benchmark embeds the full complexity of the aeroelastic problem without introducing detrimental uncertainties. The wing's chord is 0.305 m and the semi-span is 2.057 m, giving an aspect ratio 13.5. The inertial axis lays at 42.3% of the chord, with mass 8.05 kg/m and mass moment of inertia 0.0471 kg·m. The wing root is clamped at the elastic axis, with flexural stiffness 677.3 N·m² and torsional stiffness 1018.9 N·m² placed at 30% of the chord.

The coupled natural vibration frequencies of the first bending and torsion modes were observed at 1.29 and 18.1 Hz, respectively; that of the second bending mode was detected in between at 7.7 Hz. With a fluid density 1.11 kg/m³, the flutter speed and frequency were experienced at 90.3 m/s and 10.2 Hz, which give a reduced frequency around 0.11; the subsonic flow may then be considered as moderately unsteady. A Euler–Bernoulli beam model calculated the first three coupled vibration frequencies as 1.29, 7.65 and 17.98 Hz; once coupled with two-dimensional unsteady aerodynamics for a flat plate using standard strip theory, flutter was predicted at 90.7 m/s and 9.2 Hz with good accuracy.

In order to elaborate on the literature results and visualise the flutter mechanism, the aeroelastic stability analysis of Loring's wings is first performed with the same assumptions as in the original publication and the approach here described in the Problem Formulation; the p – k method (with Theodorsen's exact function [35]) has consistently been used and results have been cross-verified against the state-space representation (with a common two-term RFA of Theodorsen's function) [21]. By employing the first two bending modes and the first torsion mode, the respective coupled vibration frequencies are calculated as 1.21, 7.59 and 17.91 Hz; once still coupled with two-dimensional unsteady aerodynamics for a flat plate using standard strip theory, flutter is consistently predicted at 91.15 m/s and 9.2 Hz (which is indeed an excellent approximation, as confirmed by a modal convergence study up to the first three bending and torsion modes). The evolution of the aeroelastic system's eigenvalues is presented in Figure 3 and confirms static divergence to arise well beyond dynamic flutter (i.e., $U_d \gg U_f$).

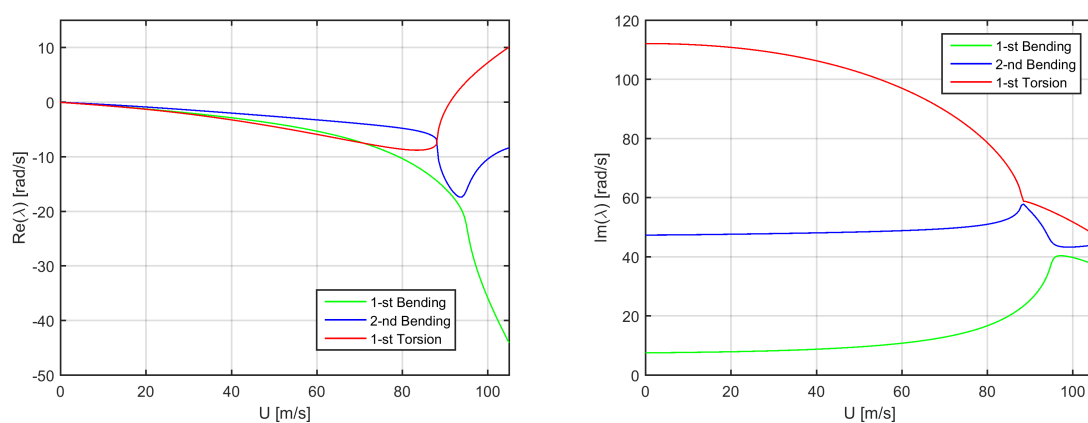


Figure 3. Real (left) and imaginary (right) parts of the aeroelastic eigenvalues for Loring's wing in incompressible flow.

Due to the remarkable agreement between measurements and simulations, the assumptions of slender beam structure and two-dimensional incompressible potential flow in the latter are hence deemed justified. Note that the instability mechanism involves second bending and first torsion modes directly, but the first bending mode is indirectly essential for their coupling to occur before that between first bending and first torsion modes (see Appendix A).

5.1. Aeroelastic Analyses

The aeroelastic stability of Loring's wing is investigated and compared using the proposed lower and higher-fidelity models, while still assuming incompressible flow. The analyses encompass parametric variations of the aero-structural properties, quantifying their effects on the aeroelastic stability boundary and critically assessing the differences in the multifidelity results from both theoretical and computational perspectives, for possible practical applications in airplane design and optimisation adopting hybrid strategies.

Figure 4 shows the aeroelastic stability analysis from the higher-fidelity model, focusing on the same flutter mechanism as found earlier: the first torsion mode becoming unstable and extracting energy from the airflow through the coupled second bending mode, flutter is found at 94.77 m/s and 10.04 Hz in excellent agreement with the experimental results and exhibits a slightly higher vibration frequency than the theoretical one. The aeroelastic stability analysis performed with Nastran and its embedded DLM for the flat wing is also presented and confirms the higher-fidelity results based on Morino's BEM with NACA0002 aerofoil, flutter being found at 94.44 m/s and 10.38 Hz. Note that both sets of code share the same structural model, and the coupled natural vibration frequencies in the void are 1.21, 7.55 and 21.03 Hz for the first three bending modes, whereas it is 17.88 Hz for the first torsion mode; these first four modes have been used in all analyses (see Appendix B). As expected from the wing aspect ratio being relatively large, three-dimensional downwash effects are actually moderate and the (beneficial) steady ones on the (attenuated) airload distribution are roughly compensated by the (detrimental) unsteady ones on the (accelerated) airload evolution [21]; thus, the flutter speed is just slightly higher than that predicted assuming unsteady two-dimensional flow.

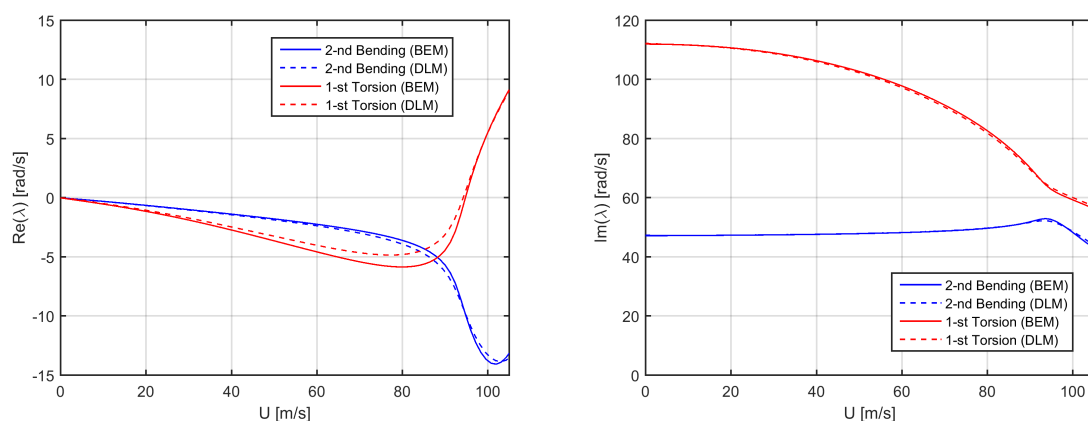


Figure 4. Higher-fidelity real (left) and imaginary (right) parts of the aeroelastic eigenvalues for Loring's wing in incompressible flow.

Still focusing on the flutter mechanism, Figure 5 then shows the aeroelastic stability analysis from the lower-fidelity model: despite its inherent simplicity, the latter predicts flutter quite accurately at 92.1 m/s and 9.09 Hz, thereby proving the effectiveness of such an idealisation (analogous stability diagrams have indeed been obtained by retaining only steady aerodynamic terms in the higher-fidelity model, for cross-verification purposes). The coupled natural vibration frequencies in the void are 1.21 and 7.59 Hz for the two bending modes, and 17.91 Hz for the torsion mode, in excellent agreement with the higher-fidelity ones. The aeroelastic response is then metastable until the first instability

occurs, as no damping is provided by either the elastic structure or static aerodynamics; to this respect, it is worth mentioning that the lift-derivative correction for the steady three-dimensional downwash (which tends to increase the flutter speed, by providing lower airload) incidentally compensates the lack of aerodynamic lag (which tends to decrease the flutter speed, by neglecting wake inflow). Note that, although the flutter reduced-frequency is rather high for steady aerodynamics to be rigorously applicable, the latter was still adopted in order to exacerbate the difference between lower and higher-fidelity models and stress the multilevel approach for more general conclusions.

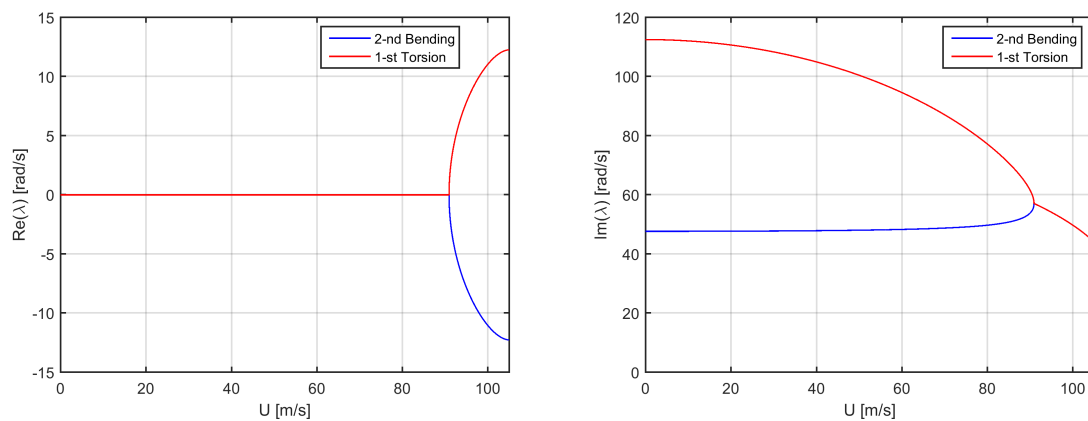


Figure 5. Lower-fidelity real (left) and imaginary (right) parts of the aeroelastic eigenvalues for Loring's wing in incompressible flow.

5.2. Sensitivity Study

Following previous studies on the aeroelastic stability boundary of slender cantilever wings and its sensitivity [27,28], linear FSI models give nonlinear flutter trends as relevant aero-structural parameters are perturbed. The reciprocal positions of aerodynamic, elastic and inertial axes being often constrained by the available space inside the wing as well as the chosen structural layout and systems arrangement, the flutter point's sensitivity to the wing's structural properties is individually explored by changing its material density ρ_m (which scales m and μ) and elastic modulus E (which scales EI and GJ), whereas varying the wing's semi-span l (which modifies the lift coefficient derivative $C_{l/\alpha}$) alters its geometry and affects both structural and aerodynamic properties at the same time.

From Figure 6, it can be seen that changing the wing's material density alters all natural frequencies through the inertial properties and hence the flutter frequency, but has marginal/no influence on the flutter speed; all symbols give the actual nonlinear percentage variation of the flutter point, whereas all lines with corresponding colour draw its normalised linear prediction. In particular, a 1% increment in the material density causes about a 0.5% decrement in the flutter frequency; the negligible variation of the flutter speed is confirmed by previous works [27] as being due to the (small) beneficial effect of an increase in sectional mass being compensated by an (almost) equal and opposite detrimental effect of an increase in mass moment of inertia. This outcome may indeed help while minimising the aeroplane weight, as reducing the material density does not significantly affect the present flutter boundary due to wing bending–torsion instability (especially in the absence of lumped masses). However, it shall be recalled that varying the wing inertia might cause other types of aero-structural instabilities to arise at the aircraft level due to modal coalescence, and monitoring the variation of the flutter frequency is then important to preventing potential resonance. It is also worth mentioning that the small higher-fidelity effect on the flutter speed is due to the unsteady airload being frequency dependent through the lift-deficiency function and the related aerodynamic lag.

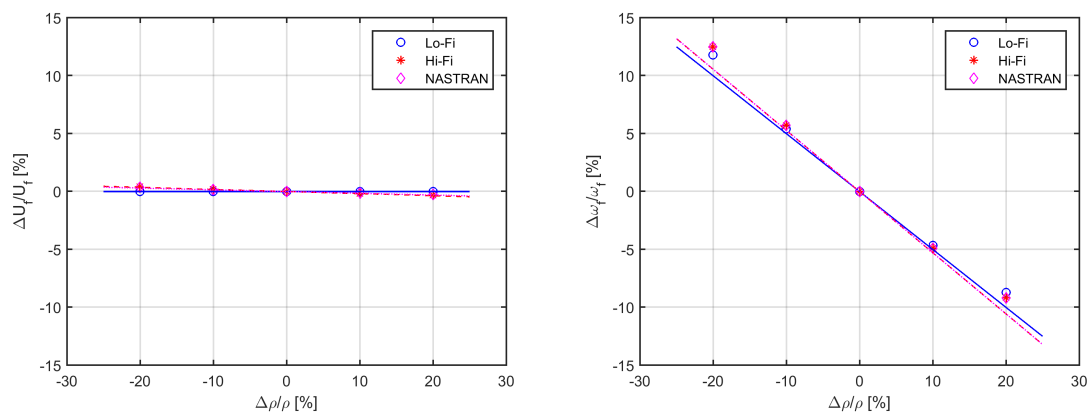


Figure 6. Flutter speed (left) and frequency (right) parametric variation and sensitivity to changes in the wing's material density.

As per Figure 7, changing the wing's material elastic modulus alters all natural frequencies through the stiffness properties and hence the flutter speed and frequency; in particular, a 1% increment in the elastic modulus induces about a 0.5% increment in all the latter, leaving the flutter reduced frequency practically unchanged. This outcome is quantitatively confirmed by previous works [27] as being due to the detrimental effect of an increase in flexural stiffness being much lower than the beneficial effect of an increase in torsional stiffness. The striking agreement between lower and higher-fidelity results is mostly driven by the respective structural models being equivalent (as seen from the close agreement between the natural vibration frequencies), while the different aerodynamics play a minor role (as the airflow is moderately unsteady). The quasi-linear trend of the percentage variations reveals a rather large confidence interval for the normalised sensitivity; however, the dimensional counterpart of the latter to be used by optimisation routines follows a highly nonlinear pattern (note that the explicit lower-fidelity expression given in Appendix A for the torsional static divergence speed provides a straightforward theoretical check).

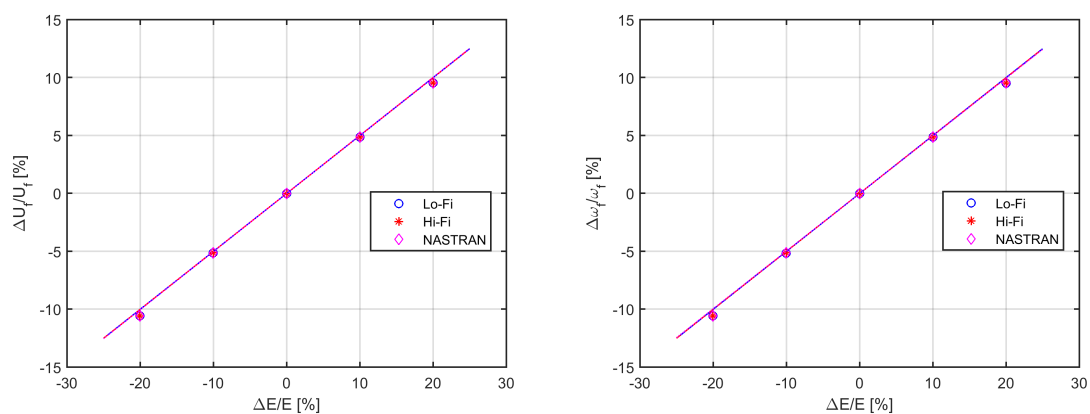


Figure 7. Flutter speed (left) and frequency (right) parametric variation and sensitivity to changes in the wing's material elastic modulus.

Finally, Figure 8 shows that changing the wing semispan has a large effect on the stability boundary through the stiffness properties as well as the aerodynamic loads and hence on the flutter speed and frequency. In particular, a 1% increment in the wing semispan induces about a 0.8% decrement in the critical speeds and about a 1.6% decrement in the flutter frequency; note that analogous trends for the variations and orders of magnitude for the sensitivities were obtained in previous studies on similar slender wings [28], as a qualitative means of validation. Lower and higher-fidelity results are still in very good agreement and differences are mainly due to unsteady downwash effect, as the aspect ratio of the wing changes considerably with the span and so does the sectional airload.

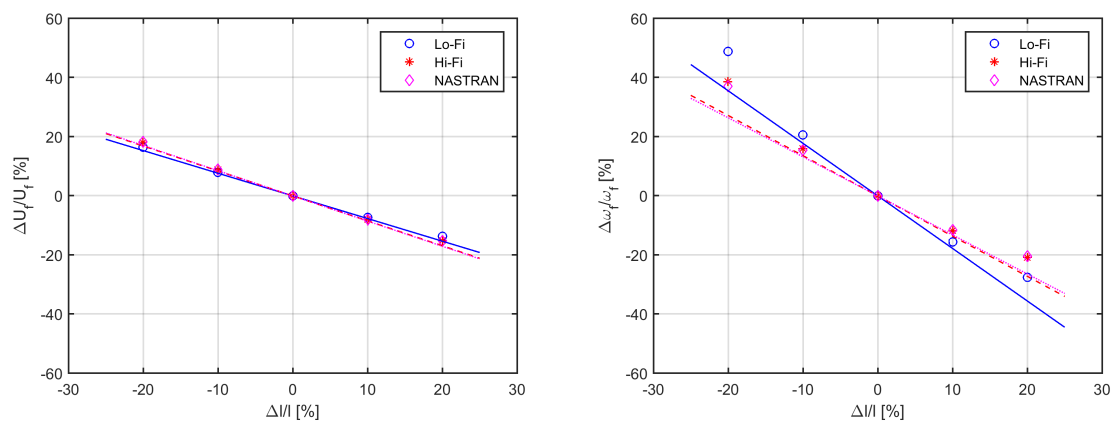


Figure 8. Flutter speed (left) and frequency (right) parametric variation and sensitivity to changes in the wing semispan.

For the sake of completeness, it is worth mentioning that variations and sensitivities of the divergence speed (see Appendix A) with respect to the same aero-structural parameters considered above were consistently found to have trends and orders of magnitude very close to those pertaining the flutter speed. In particular, it is observed that changing the wing's geometry has a much larger impact on the flutter boundary than changing the material properties (especially density); this is particularly true for the flutter frequency, the variations of which exhibit a more significant nonlinear behaviour and local curvature.

Due to the sufficient mutual separation of the natural vibration modes, it is also worth stressing that the instability mechanism did not change across the parametric variations, and the derivatives of the flutter stability boundary have accurately been calculated by the lower-fidelity model at a (marginal) fraction of the computational complexity and costs. In particular, semi-analytical solutions drastically reduced the latter, being almost instantaneous and demanding minimal pre- and post-processing (if any at all) while granting an enhanced theoretical understanding. Thus, the healthy combination of lower and higher-fidelity models enables efficient multidisciplinary exploration of a large design variable space for innovative aeroplane concepts and configurations; further numerical savings may still be obtained by exploiting reliable surrogate models for the higher-fidelity solutions, with an effective synthesis of the underlying complexity [20].

6. Conclusions

Within the context of aircraft multidisciplinary design and optimisation, a comparative sensitivity study for the bending–torsion flutter instability of flexible aircraft wings in subsonic flow has been presented. Analytical models and numerical tools with different complexities and fidelities have been used, in view of possible practical applications exploiting multilevel approaches within the conceptual and preliminary MDO phases. Parametric studies have been performed where the effects of varying the wing's aero-structural properties on the aeroelastic stability boundary have been quantified and critically assessed from both theoretical and computational perspectives. When the natural vibration modes of the wing are well separated from all other natural vibration modes of the aircraft and the aeroelastic instability mechanism does not change in nature, an efficient hybrid strategy is then recommended where the flutter analysis is performed using higher-fidelity approaches, whereas the sensitivity analysis of the flutter boundary is performed using lower-fidelity approaches, thereby improving theoretical understanding and reducing computational costs while retaining accuracy. Future works are encouraged to investigate additional effects (e.g., wing sweep and flow compressibility) and increased complexity (e.g., presence of a control surface) or perform the full MDO of a flexible aircraft wing, effectively exploiting the proposed multifidelity strategy.

Author Contributions: M.B. derived the analytical model and results; F.T. performed the numerical simulations; the authors then wrote the respective parts of the manuscript. All authors have read and agreed to the published version of the manuscript.

Funding: This research received no external funding.

Acknowledgments: The authors would like to thank Ranjan Banerjee at City University of London and Rakesh Kapania at Virginia Polytechnic Institute and State University for the precious insights into their previous works.

Conflicts of Interest: The authors declare no conflict of interest.

Abbreviations

Symbols

A	aerodynamic panel area
c	section chord
C_l	section lift
$C_{l/\alpha}$	section lift derivative
$C_{L/\alpha}$	wing lift derivative
C_p	pressure coefficient
C_T	Theodorsen's function
$[C]$	generalised damping matrix
D	aerodynamic approximation matrix (fraction denominator)
e	semiperimeter-to-span ratio
E	section Young's elastic modulus
f	cross-projection of first bending and first torsion modes
$\{F\}$	generalised load vector
g	cross-projection of second bending and first torsion modes
G	section shear elastic modulus
h	section flexural (plunge) displacement
H_n^2	Hankel's functions of the second type and n -th order
I	section flexural area moments of inertia
J	section torsional area moments of inertia
k	reduced frequency
k	equivalent spring stiffness
$[K]$	generalised stiffness matrix
l	wing semi-span
ΔL	section aerodynamic force
m	section mass
ΔM	section aerodynamic moment
$[M]$	generalised mass matrix
n	aerodynamic panel normal vector
N	aerodynamic approximation matrix (fraction numerator)
p	design parameter
Q	generalised aerodynamic forces matrix
r	squared ratio of second and first flexural vibration frequencies
s	complex reduced frequency
$[S]$	system matrix
t	time
T	aerodynamic influence coefficients matrix
$\{u\}$	eigenvector
U	horizontal airspeed
V	vertical airspeed
x	chordwise coordinate
y	spanwise coordinate
w	section vertical displacement

Greek

α	angle of attack
$\{\chi\}$	generalised coordinates
ϵ	aerofoil thickness ratio
ϕ	natural vibration mode shape
γ	flexural natural vibration constant
η	wing aspect ratio
κ	aerodynamic load scaling function
λ	eigenvalue
μ	section mass moment of inertia
ν	torsional natural vibration constant
θ	section torsional (pitch) displacement
$\mathbf{\theta}$	normal wash matrix
ρ	air density
ρ_m	material density
σ	aerodynamic potential matrix
τ	reduced time
ω	natural vibration frequency

Subscripts

A	aerodynamic
c	critical
f	flutter
d	divergence
h	flexural
S	structural
θ	torsional

Acronyms

AC	aerodynamic centre
AIC	aerodynamic influence coefficient
BEM	boundary element method
CFD	computational fluid dynamics
CG	centre of gravity
CP	control point
CSRD	closely-spaced rigid diaphragm
DLM	doublet lattice method
EA	elastic axis
FEM	finite element method
FSI	fluid-structure interaction
GAF	generalised aerodynamic forces
IPS	infinite plate spline
MAC	modal assurance criterion
MC	mid-chord
MDO	multidisciplinary design and optimisation
MFA	matrix fraction approach
MST	modified strip theory
ODE	ordinary differential equation
PDE	partial differential equation
QST	quasi-steady theory
RFA	rational function approximation
ROM	reduced order model
SST	standard strip theory
TST	tuned strip theory

Appendix A. Aeroelastic Stability of the Typical Section with Steady Aerodynamics

Providing full control on the results with respect to the specific assumptions of the methods and tools employed for the analysis, theoretical formulations grant a clear and complete overview of the problem which is essential for any engineering application. Although inherently limited in their general capabilities, analytical solutions then offer a wealth of qualitative information and quantitative details as well as fundamental insights and rigorous validation for both educational and practical purposes.

Considering a single mode for the wing bending and torsion, respectively, the aeroelastic equations for the Typical Section with steady aerodynamics read [79]:

$$m(\ddot{h} - x_{CG}f\ddot{\theta}) + k_h h = \frac{\rho}{2} U^2 c_{CL/\alpha} f \theta, \quad (A1)$$

$$\mu \ddot{\theta} - m x_{CG}(\ddot{h} - x_{CG}f\ddot{\theta}) + k_\theta \theta = -\frac{\rho}{2} U^2 x_{AC} c_{CL/\alpha} \theta, \quad (A2)$$

where $f \equiv 1$ for two-dimensional aerofoils [12], with $\phi_h \equiv 1$ and $\phi_\theta \equiv 1$. By neglecting the aerodynamic load, the coupled bending and torsion natural vibration frequencies are explicitly obtained as:

$$F_4 \omega_v^4 - F_2 \omega_v^2 + F_0 = 0, \quad \omega_v = \sqrt{\frac{1}{2F_4} \left(F_2 \pm \sqrt{F_2^2 - 4F_4 F_0} \right)}, \quad (A3)$$

$$F_0 = 1, \quad F_2 = \frac{\mu}{\mu + m x_{CG}^2 (1 - f^2)} \left[\omega_\theta^2 + \left(1 + \frac{m}{\mu} x_{CG}^2 \right) \omega_h^2 \right], \quad F_4 = \frac{\mu \omega_h^2 \omega_\theta^2}{\mu + m x_{CG}^2 (1 - f^2)}, \quad (A4)$$

where the uncoupled counterparts are resumed whenever inertial and elastic axes coincide (i.e., with $x_{CG} = 0$). Otherwise, the characteristic equation for the flutter determinant provides with the metastable boundary and gives the flutter frequency as:

$$P_4 \omega_f^4 - P_2 \omega_f^2 + P_0 = 0, \quad \omega_f = \sqrt{\frac{1}{2P_4} \left(P_2 \pm \sqrt{P_2^2 - 4P_4 P_0} \right)}, \quad (A5)$$

and setting the inner radical discriminant equal to zero then gives the flutter speed as:

$$D_4 U_f^4 + D_2 U_f^2 + D_0 = 0, \quad U_f = \sqrt{\frac{1}{\rho D_4} \left(-D_2 \pm \sqrt{D_2^2 - 4D_4 D_0} \right)}, \quad (A6)$$

where the sign before the inner radical shall provide with the smallest positive real value; finally, note that setting both ω_f and P_0 equal to zero provides with the torsional static divergence speed. In particular, when the aerodynamic centre is ahead of the elastic axis (i.e., with $x_{AC} < 0$), the latter explicitly reads:

$$U_d = \sqrt{\frac{-2k_\theta}{\rho x_{AC} c_{CL/\alpha}}}, \quad (A7)$$

regardless the bending stiffness; when the elastic axis is ahead of the inertial axis (i.e., with $x_{CG} > 0$), the flutter condition is given as:

$$U_f = \sqrt{\frac{1}{\rho D_4} \left(\sqrt{D_2^2 - 4D_4 D_0} - D_2 \right)}, \quad \omega_f = \sqrt{\frac{P_2}{2P_4}}, \quad (A8)$$

where all coefficients are analytical functions of the aero-structural parameters, namely:

$$P_0 = k_h \left(k_\theta + \frac{\rho}{2} U^2 x_{AC} c_{CL/\alpha} \right), \quad (A9)$$

$$P_2 = m \left[k_\theta + \frac{\rho}{2} U^2 (x_{AC} - x_{CG} f^2) c_{C_{L/\alpha}} \right] + k_h (\mu + m x_{CG}^2), \quad (A10)$$

$$P_4 = m \left[\mu + m x_{CG}^2 (1 - f^2) \right], \quad (A11)$$

$$D_0 = \left[m k_\theta + k_h (\mu + m x_{CG}^2) \right]^2 - 4m \left[\mu + m x_{CG}^2 (1 - f^2) \right] k_h k_\theta, \quad (A12)$$

$$D_2 = 2m \left\{ (x_{AC} - x_{CG} f^2) \left[k_\theta m + k_h (\mu + m x_{CG}^2) \right] - 2 \left[\mu + m x_{CG}^2 (1 - f^2) \right] x_{AC} k_h \right\} c_{C_{L/\alpha}}, \quad (A13)$$

$$D_4 = \left[m (x_{AC} - x_{CG} f^2) c_{C_{L/\alpha}} \right]^2. \quad (A14)$$

The formulas above were implemented and compared with literature results for the stability boundary of a Typical Section assuming standard strip theory (SST) with steady aerodynamics [12,79]: exact agreement was always found and provided rigorous validation, also with respect to the relative root locus. The same formulas have then been used to investigate the stability boundary of Loring's wing Typical Section when either the first or the second bending mode is coupled with the first torsion mode, employing tuned strip theory (TST) with steady aerodynamics [21]. Without accounting for the modal cross-projection (i.e., $f \equiv 1$ for a "pitch & plunge" apparatus), flutter is calculated at 106.5 m/s and 4.32 Hz in the former case whereas at 73.9 m/s and 11.28 Hz in the latter case; when the modal cross-projection is considered (i.e., $f < 1$ for a slender beam), flutter is calculated at 109.7 m/s and 4.28 Hz in the former case whereas at 139.2 m/s and 9.60 Hz in the latter case. The static divergence speed pertains the torsion mode only and is found at 210.2 m/s, regardless the bending modes and their cross-projections.

A direct comparison with the low-fidelity results hence reveals that the interaction between bending and torsion modes as well as their cross-projections are essential to reproduce the correct behaviour of the flutter mechanism, where the coalescence between first bending mode and torsion mode drives that between second bending mode and the latter (which have closer natural vibration frequencies) to occur earlier.

Appendix B. Higher-Fidelity Model Results Convergence Study

The number of elements for the structural and aerodynamic models was defined according to rigorous convergence studies. Following Nastran's best practice [80] with $k_{max} = 1$ the maximum reduced frequency employed in the aeroelastic analysis, fifteen DLM panels have uniformly been distributed along the wing chord. When adopting Morino's BEM, thirty aerodynamic panels were symmetrically placed along both upper and lower aerofoil surfaces according to the convergence study in Figure A1 (left), with a suitable refinement around the leading edge in order to capture high pressure gradients. The number of aerodynamic panels in the span-wise direction was determined according to another convergence study shown in Figure A1 (right) and all higher-fidelity results presented in this work were obtained with fifteen panels strips uniformly distributed along the wing span, since sufficient to grant a relative error below 1% for both flutter speed and flutter frequency. Following convergence studies in previous works [37,64], the wake extends for a hundred chords behind the wing and is modelled with a hundred rows of shed panels, the length of which is cubically increased with increasing their distance from the trailing edge. Figure A2 (left) shows the indicial lift-deficiency function $\Phi(\tau)$ (which represents the equivalent of the complex lift-deficiency function C_T in the reduced-time domain τ) from a unit step in angle of attack, whereas Figure A2 (right) depicts the normalised distribution of the steady circulation $\kappa(y)$ (which represents the ratio between the sectional circulation in three- and two-dimensional flow within the framework of modified strip theory, MST [13]); note that the unsteady lift development approaches quasi-steady theory (QST) asymptotically. These results also justify the assumption of two-dimensional flow for the lower-fidelity model, within the framework of TST [21] (to this respect, it is worth mentioning the higher-fidelity

lift coefficient derivative of the wing is obtained as $C_{L/\alpha} = 5.25$, in excellent agreement with the lower-fidelity analytical estimation ($C_{L/\alpha} = 5.21$).

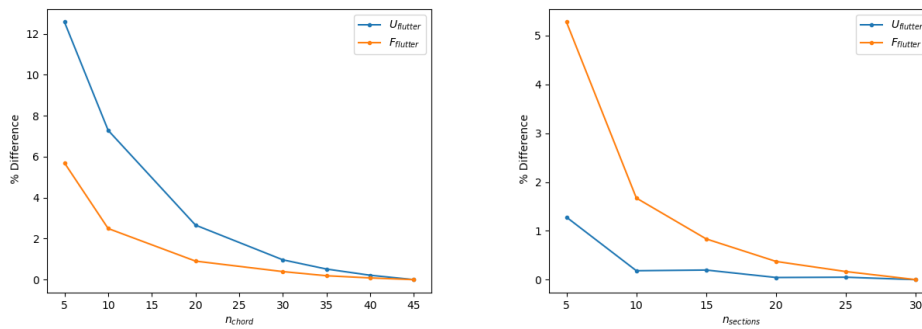


Figure A1. Flutter speed and frequency varying the number of aerodynamic panels along the wing chord (**left**) and span (**right**).

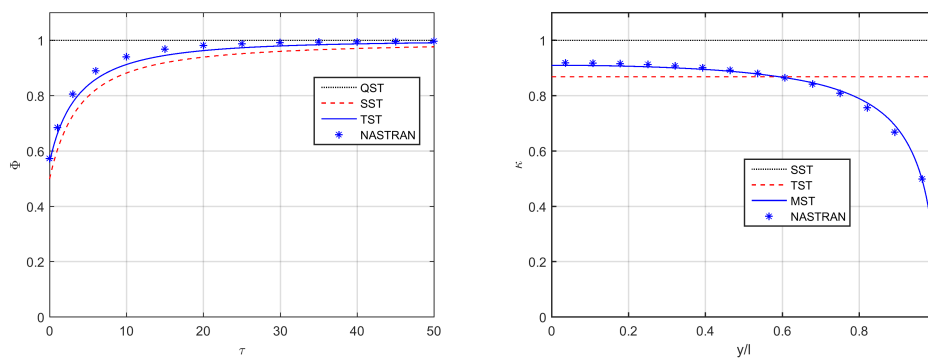


Figure A2. Indicial lift-evolution function from a step-change in the angle of attack (**left**), spanwise lift-decay function (**right**) for Loring’s wing in incompressible flow.

Figure A3 (left) then shows the evolution of the natural vibration frequencies percentage error with varying the number of FEM nodes of the structural beam; the value obtained with the most dense grid is used as reference to compute the plotted error. The first four natural vibration frequencies exhibit a good convergence behaviour, with the third one (i.e., the first torsional mode) almost insensitive to the number of nodes. All higher-fidelity results presented in this work were hence obtained with 20 nodes uniformly distributed along the wing span, since sufficient to grant a relative error below 2%. Finally, Figure A3 (right) shows that employing the first four natural vibration modes granted convergence of both flutter speed and flutter frequency.

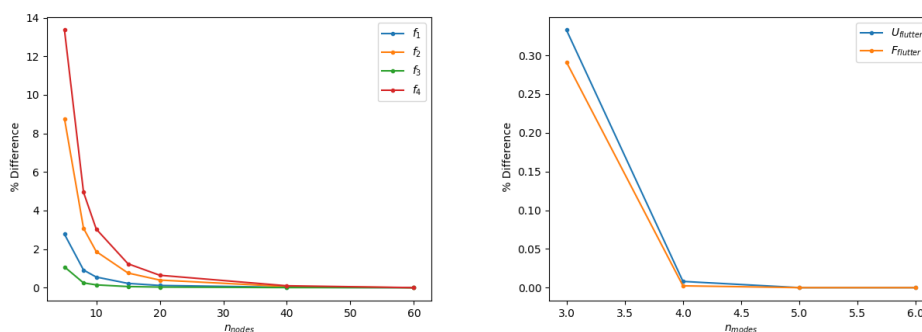


Figure A3. Natural vibration frequencies varying the number of FEM nodes along the wing span (**left**), flutter speed and frequency varying the number of natural vibration modes employed in the aeroelastic stability analysis (**right**).

References

1. Alexandrov, N.; Hussaini, M. *Multidisciplinary Design Optimization: State of the Art*; SIAM: Philadelphia, PA, USA, 1997.
2. Martins, J.; Lambe, A. Multidisciplinary Design Optimization: A Survey of Architectures. *AIAA J.* **2013**, *51*, 2049–2075. [[CrossRef](#)]
3. Quarteroni, A.; Rozza, G. *Reduced Order Methods for Modeling and Computational Reduction*; Springer International Publishing: Cham, Switzerland, 2014.
4. Qu, Z. *Model Order Reduction Techniques with Applications in Finite Element Analysis*; Springer: London, UK, 2004.
5. Ghoreyshi, M.; Jirasek, A.; Cummings, R. Reduced Order Unsteady Aerodynamic Modeling for Stability and Control Analysis Using Computational Fluid Dynamics. *Prog. Aerosp. Sci.* **2014**, *71*, 167–217. [[CrossRef](#)]
6. Livne, E. Integrated Aeroservoelastic Optimization: Status and Direction. *J. Aircr.* **1999**, *36*, 122–145. [[CrossRef](#)]
7. Cavagna, L.; Ricci, S.; Travaglini, L. NeoCASS: An Integrated Tool for Structural Sizing, Aeroelastic Analysis and MDO at Conceptual Design Level. *Prog. Aerosp. Sci.* **2011**, *47*, 621–635. [[CrossRef](#)]
8. Silva, W. AEROM: NASA's Unsteady Aerodynamic and Aeroelastic Reduced-Order Modeling Software. *Aerospace* **2018**, *5*, 41. [[CrossRef](#)]
9. Cardani, C.; Mantegazza, P. Calculation of Eigenvalue and Eigenvector Derivatives for Algebraic Flutter and Divergence Eigenproblems. *AIAA J.* **1979**, *17*, 408–412. [[CrossRef](#)]
10. Crema, L.B.; Mastroddi, F.; Coppotelli, G. Aeroelastic Sensitivity Analyses for Flutter Speed and Gust Response. *J. Aircr.* **2000**, *37*, 172–180. [[CrossRef](#)]
11. Martins, J.; Hwang, J. Review and Unification of Methods for Computing Derivatives of Multidisciplinary Computational Models. *AIAA J.* **2013**, *51*, 2582–2599. [[CrossRef](#)]
12. Hodges, D.; Pierce, G. *Introduction to Structural Dynamics and Aeroelasticity*; Cambridge University Press: Cambridge, UK, 2002.
13. Berci, M. Semi-Analytical Static Aeroelastic Analysis and Response of Flexible Subsonic Wings. *Appl. Math. Comput.* **2015**, *267*, 148–169. [[CrossRef](#)]
14. Ripepi, M.; Görtz, S. Reduced Order Models for Aerodynamic Applications, Loads and MDO. In Proceedings of the Deutscher Luft- und Raumfahrtkongress, Braunschweig, Germany, 13–15 September 2016.
15. Bungartz, H.; Schafer, M. *Fluid-Structure Interaction: Modelling, Simulation, Optimization*; Springer: Berlin/Heidelberg, Germany, 2006.
16. Dhatt, G.; Touzot, G.; Lefrancois, E. *Finite Element Method*; Wiley: Hoboken, NJ, USA, 2013.
17. Chung, T. *Computational Fluid Dynamics*; Cambridge University Press: Cambridge, UK, 2002.
18. Farhat, C.; Lesoinne, M.; LeTallec, P. Load and Motion Transfer Algorithms for Fluid/Structure Interaction Problems with Non-Matching Discrete Interfaces: Momentum and Energy Conservation, Optimal Discretization and Application to Aeroelasticity. *Comput. Methods Appl. Mech. Eng.* **1998**, *157*, 95–114. [[CrossRef](#)]
19. Cizmas, P.; Gargoloff, J. Mesh Generation and Deformation Algorithm for Aeroelasticity Simulations. *J. Aircr.* **2008**, *45*, 1062–1066. [[CrossRef](#)]
20. Berci, M.; Toropov, V.V.; Hewson, R.W.; Gaskell, P.H. Multidisciplinary Multifidelity Optimisation of a Flexible Wing Aerofoil with Reference to a Small UAV. *Struct. Multidiscip. Optim.* **2014**, *50*, 683–699. [[CrossRef](#)]
21. Berci, M.; Cavallaro, R. A Hybrid Reduced-Order Model for the Aeroelastic Analysis of Flexible Subsonic Wings—A Parametric Assessment. *Aerospace* **2018**, *5*, 76. [[CrossRef](#)]
22. Bisplinghoff, R.; Ashley, H.; Halfman, R. *Aeroelasticity*; Dover: Mineola, NY, USA, 1996.
23. Hancock, G.; Wright, J.; Simpson, A. On the Teaching of the Principles of Wing Flexure-Torsion Flutter. *Aeronaut. J.* **1985**, *89*, 285–305.
24. Dennis, S. Undergraduate Aeroelasticity: The Typical Section Idealization Re-Examined. *Int. J. Mech. Eng. Educ.* **2013**, *41*, 72–91. [[CrossRef](#)]
25. Loring, S. Use of Generalized Coordinates in Flutter Analysis. *SAE Trans.* **1944**, *52*, 113–132.
26. Abbott, I.; von Doenhoff, A. *Theory of Wing Sections: Including a Summary of Aerofoil Data*; Dover: New York, NY, USA, 1945.

27. Banerjee, J. Flutter Sensitivity Studies of High Aspect Ratio Aircraft Wings. *WIT Trans. Built Environ.* **1993**, *2*, 683–699.
28. Issac, J.; Kapania, R.; Barthelemy, J. *Sensitivity Analysis of Flutter Response of a Wing Incorporating Finite-Span Corrections*; NASA-CR-202089; NASA: Washington, DC, USA, 1994.
29. Livne, E. Future of Airplane Aeroelasticity. *J. Aircr.* **2003**, *40*, 1066–1092. [[CrossRef](#)]
30. Wright, J.; Cooper, J. *Introduction to Aircraft Aeroelasticity and Loads*; Wiley: Chichester, UK, 2014.
31. Yang, B. *Strain, Stress and Structural Dynamics*; Elsevier: London, UK, 2005.
32. Guo, S. Aeroelastic Optimisation of an Aerobatic Aircraft Wing Structure. *Aerosp. Sci. Technol.* **2003**, *11*, 396–404. [[CrossRef](#)]
33. Karamcheti, K. *Principles of Ideal-Fluid Aerodynamics*; Wiley: New York, NY, USA, 1967.
34. Diederich, F. *A Plan-Form Parameter for Correlating Certain Aerodynamic Characteristics of Swept Wings*; NACA-TN-2335; NACA: Washington, DC, USA, 1951.
35. Theodorsen, T. *General Theory of Aerodynamic Instability and the Mechanism of Flutter*; NACA-TR-496; NACA: Washington, DC, USA, 1935.
36. Jones, R. *Correction of the Lifting-Line Theory for the Effect of the Chord*; NACA-TN-817; NACA: Washington, DC, USA, 1941.
37. Katz, J.; Plotkin, A. *Low Speed Aerodynamics*; Cambridge University Press: Cambridge, UK, 2001.
38. Stanford, B.K. Role of Unsteady Aerodynamics During Aeroelastic Optimization. *AIAA J.* **2015**, *53*, 3826–3831. [[CrossRef](#)]
39. van Zyl, L. Aeroelastic Divergence and Aerodynamic Lag Roots. *J. Aircr.* **2001**, *38*, 586–588. [[CrossRef](#)]
40. Leishman, J. *Principles of Helicopter Aerodynamics*; Cambridge University Press: Cambridge, UK, 2006.
41. Fung, Y. *An Introduction to the Theory of Aeroelasticity*; Dover: Mineola, NY, USA, 1993.
42. van Zyl, L. Use of Eigenvectors in the Solution of the Flutter Equation. *J. Aircr.* **1993**, *30*, 553–554. [[CrossRef](#)]
43. Dimitriadis, G. *Introduction to Nonlinear Aeroelasticity*; Wiley: Chichester, UK, 2017.
44. Vanderplaats, G. *Numerical Optimization Techniques for Engineering Design: With Applications*; McGraw Hill: New York, NY, USA, 1984.
45. Kennedy, G.; Martins, J. A Parallel Finite-Element Framework for Large-Scale Gradient-Based Design Optimization of High-Performance Structures. *Finite Elem. Anal. Des.* **2014**, *87*, 56–73. [[CrossRef](#)]
46. Stanford, B.; Dunning, P. Optimal Topology of Aircraft Rib and Spar Structures Under Aeroelastic Loads. *J. Aircr.* **2015**, *52*, 1298–1311. [[CrossRef](#)]
47. Kennedy, G.; Martins, J. A Parallel Aerostructural Optimization Framework for Aircraft Design Studies. *Struct. Multidiscip. Optim.* **2014**, *50*, 1079–1101. [[CrossRef](#)]
48. Seyranian, A. Sensitivity Analysis and Optimization of Aeroelastic Stability. *Int. J. Solids Struct.* **1982**, *18*, 791–807. [[CrossRef](#)]
49. Pedersen, P.; Seyranian, A. Sensitivity Analysis for Problems of Dynamic Stability. *Int. J. Solids Struct.* **1983**, *19*, 315–335. [[CrossRef](#)]
50. Cardani, C.; Mantegazza, P. Continuation and Direct Solution of the Flutter Equation. *Comput. Struct.* **1978**, *8*, 185–192.
51. Bindolino, G.; Mantegazza, P. Aeroelastic Derivatives as a Sensitivity Analysis of Nonlinear Equations. *AIAA J.* **1987**, *25*, 1145–1146. [[CrossRef](#)]
52. Bisplinghoff, R.; Ashley, H. *Principles of Aeroelasticity*; Dover: Mineola, NY, USA, 2013.
53. Rodden, W.; Johnson, E. *MSC/NASTRAN Aeroelastic Analysis User's Guide*; MSC Software Corporation: Newport Beach, CA, USA, 1994.
54. Rodden, W.; Harder, R.; Bellinger, E. *Aeroelastic Addition to NASTRAN*; NASA-CR-3094; NASA: Washington, DC, USA, 1979.
55. Morino, L. *A General Theory of Unsteady Compressible Potential Aerodynamics*; NASA-CR-2464; NASA: Washington, DC, USA, 1974.
56. Morino, L.; Chen, L.; Suciu, E. Steady and Oscillatory Subsonic and Supersonic Aerodynamics around Complex Configurations. *AIAA J.* **1975**, *13*, 368–374. [[CrossRef](#)]
57. Megson, T. *Aircraft Structures for Engineering Students*; Elsevier: Oxford, UK, 2007.
58. Lanczos, C. An Iteration Method for the Solution of the Eigenvalue Problem of Linear Differential and Integral Operators. *J. Res. Natl. Bur. Stand.* **1950**, *45*, 255–282. [[CrossRef](#)]

59. Albano, E.; Rodden, W. A Doublet-Lattice Method for Calculating Lift Distributions on Oscillating Surfaces in Subsonic Flows. *AIAA J.* **1969**, *7*, 279–285. [[CrossRef](#)]
60. Rodden, W.; Taylor, P.; McIntosh, S. Further Refinement of the Subsonic Doublet-Lattice Method. *J. Aircr.* **1998**, *35*, 720–727. [[CrossRef](#)]
61. Whitham, G. *Linear and Nonlinear Waves*; Wiley: New York, NY, USA, 1999.
62. Bindolino, G.; Mantegazza, P. Improvements on a Green's Function Method for the Solution of Linearized Unsteady Potential Flows. *J. Aircr.* **1987**, *24*, 355–361. [[CrossRef](#)]
63. Chen, P. *ZAERO User's Manual*; ZONA Technology Incorporated: Scottsdale, AZ, USA, 2018.
64. Torrigiani, F.; Ciampa, P.D. Development of an Unsteady Aeroelastic Module for a Collaborative Aircraft MDO. In Proceedings of the Multidisciplinary Analysis and Optimization Conference, Atlanta, GA, USA, 25–29 June 2018.
65. Miranda, I.; Soviero, P. Indicial Response of Thin Wings in a Compressible Subsonic Flow. In Proceedings of the 18th International Congress of Mechanical Engineering, Ouro Preto, Brazil, 6–11 November 2005
66. Maskew, B. *Program VSAERO Theory Document*; NASA-CR-4023; NASA: Washington, DC, USA, 1987.
67. Murua, J.; Martínez, P.; Climent, H.; van Zylc, L.; Palacios, R. T-Tail Flutter: Potential-Flow Modelling, Experimental Validation and Flight Tests. *Prog. Aerosp. Sci.* **2014**, *71*, 54–84. [[CrossRef](#)]
68. Rodden, W. *Theoretical and Computational Aeroelasticity*; Crest Publishing: Los Angeles, CA, USA, 2011.
69. Walther, J.; Gastaldi, A.A.; Maierl, R. Integration Aspects of the Collaborative Aero-Structural Design of an Unmanned Aerial Vehicle. *CEAS Aeronaut. J.* **2020**, *11*, 217–227. [[CrossRef](#)]
70. Jones, K.; Platzer, M. Airfoil Geometry and Flow Compressibility Effects on Wings and Blade Flutter. *Aerosp. Res. Cent.* **1998**. [[CrossRef](#)]
71. Morino, L.; Troia, R.D.; Ghiringhelli, G.L.; Mantegazza, P. Matrix Fraction Approach for Finite-State Aerodynamic Modeling. *AIAA J.* **1995**, *33*, 703–711. [[CrossRef](#)]
72. Roger, K. Airplane Math Modelling Methods for Active Control Design. *AGARD* **1977**, *28*, 1–11.
73. Torrigiani, F.; Walther, J.-N.; Bombardieri, R.; Cavallaro, R.; Ciampa, P.D. Flutter Sensitivity Analysis for Wing Planform Optimization. In Proceedings of the International Forum on Aeroelasticity and Structural Dynamics IFASD 2019, Savannah, GA, USA, 9–13 June 2019.
74. Venkatesan, C.; Friedmann, P. New Approach to Finite-State Modeling of Unsteady Aerodynamics. *AIAA J.* **1986**, *24*, 1889–1897. [[CrossRef](#)]
75. Allemang, R. The Modal Assurance Criterion—Twenty Years of Use and Abuse. *Sound Vib.* **2003**, *37*, 14–23.
76. Harder, R.; Desmarais, R. Interpolation Using Surface Splines. *J. Aircr.* **1972**, *9*, 189–191. [[CrossRef](#)]
77. Hassig, H. An Approximate True Damping Solution of the Flutter Equation by Determinant Iteration. *J. Aircr.* **1971**, *8*, 885–889. [[CrossRef](#)]
78. Squire, W.; Trapp, G. Using Complex Variables to Estimate Derivatives of Real Functions. *SIAM Rev.* **1998**, *40*, 110–112. [[CrossRef](#)]
79. Dowell, E. *A Modern Course in Aeroelasticity*; Springer International Publishing: Cham, Switzerland, 2015.
80. Bellinger, D.; Pototzky, T. A Study of Aerodynamic Matrix Numerical Condition. In Proceedings of the 3rd MSC Worldwide Aerospace Conference and Technology Showcase, Toulouse, France, 16–24 September 2001.

Publisher's Note: MDPI stays neutral with regard to jurisdictional claims in published maps and institutional affiliations.



© 2020 by the authors. Licensee MDPI, Basel, Switzerland. This article is an open access article distributed under the terms and conditions of the Creative Commons Attribution (CC BY) license (<http://creativecommons.org/licenses/by/4.0/>).

Article

Multi-Fidelity Design Optimization of a Long-Range Blended Wing Body Aircraft with New Airframe Technologies

Stanislav Karpuk ^{1,*}, Yaolong Liu ^{2,*} and Ali Elham ^{1,*}

¹ Institute of Aircraft Design and Lightweight Structures, Technische Universität Braunschweig, Hermann-Blenk-Straße 35, 38108 Braunschweig, Germany

² School of Aeronautics and Astronautics, Zhejiang University, Hangzhou 310018, China

* Correspondence: s.karpuk@tu-braunschweig.de (S.K.); liuyaolong@zju.edu.cn (Y.L.); a.elham@tu-braunschweig.de (A.E.)

Received: 8 April 2020; Accepted: 26 June 2020; Published: 30 June 2020



Abstract: The German Cluster of Excellence SE²A (Sustainable and Energy Efficient Aviation) is established in order to investigate the influence of game-changing technologies on the energy efficiency of future transport aircraft. In this paper, the preliminary investigation of the four game-changing technologies active flow control, active load alleviation, boundary layer ingestion, and novel materials and structure concepts on the performance of a long-range Blended Wing Body (BWB) aircraft is presented. The BWB that was equipped with the mentioned technologies was designed and optimized using the multi-fidelity aircraft design code SUAVE with a connection to the Computational Fluid Dynamics (CFD) code SU2. The conceptual design of the BWB aircraft is performed within the SUAVE framework, where the influence of the new technologies is investigated. In the second step, the initially designed BWB aircraft is improved by an aerodynamic shape optimization while using the SU2 CFD code. In the third step, the performance of the optimized aircraft is evaluated again using the SUAVE code. The results showed more than 60% reduction in the aircraft fuel burn when compared to the Boeing 777.

Keywords: aircraft design; aerodynamics; aerodynamic design optimization; blended wing body; new airframe technologies

1. Introduction

A series of research activities have been carried out all over the world in the recent years to meet the challenges of ambitious reduction in CO₂, NO_x, and noise emission set by aviation authorities, such as in Flightpath 2050 [1]. Among which one notable effort is the German Cluster of Excellence SE²A (Sustainable and Energy Efficient Aviation). The SE²A program is based on the previous joint research project “Energy System Transformation in Aviation, EWL [2]” that has been initiated between 2016 and 2018 in Germany to identify and investigate possible unconventional energy systems that can be used for civil transport aircraft in combination with game-changing aircraft configurations and airframe technologies. The SE²A project aims at investigating the influence of new technologies as well as new operational scenarios on the sustainability of future transport aircraft. It has been inspired by a lot of relevant work that has been carried in recent decades; some are mentioned in the following.

A blended wing body (BWB) concept for long-range commercial aircraft could lead to a fuel saving of 27% as compared to a conventional A380-like tube-and-wing (TAW) configuration, according to the research of Boeing [3]. Since the first appearance of the BWB as a potential future commercial aircraft configuration, a lot of research related to the BWB has been done. Okonkwo and Smith [4] provided a summary of achievements in the design of the BWB and its benefits as compared to conventional

aircraft. Xu and Kroo [5] investigated the benefits of load alleviation and natural laminar flow and they concluded that the combination of these two technologies to a Boeing 737-800 aircraft could bring a fuel saving of 18%. NASA-MIT D8 “DoubleBubble” concept with boundary layer ingestion (BLI) and active load alleviation has conducted a fuel burn reduction of 70.87% as compared to a B737-800 baseline concept [6,7]. NASA Hybrid Wing Body (HWB) concept (with N + 3 airframe technology packages, such as BLI and distributed propulsion system) has conducted a fuel burn reduction of 54% as compared to a 777-200LR baseline [6,7]. The “Advanced Truss-Braced Wing” concept proposed by NASA and MIT with hybrid-electric propulsion has a 70% fuel burn reduction at a very low range condition [8]. Saeed et al. from Cambridge University have designed a flying wing concept with laminar flow control and concluded that with 84% of the total wetted area being laminarised, they have achieved a 70% fuel savings when neglecting the system penalties [9].

Within the EWL project, several aircraft have been initially designed to represent technology integrator for these new technologies. In particular, the following technologies have been selected via system-level studies [2].

1. **Active Flow Control:** the function of this technology is to actively suck the air from the aircraft outer surface to delay the transition of the boundary layer. The skin of each aircraft component is split into two segments: a porous sheet and an inner sheet that supports the outer sheet. The inner sheet has orifices that suck the air from the boundary layer and delay transition. In each chamber, an individual pressure is adjusted by the throttle orifices, so that the pressure difference between the outside and the chamber delivers the locally desired amount of mass flow through the surface. Figure 1 shows a schematic image of the skin layout and the AFC system for a wing section. The applied technology in this project is based on [10,11], which describes numerical approaches with active laminar flow control and also describes current progress in this technology.

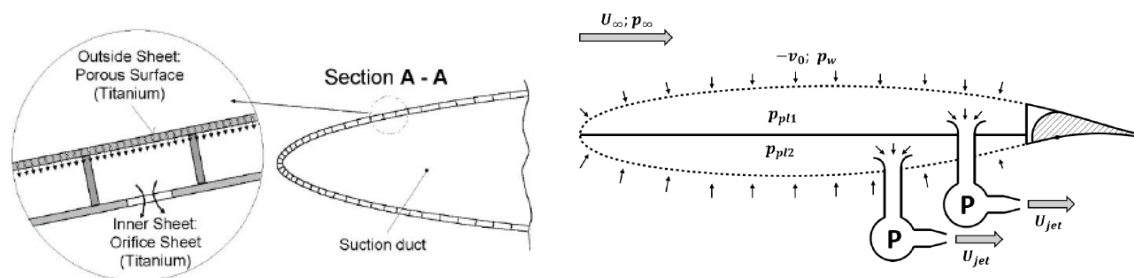


Figure 1. Schematic views of the active suction system [10].

2. **Active Load Alleviation:** the wing active load alleviation consists of several technologies that actively reduce bending moment experienced by the wing, so the limit load factor for the aircraft can be reduced and, consequently, the wing weight is reduced. Previously, researchers have approached the design of active load alleviation systems in different ways. For example, [12–14] looked at the alleviation technology from the aircraft design and MDO perspective; [15] looked at active load alleviation from the control system perspective; and, [16] demonstrated the experimental results of high aspect-ratio wing wind-tunnel test with active load alleviation while using piezoelectric control.
3. **Boundary Layer Ingestion (BLI):** in this technology, the jet engines are integrated with the aircraft body in such a way that the boundary layer of the aircraft body is ingested into the engines, which improves Specific Fuel Consumption (SFC). Extensive information about the current state of the BLI modeling, analysis, and its benefits from the aircraft design standpoint are provided in [17–21]. In addition to BLI, ultra-high bypass ratio turbofan engines that further improve fuel consumption [22] are assumed in this project.
4. **New Materials and Structure Concepts:** novel structural concepts and materials are developed to improve the aircraft structure in terms of stiffness and weight. Bishara et.al. [23] describes

advanced structural design with the integration of active flow control, which is particularly important for the presented research. Besides, aeroelastic tailoring is also considered in this project.

The focus of the current manuscript is to present the multi-fidelity design and analysis of one of the reference aircraft, i.e., a long-range BWB aircraft, which is used to demonstrate the benefits of combining the above-mentioned technologies for improving the fuel consumption of transport aircraft. The studies performed in [2] determined the initial configuration of the aircraft and estimated geometric properties that are based on mission requirements and several trade studies, such as the wing aspect ratio, taper, sweep, and thickness. This study focuses on aircraft mission analysis and optimization while using a multi-fidelity approach. In this manuscript, first, the methods and tools that are used to carry out the overall aircraft design and optimization are briefly described. Subsequently, a more complete description of analysis methods and the outcome of the initial (conceptual) design of the BWB aircraft are presented. Finally, an aerodynamic shape optimization method and its results are presented.

2. Methods and Tools

As mentioned before, the goal of this research is to investigate the influence of the new technologies mentioned above on the fuel consumption of a long-range BWB. To achieve this goal, a multi-fidelity design optimization is performed in order to design a long-range BWB aircraft equipped with the mentioned technologies. Three open-source tools were used in this research. The overall assessment of the aircraft was executed while using the Stanford University Aerospace Vehicle Environment (SUAVE) [24]. Aerodynamic analysis and optimization of the aircraft were executed while using the SU2 Computational Fluid Dynamics (CFD) code [25]. The SUAVE code was connected to the OpenVSP code [26] for automatic CAD modeling and CFD-mesh generation for SU2 from the aircraft geometry defined in SUAVE.

3. Conceptual Design and Assessment of the BWB Aircraft

3.1. Top Level Aircraft Requirements and Initial Design

Table 1 lists the top-level aircraft requirements of the reference long-range aircraft SE²A-LR, which were derived from the same category transport aircraft such as Boeing 777/787 or Airbus A330/350.

Table 1. Top-level aircraft requirements of reference long-range aircraft Sustainable and Energy Efficient Aviation-LR (SE²A-LR).

Parameter	Unit	Value
Design range	NM	8099
Design passenger number	-	300
Cruise Mach number	-	0.85
Maximum Mach number	-	0.92
Cruise altitude	m	10,600
Take-off field length (TOFL)	m	<2200
Landing distance	m	<1966

The initial design of SE²A-LR is based on the EWL project [2], where the thrust to weight ratio and wing loading values were determined by top-level aircraft requirements and design specifications derived from existing long-range transport aircraft, such as Boeing 777. The outer wing of the BWB SE²A-LR was designed via optimizing planform parameters, such as wing aspect ratio, leading-edge sweep, thickness to chord ratio, and taper ratio for the objective function of MTOW for a flight range of 15,000 km while using the NOMAD optimizer [27]. The center body of SE²A-LR was designed to carry 300 passengers using a multi-bubble concept. The supercritical DLR F15 airfoils were used for the initial design with different thickness to chord ratios at the center body and outer wing sections.

The three-dimensional (3D) view of the initial design and comparison of geometric planforms between the SE²A-LR and B777 and their wing properties are shown in Figures 2 and 3, respectively.

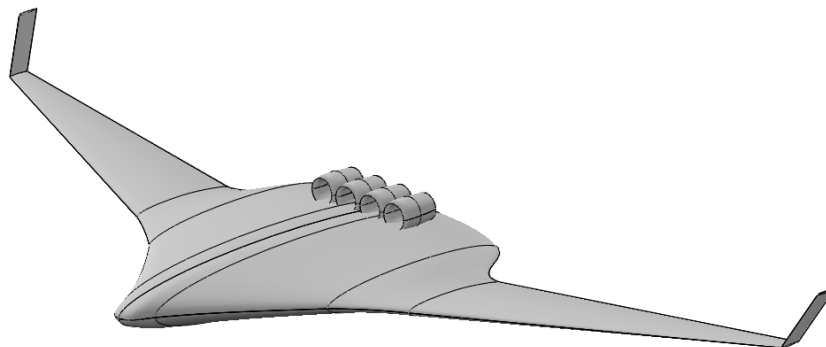


Figure 2. Three-dimensional (3D) view of the initial reference long-range blended wing body (BWB) aircraft.

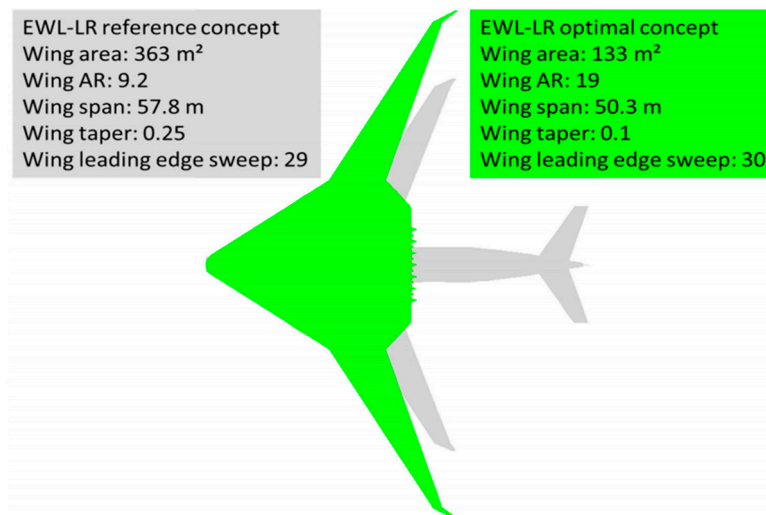


Figure 3. Geometric comparison between long range aircraft SE²A-LR and B777 outer wings planforms [2].

It has to be noted that, for the initial design of SE²A-LR, hybrid laminar flow control (80% of the blended wing area is laminarised), boundary layer ingestion (5% improvement in propulsive efficiency due to boundary layer ingestion), advanced structure design with composite materials (20% structure weight reduction as compared to baseline), as well as active load alleviation technologies (load factor is reduced to 1.5 g) were included [2]. Table 2 gives a summary of the new airframe technologies applied to the reference long-range aircraft SE²A-LR [10,12,22,23].

Table 2. A summary of new airframe technologies applied to reference long-range aircraft SE²A-LR.

SE ² A Technology	Assumption
Active Laminar Flow Control	80% of the aircraft area is laminarized
Advanced structures	20% structure weight reduction
Active Load Alleviation	Limit load factor of 1.5
Boundary layer ingestion	5% improvement in propulsive efficiency

Lateral–Directional stability and control are carried by two winglets that feature rudders. The tails were sized based on static stability requirements presented in [28]. Based on [28], and are required for

sufficient stability of the BWB. The aerodynamic derivatives required for static stability analysis and tail sizing were computed using the Vortex Lattice code AVL [29]. For the SE²A-LR, and are computed equal to and respectively at the cruise conditions. This satisfies sufficient stability requirements. Table 3 provides a summary of the geometric parameters of the SE²A-LR wing.

Table 3. Wing and vertical tail geometric properties.

Geometric Parameter	Wing	Winglet
Span (m)	57.80	3.00
AR (m)	7.40	2.00
Taper ratio (m)	0.065	1.00
Root chord (m)	30.60	1.5
Quarter chord outer wing sweep (deg)	20.00	30.00

SE²A-LR features four engines located on top of the top of the inboard wing portion close to the wing trailing edge, as shown in Figure 2. Safran CFM 56-7B22 engines were selected for the aircraft based on the required thrust. Table 4 shows the specifications of CFM 56-7B22.

Table 4. Safran CFM 56-7B22 engine specifications [30].

Engine Specifications	CFM 56-7B22
Length (cm)	250.8
Width (cm)	211.8
Height (cm)	182.9
Dry weight (kg)	2386.0
Take-off thrust (kN)	91600
Take-off Thrust-specific fuel consumption (g/kN/s)	10.1

3.2. Assessment of the Benchmark Aircraft and the Initial Design Using SUAVE

Because the initial design of the BWB aircraft in the EWL project has been done with an in-house tool (different from SUAVE), in the first step, we assessed the initial configuration of the SE²A-LR, including the game-changing technologies in SUAVE, which is an open-source, object-oriented aircraft design environment programmed in Python language with good flexibility, composability, and extensibility [24,31]. It enables multi-fidelity analyses of arbitrary aircraft and propulsion systems (both conventional and unconventional aircraft concepts as well as propulsion systems). The performance of desired components in SUAVE is calculated using individual design or analysis modules with multiple fidelities for different cases. For aerodynamics, both build-up methods (including AVL Vortex Lattice code for induced drag calculation), and higher-fidelity CFD approach (SU2 as solver and OpenVSP for CFD meshes) are used. The interfaces with Gmsh for generating a mesh for SU2 are also available in SUAVE [32]. Currently, empirical and statistical methods or surrogates are used for structure and weight estimation. A modular “energy network” has been implemented in SUAVE based on analytical methods that are used for both gas-turbine and electric energy systems (electric motor, fuel cells, batteries, etc.). The aircraft mission in SUAVE is analyzed by iteratively solving the equations of motion with a segment-based architecture [24]. By comparing SUAVE analysis results for Boeing 737–800, Embraer E-190, Concorde, and Boeing SUGAR Ray BWB with literature, the SUAVE tool has shown good accuracy for a wide range of transport aircraft [24]. The aircraft geometry in SUAVE is described using representative parameters that can be used for simple aerodynamic/structural analyses, such as VLM and Beam Theory. By using additional geometry converter, such as OpenVSP, the aircraft geometry parameterization in SUAVE can be further used to generate CFD meshes for high fidelity aerodynamic studies [33].

Initial assessment using SUAVE was performed using a low/medium fidelity model, where AVL was used for induced drag, and semi-empirical formulations were applied to estimate parasitic, compressibility, and miscellaneous drag. The detailed Operating Empty Weight (OWE) mass breakdown was also estimated while using semi-empirical formulations within SUAVE. The results were comparable with those of the EWL project [2]. Appendix A summarizes SUAVE analysis for B777 and SUAVE simulation results for the SE²A-LR concept. Table 5 shows the comparison between SE²A-LR and baseline B777, a similar mission for which was also simulated using SUAVE. From this table, one can observe that the new BWB aircraft MTOW was reduced by 58.5%, and block fuel was reduced by 73.6% as compared to the Boeing 777. Aerodynamics performance, especially the L/D, has been significantly improved due to the BWB configuration and laminar flow control technology. During the mission, L/D reaches the value of 48.0, while the B777 model reaches L/D of 21. If the SE²A-LR concept is compared against existing BWB concepts summarized in [34], significant improvements in aerodynamic efficiency are also observed. As predicted by [34,35], the range of maximum L/D does not exceed 28 for existing BWB concepts, see Figure 4. Therefore, the improvement of aerodynamic efficiency of the SE²A-LR when compared to the most efficient BWB is equal to 71.4%. Such a difference between the aerodynamic efficiency of two BWB aircraft is the result of an extended laminar flow up to 80% of the chord. In addition to that, the fuel efficiency of the SE²A-LR was compared to the BWB aircraft that was presented in [36], which has been designed for similar top-level requirements. However, the BWB of [36] was designed without considering the novel control technologies of SE²A. Due to this fact, the difference in fuel efficiency between the BWB in [36] and the SE²A-LR was equal to 73.6%.

Table 5. Comparison of key aircraft parameters of reference long-range aircraft SE²A-LR and B777.

Parameter	SE ² A-LR (In-House Tool)	SE ² A-LR (SUAVE)	B777	Relative Change Wrt B777 (%)
MTOW (kg)	132,268.0	144,308.0	347,452.0	−58.5
OWE (kg)	78,472.0	82,484.0	145,150.0	−44.2
L/D _{max}	45.5	48.0	21.0	127.0
Cruise average L/D	38.33	34.0	18.5	83.8
Block fuel (kg)	24,623.0	28,824.0	109,290.0	−73.6
Sea level static thrust (kN)	400.0	442.3	1026.0	−56.9
Fuel Efficiency (kg/seat/100 km)	0.55	0.64	2.72	−76.5

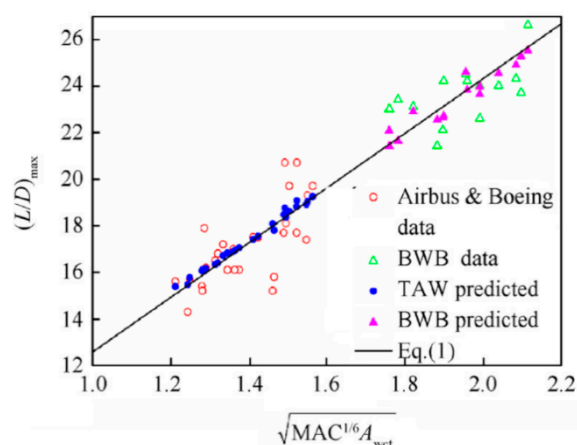


Figure 4. Summary of maximum L/D for various types of aircraft [32].

Appendix A provides details of the mission analysis of SE²A-LR, including the information of altitude and weight changes through flight mission as well as the velocity data along the flight mission. It has been noticed that there are some deviations between the results of the initial analysis of SE²A-LR and the analysis using SUAVE, as shown in Table 5. Such a difference appeared due to a more detailed

mission analysis approach in SUAVE when compared to the in-house tool, which presents a more accurate estimate of potential fuel savings of the BWB.

4. High Fidelity Aerodynamic Analysis

A higher fidelity aerodynamic analysis and optimization was performed after the initial analysis of SUAVE using low to medium fidelity methods. For high fidelity aerodynamic analysis, a Stanford University Unstructured (SU2) CFD tool [25] was used. In SU2, the finite volume method is employed to discretize the Euler and RANS equations, with both explicit and implicit methods available for time integration. Using the Free-Form Deformation (FFD) technique, SU2 computes the deformation of two-dimensional (2D) and 3D geometries within the computational mesh. Besides, the adjoint implementation of the Euler and the Navier–Stokes equations enables efficient gradient-based aerodynamic shape optimization using SU2. More details on SU2 can be found in the literature [25,37].

The NASA OpenVSP tool [26] is used to link SUAVE and SU2. In OpenVSP, the aircraft geometry is described in XML format, which can be easily connected to high fidelity analysis tools, such as SU2. For example, the surface triangulations in OpenVSP can be read by the open-source Gmsh tool with MSH output format. More recently, OpenVSP has also enabled the capability of creating CFD and FEM mesh directly from geometry data (.VSP3 file). Additional information on OpenVSP is available in references [12]. Via an automatic link between SUAVE and SU2, as illustrated in Figure 5, the aerodynamic performance of the aircraft was evaluated using Euler analysis in SU2 (induced and wave drag) in order to improve the accuracy of the analysis. The low-fidelity flat plate analogy [38] method was used for the viscous drag estimation.

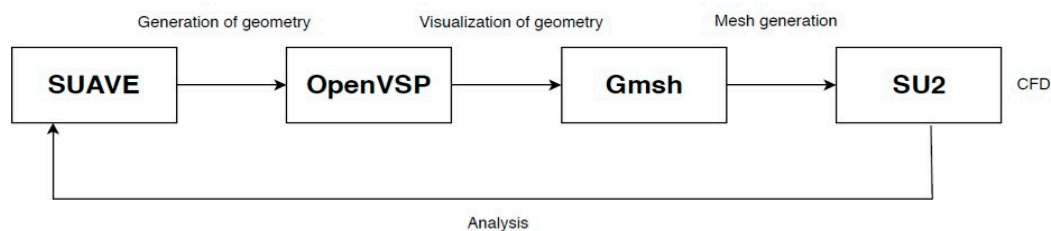


Figure 5. Sequential build-up from Stanford University Aerospace Vehicle Environment (SUAVE) geometry and to SU2 CFD analysis.

To extract the compressibility drag from Euler analysis, the following formulation was used

$$C_{D_{comp}} = C_D - C_{D|M=0.3} \quad (1)$$

where $C_{D_{comp}}$ is the drag component due to compressibility and $C_{D|M=0.3}$ is the drag at $M = 0.3$, the Mach number where compressibility effects are negligible. An additional SUAVE script was written to extract compressibility drag from SU2 and include it in the analysis as a surrogate. For the surrogate model, instead of the default Gaussian process surrogate model in SUAVE, the Surrogate Modeling Toolbox (SMT) developed by the MDO lab of the University of Michigan [39] was integrated in SUAVE. The RMTB B-spline method was used to fit the data. The SMT-toolbox was chosen because of its superior fitting capabilities when compared to the default Gaussian process method with SUAVE. A comparison of the lift and compressibility drag coefficients between the two methods are shown in Figures 6 and 7. From these figures, one can observe that the RMTB method presents much better flexibility to accurately fit both lift and drag compared to the Gaussian process.

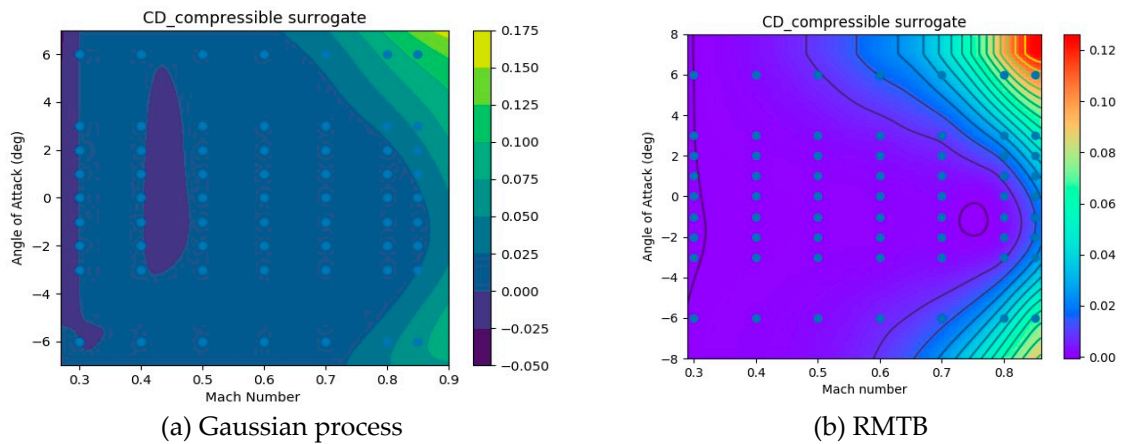


Figure 6. Comparison between the RMTB and Gaussian process surrogates for the compressibility drag coefficient.

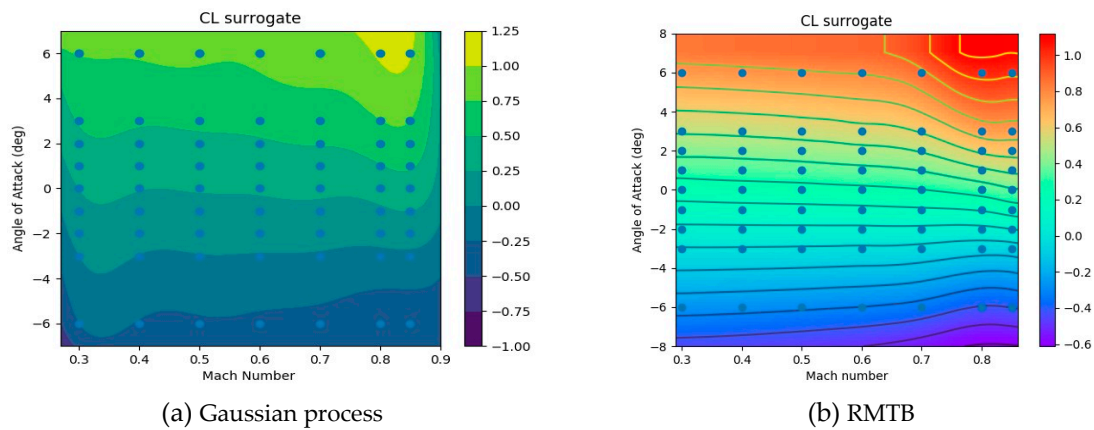


Figure 7. Comparison between the RMTB and Gaussian process surrogates for the compressibility drag coefficient.

The aerodynamic results that were calculated with SU2 were used to build up surrogates for SUAVE overall aircraft aerodynamic performance estimation. Figure 8 shows the airframe geometry and an example CFD mesh of half of the SE²A-LR aircraft geometry. It is important to note that the effect of winglets is excluded in the present CFD analysis. Such a decision was made due to limitations in the definition of the FFD-box (see Section 5) and to adequately compare planforms before and after the aerodynamic optimization. It is assumed that the winglet aerodynamic problem will be directly solved during the next design iteration and the wing optimal planform will be updated again.

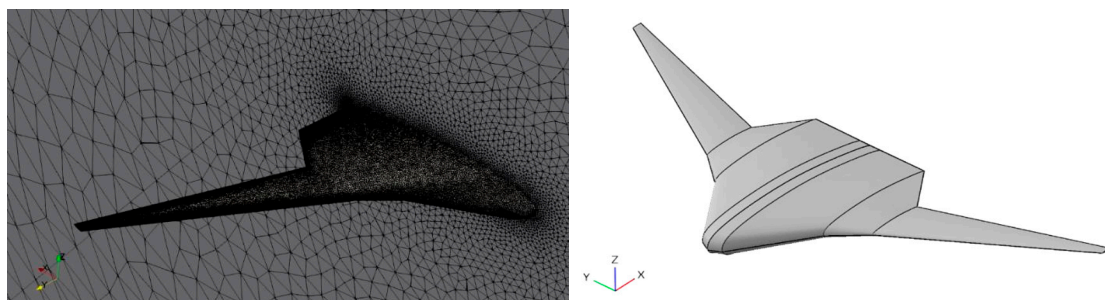


Figure 8. Airframe geometry of SE²A-LR aircraft visualized in OpenVSP.

A mesh convergence analysis has been performed to accurately capture the compressibility effect. The results of the drag coefficient sensitivity to mesh resolution at zero angle-of-attack and $M = 0.85$ are shown in Table 6. Here, an extrapolated value was estimated using the following procedure.

Table 6. Mesh convergence study for the cruise configuration in SU2 ($\alpha = 0$ deg, $M = 0.85$).

Mesh Number	Cell	C_D	Error (%)
1	343,612	0.01733	9.02
2	660,528	0.01673	5.25
3	835,000	0.01670	5.03
4	1,012,683	0.01665	4.72
Extrapolation	∞	0.01590	0.00

The computational domain volume is assumed as

$$V = N\bar{h}^3 \quad (2)$$

where N is the number of cells and \bar{h} is the average cell side length. Subsequently, the surface cell area is described as

$$\bar{h}^2 = \frac{V}{N^{2/3}} \propto \frac{1}{N^{2/3}} \quad (3)$$

It is assumed that, as long as it is proportional to, it is also proportional to. Therefore, an ideal can be estimated by approaching the number of cells to infinity.

From the mesh convergence analysis, 660,528 cells were used to combine accuracy and minimize the computational costs. Figure 9 shows the aircraft pressure coefficient contours at the cruise conditions using this mesh. A surrogate model using the RMTB method was created for drag based on the SU2 analysis in order to evaluate the aircraft performance in SUAVE.

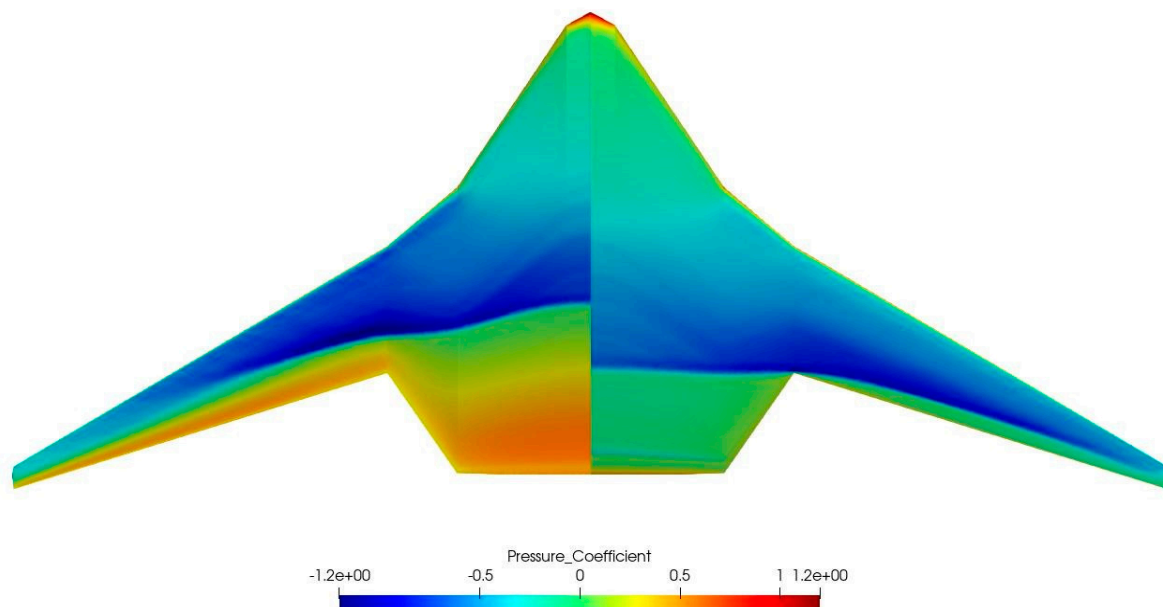


Figure 9. Pressure coefficient contours of lower (left) and upper (right) aircraft surfaces. ($\alpha = 0^\circ$, $M = 0.85$).

From this figure, one can observe that strong shock waves along the aircraft span on both the upper and lower surfaces of the BWB aircraft, which results in large compressibility drag. Such behavior has not been captured by the low-fidelity analysis. In the low-fidelity analysis, a semi-empirical formulation was used to calculate drag due to compressibility. Although semi-empirical methods

provide good accuracy without computational costs, they may have limitations when the analysis is done for an unconventional configuration. Consequently, the higher aircraft drag predicted by SU2 increased the fuel required to complete the mission by 24.1%. Therefore, the difference in fuel efficiency between the SE²A-LR, and B777 became equal to 10.6%, i.e., the new BWB aircraft has higher fuel consumption than Boeing 777. Table 7 shows a modified comparison between the SE²A-LR aircraft and B777 weights and fuel efficiency while using the higher-fidelity analysis. Appendix A presents details of the mission analysis using the results of the higher fidelity aerodynamic analysis.

Table 7. Comparison of key aircraft parameters of reference long range aircraft SE²A-LR and B777 using high-fidelity analysis.

Parameter	SE ² A-LR (SUAVE-SU2)	B777	Relative Change (%)
MTOW (kg)	255,859.0	347,452.0	−26.4
OWE (kg)	87,170.0	145,150.0	−39.9
L/Dmax	43.0	21.0	104.8
Cruise average L/D	5.0	18.5	−71.0
Block fuel (kg)	135,681.0	109,290.0	24.1
Fuel Efficiency (kg/seat/100 km)	3.01	2.72	10.6

5. Aerodynamic Shape Optimization

To mitigate losses that are created by compressibility drag, a discrete adjoint aerodynamic shape optimization using SU2 was performed. For the present optimization problem, the SLSQP algorithm available through the Python interface Scipy [40] was used. Only a single-point optimization for an average cruise condition was considered. The objective function was to minimize the aircraft drag, subjected to geometric constraints for 10 selected sections along with the aircraft. A Free-From Deformation Box (FFD) with $15 \times 11 \times 2$ (total of 330) control points was used to modify the geometry at every optimization iteration. Table 8 shows the optimization problem statement and Figure 10 shows the geometric representation of the FFD and constrained sections.

Table 8. Objective function definition.

	Function/Variable	Description	Quantity
minimize	C_D	Drag coefficient	
With respect to	z	FFD control point z-coordinate	330
Subject to	$C_L = 0.15$	Lift coefficient constraint	1
	$t > 0.8t_{base}$	Max thickness constraint for a given section	10
	$R_{LE} > 0.8R_{LE_{base}}$	Leading-edge radius constraint for a given section	10

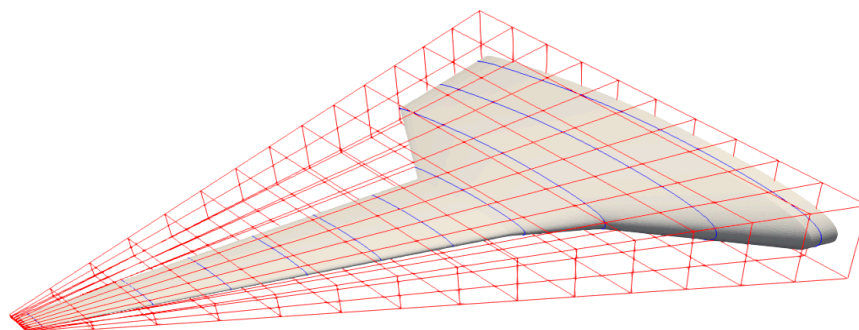


Figure 10. Free-Form Deformation (FFD) Box (red) and control sections (blue) of the SE²A-LR aircraft geometry.

The lift coefficient constraint is based on an average lift coefficient during the cruise. The thicknesses of the initially selected airfoils satisfied the required volume for both passenger and fuel, however,

it was found that such a choice was conservative. The reduction of maximum thickness by 20% still satisfies volume requirements for fuel and passengers (although it negatively influenced the structural weight). Therefore, the thickness constraints for the optimization were defined to avoid getting a thickness reduction of more than 20% when compared to the initial design. Finally, a constraint of leading-edge radii reduction not exceeding 20% was imposed to avoid the possibilities of sharp-edge sections generation.

Figure 11 shows a comparison between the initial and optimized designs. From this figure, one can observe that the shock wave strength was substantially reduced, which caused a reduction in inviscid drag by 77%. However, because the optimization has thickness constraints, shock waves have not been completely removed, so the compressibility drag is not equal to zero. Figure 12 shows a comparison of lift distributions between initial and final designs and elliptical lift distribution. The results show that the optimized geometry approached elliptical lift distribution when compared to the initial design which has a significant portion of lift produced by the fuselage and a mid-span loaded wing. However, from the structural perspective, elliptical lift distribution does not give the benefits from the structural point of view. Qin et al. [41] show that an elliptical/triangular lift distribution provides the best combination of minimum drag achievements and structural weight benefits. Present optimization has not captured this trend due to the absence of structural optimization coupling. Coupled aero-structural optimization will be performed during the next design iteration.

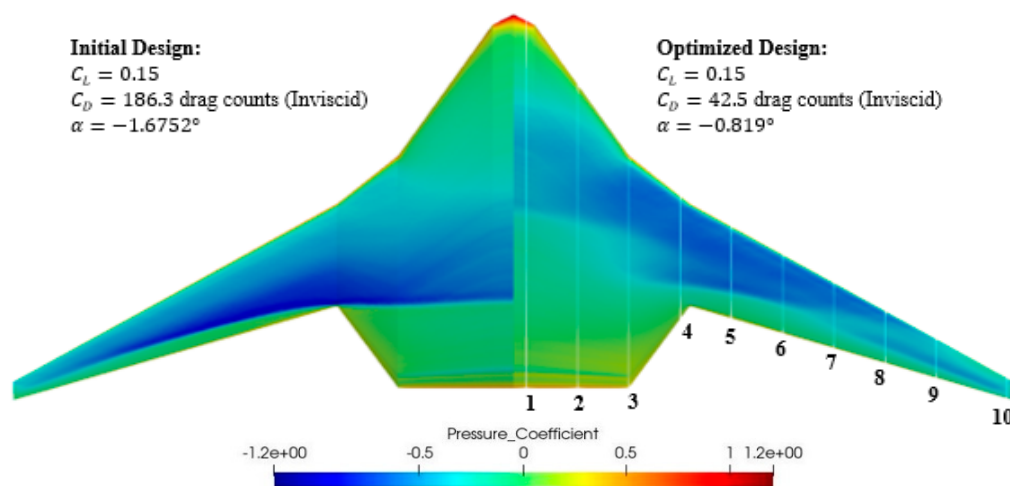


Figure 11. Pressure coefficient contours of the upper aircraft surfaces for initial and optimized configurations.

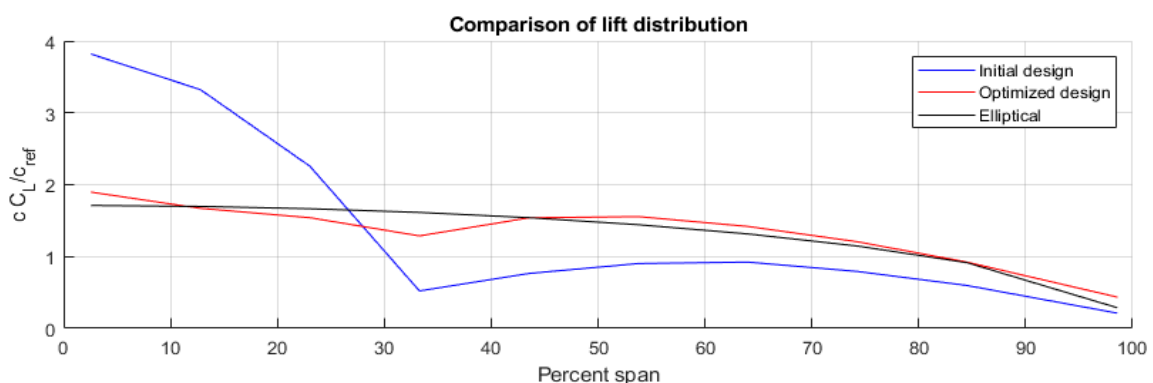


Figure 12. Comparison of lift distribution between initial and optimized designs.

Figure 13 demonstrates the distribution of pressure coefficient along 10 control sections of the geometry. The blue lines show initial sections, while the red lines illustrate the modifications after optimization. From this figure, the smoothing of all the pressure distributions can be observed.

Besides, three trends can be observed: first of all, the maximum thickness of the inboard sections has not been substantially reduced, although a 20% reduction of thickness was allowed for all sections. The airfoil maximum thickness moved towards the leading edge making the aft part thinner. On the other hand, more significant thickness reduction is observed towards the wingtip. Second, the optimized wing demonstrates a 1 deg washout and increase the flight angle-of-attack from -1.68 deg to -0.82 deg to reduce the shock wave strength, but still satisfying the lift coefficient requirements. Finally, a minor increase in the wing dihedral is observed.

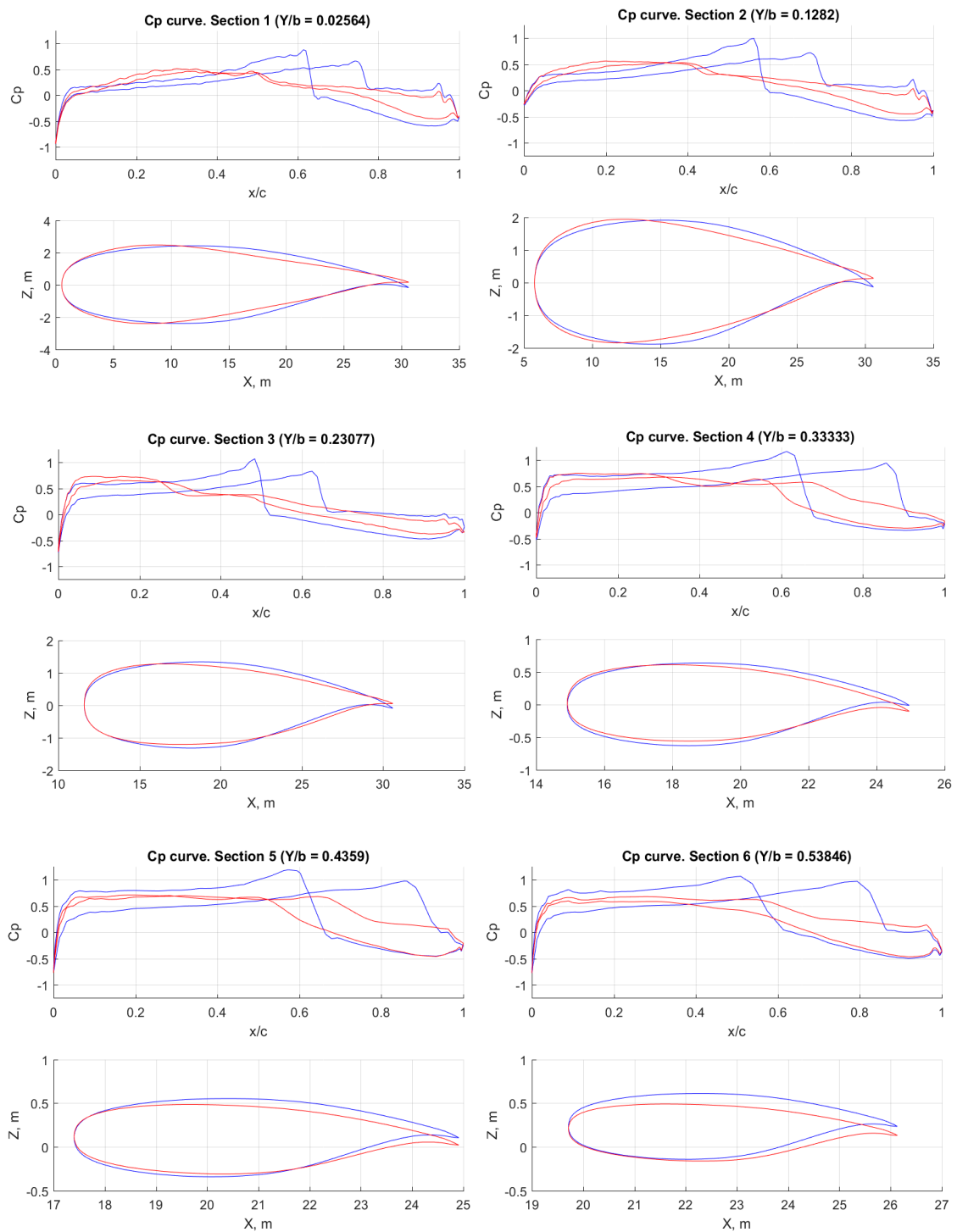


Figure 13. Cont.

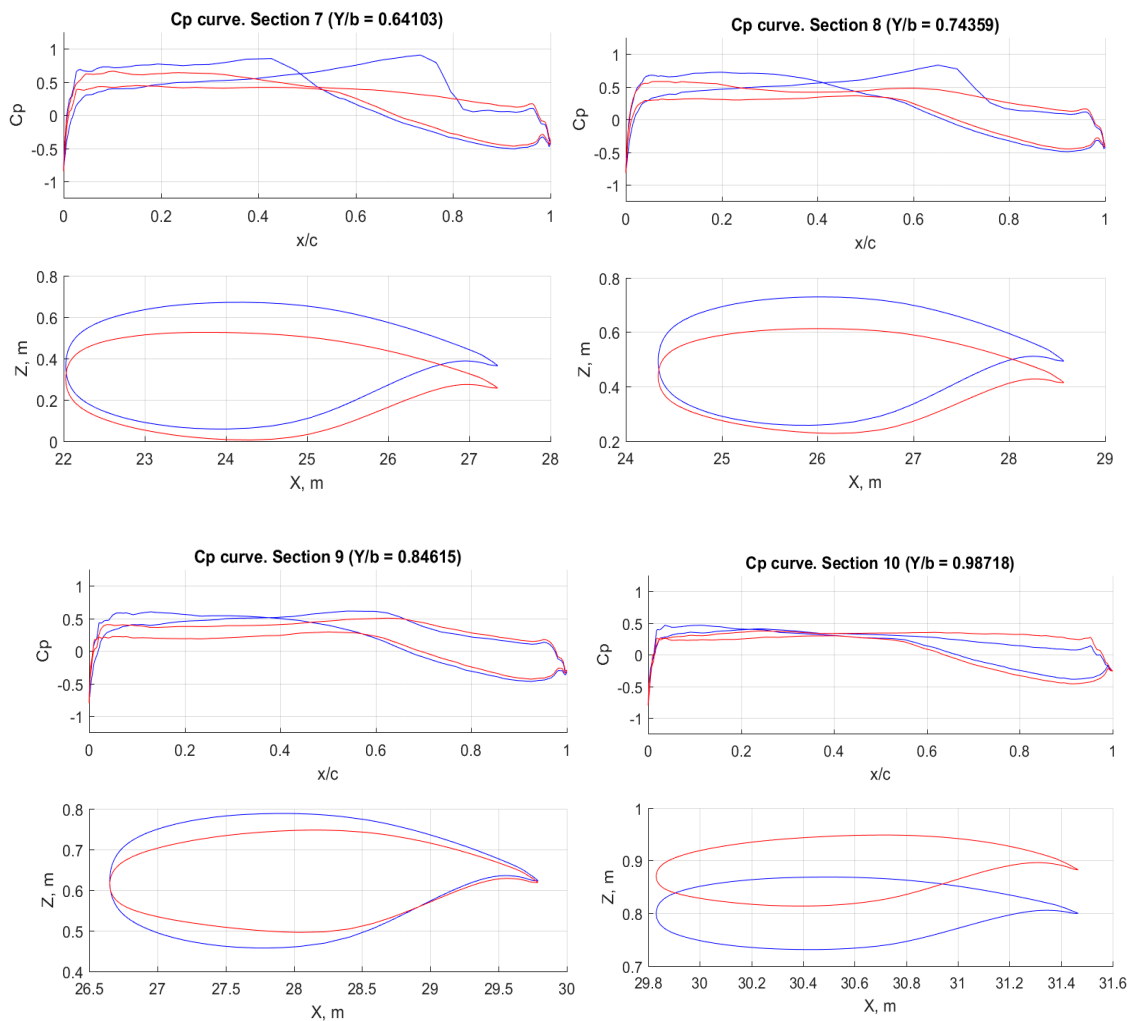


Figure 13. Pressure coefficient and geometry sections. Blue curves represent the initial design and red curves represent the optimized design.

6. Validation of the Drag Estimation Method using the Mixed Fidelity Model

Because the Euler method is based on an inviscid flow assumption, its results lack the viscous drag. Although the lower fidelity method based on the flat plate analogy was used to compute the friction drag and add it to the inviscid drag of the Euler analysis, the accuracy of such a multi-fidelity method needs to be checked. For this purpose, a series of RANS analysis of the optimized geometry at the cruise Mach number of 0.85 at 35,000 ft for a fully turbulent wing was performed at different angles of attack. A mixed mesh that combines quadrilateral cells at the boundary layer and pyramid cells everywhere else was created while using Pointwise [42] software package. Figure 14 shows the mesh of half of the airplane. The mesh has seven-million cells, while the boundary layer was sized for Y^+ of 1. SU2 was used for the Navier–Stokes equations solutions with the Spallart–Almaras turbulence model. Appendix A gives a summary of the pressure coefficient comparison between the Euler and the RANS solutions. Figure 15 shows a comparison of aerodynamic data between the RANS and the combined Euler and semi-empirical solutions.

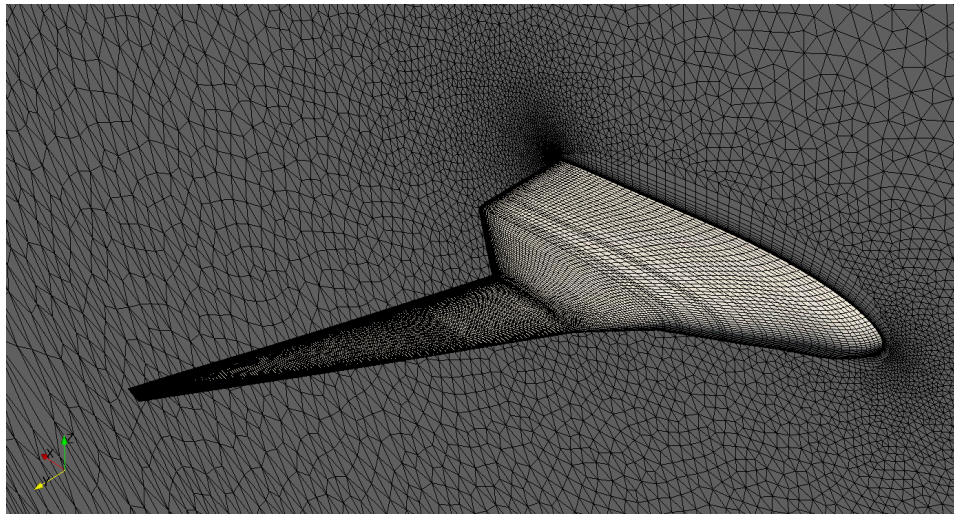


Figure 14. CFD mesh for the RANS simulation.

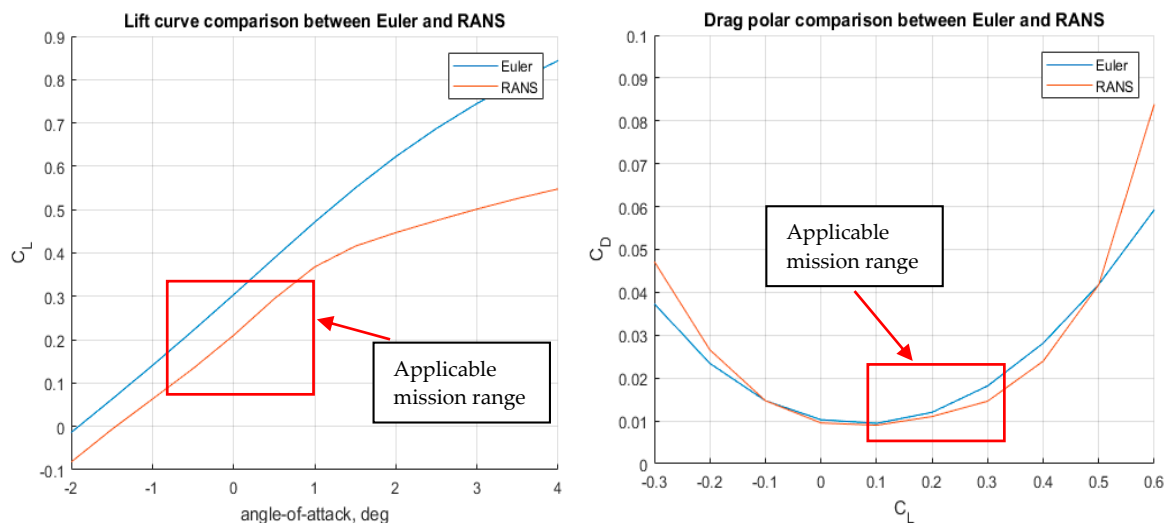


Figure 15. Aerodynamic performance comparison between RANS and Euler with the flat plate analogy for the skin friction drag.

The results show multiple trends. First, the RANS lift curve has a lower lift magnitude at a similar angle of attack when compared to the Euler solution. That is the cause of differences in pressure distribution and estimation of the shock wave strength. A similar trend was observed in [43] for the lift curve, where the lift coefficients at low angles of attack were similar with 0.5 deg difference between the experimental data and Euler solutions. After the angle of attack of 1 deg, the RANS lift curve starts showing non-linear behavior due to the generation of strong shock waves on the wing suction side. Such a trend is also observed for Euler solutions, but the Euler solution also does not simulate shock-induced separation, which happens in the RANS case; therefore, the reduction in the lift is lower in Euler compared to RANS. The drag polar shows that at low lift coefficient, the drag coefficient of RANS matches well with the Euler solutions plus the friction drag from flat plate analogy. However, deviations after the lift coefficient of 0.2 starts appearing. There is a good match between Euler (and friction drag) and RANS solution in drag polar until the lift coefficient of 0.5, but the drag polar of RANS then rises more rapidly due to the shock-induced separation. A similar increase in drag happens for lift coefficients below -0.1. The range of the whole mission lift coefficients falls between 0.1 and 0.35, while the cruise segment is completed at lift coefficients between 0.12 and 0.2. For such a range, a

combination of Euler results with the flat plate analogy shows sufficient accuracy for capturing the aircraft aerodynamics and estimating its mission performance.

7. Mission Performance Analysis of an Optimized Geometry

After a single-point optimization, the mission was calculated again to obtain modified results with the account of high-fidelity aerodynamics. Appendix A shows this simulation results, while Table 9 provides a comparison of relative changes among low/medium fidelity, high-fidelity analysis of the initial aircraft and optimized high-fidelity results with respect to B777 results

Table 9. Comparison of relative changes in key aircraft parameters with respect to B777.

Parameter	Initial SE ² A-LR Low Fidelity (%)	Initial SE ² A-LR High Fidelity (%)	Optimized SE ² A-LR High Fidelity (%)
MTOW (kg)	−58.5	−26.4	−51.1
OWE (kg)	−44.2	−39.9	−39.2
L/D _{max}	127.0	104.8	109.5
Average cruise L/D	83.8	−71.0	21.6
Block fuel (kg)	−73.6	24.1	−55.5
Fuel Efficiency (kg/seat/100 km)	−76.5	10.6	−60.3

The results show substantial improvements in mission analysis. However, improvements that are caused by new technologies do not match the low-fidelity analysis. Fuel efficiency improvement does not exceed 61% for the analysis while using higher fidelity tools. In addition, maximum L/D reduced from 50.5 to 39.5, which also demonstrates an increase in aircraft total drag. This shows that higher fidelity analysis plays an important role in initial stages of design and it should not be avoided if the design considers unconventional configurations.

Although the results demonstrate substantial improvement in aircraft performances, there are still uncertainties in the results, which will be addressed in future works. Limitations of analysis are driven by the uncertainty of expected technological benefits and their real performance. It was assumed that 80% of the wing will be laminar. However, no additional power required for the suction system was considered in the current analysis. Moreover, the effects of surface irregularities, such as landing gear doors, access panels, windows, etc., have not been considered. They might substantially reduce the laminarization of the vehicle or require unacceptable power for the suction system. In addition, the suction system weight was not considered at the moment due to a lack of information regarding the power required to suck the boundary layer from the wing. Other technologies, such as active load alleviation, boundary layer ingestion, and advanced structure concepts, also lack any surrogate data, which will be developed later under this research program.

8. Conclusions

The present manuscript describes a multi-fidelity design approach to design a fuel-efficient BWB aircraft. Multiple novel technologies have been integrated at the conceptual design phase to increase the aircraft efficiency and minimize negative environmental impact: active flow control (boundary layer suction), active load alleviation, boundary layer ingestion, and new materials and structure concepts. The presented approach was used to design a long-range BWB aircraft.

A multi-fidelity approach has been used to increase design accuracy. The SUAVE aircraft design environment with the integration of novel technologies module was used for mission analysis, OpenVSP and Gmesh were used for geometry modeling and mesh generation, and AVL and SU2 were used for aerodynamic analysis. Euler equations CFD analysis was used to minimize the computational costs and capture transonic aerodynamic effects.

A low/medium fidelity approach (using AVL for CFD) has shown significant improvement in fuel efficiency of a potential long-range aircraft—almost 76% increase in fuel efficiency as compared

to B777. However, mission analysis using SU2 demonstrated a substantial increase in drag due to compressibility that has not been captured by the lower fidelity analysis. A large increase in drag reduced fuel efficiency by 10.6% as compared to B777.

High-fidelity discrete-adjoint aerodynamic shape optimization using SU2 was performed to minimize the adverse effects of the wave drag. FFD approach was used to modify the aircraft geometry, and an SLSQP algorithm was used for optimization. The objective function was to reduce drag for an average cruise condition and geometric constraints of a maximum thickness not being less than 80% when compared to the initial design. The results showed a reduction of inviscid drag by 77% as compared to the initial configuration.

The validation of the combination of Euler surrogate data and the flat plate analogy was also performed and the results used in SUAVE were compared to RANS simulations for cruise conditions. The results show sufficient accuracy between two methods for low lift coefficients. In addition, the cruise segment is performed at similar low angles of attack, so the method is sufficiently accurate to simulate the flight mission.

A modified mission analysis with an optimized aircraft and higher fidelity aerodynamic analysis significantly improved the fuel efficiency as compared to the initial design: the fuel efficiency changed from +10.6% to −59.2% when compared to B777. However, an optimized solution did not match the lower fidelity analysis, which indicates the desire to introduce higher fidelity tools as early as possible in the conceptual design stage to have more accuracy during the design of unconventional aircraft configurations.

Future work will focus on multiple tasks. First, a new design iteration with focus on stability and control, weights and balance, and system layouts will be performed. Second, the refinement of drag coefficient estimation needs to be performed: RANS analysis with embedded porous wall boundary condition responsible for the boundary layer suction will be performed, and new surrogate drag values will be obtained and used in SUAVE to more accurately determine potential fuel savings. In addition, surrogate models of structural weight reduction, boundary layer ingestion, and active load alleviation will be implemented in SUAVE to more accurately estimate the potential benefits of novel technologies. Finally, an improved technique for the FFD definition will be implemented in SU2 to more uniformly distribute control points along with the aircraft geometry and increase the accuracy and flexibility of the shape optimization.

The present manuscript only covers very preliminary results based on the methods developed in the first stage of the project. The major concerns include the actual capabilities of investigated technologies. Changes in technology assumptions may significantly affect aircraft performance and fuel savings. The design will face multiple iterations with progressively increasing levels of design and analysis accuracy, fidelity, and depth.

Author Contributions: Conceptualization, S.K., Y.L., A.E.; methodology, S.K., Y.L., A.E.; software, S.K., Y.L.; validation, S.K.; formal analysis, S.K.; investigation, S.K.; writing—original draft preparation, S.K., Y.L.; writing—review and editing, A.E.; visualization, S.K.; supervision, A.E.; funding acquisition, A.E. All authors have read and agreed to the published version of the manuscript.

Funding: We would like to acknowledge the funding by the Deutsche Forschungsgemeinschaft (DFG, German Research Foundation) under Germany's Excellence Strategy—EXC 2163/1-Sustainable and Energy Efficient Aviation—Project-ID 390881007. Furthermore, we acknowledge support by the Open Access Publication Funds of the Technische Universität Braunschweig.

Conflicts of Interest: The authors declare no conflict of interest.

Appendix A Summary of SUAVE Analysis for All Analyzed Cases

Table A1. Weight break-down of B777 calculated using SUAVE.

Mass Items	Unit	Value
Maximum Take-off Weight (MTOW)	kg	347,452.0
Operating Weight Empty (OWE)	kg	157,432
Wing	kg	53,959
Fuselage	kg	29,032
Empennage	kg	7896.0
Propulsion group	kg	28,530
Landing gear	kg	13,898
Systems (including opt. and furn.)	kg	24,117
Breakdown of system mass		
Control systems	kg	2691
APU	kg	953
Hydraulics	kg	1386
Instruments	kg	363
Avionics	kg	408
Optionals	kg	3810
Electrical	kg	1769
Air conditioner	kg	2041
Furnish	kg	10,696

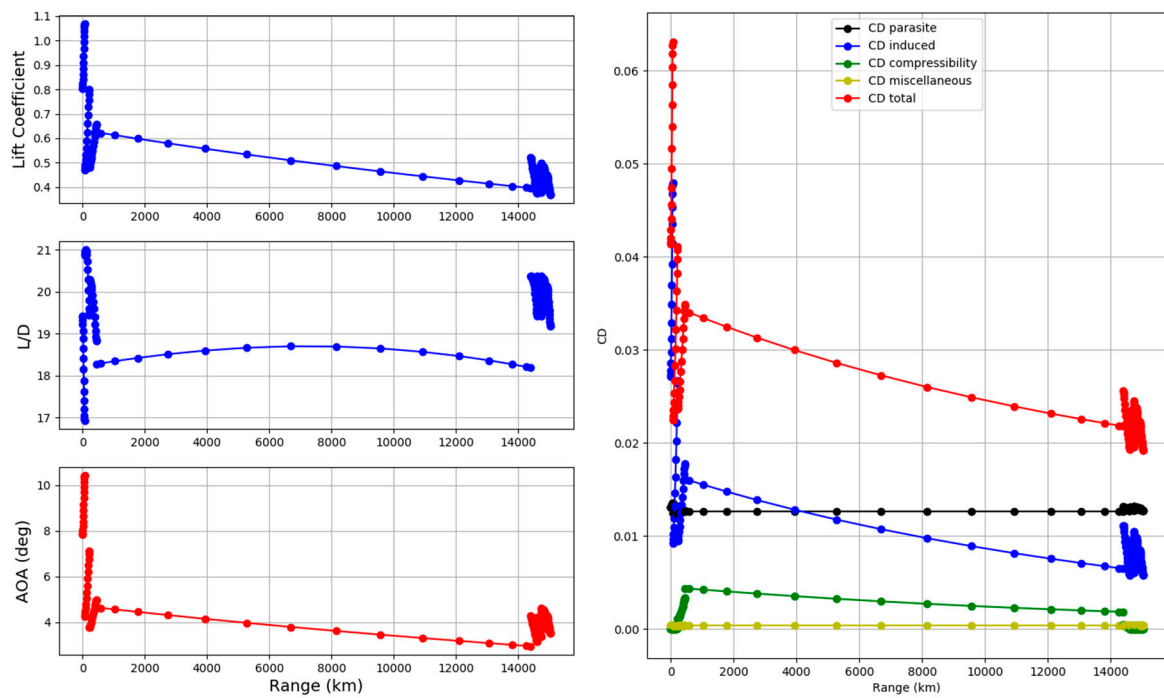


Figure A1. Aerodynamic performance of B777.

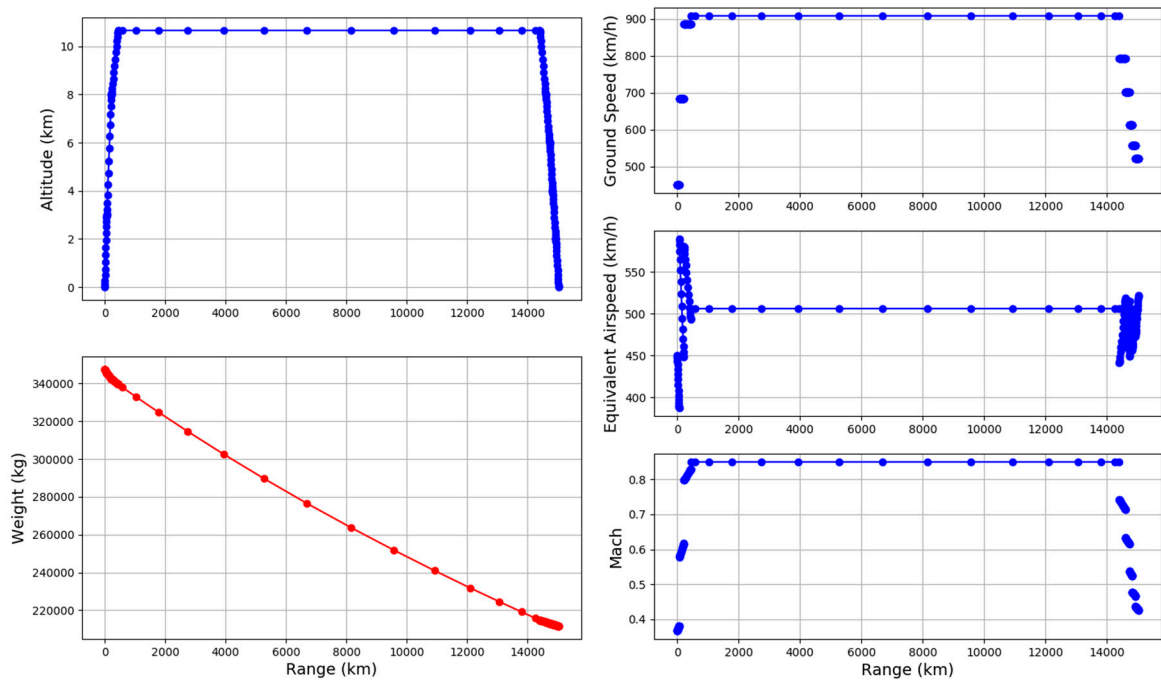


Figure A2. Mission performance of B777.

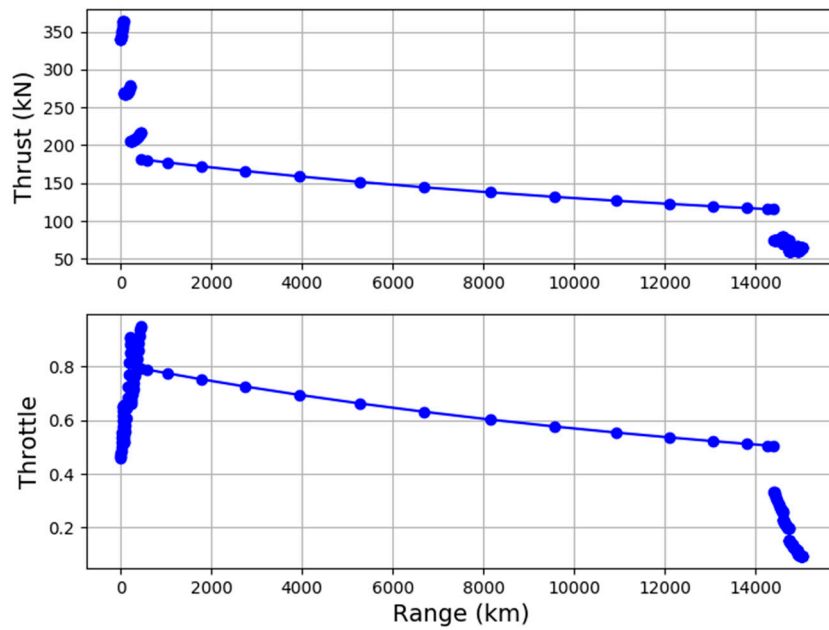


Figure A3. Thrust and throttle settings of SE²A-LR.

Table A2. Initial Weight break-down of SE²A-LR calculated using SUAVE.

Mass Items	Unit	Value
Operating Weight Empty (OWE)	kg	82,484
Wing	kg	10,930
Fuselage	kg	32,441
Propulsion group	kg	11,057
Landing gear	kg	5,699
Systems (including opt. and furn.)	kg	22,357
Breakdown of system mass		
Control systems	kg	1,489
APU	kg	953
Hydraulics	kg	828
Instruments	kg	363
Avionics	kg	408
Optionals	kg	3,810
Electrical	kg	1,769
Air conditioner	kg	2,041
Furnish	kg	10,696

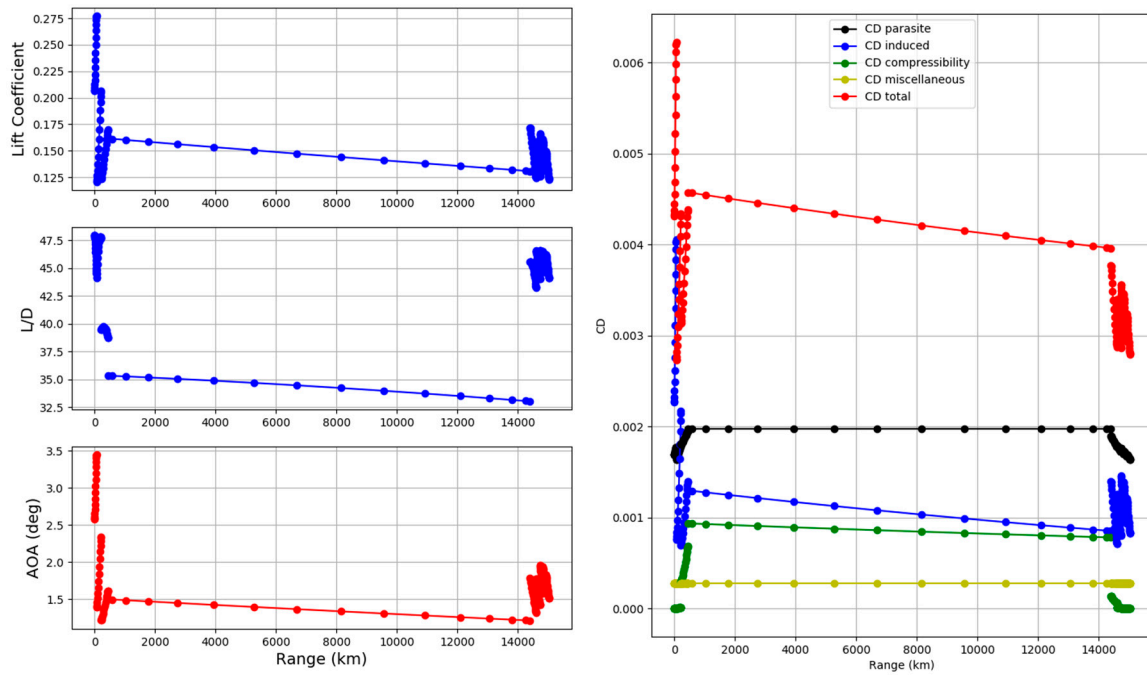


Figure A4. Aerodynamic performance of SE²A-LR.

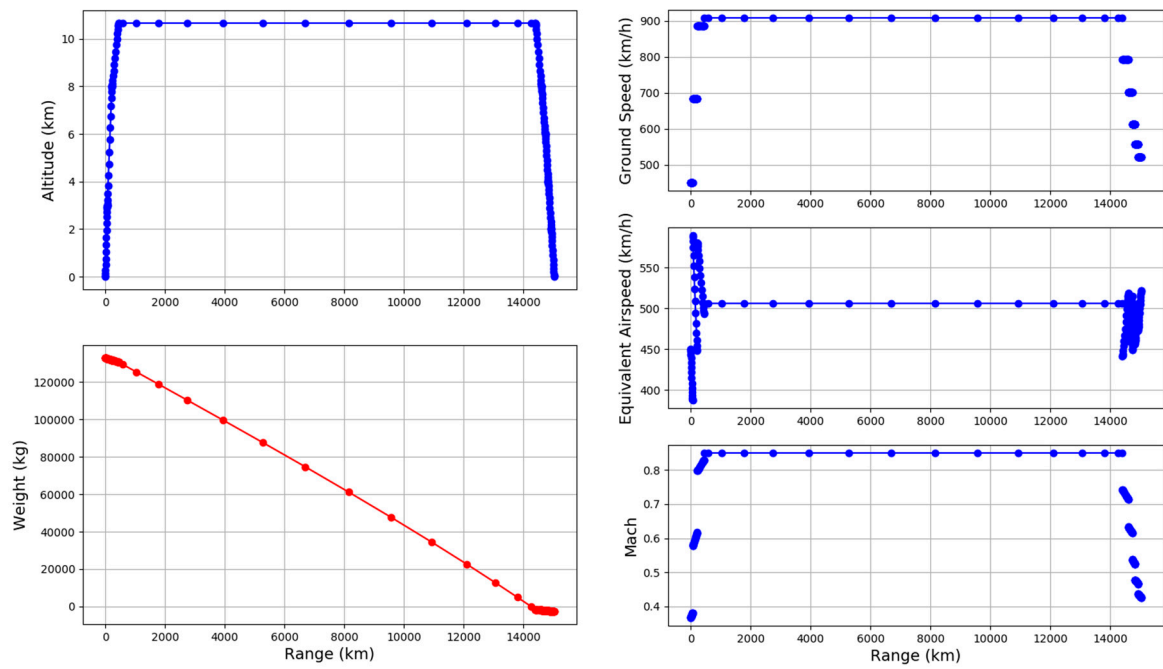


Figure A5. Mission performance of SE²A-LR.

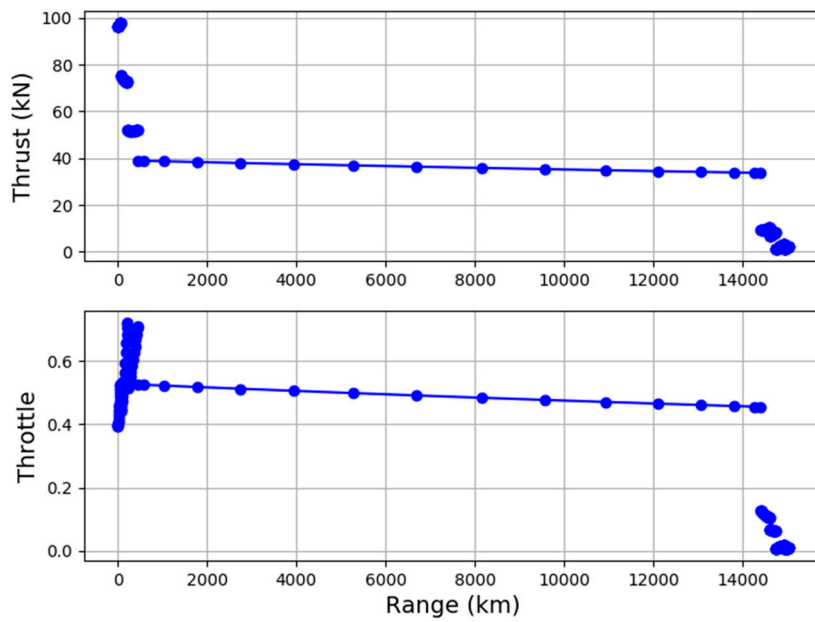


Figure A6. Thrust and throttle settings of SE²A-LR.

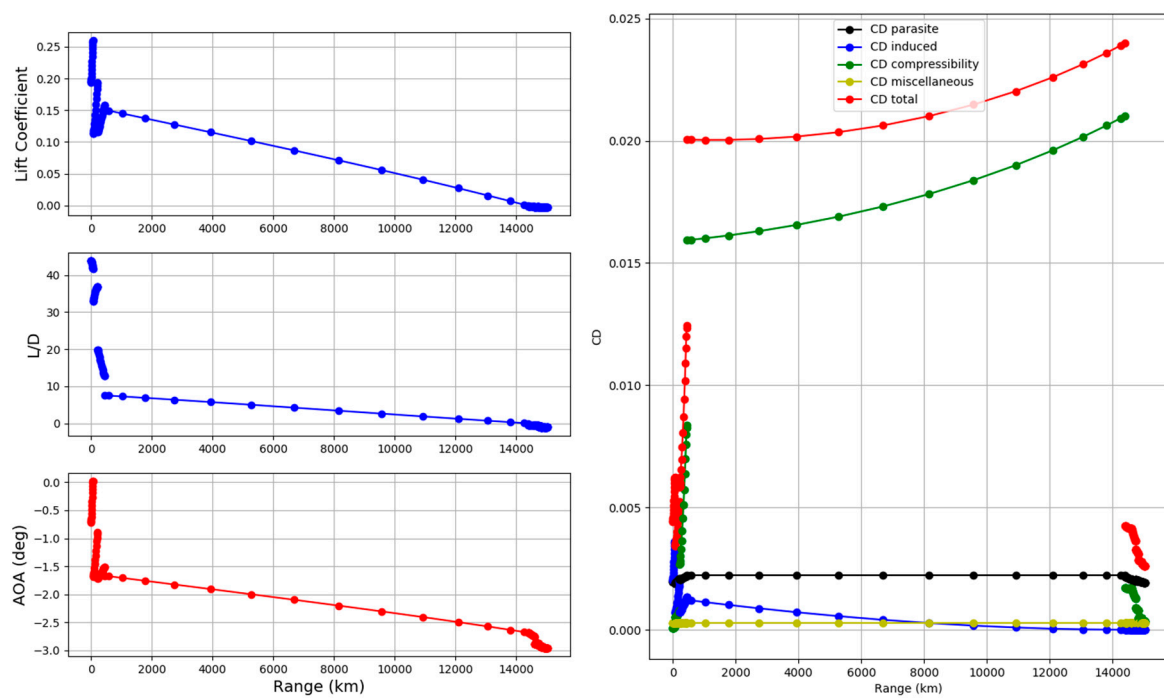


Figure A7. Aerodynamic performance of SE²A-LR calculated using SUAVE for higher-fidelity analysis.

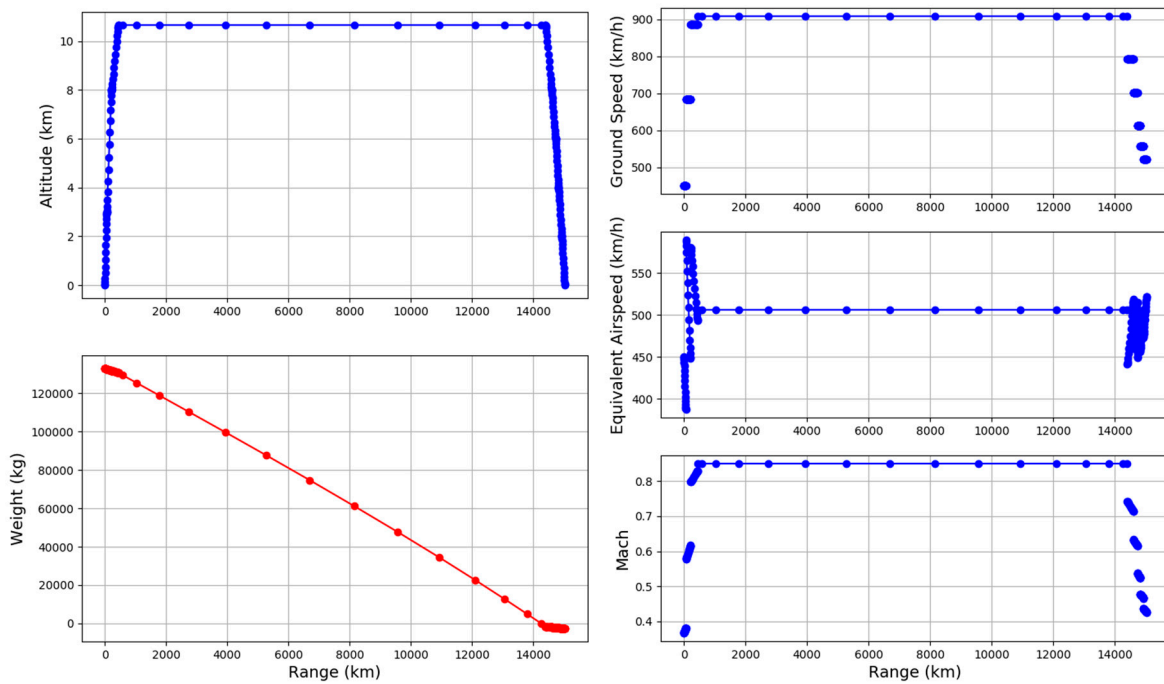


Figure A8. Mission performance of SE²A-LR.

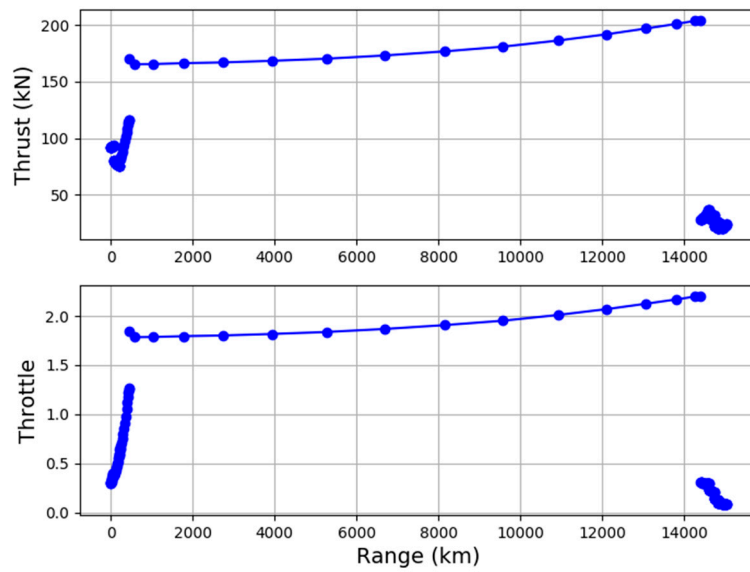


Figure A9. Thrust and throttle settings of SE²A-LR.

Table A3. Weight break-down of SE²A-LR calculated using SUAVE after optimization.

Mass Items	Unit	Value
Operating Weight Empty (OWE)	kg	88,318
Wing	kg	12,180
Fuselage	kg	33,412
Propulsion group	kg	13,594
Landing gear	kg	6774
Systems (including opt. and furn.)	kg	22,357
Breakdown of system mass		
Control systems	kg	1489
APU	kg	953
Hydraulics	kg	828
Instruments	kg	363
Avionics	kg	408
Optionals	kg	3810
Electrical	kg	1769
Air conditioner	kg	2041
Furnish	kg	10,696

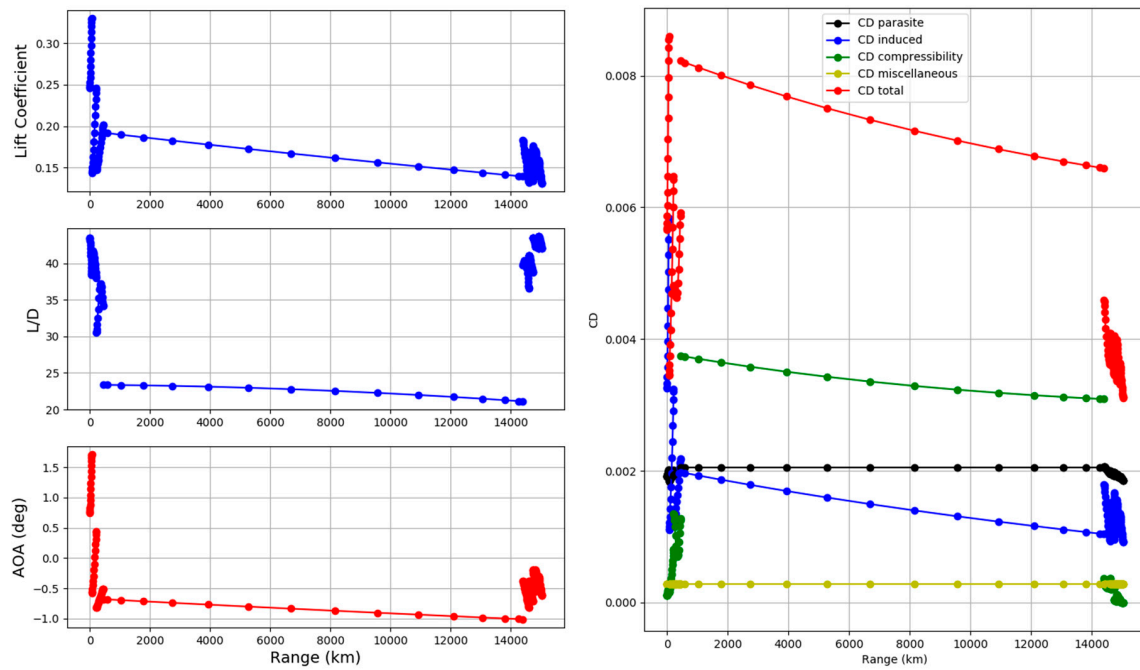


Figure A10. Aerodynamic performance of SE²A-LR.

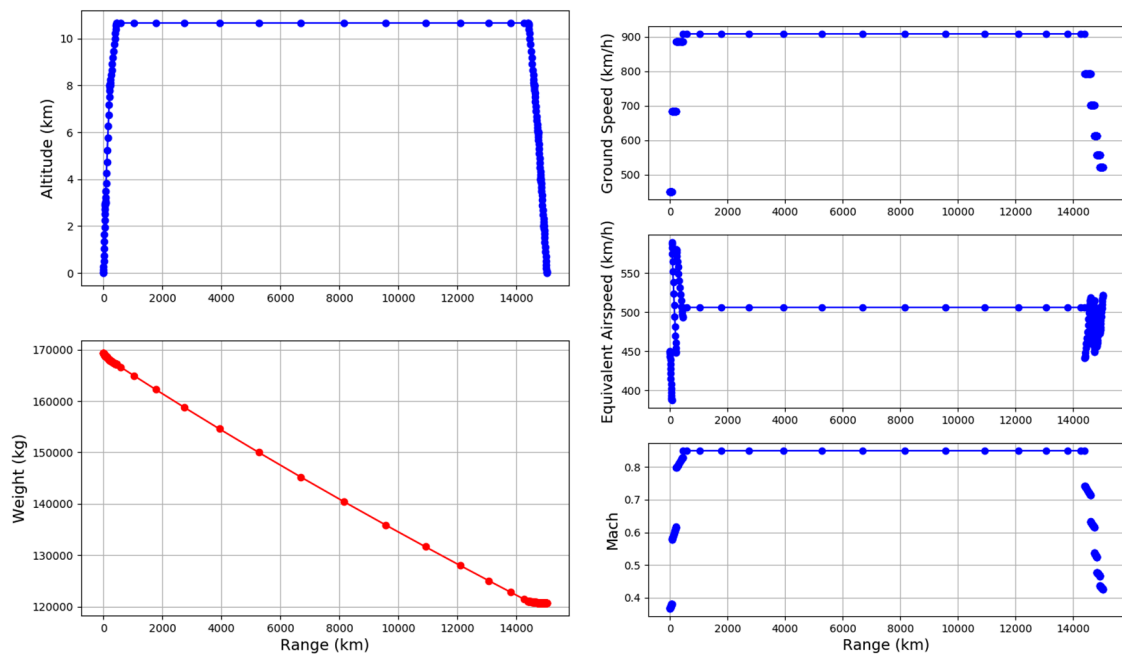


Figure A11. Mission performance of SE²A-LR.

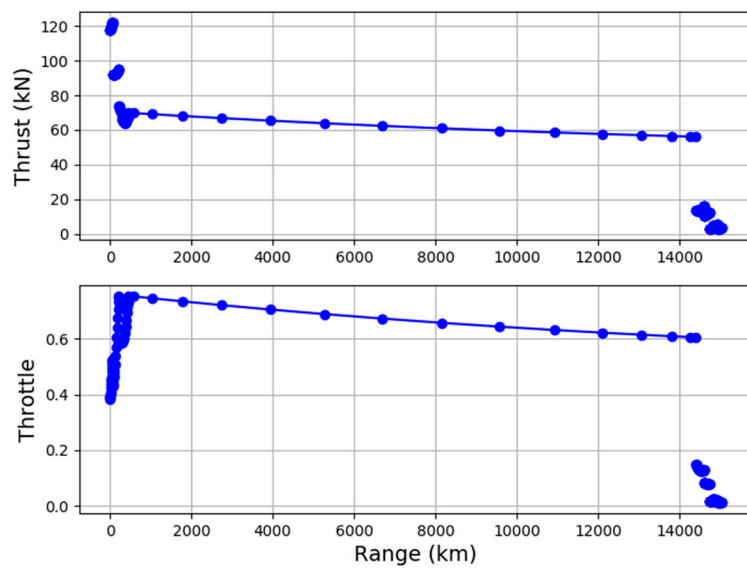


Figure A12. Thrust and throttle settings of SE²A-LR.

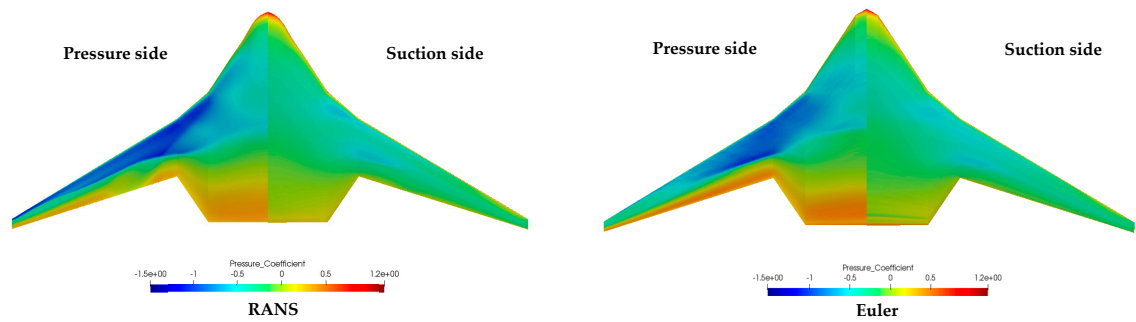


Figure A13. Pressure coefficients for RANS and Euler simulations at AoA = -2 deg.

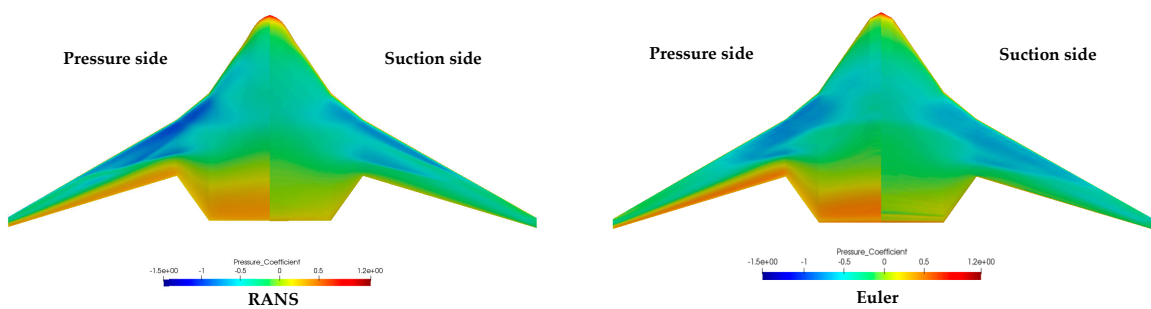


Figure A14. Pressure coefficients for RANS and Euler simulations at AoA = -1 deg.

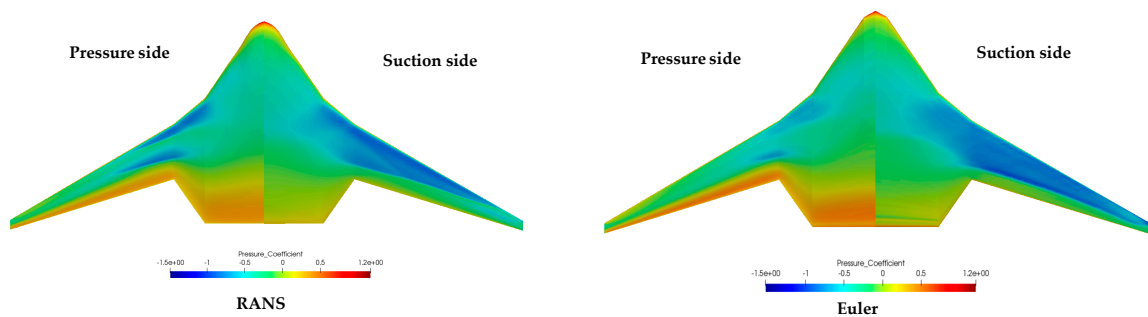


Figure A15. Pressure coefficients for RANS and Euler simulations at AoA = 0 deg.

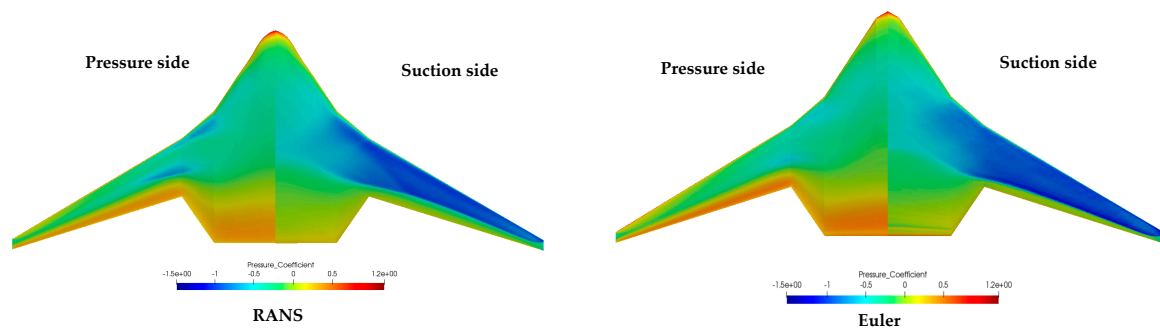


Figure A16. Pressure coefficients for RANS and Euler simulations at AoA = 1 deg.

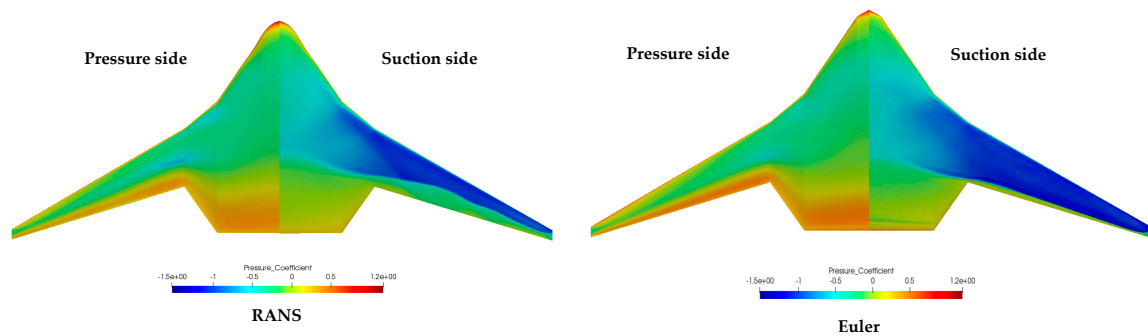


Figure A17. Pressure coefficients for RANS and Euler simulations at AoA = 2 deg.

References

1. *Flightpath 2050-Europe's Vision for Aviation: Advisory Council for Aeronautics Research in Europe*; EUROPEAN COMMISSION: Brussels, Belgium, 2011.
2. Liu, Y.; Elham, A.; Horst, P.; Hepperle, M. Exploring Vehicle Level Benefits of Revolutionary Technology Progress via Aircraft Design and Optimization. *Energies* **2018**, *11*, 166. [[CrossRef](#)]
3. Liebeck, R.H. Design of the Blended Wing Body Subsonic Transport. *J. Aircr.* **2004**, *41*, 10–25. [[CrossRef](#)]
4. Okonkwo, P.; Smith, H. Review of evolving trends in blended wing body aircraft design. *Prog. Aerosp. Sci.* **2016**, *82*, 1–23. [[CrossRef](#)]
5. Xu, J.; Kroo, I. Aircraft Design with Active Load Alleviation and Natural Laminar Flow. *J. Aircr.* **2014**, *51*, 1532–1545. [[CrossRef](#)]
6. Greitzer, E.M.; Bonnefoy, P.A.; DelaRosaBlanco, E.; Dorbian, C.S.; Drela, M.; Hall, D.K.; Hansman, R.J.; Hileman, J.I.; Liebeck, R.H.; Lovegren, J.; et al. *N+ 3 Aircraft Concept Designs and Trade Studies. Volume 2: Appendices-Design Methodologies for Aerodynamics, Structures, Weight, and Thermodynamic Cycles*; NASA/CR—2010-216794/VOL2; NASA: Washington, DC, USA, 2010.
7. Greitzer, E.M.; Bonnefoy, P.A.; DelaRosaBlanco, E.; Dorbian, C.S.; Drela, M.; Hall, D.K.; Hansman, R.J.; Hileman, J.I.; Liebeck, R.H.; Levegren, J.; et al. *N+ 3 Aircraft Concept Designs and Trade Studies*; NASA: Washington, DC, USA, 2010; Volume 1.
8. Bradley, M.K.; Droney, C.K. *Subsonic Ultra-Green Aircraft Research Phase II: N+ 4 Advanced Concept Development*; NASA/CR-2012-217556; NASA: Washington, DC, USA, 2012.
9. Saeed, T.I.; Graham, W.R. Design Study for a Laminar-Flying-Wing Aircraft. *J. Aircr.* **2015**, *52*, 1373–1385. [[CrossRef](#)]
10. Beck, N.; Landa, T.; Seitz, A.; Boermans, L.; Liu, Y.; Radespiel, R. Drag Reduction by Laminar Flow Control. *Energies* **2018**, *11*, 252. [[CrossRef](#)]
11. Risse, K.; Stumpf, E. Conceptual Aircraft Design including Hybrid Laminar Flow Control. *CEAS Aeronaut. J.* **2014**, *5*, 333–343. [[CrossRef](#)]
12. Bussemaker, J.H. Wing Optimization with Active Load Control. Master's Thesis, Faculty of Aerospace Engineering, Flight Performance, and Propulsion, TU Delft, Delft, The Netherlands, 2018.

13. Xu, J. Aircraft Design with Active Load Alleviation and Natural laminar Flow. Ph.D. Thesis, Department of Aeronautics & Astronautics, Stanford University, Stanford, CA, USA, 2014.
14. Rossow, C.-C.; von Geyr, H.; Hepperle, M. *The 1g-Wing, Visionary Concept or Naive Solution?* DLR-IB-AS-BS-2016-121; DLR Interner Bericht: Braunschweig, Germany, 2016.
15. Liu, X.; Sun, Q. *Gust Load Alleviation with Robust Control for a Flexible Wing, Shock and Vibration*; ID 1060574; Hindawi Publishing Corporation: London, UK, 2016; Volume 2016. [[CrossRef](#)]
16. Ying, B.; Changchun, X. Gust load alleviation wind tunnel tests of a large-aspect-ratio flexible wing with piezoelectric control. *Chin. J. Aeronaut.* **2017**, *30*, 292–309.
17. Blumenthal, B.; Elmiligui, A.; Geiselhart, K.; Campbell, R. Computational Investigation of a Boundary-Layer-Ingestion Propulsion System. *J. Aircr.* **2018**, *55*, 1141–1153. [[CrossRef](#)]
18. Uranga, A.; Drela, M.; Greitzer, E.; Hall, D.; Tichener, N.; Lieu, M.; Siu, N.; Casses, C.; Huang, A. Boundary Layer Ingestion Benefit of the D8 Transport Aircraft. *AIAA J.* **2017**, *55*, 3693–3708. [[CrossRef](#)]
19. Zhang, J.; Kang, W.; Yang, L. Aerodynamic benefits of boundary layer ingestion for distributed propulsion configuration. *Aircr. Eng. Aerosp. Technol.* **2019**, *91*, 1285–1294. [[CrossRef](#)]
20. Gray, J.; Martins, J. Coupled Aeropropulsive Design Optimization of Boundary Layer Ingestion Propulsor. *Aeronaut. J. R. Aeronaut. Soc.* **2018**, *123*, 1–19.
21. Budziszewski, N.; Friedrichs, J. Modelling of a Boundary Layer Ingesting Propulsor. *Energies* **2018**, *21*, 708. [[CrossRef](#)]
22. Giesecke, D.; Lehmler, M.; Friedrichs, J.; Blinstrub, J.; Bertsch, L.; Heinze, W. Evaluation of ultra-high bypass ratio engines for an over-wing aircraft configuration. *GPPS J.* **2018**. [[CrossRef](#)]
23. Bishara, M.; Horst, P.; Madhusoodanan, H.; Brod, M.; Daum, B.; Rolfes, R. A Structural Design Concept for a Multi-Shell Blended Wing Body with Laminar Flow Control. *Energies* **2018**, *11*, 383. [[CrossRef](#)]
24. Lukaczyk, T.W.; Wendorff, A.D.; Colonno, M.; Economon, T.D.; Alonso, J.J.; Orra, T.H.; Ilario, C. SUAVE: An Open-Source Environment for Multi-Fidelity Conceptual Vehicle Design. In Proceedings of the 16th AIAA/ISSMO Multidisciplinary Analysis and Optimization Conference, American Institute of Aeronautics and Astronautics, Dallas, TX, USA, 22–25 June 2015.
25. Economon, T.D.; Palacios, F.; Copeland, S.R.; Lukaczyk, T.W.; Alonso, J.J. SU2: An Open-Source Suite for Multiphysics Simulation and Design. *AIAA J.* **2016**, *54*, 828–846. [[CrossRef](#)]
26. Fredericks, W.; Antclif, K.; Costa, G.; Deshpande, N.; Moore, M.; Miguel, E.S.; Snyder, A. Aircraft Conceptual Design Using Vehicle Sketch Pad. In Proceedings of the 48th AIAA Aerospace Sciences Meeting including the New Horizons Forum and Aerospace Exposition, Orlando, FL, USA, 4–7 January 2010.
27. Abramson, M.A.; Audet, C.; Couture, G.; Dennis John, E., Jr.; Le Digabel, S.; Tribes, C. The NOMAD Project. 2014. Available online: <http://www.gerad.ca/nomad> (accessed on 6 June 2020).
28. van Dommelen, J.; Vos, R. Conceptual Design and Analysis of a Blended-Wing-Body Aircraft. *SAGE J.* **2014**. [[CrossRef](#)]
29. Drela, M.; Youngeren, H. AVL-Athena Vortex Lattice code. *MIT Aero Astro. Proc IMechE Part G J. Aerosp. Eng.* **2014**, *228*, 2452–2474.
30. Safran CFM 56-7B22 Engine Specifications. Available online: <https://www.safran-aircraft-engines.com/commercial-engines/single-aisle-commercial-jets/cfm56/cfm56-7b> (accessed on 6 June 2020).
31. Botero, E.M.; Wendorff, A.; MacDonald, T.; Variyar, A.; Vegh, J.M.; Lukaczyk, T.W.; Alonso, J.J.; Orra, T.H.; da Silva, C.I. SUAVE: An Open-Source Environment for Conceptual Vehicle Design and Optimization. In Proceedings of the 54th AIAA Aerospace Sciences Meeting, American Institute of Aeronautics and Astronautics, San Diego, CA, USA, 4–8 January 2016.
32. MacDonald, T.; Botero, E.; Vegh, J.M.; Variyar, A.; Alonso, J.J.; Orra, T.H.; da Silva, C.R.I. SUAVE: An Open-Source Environment Enabling Unconventional Vehicle Designs through Higher Fidelity. In Proceedings of the 55th AIAA Aerospace Sciences Meeting, American Institute of Aeronautics and Astronautics, Grapevine, TX, USA, 9–13 January 2017.
33. MacDonald, T.; Clarke, M.; Botero, E.M.; Vegh, J.M.; Alonso, J.J. SUAVE: An Open-Source Environment Enabling Multi-Fidelity Vehicle Optimization. In Proceedings of the 18th AIAA/ISSMO Multidisciplinary Analysis and Optimization Conference, Denver, CO, USA, 5–9 June 2017.
34. Chen, Z.; Zhang, M.; Chen, Y.; Sang, W.; Tan, Z.; Li, D.; Zhang, B. Assessment on critical technologies for conceptual design of blended-wing-body civil aircraft. *Chin. J. Aeronaut.* **2019**, *32*, 1797–1827. [[CrossRef](#)]



35. Kozek, M.; Schirrer, A. *Modeling and Control for a Blended Wing Body Aircraft*; Springer International Publishing: Berlin, Germany, 2015; ISBN 978-3-319-10791-2.
36. Peifeng, L.; Binqian, Z.; Yingchun, C.; Changsheng, Y.; Yu, L. Aerodynamic Design Methodology for Blended Wing Body Transport. *Chin. J. Aeronaut.* **2012**, *25*, 508–516.
37. Palacios, F.; Economon, T.D.; Aranake, A.; Copeland, S.R.; Lonkar, A.K.; Lukaczyk, T.W.; Manosalvas, D.E.; Naik, K.R.; Padron, S.; Tracey, B.; et al. Stanford University Unstructured (SU2): Analysis and Design Technology for Turbulent Flows. In Proceedings of the 52nd Aerospace Sciences Meeting, American Institute of Aeronautics and Astronautics, Harbor, MD, USA, 13–17 January 2014.
38. Gudmundsson, S. *General Aviation Aircraft Design: Applied Methods and Procedures*; Butterworth-Heinemann: Oxford, UK, 2013; ISBN 0123973295.
39. Bouhlel, M.A.; Hwang, J.T.; Bartoli, N.; Lafage, R.; Morlier, J.; Martins, J.R.R.A. A Python surrogate modeling framework with derivatives. *Adv. Eng. Softw.* **2019**, *135*, 102662. [[CrossRef](#)]
40. Pauli, V.; Ralf, G.; Travis, E.O.; Matt, H.; Tyler, R.; David, C.; Evgeni, B.; Pearu, P.; Warren, W.; Jonathan, B.; et al. SciPy 1.0: Fundamental Algorithms for Scientific Computing in Python. *Nat. Methods* **2020**, in press.
41. Qin, N.; Vavalle, A.; le Moigne, A.; Laban, M.; Hackett, K.; Weinerfeit, P. Aerodynamic Studies for Blended Wing Body Aircraft. In Proceedings of the 9th AiAA/ISSMO Symposium on Multidisciplinary Analysis and Optimization, Atlanta, GA, USA, 4–6 September 2002.
42. Pointwise Mesh Generation Software. Available online: <https://www.pointwise.com/> (accessed on 6 June 2020).
43. Hicks, R.; Cliff, S.; Melton, J.; Langhi, R.; Goodsell, A.; Robertson, D.; Moyer, S. *Euler and Potential Experiment/CFD Correlations for a Transport and Two Delta-Wing Configurations*, NASA Technical Memorandum 102208; NASA: Washington, DC, USA, 1990.



© 2020 by the authors. Licensee MDPI, Basel, Switzerland. This article is an open access article distributed under the terms and conditions of the Creative Commons Attribution (CC BY) license (<http://creativecommons.org/licenses/by/4.0/>).

Article

Simulation and Test of Discrete Mobile Surfaces for a RC-Aircraft

Francesco Nicassio [†] and Gennaro Scarselli ^{*,†}

Department of Engineering for Innovation, University of Salento, Via per Monteroni, 73100 Lecce, Italy; francesco.nicassio@unisalento.it

* Correspondence: gennaro.scarselli@unisalento.it; Tel.: +39-0832-299720

† These authors contributed equally to this work.

Received: 10 June 2019; Accepted: 1 November 2019; Published: 5 November 2019



Abstract: Morphing structures suitable for unmanned aerial vehicles (UAVs) have been investigated for several years. This paper presents a novel lightweight, morphing concept based on the exploitation of the “lever effect” of a bistable composite plate that can be integrated in an UAV horizontal tail. Flight dynamics equations are solved in Simulink environment, thus being able to simulate and compare different flight conditions with conventional and bistable command surfaces. Subsequently, bistable plates are built by using composite materials, paying particular attention to dimensions, asymmetric stacking sequence and total thickness needed to achieve bistability. NACA0011 airfoil is chosen for proving this concept. Wind tunnel tests demonstrate that the discrete surface is capable of withstanding the aerodynamic pressure. A remotely piloted vehicle is employed to test the discrete horizontal tail command during the take-off. The results show that, choosing a proper configuration of constraints, stacking sequence and aspect ratio for the bistable laminate, it is possible to tailor the snap-through mechanism. The proposed concept appears lighter and increases aerodynamic efficiency when compared to conventional UAV command surfaces.

Keywords: morphing surfaces; bistable materials; RC-UAV

1. Introduction

Unmanned aerial vehicles (UAVs) may operate with various degrees of autonomy: either under remote control (RC) by a human operator or autonomously by on-board computers [1–3]. Compared to manned aircraft, UAVs were originally used for missions dull, dirty or dangerous and they can operate in environments contaminated by chemical, biological or radioactive agents. While they originally fitted mostly military applications, now their use is rapidly expanding to commercial, scientific, agricultural, recreational and other civil applications [4–8]. For this reason, in recent years there has been an increasing interest for (i) lighter-than-air UAVs with significantly higher endurance that can be used for persistent area surveillance [9]; (ii) long-endurance UAVs that can fly for several days [10–12] and (iii) small UAVs that are versatile, portable and easy to maintain [13,14].

In addition to these applications, UAVs provide an ideal platform for exploring and developing innovative solutions in the aeronautical engineering since the risk level is acceptable at this scale, and they have more manageable fabrication and less operational costs [15]. One example of this is the emergent idea of a morphing concept applied to aircraft lifting surfaces, which is the focus of this work. On this topic, several alternatives are reported in the technical literature, in terms not only of materials and structural parameters but also of feasibility and efficiency of the proposed solutions [16]. De Breuker and Werter in [17] demonstrated the strong influence of the aircraft speed on the maximum values of actuation forces in a morphing mechanism as well as the importance of the order in which various morphing deformations are executed. An adaptive trailing edge concept

was presented in [18] by combining conventional parts and innovative concepts, as the morphing skin assembled into a new structural system: an outboard wing trailing edge, consisting of three articulated (finger-like) rib covered by a multi-material hyperelastic skin. In [19] the antagonistic shape memory alloys (SMA) were used for wing morphing of small RC UAVs reducing the weight due to the actuation systems. Pecora et al. in [20,21] studied the design assessment of an innovative flap architecture for a variable-camber trailing edge: the reference geometry was based on a wing, where the conventional flap component was replaced by a morphing trailing edge based on compliant ribs.

Among the morphing solutions proposed in last years, in terms of materials able to withstand aerodynamic loads, multistable materials were investigated for UAV morphing concepts: multistability is the property of varying geometrical shape with only small energy input and structures having this attribute represent an interesting candidate for the development of morphing solutions. Nicassio et al. in [22] explored bistable plates dynamic behavior for designing novel morphing command surfaces. In order to improve the UAVs aerodynamic performances, in [23] a prototype of morphing winglet utilizing a metallic bistable structure and polymer was presented. The metallic bistable structure was manufactured by bending a metal sheet and had two stable shapes: one was flat and the other was curved. To obtain an airfoil shape, the metallic bistable structure was placed in a mold with the shape of the airfoil and the polymer was poured into the mold for keeping the shape. The main finding of [24] is that multistable winglets are effective (especially at large dynamic pressure and angles of attack (AOAs)) in controlling the lateral and directional stability, but their efficiency in the lateral control, especially at low dynamic pressures, strongly diminishes respect to conventional ailerons. In addition, since their operational capabilities are strongly affected by the AOA, they can suffer roll reversal phenomena when wing's AOAs are negative. Wang in [25] demonstrated that a morphing bistable composite structure could be produced, based on the principles of viscoelastically generated prestress: a composite plate structure was created in order to snap into one of two cylindrical states. In [26] guidelines were proposed to design a morphing unsymmetric panel/actuator assembly, while in [15] a passive mobile surface with a bistable plate was presented. In the latter paper, the bistable morphing surface was activated using a proper configuration of constraints. These ad-hoc boundary conditions allowed the snap-through with activating forces of magnitude comparable with the differential pressure around a typical aeronautical airfoil. The possible applications of such behavior were the bistable composite integration in a low energy passive mobile surface able to autonomously react to pressure variations with a lift reduction when a maximum altitude was reached and vice versa.

In the present manuscript a novel horizontal stabilizer concept for small RC-UAV (illustrated in the schematic of Figure 1) is designed by using composite bistable plates on which, in the future, micro fiber composite (MFC) will be applied and used as actuators. The main goals of this work are to (i) enhance the aerodynamic efficiency of the UAV control surfaces through the activation system integrated in the wing/tail box, (ii) replace the conventional UAV mechanical flight control system with an electronic one, with a resulting weight reduction, (iii) reduce the energy/load requirement since this system does not require transducers or servo-actuators to maintain the stable shapes but just to activate the snap-through.

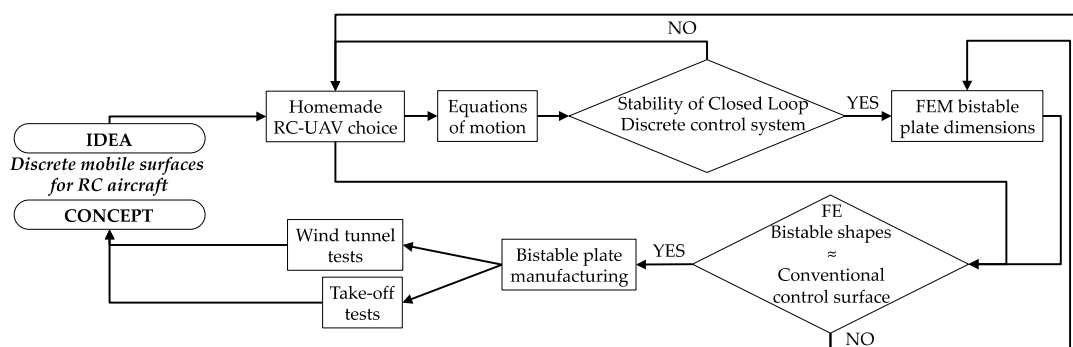


Figure 1. Schematic of the present research.

The main advantages of this proposed concept are the following: the concept based on the activation of bistable is mechanically much simpler than the conventional mechanisms needed for the control of the mobile surfaces, consisting in command lines, pulleys, hinges and so on; one direct consequence of the simplicity is that also the inspection and maintenance are relatively easier for the bistable command system than the conventional one; in addition, the energy/load requested by the proposed solution is also lower than the one requested by the common kinematic chains, since in the latter the deflection of the mobile surface must be kept by an external reaction force able to withstand the aerodynamic pressure while in the former the deflection of the mobile surface is kept by an internal reaction force due to the thermal residual stresses inside the bistables.

The present manuscript is not intended to cover all the design aspects typical of an aeronautical part even simple like the control surface of a small UAV. The activities hereinafter reported are a preliminary investigation about the technical feasibility of a control surface based on the employment of bistable materials. As such, the following research questions are addressed and answered: is it possible to control the flight of a typical UAV relying on a control surface capable only of discrete displacements? Can a bistable plate mimicking the conventional control surface with a reasonable weight and cost be designed and manufactured? Can such a plate actually be integrated into an aeronautical base profile?

Following the choice of the UAV benchmark, the flight dynamics equations are implemented in MATLAB (Version R2015, The MathWorks, Inc., Natick, MA, USA) and Simulink environment in order to simulate different flight conditions (e.g., open and closed loop simulation, gust response and take-off maneuver). After checking the stability of closed loop bistable control system, the analytical results, in terms of discrete displacement of mobile surfaces to reach specific mission goals (i.e., elevator, ailerons and rudder), are used for the finite element (FE) simulations as design requirements (how much the bistable plate must deform). By using appropriate boundary conditions, it is demonstrated that the bistable shapes can be tailored to match these requirements. From the results of the FE analyses, carbon fiber reinforced polymers (CFRPs) plates were manufactured with aspect ratio (AR), total thickness, dimensions and asymmetric stacking sequence previously simulated in order to achieve the bistability. In the next step, wind tunnel tests are carried out in order to prove that the bistable system (integrated in a wing sample with the same UAV airfoil) remains in one of two stable geometries during the test and both the states are able to withstand the aerodynamic loads without any additional holding forces or locking mechanisms. Eventually, the discrete mobile surface behavior is validated by real flight tests. At this stage of the investigation using a conventional mobile surface in the “discrete mode” (just two possible deflections) is the only possible experiment. Following the experiments, the numerical model is furthermore validated matching the experimental take-off lengths with the numerical ones. The main finding is that the proposed innovative concept of bistable control surfaces actually works and the research can go to the next step: the implementation of an actual prototype of new horizontal stabilizer, by using bistable plates for the vehicle subject of study.

2. Models, Materials and Methods

2.1. Flight Dynamics Equations and UAV Features

Under the hypotheses of flight in calm air, the motion equations valid for the UAV subject of investigation in the present study [27] can be expressed in an inertial frame and projected over a set of body-axes (see Figure 2).

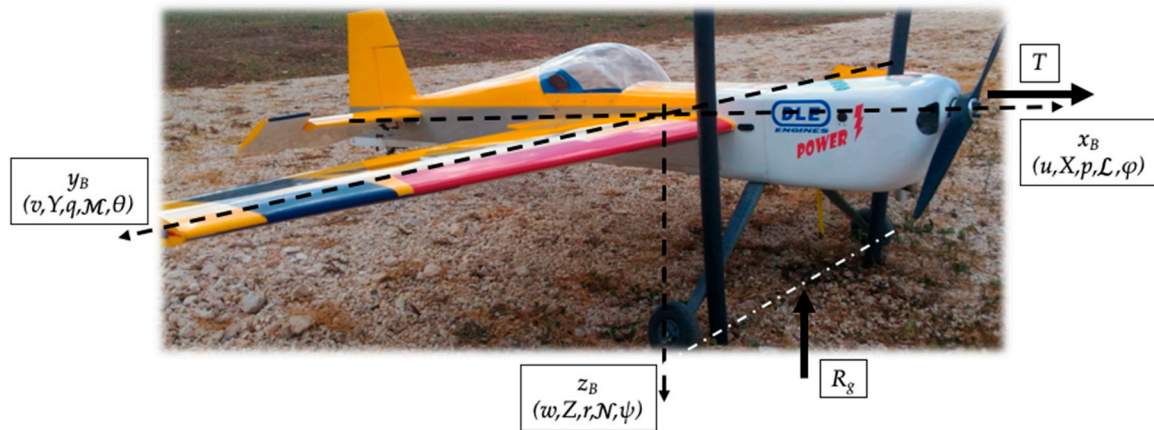


Figure 2. Unmanned aerial vehicle (UAV) body axes (x_B, y_B, z_B) with: (u, v, w) velocities of the UAV centre of mass; (X, Y, Z) aerodynamic forces; (p, q, r) angular speeds; (L, M, N) roll, pitch and yaw aerodynamic moments, (ϕ, θ, ψ) roll, pitch and yaw angles; T thrust; R_g ground reaction; m mass.

They form a system of 12 first order nonlinear ordinary differential equations (ODEs):

- Dynamics of the centre of mass:

$$\begin{cases} \dot{u} + qw - rv = (X + T_x)/m - g \sin \theta \\ \dot{v} + ru - pw = (Y + T_y)/m + g \cos \theta \sin \phi \\ \dot{w} + pv - qu = (Z + T_z)/m + g \cos \theta \cos \phi - R_g \end{cases} \quad (1)$$

- Attitude dynamics:

$$\begin{cases} I_x \dot{p} - I_{xz}(\dot{r} + pq) - (I_y - I_z)qr = L \\ I_y \dot{q} - I_{xz}(r^2 - p^2) - (I_z - I_x)rp = M \\ I_z \dot{r} - I_{xz}(\dot{p} - qr) - (I_x - I_y)pq = N \end{cases} \quad (2)$$

- Attitude kinematics:

$$\begin{cases} \dot{\phi} = p + q \sin \phi \tan \theta + r \cos \phi \tan \theta \\ \dot{\theta} = q \cos \phi - r \sin \phi \\ \dot{\psi} = q \sin \phi / \cos \theta + r \cos \phi / \cos \theta \end{cases} \quad (3)$$

- Trajectory of the centre of mass:

$$\begin{cases} \dot{R}_N = u \cos \theta \cos \psi + v(\sin \phi \sin \theta \cos \psi - \cos \phi \sin \psi) + w(\cos \phi \sin \theta \cos \psi + \sin \phi \sin \psi) \\ \dot{R}_E = u \cos \theta \sin \psi + v(\sin \phi \sin \theta \sin \psi + \cos \phi \cos \psi) + w(\cos \phi \sin \theta \sin \psi - \sin \phi \cos \psi) \\ \dot{h} = -(-u \sin \theta + v \sin \phi \cos \theta + w \cos \phi \cos \theta). \end{cases} \quad (4)$$

In order to carry out the experimental campaign, a homemade RC UAV was selected. The choice of this UAV was based on the following reasons: it is simple to be managed; its basic main structure allows the future use of bistable surfaces; its aerodynamic behavior is easy to be simulated and many investigations on this type of aircraft are reported in the literature and research works; lastly the installed airfoil is widely used in mini UAV and small UAV, that represent the final application of this study. Geometric dimensions of the RC UAV are reported in Figure 3, mass, aerodynamic and thrust features in Table 1.

In order to verify the centre of mass position and to obtain the inertia moments of the actual UAV, a CAD model was developed using CATIA software (Version V5-6 R24 R2014, Dassault Systèmes SE, Vélizy-Villacoublay, France).

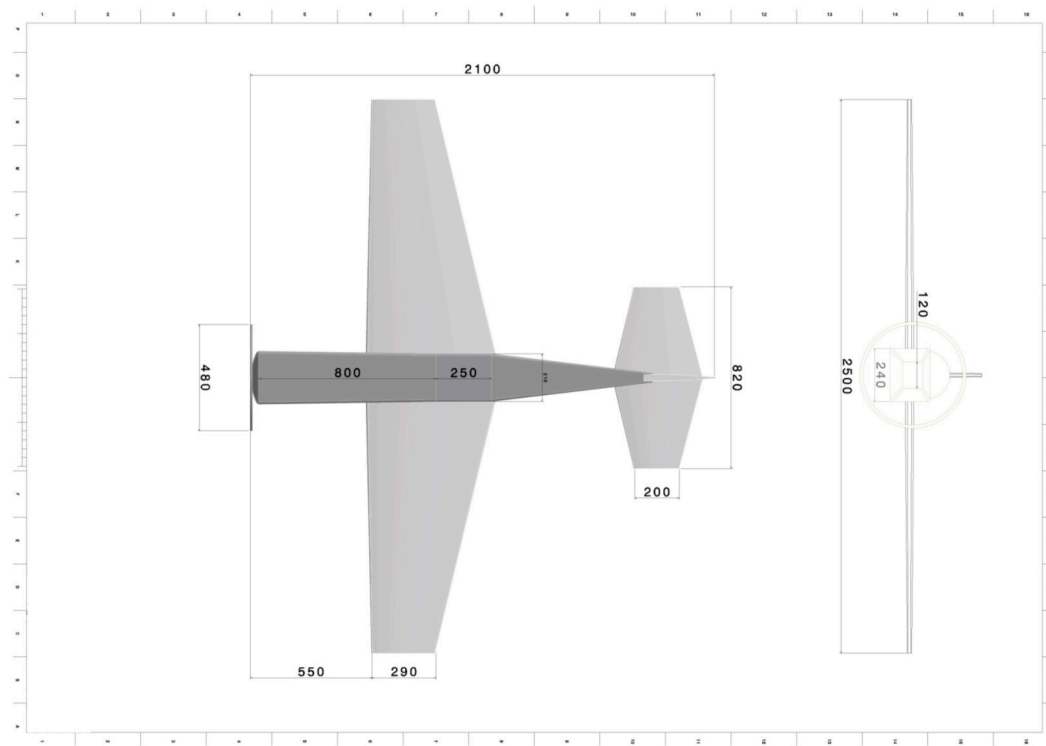


Figure 3. UAV geometric drawing, dimensions in millimeters.

Table 1. Unmanned aerial vehicle (UAV) main features.

Specification	Symbol	Value	Specification	Value
Mass and Inertia			Aerodynamics	
Mass	M	6.5 kg	Wing and Tail Profile	NACA 0011
UAV moment of inertia	I_x	0.681 kg m ²	Thrust	
	I_y	1.375 kg m ²	DLE Engine Power	5 CV
	I_z	2.0121 kg m ²	DLE Engine Displacement	30 cc
	I_{xy}	−0.001 kg m ²	Propeller Diameter	0.48 m
	I_{xz}	0.022 kg m ²	Propeller Pitch	0.30 m
	I_{yz}	0.0001 kg m ²	-	-

To evaluate the aerodynamic characteristics of the NACA0011 airfoil (wings, horizontal and vertical tail), XFOIL software [28] was used. This is an interactive program widely used for the design and analysis of subsonic isolated airfoils. The main airfoil characteristics are reported in Figure 4 and, according to the low speed considered in this work, Reynolds and Mach numbers were found to be equal to 400,000 and 0.04 respectively for all simulations.

The data in Figure 3, Table 1 and Figure 4 were used to perform in Simulink the following studies:

- Open-loop simulations by applying a specific command input to the elevator, ailerons and rudder: the command consisted in a 1 degree positive step;
- Closed-loop simulations (gust response by using Dryden wind turbulence model) with a full-state feedback control by means of the linear quadratic regulator (LQR) method;
- Take-off length simulations.

The last two simulations were carried out with both continuous and discrete operation modes of the mobile surface, to compare their effect on the UAV motion.

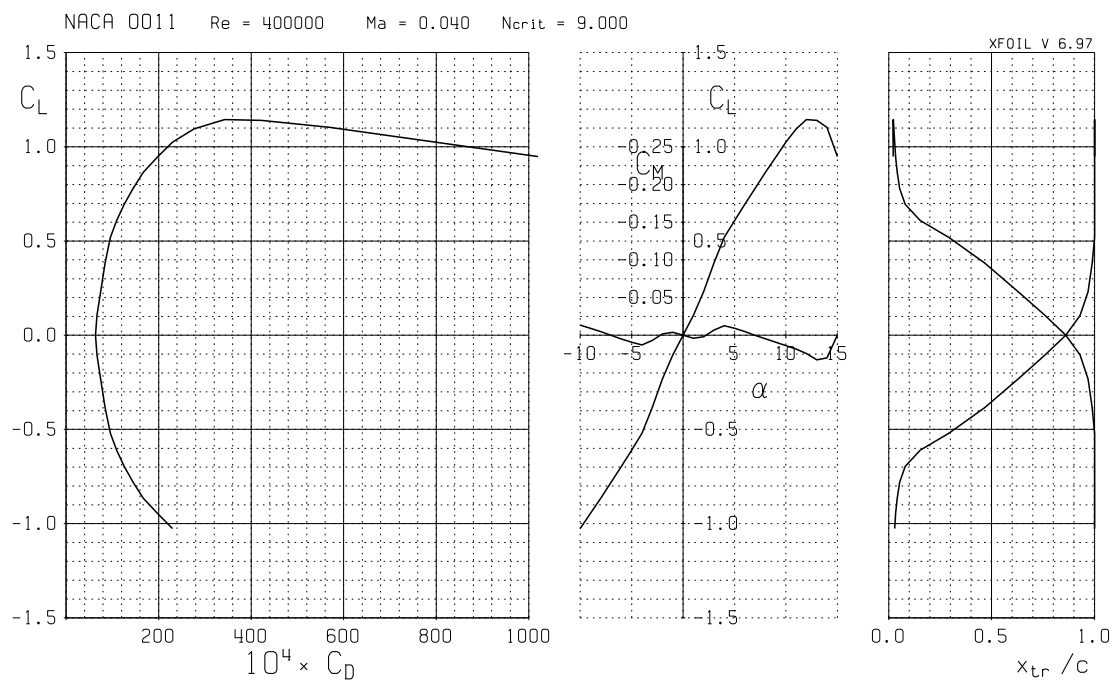


Figure 4. XFOIL aerodynamic properties of NACA0011.

2.2. FE Simulations and Manufacturing of Bistable Plates

A thermomechanical FE model [29] was developed to design the bistable composite plate as a morphing surface able to provide the same deflections of the continuous mobile surfaces. The entire analyses were split up in two load cases: the thermal simulation to induce the curved shapes and the transient simulation of the snap-through. The commercial software ANSYS® (Transient Structural Module, version 2019 R3, Ansys Inc., Canonsburg, PA, USA) was used [30]. To create the bistable stabilizer (for replacing the conventional one in Figure 2), a bistable rectangular plate with an AR of 2 (80 mm × 160 mm) was simulated by stacking four laminae following a (0₂/90₂) sequence and exploiting the “lever effect” [15]: the leverage amplifies the input force to provide a bigger output effect. The ratio of the output force to the input is the mechanical advantage of the lever. This mechanism allows us to gain mechanical advantages by moving the septum, in terms of plate displacements and activation forces: to increase the displacement and decrease the activation load, the distance between the constrained edge and the septum must be as small as possible (see Figure 5a). The actual characteristic boundary conditions were carried out with one constrained edge and the adjustable septum (as in Figure 5b).

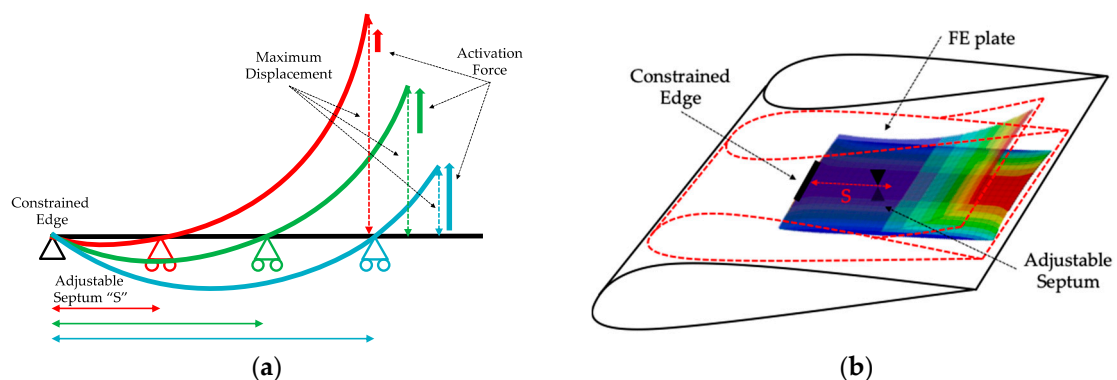


Figure 5. (a) Lever effect graphic and (b) finite element (FE) model (two stable states) on a UAV stabilizer.

The FE model consisted of shell elements. Convergence studies on the mesh size were carried out in order to achieve an acceptable accuracy of the results. The option “Large Deflection” was employed in each step because large deformations are associated with small displacement increments of the plate during the process (geometric non-linearity).

The available material was the prepregs Hexply 8552 with unidirectional carbon fibers IM7 (used in primary aerospace structures [31]). The main mechanical properties shown in Table 2 filled the engineering data module of the software for all simulations.

Table 2. Hexply 8552 data.

Technical Data	Value
Nominal cured ply thickness	0.131 mm
Nominal laminate density	1570 kg m ⁻³
Young’s modulus 0° direction	165 GPa
Young’s modulus 90° direction	11.4 GPa
Coefficient of thermal expansion 0° direction	6 × 10 ⁻⁷ C ⁻¹
Coefficient of thermal expansion 90° direction	2.86 × 10 ⁻⁵ C ⁻¹

The numerical results provided by FE models allowed us to know: (i) the displacements evaluated at the free end of the plate for different septum positions, (ii) the maximum deformations and (iii) the activation forces. The displacements values allowed us to evaluate the deflection capabilities of the discrete mobile surface. The knowledge of plate deformations was useful since it drives the choice of possible locations for a proper use of MFC P1/F1 actuators [32]: these actuators, in fact, bonded onto the plate and electrically activated, are deformed inducing the bistable snap-through. The activation forces intensity is strictly related to the amount of charge requested by the MFC.

In order to obtain experimentally the discrete shapes of bistable plates, four laminates with four layers of Hexply prepregs (see Figure 6) were manufactured.



Figure 6. Bistable laminates manufacturing: (a) Hexply 8552 prepregs on the mold and (b) vacuum bag.

The samples were cured following the conventional cycle suggested by the manufacturer, setting the temperature at 180 °C, with the overall curing cycle of 3 h. In order to increase the thermal residual stresses and to obtain a higher level of curvature in the samples, the laminates, after the curing was completed in the autoclave, were immediately brought out so that a fast cooling down occurred in open air at room temperature. After the cooling down, each laminate was observed to have the two expected stable states (in Figure 7).

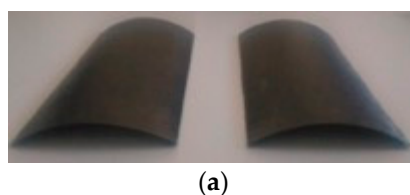


Figure 7. Cont.

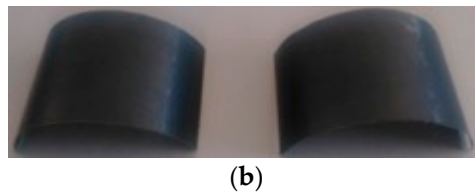


Figure 7. Experimental bistable plates: (a) first stable state and (b) second stable state.

3. Results and Discussion

3.1. Simulink Results

In this subsection the UAV response to input commands considered in the previous section was analyzed. The open-loop simulations were run to demonstrate that the Simulink model was effective. If a unit step is assigned to a mobile surface, its effect on the flight dynamics will be the same regardless if the command will be continuous or discrete. The closed-loop simulations instead provided information on how the control actions from the controller were dependent on the system dynamics. The closed-loop simulations were performed to make a comparison between continuous and discrete bistable command surfaces providing information useful to understand the technical feasibility of a discrete command.

3.1.1. Open-Loop Simulations

Unit step inputs after 1 s of trimmed flight were considered in all cases as inputs to the control mobile surfaces (initial trim conditions corresponding to an horizontal flight with speed and altitude equal to 10 m/s and 50 m respectively), in order to validate the Simulink model by means of flight mechanics equations.

Figure 8 represents the dynamic response in terms of motion variables to a positive (pitch-down) step input on the elevator. The first 20 s of simulation are reported, where it is possible to recognize the short-term response of short period variables, namely α and q . The AOA rapidly reaches a new equilibrium with well damped oscillations, whereas the pitch rate converges towards a small value. When a positive elevator step is applied, the initial force increment coming into play is directed upwards, and it causes a small but strictly positive increment to the flight-path angle. This causes the aircraft to enter an accelerating dive and u increasing.

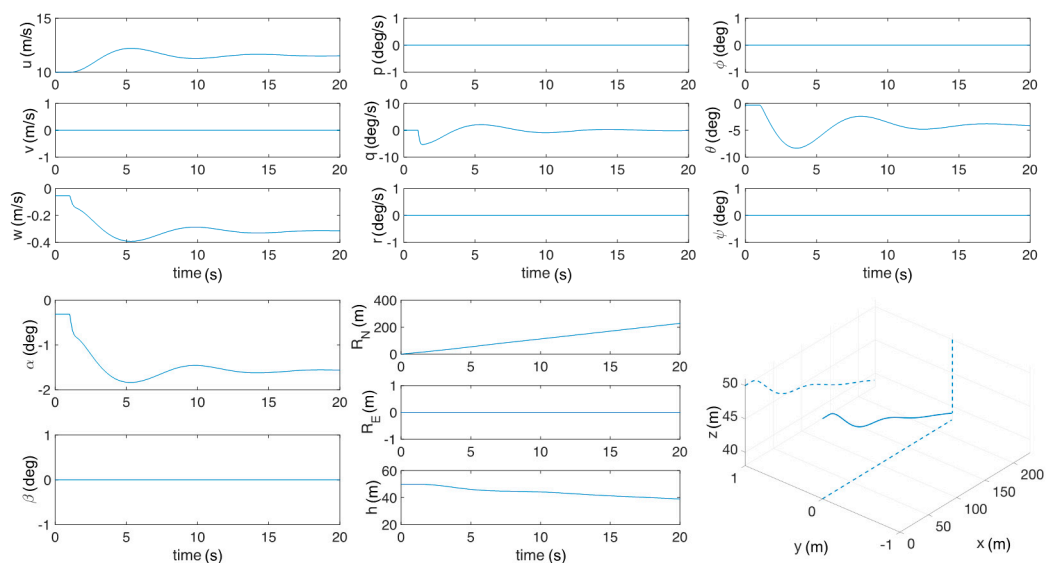


Figure 8. UAV response to the unit step elevator.

The response to a positive aileron step command was characterized by an initial transient (5–6 s) dominated by the roll mode, during which the UAV achieved a negative roll rate (Figure 9). The increment in the roll angle achieved during this phase caused the aircraft to sideslip (β became negative). A steady state yaw rate r was achieved for a constant roll angle φ , which means that the aircraft entered a steady turn. From the practical standpoint, it should be noted that the aileron control power in this case was related to the ailerons placed close to the root of the half-wing in order to limit the excitation of wing bending and torsional modes. This explains the small value of the roll rate p achieved in the maneuver.

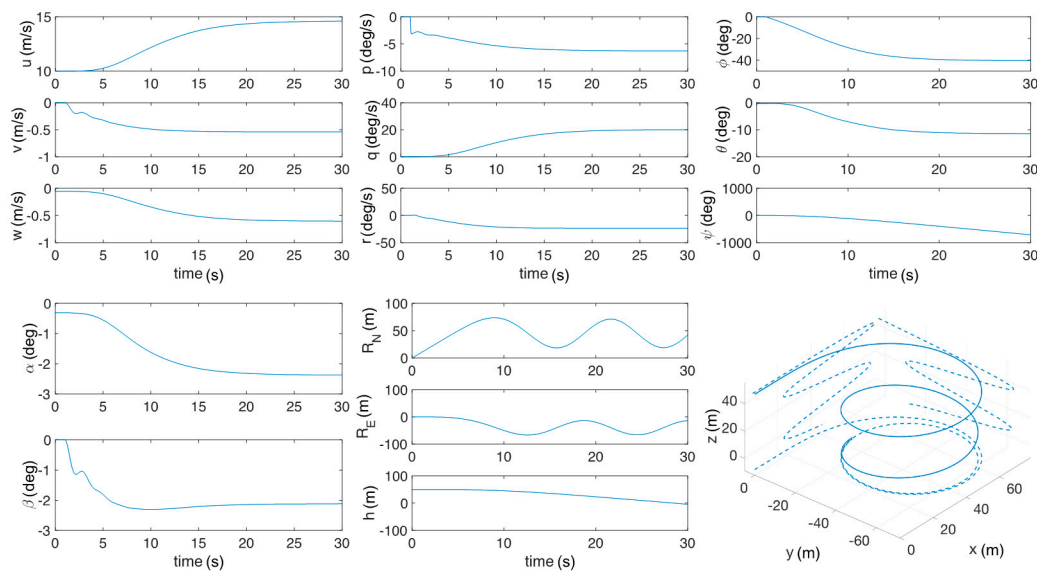


Figure 9. UAV response to unit step ailerons.

When a positive step command was applied to the rudder, the first effect was a linear acceleration around the yaw axis and the growth of the sideslip angle β , which became positive (Figure 10). The sideslip angle generated a negative rolling moment, thus inducing an increment of the roll angle φ , as achieved by the aileron command, but related to a different source. The response was clearly dominated by sizeable Dutch-roll oscillations, superimposed over a slow spiral convergence. At the steady state, also in this case, the UAV was significantly banked.

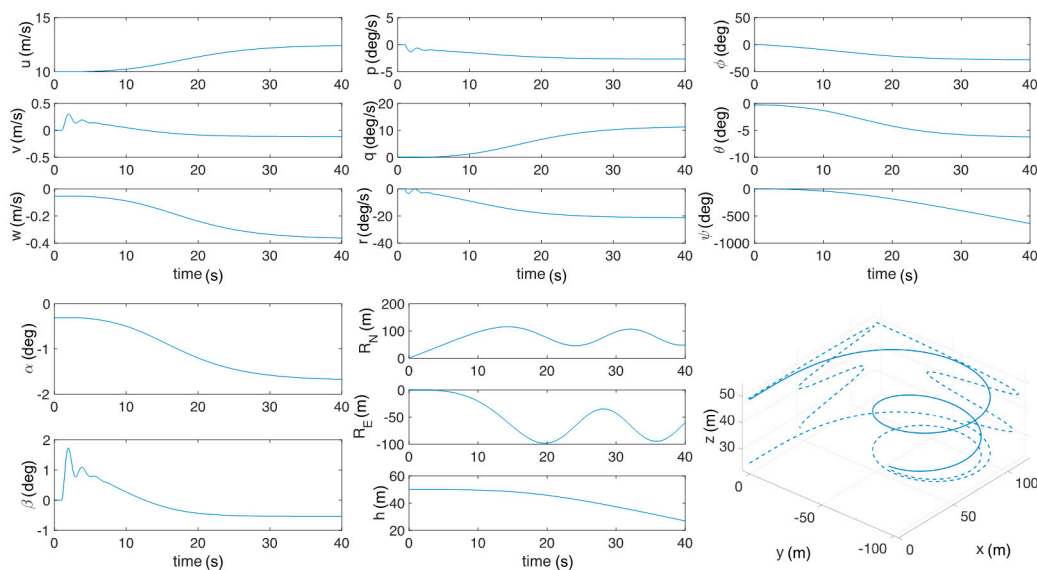


Figure 10. UAV response to the unit step rudder.

3.1.2. Closed-Loop Simulations

Discrete displacements of mobile surfaces give the possibilities of performing a wide range of maneuvers. Simulink was used to develop a stability and control augmentation system suitable for the chosen UAV: the comparison between continuous and discrete commands on closed-loop performance was made. As in [33], a LQR was developed for the virtual model, with full-state feedback on:

- $(\alpha_{DES} - \alpha)$ and $(q_{DES} - q)$, with α_{DES} and q_{DES} equal to α_{TRIM} and to zero respectively, for longitudinal stability;
- $(p_{DES} - p)$ and $(r_{DES} - r)$, with p_{DES} and r_{DES} equal to zero for lateral-directional stability.

The subscript *DES* refers to the target value. The resulting closed-loop behavior for a 3D gust disturbance (duration 30 s in Figure 11) on the desired value of α , q , p and r is presented by the following pictures.

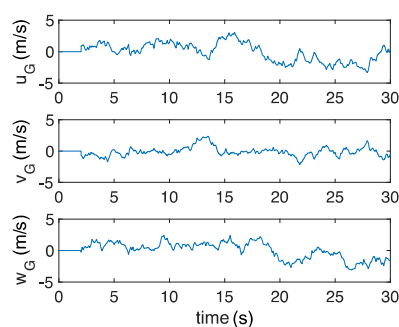


Figure 11. Dryden wind turbulence velocities.

By using a Simulink function, it was possible to implement the Dryden wind turbulence model (continuous) block that uses the Dryden spectral representation to make turbulence acting on the UAV model (in Figure 11 the component velocities of the used Dryden gust were plotted). As it is also possible to see from the figure, the speed components were not correlated with each other and never exceeded ± 5 m/s. Since the turbulence in a real scenario was highly dependent on the considered altitude, for the specific case subject of study, the pertinent turbulence model was adopted considering that the evolution of the UAV was enclosed in an altitude range between 45 and 55 m. Another aspect was the turbulence duration: most of the actual gusts lasted a few seconds; in the case of the present investigation a gust lasting about 30 s was used for the simulations representing the worst dynamic scenario. The gust components were incorporated directly into the nonlinear dynamics equations simulating UAV behavior, like perturbations of the aircraft velocity.

The LQ regulator was thus synthesized for the model: the cost functions, previously defined, were associated with the deviations due to the gust perturbation of UAV altitude and attitude from the trim values. The control law developed by LQR obviously does not take into account if the command is continuous or discrete, but simply provides a deflection value of the surface needed for achieving the DES (i.e., desired) conditions. The resulting closed-loop gust response with continuous mobile surfaces is provided by the dotted lines in Figure 12a. In order to satisfy the cost functions, the resulting elevator deflection falls in the range between $\pm 20^\circ$ (Figure 12a top); the ailerons instead show very low deflections needed to guarantee the desired flight conditions (Figure 12a centre); the rudder must deflect $\pm 10^\circ$ to maintain the lateral directional stability (Figure 12a bottom). The closed-loop behavior of the conventional LQR controller was acceptable, with minor changes around the trim conditions (these results are not reported in Figure 12b for the sake of clearness of the plot). These results confirm the good stability performance of the chosen UAV.

A control law was then developed for the UAV model operated by discrete commands: $\pm 2^\circ$ for the elevator and $\pm 0.5^\circ$ for the ailerons were the discrete limit deflections. The resulting control law is represented by continuous blue lines in Figure 12a where the deflections were evaluated in order

to satisfy the cost functions. In this case the closed-loop behavior was also clearly acceptable (see Figure 12b): the UAV trajectory almost always remained within a 5 m diameter cylinder, centered at the trim trajectory. More in details, in Figure 12b the different trajectory components were reported: z represents the altitude and (x,y) plane was the horizontal plane parallel to the ground. From the Figure 12b it is clear that the vehicle, under the action of the gust and the reaction of the discrete controls, moved around the trim conditions with apparent oscillations that were always confined in about 5 m. To simulate also the actual bistable devices, the piezoelectric MFC actuator was integrated into the Simulink model taking into account its activation law. For the snap transition between the two stable positions of the control plate, it is necessary to send an electric discharge to the MFC actuator. Therefore, a charging time, allegedly affecting the overall dynamics of the system, was added to the control law. The charging time was needed by the condenser for the subsequent discharge generation activating the MFC: the numerical simulations including this charging time (order of 1 s) demonstrated that this aspect was not critical for the control of the vehicle.

The results showed in this section proved that the discrete controller concept was actually working.

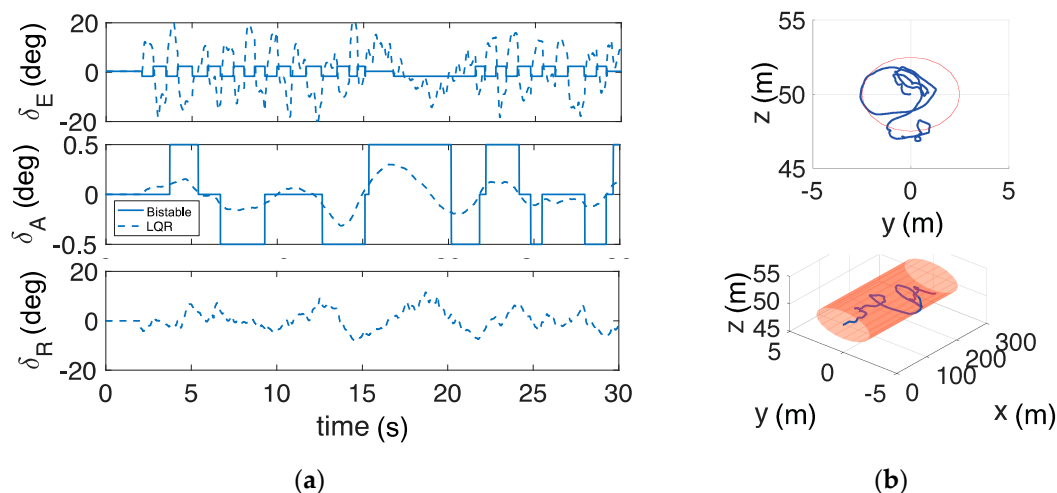


Figure 12. UAV gust response: (a) elevator, ailerons and rudder deflections (continuous and discrete behavior) and (b) UAV 3D trajectory with discrete command surfaces.

3.1.3. FEM vs. Experimental Plate Results

The numerical FE model was developed (i) to numerically evaluate the plate geometry after the cooling down, (ii) to simulate the plate displacements in order to compare these results with the experiments and (iii) to obtain the maximum cambers with different degrees of application of the “lever effect”. FE models furthermore drive the choice of the bistable dimensions and stacking sequence to replace UAV conventional mobile surfaces. A plate 80 mm × 160 mm was simulated by stacking four laminas ($0_2/90_2$) of Hexply 8552 (Hexcel, Stamford, CT, USA). Typical results (deformations) are shown in Figure 13: the numerical maximum cambers are also reported and compared with the experimental results.

The “lever effect” was introduced to constrain the laminate used like an aerodynamic mobile surface (see Figure 14): “ S ” indicates the distance in mm from the septum position to the bistable constrained edge (in order to better understand the meaning of the symbol “ S ” used throughout the text, Figure 5 can be looked at). At each value of “ S ” it is possible to evaluate the maximum deflection of the discrete mobile surface (vertical displacement f , rotation angle).

The airfoil NACA0011, currently used for the stabilizer of the chosen UAV, was virtually integrated with the design bistable plate: the discrete deflections of the bistable plate (a) and of the compliant profile (b) are plotted in Figure 14. Table 3 summarizes the geometric results: these proved that by choosing proper configuration of constraints, lay-up and AR for the bistable plates it is possible to

tailor the snap-through mechanism to make bistables actually operating like mobile surfaces. For each S value, the bistable discrete mobile surface had a deflection angle (in Table 3) comparable with a conventional UAV control surface.

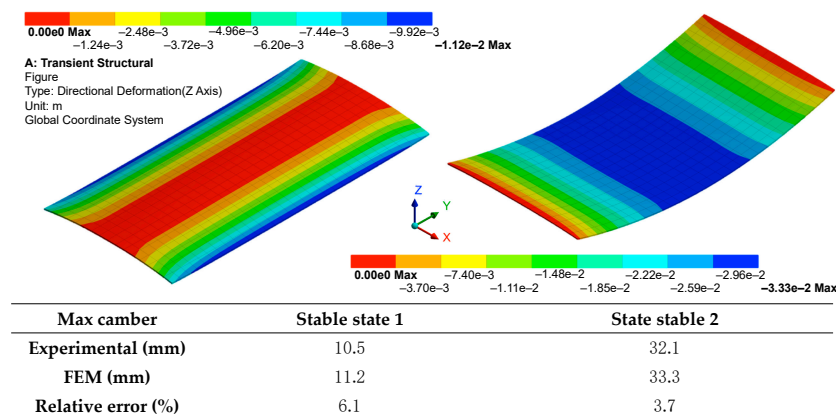


Figure 13. FE bistable model (two stable state shapes deformations): simulated and measured cambers.

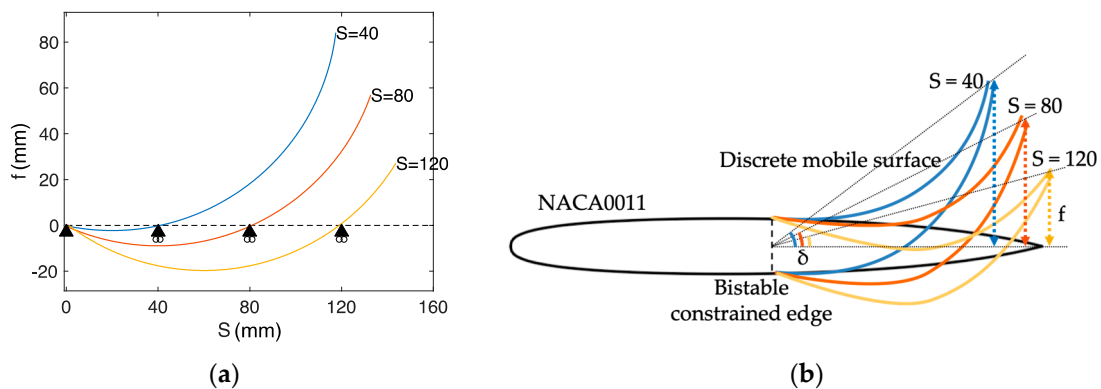


Figure 14. Discrete mobile surface with “lever effect”: (a) plate deflection f with different value of S ; and (b) airfoil NACA0011 with different bistable angles δ and deflections f .

Table 3. Deflection f and δ for each values of S .

S (mm)	Deflection f (mm)	Deflection Angle δ ($^\circ$)
40	84.1	≈ 28
80	56.9	≈ 20
120	27.1	≈ 10

3.2. Wind Tunnel Experiment

The FE simulations showed that, using the “lever effect”, the deflection of an aerodynamic surface made of bistable can be comparable with the one of conventional configuration. In order to prove experimentally this idea, a wing sample was made up of balsa, using NACA0011 as a base profile. A bistable plate exploiting the lever effect was integrated in the base profile (Figure 15a). The forward spar was used as clamp for the short side of the plate, while the intermediate support was realized by a mobile septum in order to achieve the lever effect before presented and discussed. In this way the MFC actuator in future developments of this concept will be able to activate the snap-through: each stable state of the composite laminate provided a discrete position of the mobile control surface, due to the compliant skin at the profile trailing edge (Figure 15b).

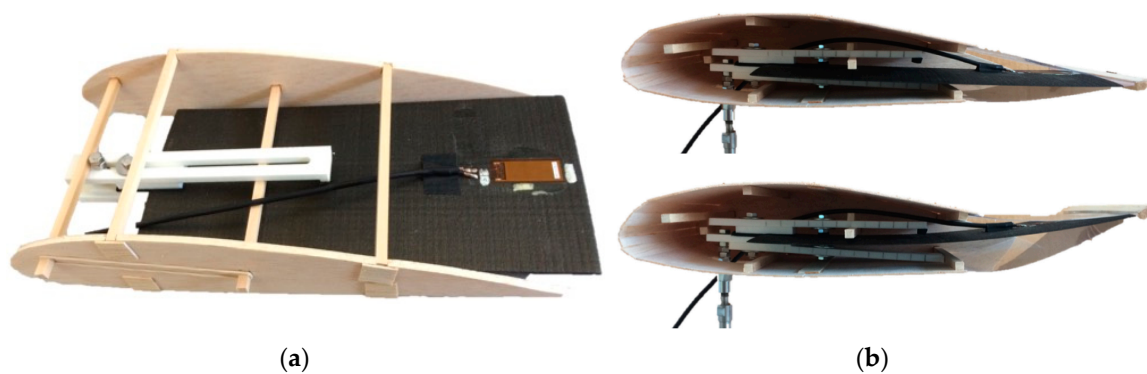


Figure 15. Experimental NACA 0011 airfoil (a) sample without the skin and (b) discrete mobile surface OFF (top) and ON (bottom).

The capability of the wing sample to keep the shapes at several flight speeds and at different AOAs was evaluated by carrying out specific tests represented in Figure 16.

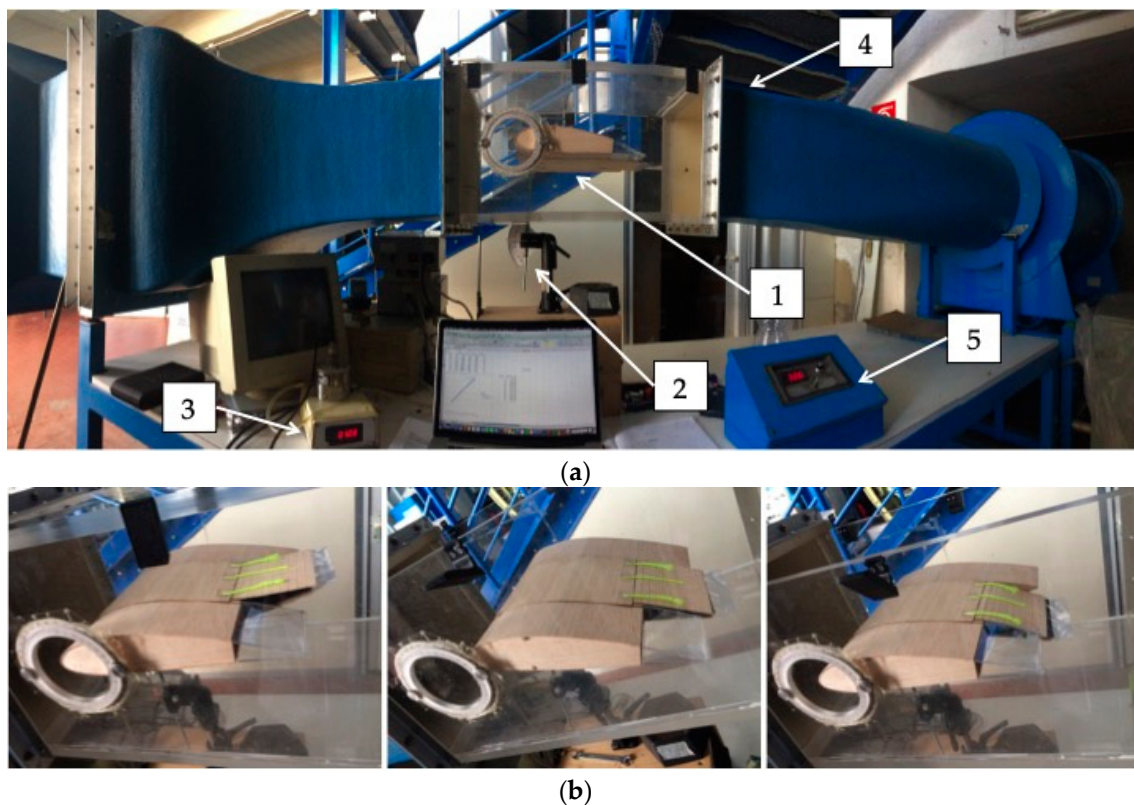


Figure 16. Wind tunnel experiment: (a) 1. Sample profile with discrete mobile surface, 2. angles of attack (AOA) tool (min -15° , max $+20^\circ$), 3. pitot tube, 4. test chamber and 5. wind speed regulator and (b) negative (LEFT), neutral (CENTRE) and positive (RIGHT) deflection of discrete mobile surface.

The scope of the aerodynamic campaign was to demonstrate the stability of every state of the mobile surface when operating in an external field. In this context stability of an initial state means that, following a small perturbation of the external flow (i.e., caused by a local separation of the flow around the profile or by the turbulence), the bistable keeps its geometric shape without snapping to the other shape. The possible bistable initial states were four, two for each stable state (see Figure 17, where it is clear that the plate can be installed in one specific geometric configuration and the corresponding reverse one, UP and DOWN respectively). During the experimental tests the external field was accelerated at different AOAs waiting for a “natural” snap through, i.e., not activated by any sensor

(MFC). This campaign was extremely useful for understanding if the mobile surface can be prone to unwanted deflection.

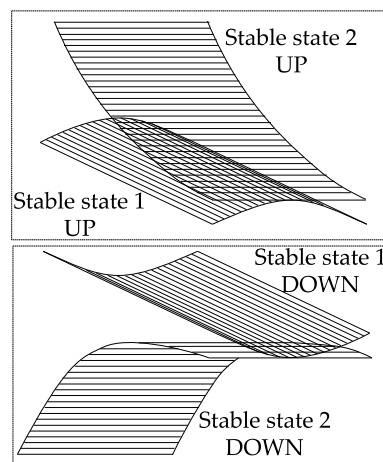


Figure 17. Bistable plates configurations.

An accurate aerodynamic experimental campaign was carried out in a wind tunnel of the type “open circuit”. S was equal to 80 mm, to which corresponds a deflection angle of about 20° , as it can be seen in Table 3. Two different sample configurations were tested, according to the scheme in Figure 17, to allow the study (varying AOA and flight speed) of the snap behavior, due to the aerodynamic load, for positive and negative deflections of the mobile surface. Table 4 lists the speeds at which the snap through occurred: the stable state 1 (in both the configurations) was the most suitable to withstand the aerodynamic external pressure, whereas the stable state 2—UP configuration suffered negative AOAs and the stable state 2—DOWN configuration suffered positive AOAs, i.e., snapping without external activation. This result was consistent with the static characterization of the bistable plates reported in [15] where it is experimentally shown that the stable state 1 is stiffer (i.e., requires more energy for the transition to the other state) than stable state 2.

Table 4. Experimental wind tunnel results.

AOA ($^\circ$)	Initial Stable State			
	1—UP	2—UP	1—DOWN	2—DOWN
Snap Speed (km/h)				
+20	85	-	-	35
+15	-	-	-	45
+10	-	-	-	50
+5	-	-	-	65
0	-	60	-	70
-5	-	70	-	-
-10	-	55	-	-
-15	-	45	-	-

In conclusion, the proposed morphing concept passed the wind tunnel test, showing significant aerodynamic withstanding at AOAs and flight speeds that are typical of the size of the employed UAV. These results also suggested a solution to replace the conventional UAV stabilizer (with weight around 0.5 kg) with an innovative horizontal tail with discrete bistable elevators (see CAD in Figure 18a). The proposed concept appeared lighter (bistable plates and lever effect tool weigh around 0.3 kg) and increased aerodynamic efficiency (without any servomechanism outside of the tail airfoil) when compared to conventional UAV command surfaces.

Four bistable plates (in Figure 18a) could be installed on a modified leading edge of the new horizontal tail with the lever effect tool integrated (Figure 18b): a pair of plates could be installed in the UP configuration, and a pair of plates could be installed in the DOWN configuration (see Figure 17). In this way when they are not activated, their first stable shape provides the neutral position of the stabilizer; when one pair is activated it is possible to achieve a deflection of the stabilizer upwards/downwards depending on which one of the two pairs (UP/DOWN respectively) is activated.



Figure 18. New horizontal tail concept: (a) bistable horizontal tail in CATIA and (b) UAV equipped with the concept of a horizontal bistable stabilizer.

3.3. Takeoff Length: Numerical vs. Experimental Results

This final subsection summarizes the results of three experimental tests and Simulink simulations related to the UAV take-off length. The experimental campaign was carried out with the conventional UAV stabilizer operating in “discrete” mode (just two possible deflections): this choice of using the conventional stabilizer and not the bistable one was motivated by the circumstance that, in the event of failure or an unwanted dynamic evolution of the UAV, the conventional commands would have allowed a prompt and full recovery of the UAV. As suggested by the RC UAV manufacturer, during the maneuver and the Simulink simulations, the engine throttle underwent a gradual increase up to 60% of the maximum in 10 s for the take-off maneuver. In the following pictures, white-red reference elements were placed at a distance of 5 m from each other.

The first take-off test was carried out assuming the stabilizer deflection equal to -10° ; this deflection was constant from the beginning of the test until the UAV took off from the ground: the vehicle was soared in flight after having covered 18.7 m of runway in 4 s (Figure 19).

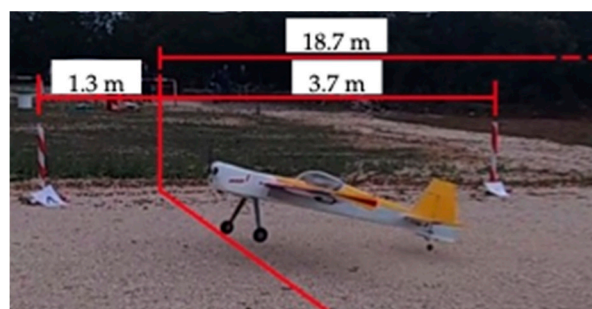


Figure 19. Runway length at first takeoff time.

The second take-off test was carried out assuming the stabilizer deflection equal to 0° ; this deflection was constant: the UAV was not able to take-off using the whole runway length of 35 m. The last take-off test was performed like a traditional maneuver: taxiing with the stabilizer in neutral position until 3 s, and subsequent -10° deflection on the horizontal tail command. Under these conditions, the UAV was able to lift off after 12.5 m of runway, in 3.5 s.

Table 5 reports the numerical results obtained Simulink in which the motion equations were solved and the experimental results.

Table 5. Take-off results.

	Test	Results	Experimental	Simulink	Error (%)
1	$\delta_E = -10^\circ$	Runway (m)	18.7	17.6	5.9
		Time (s)	4	3.8	5.0
2	$\delta_E = 0^\circ$	Runway (m)	35	35	-
		Time (s)	6	5.7	5.0
3	0–3 s, $\delta_E = 0^\circ$ from 3 s on, $\delta_E = -10^\circ$	Runway (m)	12.5	13.6	–8.8
		Time (s)	3.5	3.2	5.7

The errors on time and space were so explained:

- Ground friction coefficient: in Simulink simulations this was constant, in actual tests the runway was definitely uneven and not properly described by a constant friction coefficient;
- Measurement time: the error of human reaction was about three tenths of a second;
- Wind: the actual weather was quickly changing, with small gusts from different directions, while no gust model was included in the Simulink code;
- UAV weight distribution: it was assumed homogeneous in the Simulink model for sake of simplicity, and at this stage of the research this small error can be accepted;
- Ground effect: it was not included in the Simulink model.

In conclusion, the Simulink code was able to predict the UAV behavior, either during taxing and flight maneuver, either with conventional and discrete mobile control surfaces. Now it can be stated that the proposed innovative concept of bistable morphing control surfaces on a RC-UAV can go to the next research step: implementation of the actual prototype of new UAV horizontal stabilizer, by using composite bistable plates integrated with the lever effect tool due to the data gathered during this research phase.

4. Conclusions

In this study a new horizontal stabilizer was presented for RC-UAV application, by using composite bistable laminates. The nonlinear flight dynamics equations were implemented in Simulink to study different flight conditions. These numerical results were used as inputs to the FE model of bistable composite plates. By using the “lever effect”, it was demonstrated that the shapes of the bistable plates could be tailored to mimic the conventional command surfaces behavior. Composite bistable plates were built with AR, dimensions, asymmetric stacking sequence and total thickness, previously simulated. The new bistable elevator was tested in the wind tunnel and the discrete mobile surface behavior was validated through real flight tests, carried out using a actual RC-UAV. The present manuscript just reports a preliminary investigation on the technical feasibility of a control surface based on the employment of bistable materials. Basic research questions aimed at proving that the concept could actually work were addressed positively. Future work will be based on a robust design of the control surface consisting in the optimization of the aerodynamic efficiency of the surface, through numerical and wind-tunnel tests, and in a proper evaluation of the energy required for the operation of the control. After all the design stages will be completed, a prototype of bistable horizontal stabilizer, activated by a MFC actuator, will be installed on a UAV and flight tested.

Author Contributions: Conceptualization, G.S.; methodology, G.S. and F.N.; software, F.N.; validation, G.S. and F.N.; formal analysis, G.S.; investigation, F.N.; resources, G.S.; data curation, F.N.; writing—original draft preparation, F.N.; writing—review and editing, G.S.; visualization, G.S. and F.N.; supervision, G.S.; project administration, G.S.

Funding: This research received no external funding.

Acknowledgments: All the authors are grateful to Giuseppe Del Core (Uniparthenope) and Giulio Avanzini (Unisalento) for their kind scientific suggestions and they acknowledge the thesis work done by Giammario Ferrara, who helped them in testing the actual UAV with discrete mobile surface.

Conflicts of Interest: The authors declare no conflict of interest.

References

1. Dalamagkidis, K. Definitions and terminology. In *Handbook of Unmanned Aerial Vehicles*; Springer: Dordrecht, The Netherlands, 2015; pp. 43–55. ISBN 9789048197071.
2. Valavanis, K.P. Introduction. In *Advances in Unmanned Aerial Vehicles: State of the Art and the Road to Autonomy*; Springer: Berlin/Heidelberg, Germany, 2007; Volume 33, ISBN 978-1-4020-6113-4.
3. Zeng, Y.; Zhang, R.; Lim, T.J. Wireless communications with unmanned aerial vehicles: Opportunities and challenges. *IEEE Commun. Mag.* **2016**, *54*, 36–42. [[CrossRef](#)]
4. Saad, W.; Mozaffari, M.; Yin, C.; Hong, C.S.; Chen, M.; Debbah, M. Caching in the Sky: Proactive Deployment of Cache-Enabled Unmanned Aerial Vehicles for Optimized Quality-of-Experience. *IEEE J. Sel. Areas Commun.* **2017**, *35*, 1046–1061.
5. Hodgson, J.C.; Koh, L.P. Best practice for minimising unmanned aerial vehicle disturbance to wildlife in biological field research. *Curr. Biol.* **2016**. [[CrossRef](#)] [[PubMed](#)]
6. Anderson, K.; Gaston, K.J. Lightweight unmanned aerial vehicles will revolutionize spatial ecology. *Front. Ecol. Environ.* **2013**, *11*, 138–146. [[CrossRef](#)]
7. Cano, E.; Horton, R.; Liljegren, C.; Bulanon, D. Comparison of Small Unmanned Aerial Vehicles Performance Using Image Processing. *J. Imaging* **2017**. [[CrossRef](#)]
8. Balek, J.; Blahůt, J. A critical evaluation of the use of an inexpensive camera mounted on a recreational unmanned aerial vehicle as a tool for landslide research. *Landslides* **2017**. [[CrossRef](#)]
9. Battipede, M.; Vazzola, M.; Tancredi, D. Innovative Piloting Technique for a Semi-Autonomous UAV Lighter-Than-Air Platform Simulator. In *Proceedings of the AIAA Modeling and Simulation Technologies Conference*; American Institute of Aeronautics and Astronautics: Reston, VA, USA, 2012.
10. Hosseini, S.; Mesbahi, M. Energy-Aware Aerial Surveillance for a Long-Endurance Solar-Powered Unmanned Aerial Vehicles. *J. Guid. Control Dyn.* **2016**, *39*, 1980–1993. [[CrossRef](#)]
11. Panagiotou, P.; Kaparos, P.; Salpingidou, C.; Yakinthos, K. Aerodynamic design of a MALE UAV. *Aerosp. Sci. Technol.* **2016**, *50*, 127–138. [[CrossRef](#)]
12. Panagiotou, P.; Giannakis, E.; Savaidis, G.; Yakinthos, K. Aerodynamic and structural design for the development of a MALE UAV. *Aircr. Eng. Aerosp. Technol.* **2018**, *90*, 1077–1087. [[CrossRef](#)]
13. Sharma, R.; Panigrahi, R.K. Stokes based sigma filter for despeckling of compact PolSAR data. *IET Radar Sonar Navig.* **2018**, *12*, 475–483. [[CrossRef](#)]
14. Kontogiannis, S.G.; Ekaterinaris, J.A. Design, performance evaluation and optimization of a UAV. *Aerosp. Sci. Technol.* **2013**, *29*, 339–350. [[CrossRef](#)]
15. Nicassio, F.; Scarselli, G.; Pinto, F.; Ciampa, F.; Iervolino, O.; Meo, M. Low energy actuation technique of bistable composites for aircraft morphing. *Aerosp. Sci. Technol.* **2018**, *75*, 35–46. [[CrossRef](#)]
16. Scarselli, G.; Maffezzoli, A.; Nicassio, F. Mechanical characterization of bistable laminates for very small aircraft morphing applications. In *Proceedings of the Health Monitoring of Structural and Biological Systems XII*, Denver, CO, USA, 4–8 March 2018; p. 61.
17. De Breuker, R.; Werter, N. On the Importance of Morphing Deformation Scheduling for Actuation Force and Energy. *Aerospace* **2016**, *3*, 41. [[CrossRef](#)]
18. Arena, M.; Nagel, C.; Pecora, R.; Schorsch, O.; Concilio, A.; Dimino, I. Static and Dynamic Performance of a Morphing Trailing Edge Concept with High-Damping Elastomeric Skin. *Aerospace* **2019**, *6*, 22. [[CrossRef](#)]
19. Sofla, A.Y.N.; Meguid, S.A.; Tan, K.T.; Yeo, W.K. Shape morphing of aircraft wing: Status and challenges. *Mater. Des.* **2010**, *31*, 1284–1292. [[CrossRef](#)]
20. Pecora, R.; Barbarino, S.; Concilio, A.; Lecce, L.; Russo, S. Design and functional test of a morphing high-lift device for a regional aircraft. *J. Intell. Mater. Syst. Struct.* **2011**, *22*, 1005–1023. [[CrossRef](#)]
21. Della Vecchia, P.; Corcione, S.; Pecora, R.; Nicolosi, F.; Dimino, I.; Concilio, A. Design and integration sensitivity of a morphing trailing edge on a reference airfoil: The effect on high-altitude long-endurance aircraft performance. *J. Intell. Mater. Syst. Struct.* **2017**, *28*, 2933–2946. [[CrossRef](#)]
22. Nicassio, F.; Scarselli, G.; Avanzini, G.; Del Core, G. Numerical and experimental study of bistable plates for morphing structures. In *Proceedings of the Active and Passive Smart Structures and Integrated Systems 2017*, Portland, OR, USA, 25–29 March 2017; p. 101640K.

23. Kim, S.W.; Lee, J.Y.; Cho, K.J. Towards a bistable morphing winglet for unmanned aerial vehicle (UAV). In Proceedings of the 2013 44th International Symposium on Robotics, Seoul, Korea, 24–26 October 2013; pp. 1–3.
24. Mills, J.; Ajaj, R. Flight Dynamics and Control Using Folding Wingtips: An Experimental Study. *Aerospace* **2017**, *4*, 19. [[CrossRef](#)]
25. Wang, B.; Fancey, K.S. A bistable morphing composite using viscoelastically generated prestress. *Mater. Lett.* **2015**, *158*, 108–110. [[CrossRef](#)]
26. Tawfik, S.A.; Stefan Dancila, D.; Armanios, E. Unsymmetric composite laminates morphing via piezoelectric actuators. *Compos. Part A Appl. Sci. Manuf.* **2011**, *42*, 748–756. [[CrossRef](#)]
27. Soken, H.E.; Ersin Soken, H.; Yenal Vural, S.; Hajiyev, C.; Vural, S.Y. Equations of Motion for an Unmanned Aerial Vehicle. In *State Estimation and Control for Low-cost Unmanned Aerial Vehicles*; Springer International Publishing: Cham, Switzerland, 2015; pp. 9–23.
28. XFOIL Subsonic Airfoil Development System. Available online: <http://web.mit.edu/drela/Public/web/xfoil> (accessed on 6 March 2019).
29. Scarselli, G.; Nicassio, F.; Pinto, F.; Ciampa, F.; Iervolino, O.; Meo, M. A novel bistable energy harvesting concept. *Smart Mater. Struct.* **2016**. [[CrossRef](#)]
30. ANSYS Product Launcher. Available online: <https://ansyshelp.ansys.com> (accessed on 6 March 2019).
31. Hexcel Prepreg. Available online: <https://www.hexcel.com/Resources/DataSheets/Prepreg> (accessed on 6 March 2019).
32. MACRO FIBER COMPOSITE–Smart-Material. Available online: <https://www.smart-material.com/Datasheets-MFC.html> (accessed on 6 March 2019).
33. Avanzini, G.; Nicassio, F.; Scarselli, G. Reduced-Order Short-Period Model of Flexible Aircraft. *J. Guid. Control Dyn.* **2017**, *40*, 2017–2029. [[CrossRef](#)]



© 2019 by the authors. Licensee MDPI, Basel, Switzerland. This article is an open access article distributed under the terms and conditions of the Creative Commons Attribution (CC BY) license (<http://creativecommons.org/licenses/by/4.0/>).

Article

Studies on the Electro-Impulse De-Icing System of Aircraft

Xingliang Jiang * and Yangyang Wang *

State Key Laboratory of Power Transmission Equipment & System Security and New Technology, Chongqing University, Chongqing 400044, China

* Correspondence: Xingliangjiang@cqu.edu.cn (X.J.); 20161101022@cqu.edu.cn (Y.W.)

Received: 18 March 2019; Accepted: 28 May 2019; Published: 5 June 2019



Abstract: In order to solve the accidents caused by aircraft icing, electro-impulse de-icing technology was studied through numerical simulation and experimental verification. In addition, this paper analyzed in detail the influence of the number, placement arrangement, and starting time of pulse coils on the de-icing effect, which plays a guidance role in the design and installation of the subsequent electro-impulse de-icing system. In an artificial climate chamber, the new de-icing criteria were obtained by tensile test, and the platform for the electro-impulse de-icing system was built. Replacing the skin with an aluminum plate, an electro-impulse de-icing system with a single coil was used. A three-dimensional skin-ice layer model was established by using Solidworks software. The finite element method was adapted. Through comparison between the de-icing prediction results and the test results in the natural environment, it was proven that the calculation process of de-icing prediction was correct, which laid a theoretical foundation for the selection of the number, placement arrangement, and starting time of the pulse coils. Finally, in this paper, by choosing the leading edge of NACA0012 wing as the research object, the influence of the number, placement arrangement, and starting time of pulse coils on the de-icing effect was analyzed. The results show that to get a better de-icing effect, the electro-impulse de-icing system with two impulse coils should be selected. The two coils were installed in the central position of the top and bottom surfaces of the leading edge, respectively. In addition, one of the impulse coils started working 1200 μ s later than the other one.

Keywords: aircraft; wing; system; ice; icing; deicing; ice mechanics; electro-impulse; coils; structural dynamics

1. Introduction

Since the earliest days of aeronautics, icing was found to be a crucial problem for aircraft flight. In-flight ice accretion occurs on the leading edge of an aircraft wing and usually covers only 2% of the wing chord, with the thickness of the ice layer being about a few centimeters. However, even an ice layer of a few centimeters thickness at the key parts of the aircraft is enough to cause flow separation and destroy lift, increase drag and reduce the maximum lifting capability, affect the control surface effectiveness, and in some cases decrease engine performance and stability [1–3]. Therefore, people have been working on aircraft anti-icing methods for many years [4–6]. The present ice protection methods are hot bleed air, freezing point depressants, and electro-thermal resistance heating. However, they all have potential limitations, for example, pneumatic boots bonded to the ice prone surface are subject to corrosion and damage by external objects, therefore, they need to be replaced every two or three years. The freezing-point depressant systems achieve the purpose of aircraft anti-icing by releasing ethylene glycol through many orifices in the leading edge of an aircraft. There are two main hazards: on the one hand, it increases the weight of the aircraft; on the other hand, since ethylene glycol is a toxic

substance, release of this substance into the air can cause environmental pollution. The principle of electro-thermal systems is to use resistance pads to heat the aircraft to above the melting temperature of ice, and in general it requires dedicated generators, which results in significant cost.

The aforementioned methods cannot meet the performance requirements for new aircraft. Therefore, it is imperative to develop a safe and reliable de-icing system. A new method for electro-impulse de-icing has emerged.

Electro-impulse de-icing (EIDI) is one of the mechanical de-icing systems, and it assures the safety of aircrafts in an icing condition. It has major advantages, such as low energy, minimal maintenance, great reliability, and low cost and weight [7,8].

The basic circuit of the electro-impulse de-icing system is shown in Figure 1. The working principle is the pulse coils are connected to a high voltage capacitor by low resistance, low inductance cables. When the switch is turned on, the discharge of the capacitor through the impulse coils creates a rapidly forming and collapsing electro-magnetic field. According to Maxwell's law, we know that the time-dependent magnetic field induces eddy currents in the metal skin. Therefore, the instantaneous impulse force of several hundred pounds magnitude is obtained by the Lorentz force formula, but the duration is only a few hundred microseconds. A small amplitude, high acceleration movement of the skin acts to shatter, de-bond, and expel the ice.

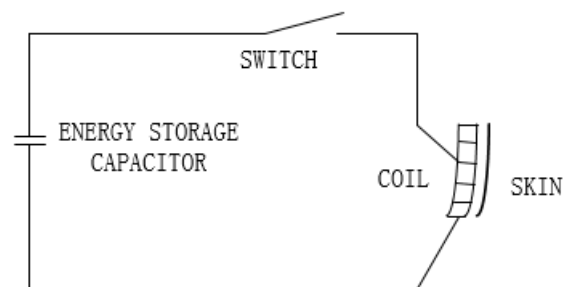


Figure 1. Electro-impulse system basic circuit.

Researchers [9–11] have studied the phenomenon of ice layer peeling on the surface of the skin under the action of a single coil system. The number of coils is greater than one when a real EIDI system is installed on the aircraft [12–14], so the position arrangement and start-up time of the multiple coils may affect the vibration condition to the effect of the ice removing effect. The de-icing criteria used in previous studies [15–17] are from the literature [18]. The adhesion between the ice layer and the skin is different under different icing conditions. Therefore, the conclusions of [18] are not suitable for all icing environments. Ice tensile strength and ice/aluminum adhesive shear strength used in [19] are 1.5 Mpa and 0.5 Mpa, respectively. However, this does not explain how the values are obtained. Therefore, the study of de-icing criteria is very important for the electro-impulse de-icing system.

All the experiments in this paper were obtained in an artificial climate chamber. Replacing the skin with an aluminum plate, the electro-impulse de-icing system with a single coil was used. The de-icing range obtained by experiments after each pulse was compared with the calculated result, and it was proven that the calculation process for de-icing prediction was correct. In addition, in the same icing environment, the adhesion between the ice layer and the skin was measured by a tensile test, and the new de-icing criteria was obtained. Finally, a three-dimensional NACA0012 wing-ice layer model was established; the effect of the number, placement arrangement, and the start-up time of pulse coils on the de-icing ratio was analyzed, which provided a reference for the design and installation of the subsequent electro-impulse de-icing system.

2. System Composition and Structural Dynamic Studies

The structural dynamics equation is expressed as [20]

$$[M]\ddot{U} + [C]\dot{U} + [K]U = F, \quad (1)$$

where [M] is the overall quality matrix, [C] is the overall damping matrix, [K] is the overall stiffness matrix, F is the impulse force, and U is the node displacement, \ddot{U} is the node accelerated velocity, \dot{U} is the node velocity.

In the continuous linear elastic body vibration, the relationship between normal stress, shear stress and displacement and external force is described. The expression for the stress can be written as

$$[\sigma] = [D][B]\{U\}^e. \quad (2)$$

Substituting the node displacement into Equation (2), $\sigma_x, \sigma_y, \sigma_z, \tau_{xy}, \tau_{yz}, \tau_{xz}$ for each node can be obtained.

The characteristic equation for the stress state is solved by the theory of one-dimensional cubic equation. Therefore, the practical calculation formulae for the principal stress can be written as

$$\sigma_1 = \frac{I_1}{3} + 2\sqrt{\frac{-P}{3}}\cos\frac{\theta}{3},$$

$$\sigma_2 = \frac{I_1}{3} - \sqrt{\frac{-P}{3}}\left(\cos\frac{\theta}{3} - \sqrt{3}\sin\frac{\theta}{3}\right),$$

$$\sigma_3 = \frac{I_1}{3} - \sqrt{\frac{-P}{3}}\left(\cos\frac{\theta}{3} + \sqrt{3}\sin\frac{\theta}{3}\right),$$

where $P = \frac{3I_2 - I_1^2}{3}$; $q = \frac{9I_1I_2 - 2I_1^3 - 27I_3}{27}$; $\theta = \arccos\left[-\frac{q}{2}\left(-\frac{P}{27}\right)^{-\frac{1}{2}}\right]$ ($0 < \theta < \pi$).

From the formulae above, $\sigma_1, \sigma_2, \sigma_3$ can be obtained. Substituting $\sigma_1, \sigma_2, \sigma_3$ into Equation (3), the equivalent stress can be written as

$$\sigma = \sqrt{\frac{1}{2}[(\sigma_1 - \sigma_2)^2 + (\sigma_2 - \sigma_3)^2 + (\sigma_3 - \sigma_1)^2]}. \quad (3)$$

3. Calculation Method Verification

3.1. Geometric Model

In this paper, an aluminum plate was used as the research object, and the material was the same as the wing skin. The research of electro-impulse de-icing systems mainly includes three parts: electro-dynamics research, structural dynamics research, and de-icing prediction. The electro-dynamics studies of this EIDI included the calculation of impulse current, the study of the magnetic field behavior, and the calculation of the impulse force of each grid point on the surface of the aluminum plate, which provided the basis for structural dynamic research. Structural dynamics studies include stress calculations, which provide the basis for de-icing prediction. The model was established by using Solidworks, with a length of 420 mm, width of 420 mm, and thickness of 1.5 mm. The pulse coil was located on the lower surface of the aluminum plate, and the gap between the impulse coil and the skin was 1 mm. It had an inner diameter of 20 mm and an outer diameter of 128 mm. The material characteristics are shown in Table 1.

The structural dynamics associated with electro-impulse de-icing have proven to be a difficult and challenging problem. The structural dynamics study is mainly to calculate the equivalent stress between the ice layer and aluminum plate under the action of pulse force. If the total pulse force is

applied to the aluminum plate, the calculation accuracy will be affected. Therefore, the aluminum plate was divided into different regions in the radial direction. Then, the impulse pressure at different radial points and different times was placed on the corresponding regions on the surface of the aluminum plate. This greatly improved the accuracy of the de-icing prediction. It is assumed that the ice layer with 4 mm thickness was evenly covered on the aluminum plate with 2.0 mm thickness. The material properties are shown in Table 2.

Table 1. Material characteristics.

Material	Relative Permeability	Conductivity (S/m)	Density (Kg/m ³)
Aluminum plate	1.000021	1.74×10^7	2780
Impulse coil	0.999991	5.8×10^7	8933

Table 2. Material properties.

Material	E/GPa	ν	ρ /(kg·m ³)
Aluminum	7.1	0.33	2700
Ice	5.5	0.3	897

The size of the meshing affects the calculation results of structural dynamics. In this paper, the modal analysis of the aluminum plate was calculated by the finite element method. The calculated result of first-order natural frequency was 46.5 Hz. Considering the boundary conditions and bending vibration of the aluminum plate, the aluminum plate was regarded as a free Bernoulli–Euer beam model at both ends, and its natural frequency theoretical calculation formula [17,18] is as follows:

$$f_n = \frac{\pi}{2} \left(n + \frac{1}{2}\right)^2 \sqrt{\frac{EI}{\rho A l^4}}, \quad n = 1, 2, \dots, \quad (4)$$

where l is the length of the aluminum plate, A is the cross-sectional area, ρ is the density, I is the moment of inertia of the section, and E is the elasticity modulus.

The first-order natural frequency obtained by the finite element method was 46.5 Hz, and the theoretical calculation was 44.5 Hz. The relative error between the two was very small, only 4.3%. It indicates that the meshing sizes above were feasible, which provided a basis for the correct structural dynamics calculation.

3.2. De-Icing Criteria

The key factor of de-icing prediction research is the de-icing criteria. According to [9], there are two main de-icing criteria. One is to consider only a single strength factor at the ice-skin interface, and the other is to consider the tensile and shear stresses at the ice-skin interface. However, no matter which kind of the de-icing criteria is used, the equivalent stress and the shear stress are both determined values ($\sigma_U = 1.44$ MPa, $\tau_U = 0.4$ MPa). This is contrary to the fact that the equivalent stress and the shear stress between the ice layer and aluminum plate is different under different icing environments.

In this paper, the equivalent stress and the shear stress between the ice and aluminum plate was measured by a tensile test. Figures 2 and 3 show the icing box and tension test device, respectively. The icing test was carried out in an artificial climate chamber. As shown in Figure 4, the height and the diameter of the artificial climate chamber were 11.6 m and 7.8 m, respectively. The wind speed in the built-in wind tunnel can be up to 10 m/s. The sprinkler system consisted of 14 high-pressure water mist nozzles.



Figure 2. Icing box.



Figure 3. Tension sensor.



Figure 4. Artificial icing test.

The temperature curve during whole test was -20 degrees. Note that if a large amount of water is to be poured into the icing box at first, the water easily overflows. This causes icing around the outer surface of the icing box, resulting in inaccurate measurements. Therefore, a better option is to pour a little water into the icing box at first until the water in the icing box freezes completely, and repeat this procedure until the icing box is full of ice. In the natural icing environment, the outer surface of the icing box can also freeze. Before the tensile test, the icing around the icing box should be carefully removed so that the measurement result is accurate.

In addition, to improve measurement accuracy, the aluminum plate should be polished with gauze to remove the oxide film and rust on its surface. During the measurement process, the operating speed was controlled so that it accurately read the sensor readings. The results for the adhesion between the ice and the aluminum plate are shown in Table 3.

The tangential force is produced by electro-impulse de-icing system is small, therefore, this paper only needed to consider that the ice layer falls off when the tensile stress between the ice and aluminum

plate is greater than the maximum tensile stress. As shown in Table 3, the maximum tensile stress σ_{\max} between the ice and aluminum plate is

$$\sigma_{\max} = \frac{F_{zave}}{S} = 0.15 \text{ MPa,}$$

where F_{zave} is the average value of the adhesion and S is the area of the ice box, 20.25 cm².

Table 3. The adhesion between the ice and the aluminum plate.

Test Object	Equivalent Stress (kN)
(1)	0.323
(2)	0.325
(3)	0.274
(4)	0.299
(5)	0.289
(6)	0.252
(7)	0.310

The maximum stress σ_{\max} between the ice and aluminum plate obtained in this paper and the result obtained by [21] are not much different. Therefore, it is indicative that the maximum stress σ_{\max} measured by tensile test is correct.

3.3. Result Analysis

3.3.1. Analysis of Experimental Results

The icing test was carried out in natural icing station. The icing results of aluminum plates are shown in Figure 5. Icing thickness was 4 mm, as shown in Figure 6.

The circuit parameters are: voltage: $U_0 = 780 \text{ V}$; charging capacitor: $C = 990 \text{ }\mu\text{f}$; inductance: $L = 19 \text{ }\mu\text{H}$, $L_w = 5 \text{ }\mu\text{H}$. The de-icing results of skin are shown in Figure 7.

It can be seen from Figure 7 that the de-icing rate reached 73.6% after three-pulse. It is indicative that the electro-impulse de-icing system was feasible.



Figure 5. Icing results of the aluminum plate.



Figure 6. Icing thickness.

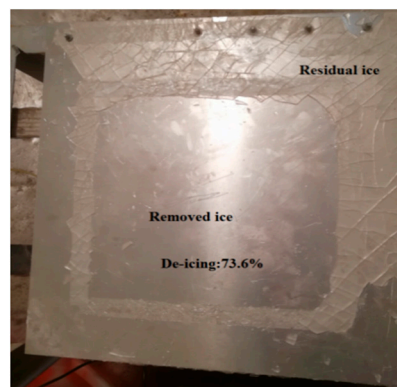


Figure 7. Ice layer shedding process.

3.3.2. Analysis of Calculation Results

A three-dimensional impulse coil-aluminum plate model was established by using Solidworks software. The importing of the model into the Maxwell software is shown in Figure 8a. An external circuit shown in Figure 8b was applied at the cross section of the impulse coil.

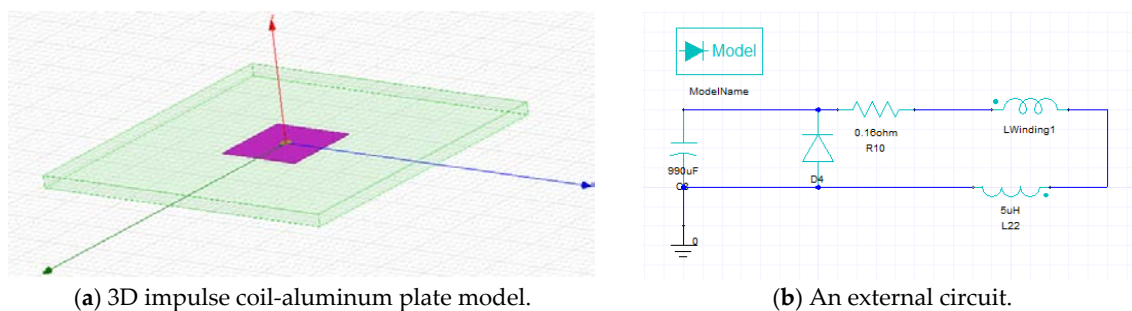


Figure 8. Electro-dynamic simulation model.

Under the action of the instantaneous impulse force F , the equivalent stress between the skin and the ice layer can be obtained by Equations (1)–(3). The de-icing range on the surface of skin was found by using the new de-icing criteria. In order to improve the calculation result accuracy of de-icing prediction, the structural dynamic response was obtained by using the finite element method. The force at different times in different positions of the skin was applied to the corresponding position, as shown in Figure 9. The tangential magnetic field B_r and the eddy current density J_{eddy} at different positions and at different times of the aluminum plate were obtained by simulating. Therefore, the instantaneous impulse force can be obtained by Equation (5), as shown in Figure 10.

$$\vec{F} = \int_V \vec{J}_{eddy} \times \vec{B} dv, \quad (5)$$

where F is the impulse force, J_{eddy} is the eddy current density, and B is the magnetic field.

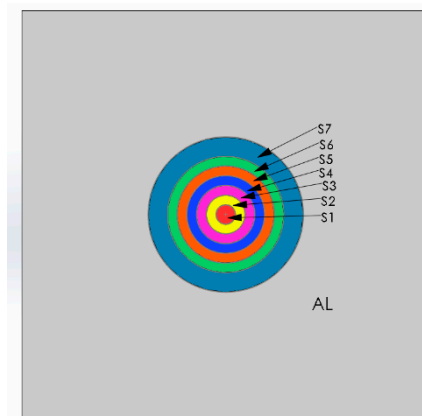


Figure 9. Excitation and loading area.

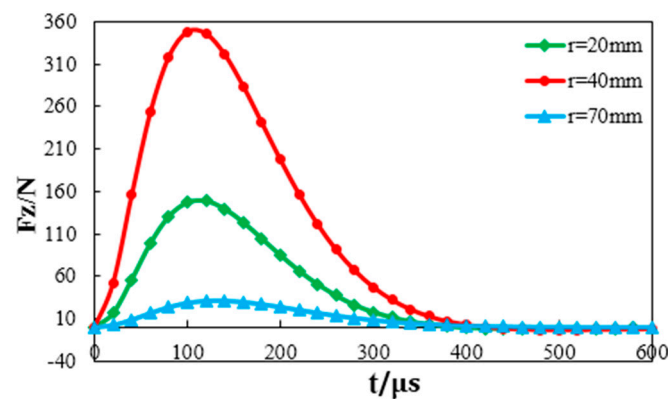


Figure 10. Relationship between force and time.

As shown in Figure 10, the distribution of force increased first and then decreased along the radial distance. The time required to reach the peak pressure was 100 μs , which meets the requirements of narrow pulse width.

According to the process of calculation, the equivalent stress was obtained by the finite element method, as shown in Figures 11 and 12.

The de-icing ratio obtained by the experiment was 73.6% after three pulses, and the de-icing ratio obtained by calculation reached 72.1% after three pulses. Although the de-icing ratio was very close, there was a difference in the de-icing range. The experimental results show that the lower and left side of the ice layer on the surface of the aluminum plate were completely detached, and the calculation results did not fall off. This was due to the effect of the external factors, such as wind speed. During the experiment, the ice on the top of the skin was easily able to fall off under the action of external wind speed. This factor was not considered in the calculation process of de-icing prediction.

In summary, the de-icing ratio obtained by the experiment was 73.6% after three pulses, and the de-icing ratio obtained by calculation reached 72.1% of the de-icing prediction after three pulses. In the range of errors permitted, the comparison between the experimental results and the predicted results indicated that the calculation process of de-icing prediction was correct.

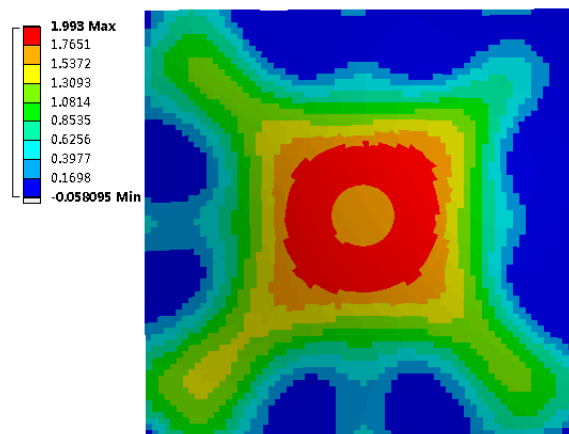


Figure 11. Equivalent stress.



Figure 12. De-icing prediction results.

3.3.3. The Effect of Ice Thickness on the De-Icing Ratio

To study the changes of de-icing ratio with ice thickness while maintaining all other parameters unchanged, we assumed that the thicknesses of ice is 1 mm, 6 mm, 8 mm, and 10 mm, respectively. The de-icing ratios obtained by calculation are shown in Table 4.

Table 4. Effect of ice thickness on de-icing ratio.

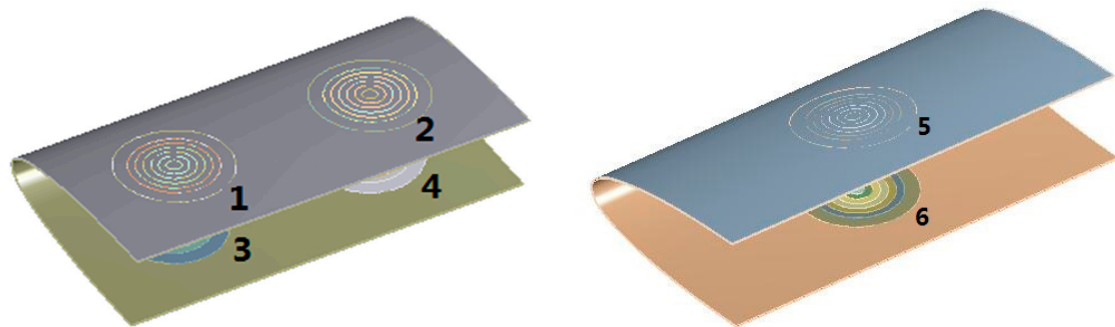
Ice Thickness (mm)	1	6	8	10
De-icing ratio	80.7%	71.04%	53.44%	10.42%

It can be seen from Table 4 that the thicker the ice is, the smaller the de-icing ratio will be while maintaining all other parameters unchanged.

4. Example

The number of pulse coils was greater than one when a real EIDI system was installed on the aircraft, so the number, position arrangement, and start-up time of the multiple coils may have affected the vibration condition to the effect of the ice removing effect. The NACA0012 wing with a chord length of 1000 mm was taken as the research object in this paper. Since the wing was covered with ice mostly in the leading edge part [22–24], it was only necessary to analyze the de-icing ratio of the leading edge of the wing. A three-dimensional wing leading edge-ice layer model was established by using Solidworks, as shown in Figure 13. Its length along the chord was 300 mm, the length along the

exhibition was 600 mm, and the span of one bay of the leading edge was 300 mm. The thickness of the leading edge was 1.5 mm and the thickness of the ice layer was 1.0 mm.



(a) Electro-impulse de-icing system with four coils. (b) Electro-impulse de-icing system with two coils.

Figure 13. Position arrangement of multiple pulse coils.

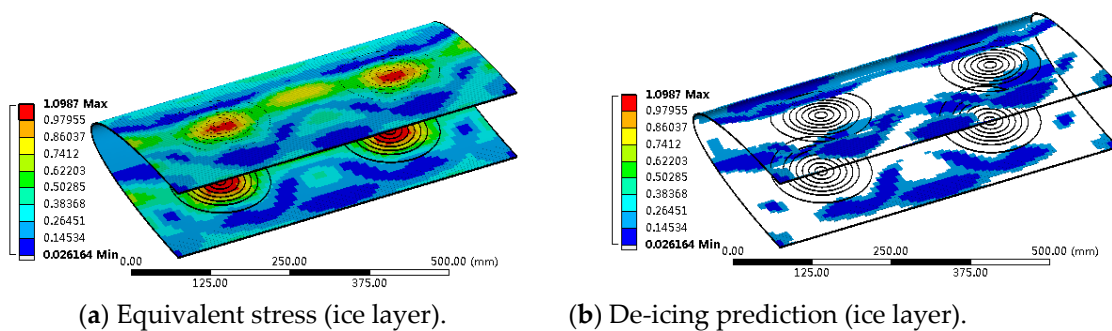
4.1. Position Arrangement of the Multiple Coils

In order to study the influence of multiple coils on the de-icing ratio, the single coil simulation method was extended to a multiple coil simulation. Regarding the possibilities for weight reduction of EIDI systems, it was also important to determine the minimum number of coils, that is, whether it is necessary to place a coil in every bay of the leading edge. Because the established model was symmetrical, it only needed to select two or four pulse coils. The position arrangements of the four and two pulse coils are as shown in Figure 13a,b, respectively. The structure dynamics simulation of the four coil system was carried out. If only two of four coils were used, it was divided into three kinds of modes, which are respectively Mode 1, Mode 2 and Mode 3, as shown in Table 5. Mode 4 is the two coil system.

Table 5. Four kinds of two coils.

Mode	(1)	(2)	(3)	(4)
Position arrangement	1, 2 or 3, 4	1, 3 or 2, 4	1, 4 or 2, 3	5, 6

The de-icing results of simultaneous vibration of the four coils are shown in Figure 14. For the electro-impulse de-icing system of the four coils, the de-icing results of the simultaneous vibration are shown in Figures 15–17, in which only two of four coils were used. The de-icing results of simultaneous vibration of the two coils are shown in Figure 18.



(a) Equivalent stress (ice layer). (b) De-icing prediction (ice layer).

Figure 14. Electro-impulse de-icing system of four coils.

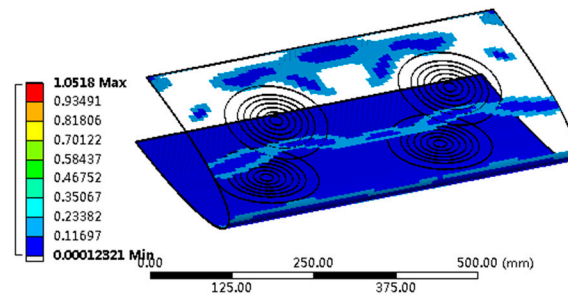


Figure 15. 1, 2 or 3, 4 of four coils are used (Mode 1).

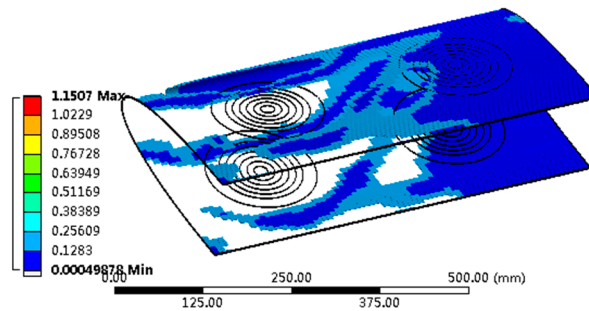


Figure 16. 1, 3 or 2, 4 of four coils are used (Mode 2).

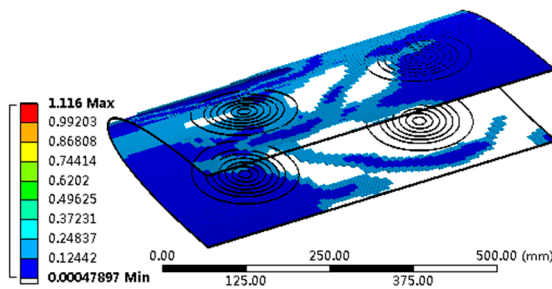


Figure 17. 1, 4 or 2, 3 of four coils are used (Mode 3).

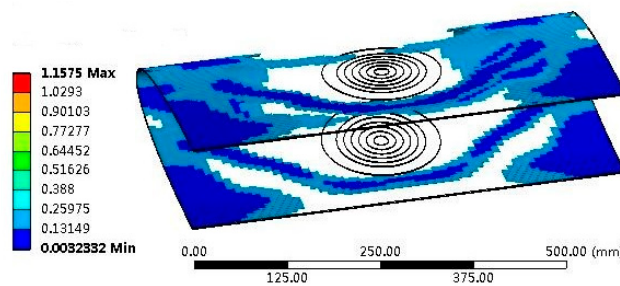


Figure 18. Electro-impulse de-icing (EIDI) system of two coils (Mode 4).

It can be seen from Figures 14–18 that the de-icing ratios varied with the number or the position arrangement of pulse coils. In addition, the ice layer fell off within a certain distance from the central position of the pulse coil. This was because the magnetic field was stronger in this range. The stronger the magnetic field, the bigger its magnetic force, thus, the ice layer was easy to fall off. The de-icing ratios of the several models above of the electro-impulse de-icing system are shown in Table 6.

It can be seen from Table 6 that for the electro-impulse de-icing system with two pulse coils, the de-icing ratio of Modes 1, 2, and 3 were only 36.19%, 38.35%, and 41.43%, respectively. The de-icing ratio of Mode 4 was 47.22%, which was the maximum. The de-icing ratio of the electro-impulse de-icing system with four coils was 69.83%. According to the experimental results, the ice layer at the

boundary of the skin would also fall off under the influence of external factors. Therefore, from the perspective of not affecting aircraft flight and low energy consumption, the position arrangement of Mode 4 is optimal for the research objects mentioned above.

Table 6. De-icing ratio comparison.

	Electro-Impulse De-Icing System with Four Coils	Electro-Impulse De-Icing System with Two Coils			
		Mode 1	Mode 2	Mode 3	Mode 4
De-icing ratio	69.83%	36.19%	38.35%	41.43%	47.22%

4.2. The Effect of Start-Up Time of Pulse Coil

In the case of Mode 4, the starting times of the pulse coils 5 and 6 were different, and the de-icing ratios obtained by the calculation were different. Take as an example the system with two pulses, pulse coil 5 started to work at 0 μ s, and pulse coil 6 started to vibrate from 0 μ s, 100 μ s, 600 μ s, and 1200 μ s, respectively. The vibration de-icing result at 0 μ s was the same as that of Mode 4. The results of the ice layer detachment of pulse coil 6 starting to work from 100 μ s is shown in Figure 19b. Figure 19c shows the pressure waveform at the coil radial direction $r = 30$ mm. The results of the ice layer detachment of pulse coil 6 starting to work from 600 μ s and 1200 μ s are shown in Figures 20 and 21, respectively.

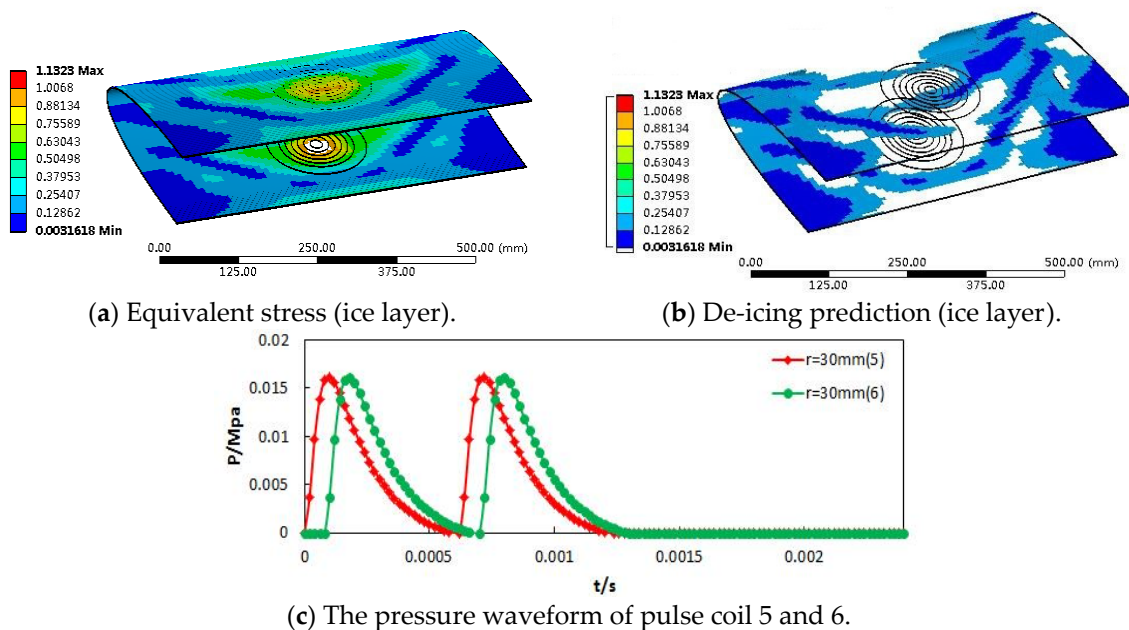


Figure 19. De-icing results of pulse coil 6 starting 100 μ s later than coil 5.

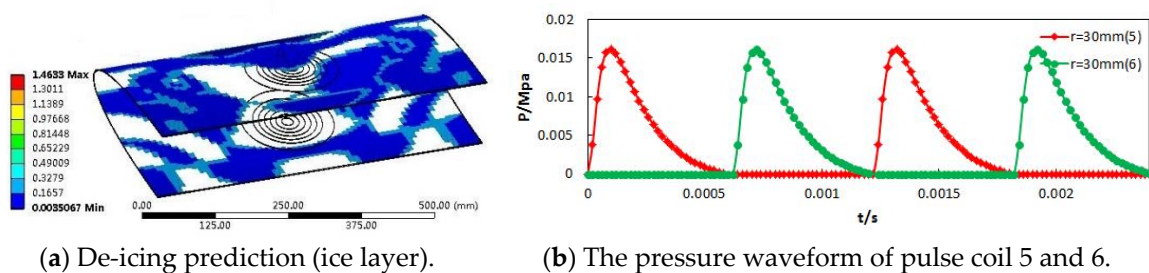


Figure 20. De-icing results of pulse coil 6 starting 600 μ s later than coil 5.

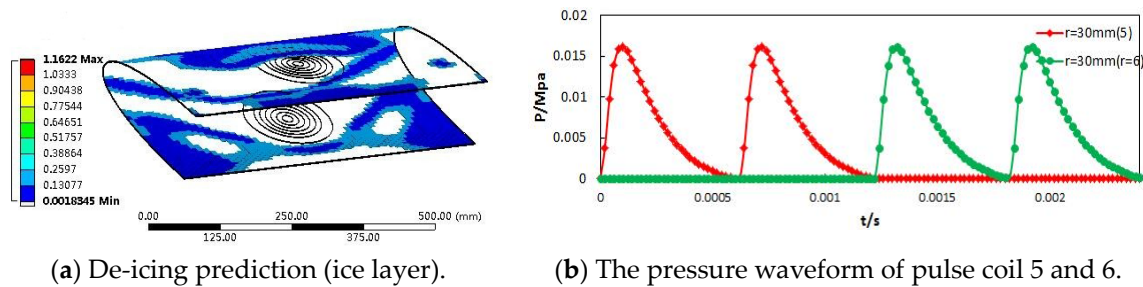


Figure 21. De-icing results of pulse coil 6 starting 1200 μ s later than coil 5.

It can be seen from Figure 19 that the de-icing ratios obtained by calculation were different under the different starting times of pulse coil 6. De-icing prediction results are shown in Table 7.

Table 7. De-icing ratios.

Start Time Delay of Coil 6 with Respect of Start Time of Coil 5	0 μ s	100 μ s	600 μ s	1200 μ s
De-icing ratio	47.22%	51.38%	45.42%	54.03%

It can be seen from Table 7 that if pulse coil 6 started working at the same time as coil 5, or 600 μ s later, the de-icing ratios obtained by calculation were almost the same. This was because the interval between the continuous applied force at the same position of the wing was the same. However, if pulse coil 6 started working 1200 μ s later than coil 5, the de-icing ratio was the largest, which served as a guiding function for the subsequent pulse coil vibration control.

5. Conclusions

- (1) In an artificial climate chamber, the maximum adhesion between ice layer and aluminum plate was 0.15 Mpa obtained by the tensile test. Since the tangential force generated by the electro-impulse de-icing system was very small, as long as the equivalent stress between the ice layer and the aluminum plate was greater than 0.15 Mpa, the ice layer fell off, which laid a foundation for the simulation calculation of the subsequent electro-impulse de-icing system.
- (2) We replaced the skin with an aluminum plate and built a platform of the electro-impulse de-icing system in an artificial climate chamber. The range of de-icing of the skin surface obtained by the experiments was recorded under different pulse times. A three-dimensional aluminum plate-ice layer model was established by using Solidworks. The results obtained by the three-step calculation of electrodynamics, structural dynamics, and de-icing prediction were compared with the experiment results of the electro-impulse de-icing system. It was indicative that the calculation process of de-icing prediction obtained by this paper was correct.
- (3) Taking the leading edge of the NACA0012 wing with a chord length of 1 m as the research object, its length along the chord was 300 mm, the length along the exhibition was 600 mm, and the span of one bay of the leading edge was 300 mm. The leading edge had a thickness of 2.0 mm and the ice thickness was 4.0 mm. The de-icing ratio of the four pulse coil system was 69.83%. Under the action of the two pulse coil system, the de-icing ratio of Mode 1, 2, and 3 was lower, and the de-icing ratio of Mode 4 reached 47.22%. From the perspective of low energy consumption and without affecting the safe flight of the aircraft, the aforementioned structure was best to select the electro-impulse de-icing system with two pulse coils.
- (4) With regard to the electro-impulse de-icing system with two-pulse coils, the starting time of the pulse coil was different, and the de-icing effect was different. If pulse coil 6 started working at the same time as coil 5 or 600 μ s later, the de-icing ratio was almost the same. This was because the interval between the continuous applied pressure at the same position of the wing was the

same. However, if pulse coil 6 started working 1200 μ s later than coil 5, the de-icing ratio was the largest, which served as a guiding function for the subsequent pulse coil vibration control.

Author Contributions: Conceptualization, X.J. and Y.W.; methodology, Y.W.; software, Y.W.; writing—original draft preparation, Y.W.; writing—review and editing, X.J. and Y.W.

Funding: (1) This research was funded by the National Natural Science Foundation of China, grant number 51637002. (2) This research was funded by State Grid Science and Technology Project: Research on numerical prediction technology of grid icing in micro-topography and micro-meteorological areas, grant number 521999180006. (3) This research was funded by the Fundamental Research Funds for the Central Universities, grant number 2019CDXYDQ0010.

Acknowledgments: The presented work is part of the electro-impulse de-icing system for aircraft, which is funded by State Grid Corporation of China.

Conflicts of Interest: The authors declare no conflict of interest.

References

1. Zumwalt, G.W.; Schrag, R.L.; Bernhart, W.D.; Friedberg, R.A. *Electro-Impulse De-Icing Testing Analysis and Design*; Technical Report; NASA CR-4175; NASA: Washington, DC, USA, September 1988.
2. Lynch, F.T.; Khodadoust, A. Effects of Ice Accretions on Aircraft Aerodynamics. *Prog. Aerosp. Sci.* **2001**, *37*, 669–767. [[CrossRef](#)]
3. Anon. “Reduce Dangers to Aircraft Flying in Icing Conditions”, Most Wanted Transportation Safety Improvements-Federal Issues: Aviation [Online Bulletin], National Transportation Safety Board Recommendations and Accomplishments. Available online: http://www.nts.gov/Recs/most-wanted/air_ice.htm (accessed on 17 November 2005).
4. Feher, L.; Thumm, M. Design of avionic microwave de-/anti-icing systems. In *Advances in Microwave and Radio Frequency Processing*; Springer: Berlin/Heidelberg, Germany, 2006; pp. 695–702.
5. Martin, C.A.; Putt, J.C. Advanced pneumatic impulse ice protection system (PIIP) for aircraft. *J. Airc.* **1992**, *29*, 714–716. [[CrossRef](#)]
6. Thomas, S.K.; Cassoni, R.P.; MacArthur, C.D. Aircraft anti-icing and de-icing techniques and modeling. *J. Airc.* **1996**, *33*, 841–854. [[CrossRef](#)]
7. Li, Q. Research on the Experiments, Theories, and Design of the Electro-Impulse De-Icing System. Ph.D. Thesis, Nanjing University of Aeronautics and Astronautics, Nanjing, China, 2012.
8. Li, Q.Y.; Bai, T.; Zhu, C.L. De-icing excitation simulation and structural dynamic analysis of the electro-impulse de-icing system. *Appl. Mech. Mater.* **2011**, *66–68*, 390–395.
9. Li, G.; He, J.; Lin, G. Analysis on structural dynamics of simplified EIDI system. *J. Beijing Univ. Aeronaut. Astronaut.* **2015**, *5*, 1–6.
10. Li, Q.Y.; Zhu, C.L.; Bai, T. Simplification of de-icing excitation and influential factors of the electro-impulse de-icing system. *J. Aviat.* **2012**, *25*, 1384–1393. (In Chinese)
11. Moehle, E.; Haupt, M.; Horst, P. Coupled Magnetic and Structural Numerical Simulation and Experimental Validation of the Electro-Impulse De-Icing. In Proceedings of the 54th AIAA/ASME/ASCE/AHS/ASC Structures, Structural Dynamics, and Materials Conference, Boston, MA, USA, 8–11 April 2013.
12. Endres, M.; Sommerwerk, H.; Mendig, C.; Sinapius, M.; Horst, P. Experimental study of two electro-mechanical de-icing systems applied on a wing section tested in an icing wind tunnel. *CEAS Aeronaut. J.* **2017**, *8*, 429–439. [[CrossRef](#)]
13. Sommerwerk, H.; Horst, P.; Bansmer, S. Studies on electronic impulse de-icing of a leading edge structure in an icing wind tunnel. In Proceedings of the 8th AIAA Atmospheric and Space Environments Conference 2016, Washington, DC, USA, 13–17 June 2016.
14. Feng, J.X.; Ruan, J.H.; Li, Y.B. Study on intelligent vehicle lane change path planning and control simulation. In Proceedings of the 2006 IEEE International Conference on Information Acquisition, Weihai, China, 20–23 August 2006; pp. 683–688.
15. Labeas, G.N.; Diamantakos, I.D.; Sunaric, M.M. Simulation of the electroimpulse de-icing process of Aircraft Wings. *J. Airc.* **2006**, *43*, 1876–1885. [[CrossRef](#)]

16. Zhang, Y.; Dong, W.; Wang, B.; Liao, K. Study on de-icing criterion of electro-impulse de-icing simulation. *Comput. Eng. Appl.* **2012**, *48*, 232–233.
17. Chu, M.C.; Scavuzzo, R.J. Adhesive Shear Strength of impact Ice. *AIAA J.* **1991**, *29*, 1921–1926.
18. Pommier-Budinger, V.; Budinger, M.; Rousset, P.; Dezitter, F.; Huet, F.; Wetterwald, M.; Bonaccorso, E. Electromechanical Resonant Ice Protection Systems: Initiation of Fractures with Piezoelectric Actuators. *AIAA J.* **2018**, *11*, 4400–4409. [[CrossRef](#)]
19. Jiang, J.W.; He, F. *Finite Element Method and Its Application*; China Machine Press: Beijing, China, 2012.
20. Dong, W.; Ding, J. Experimental study on the ice freezing adhesive characteristics of metal surface. In Proceedings of the 51st AIAA Aerospace Sciences Meeting including the New Horizons Forum and Aerospace Exposition, Grapevine, TX, USA, 7–10 January 2013.
21. Sun, J. *Modal Test and Analysis of Automobile Engine Structure*; Chongqing University: Chongqing, China, 2013.
22. Hu, H. *Mechanical Vibration Foundation*; Beijing University of Aeronautics and Astronautics Press: Beijing, China, 2005.
23. Al-Khalil, K.; Horvath, C.; Miller, D.; Wright, W. Validation of NASA thermal ice protection computer Codes: Part III-The validation of ANTICE. In Proceedings of the AIAA 35th Aerospace Sciences Meeting and Exhibit, Reno, NV, USA, 6–9 January 1997. Paper 97-0051.
24. Wright, W.B. *User Manual for the NASA Glenn Ice Accretion Code LEWICE Version 2.0*; NASA CR-209409; QSS Group, Inc.: Cleveland, OH, USA, 1999.



© 2019 by the authors. Licensee MDPI, Basel, Switzerland. This article is an open access article distributed under the terms and conditions of the Creative Commons Attribution (CC BY) license (<http://creativecommons.org/licenses/by/4.0/>).